Drift-flux modeling of hyper-concentrated solid-liquid flows in dredging applications

Goeree, Joep

DOI
10.4233/uuid:2d432d11-cce4-40de-b951-e89dfebbef27

Publication date
2018

Document Version
Final published version

Citation (APA)
Goeree, J. (2018). *Drift-flux modeling of hyper-concentrated solid-liquid flows in dredging applications*. [Dissertation (TU Delft), Delft University of Technology]. https://doi.org/10.4233/uuid:2d432d11-cce4-40de-b951-e89dfebbef27

Drift-flux modeling of hyper-concentrated solid-liquid flows in dredging applications

Drift-flux modeling of hyper-concentrated solid-liquid flows in dredging applications

Proefschrift

ter verkrijging van de graad van doctor
aan de Technische Universtiteit Delft,
op gezag van de Rector Magnificus Prof.dr.ir. T.H.J.J. van der Hagen,
voorzitter van het College voor Promoties,
in het openbaar te verdedigen
op woensdag 26 september 2018 om 14:30 uur
door

Johannes Cornelis GOEREE

Werktuigbouwkundig ingenieur
geboren te Geldrop.

Dit proefschrift is goedgekeurd door de promotor:

Prof.dr.ir. C. van Rhee

Copromotor:

Dr.ir. G.H. Keetels

Samenstelling promotiecommissie:

Rector Magnificus,	voorzitter
Prof.dr.ir. C. van Rhee,	Technische Universiteit Delft
Dr.ir. G.H. Keetels,	Technische Universiteit Delft
Onafhankelijke leden:	
Prof.dr.ing. V. Matoušek,	Czech Technical University
Prof.dr. R.F. Mudde,	Technische Universiteit Delft
Prof.dr. J.G.M. Kuerten,	Technische Universiteit Eindhoven
Prof.dr. R.S. Sanders,	University of Alberta
Overig lid:	
Prof.dr.ir. H.W.M. Hoeijmakers,	Universiteit Twente
Reserve lid:	
Prof.dr.ir. A.P. van 't Veer,	Technische Universiteit Delft

Keywords: hydraulic transport, solids, numerical, dredging, drift-flux

Printed by: Ridderprint, The Netherlands
PRINTED IN THE NETHERLANDS

Financial support
The work presented in this thesis was financed by Royal IHC and Ondernemend Nederland.

Voor Joanne, Floortje en Nina

Contents

Summary

Transporting large amounts of sand is mostly done hydraulically in dredging and mining. This method of sand transport is efficient and is used in land reclamation projects or extraction of oil from tar sands. Large pieces of equipment, such as pumps and pipe line systems, dredging vessels etc., are used enabling the sand water mixtures to be transported hydraulically. Therefore, a good understanding of the hydrodynamical behavior of sand water mixtures is eminent in order to further improve these kind of systems.
In this thesis a numerical model has been developed which describe the hydraulic behavior of sediment fluid mixtures. In the model the volume concentration of solids varies from 0.0 to 0.6. Moreover, the model is able to describe mixtures consisting of multiple sized sand particles.
Sand water mixtures, or in general solid fluid mixtures, consist of individual sand particles suspended in water. At todays available computing power it is impossible to calculate all the states governing the motion of the particles. Therefore, a continuum approach is used, describing averaged quantities of sand water mixtures. The drift-flux model is a continuum approach describing mixture flows. The model is able to describe mixture flows with multiple particles sizes. A major advantage is that only one momentum equation needs to be solved, saving computational costs.
The motion of the mixture flow is described with the Navier-Stokes equations. This set of partial differential equations are discretized on a Cartesian equidistant grid using the Finite Volume Method (FVM). The motion of the mixture flow solved numerically using the de fractional step method. The WALE LES (Large Eddy Simulation) model is employed as a turbulence model. The LES model resolves eddies at grid level. The eddies at sub grid level are solved using a spatial filter. Transport equations are used for the motion of each sediment fraction. A bounded numerical scheme, preventing unphysical over and undershoots, is used as discretization for the advective part of the

transport equation. These bounded schemes are called TVD (Total Variation Diminishing). The settling of particles is accounted for using an additional particle velocity and is called a drift velocity. This drift velocity depends on the particle size and the volume concentration of solids, i.e. sediment particles, present in the mixture. Particles settle at a lower velocity, compared to the terminal settling velocity of a single particle in an infinite domain, when the volume concentration of sediment is increased. This effect is called hindered settling. In this work the relation of Richardson and Zaki has been used describing the hindered settling effect. Here open channel flow experiments have been used as validation for the flow model. Velocity and concentration profiles from experiments have been compared with velocity and concentration profiles from the numerical results. The agreement between the numerical and experimental results are satisfactory. Except for one experiment, it is suspected that the length of the channel in the experimental setup was not sufficient in order for the mixture flow to reach steady state. However, this needs further investigation, preferably with additional open channel flow experiments with sufficient channel length.

When dealing with a sediment bed, i.e. a dense granular flow, the mixture properties change. Dense granular flows, with a volume concentration of solids of approximately $\alpha_t = 0.5\,[-]$, has been modeled as a non-Newtonian Bingham like liquid. These liquids are characterized by a threshold, the so-called yield stress. If the shear stress is below this threshold the liquid is solid and if the shear stress exceeds this yield stress the liquid flows. A Coulomb friction law is employed, which determines the value of the yield stress. The friction law depends on a friction factor and a pressure contribution. The friction factor is a function of a dimensionless shear number. The pressure contribution consists of two components, the submerged weight and the pore pressure. The pore pressure depends on the particle size, the initial volume concentration and the shear rate of the material. The initial volume concentration of a dense granular flow is important in the flow behavior. The behavior described above has been incorporated in the numerical model and validated with experimental results. From literature it is known that two different behaviors can be observed. This has been investigated with a granular collapse of a column. These flow behaviors correspond to a loose and dense regime. When dealing with an initial loose packing the sediment flows rapidly and the run-out length of the deposit is large. This in contrast to the initial dense packing. The material flows much more slowly. The final angle of the deposit is more or less constant and steeper in comparison with the loose initial packing. Moreover the run-out

length of the deposit is small in comparison with the loose regime. In this work the loose and dense regime has been used as a validation of the numerical model. The numerical results compare well with the experimental results.

Samenvatting

Het transporteren van grote hoeveelheden zand gebeurt voornamelijk hydraulisch in de bagger- en mijnbouwindustrie. Deze methode van zandtransport is efficiënt en wordt gebruikt in landaanwinningsprojecten of extractie van teer uit teerzand. Grote componenten, zoals pompen en pijpleidingsystemen of baggerschepen, worden gebruikt om zandwatermengsels hydraulisch te transporteren. Daarom is een goed begrip, van het hydrodynamisch gedrag van zandwatermengsels, van groot belang om dit soort systemen verder te verbeteren.
Een numeriek model is ontwikkeld, in dit proefschrift, dat het hydraulische gedrag van zand watermengsels beschrijft. In het model varieert de volume concentratie van zand van 0 tot 60 procent. Bovendien, is het model in staat om mengsels te beschrijven die bestaan uit zanddeeltjes van verschillende deeltjesgrootte.
Zandwatermengsels zijn zandkorrels gesuspendeerd in water. Met de huidige beschikbare rekenkracht is het onmogelijk, om alle posities, snelheden en versnellingen van de gesuspeendeerde deeltjes te berekenen. Daarom wordt een continuumbenadering gebruikt om gemiddelde hoeveelheden zandwatermengsels te beschrijven. Het drift-flux model is een continuumaanpak die de beweging van suspensies beschrijft. Het model beschrijft suspensies van zand en water, met meerdere deeltjesgroottes van zand. Een groot voordeel is dat slechts één impulsbalans dient te worden opgelost, wat de rekentijd reduceert. De bewegingsvergelijking van een vloeistof, zoals een zandwatermengsel, wordt beschreven door de Navier-Stokes vergelijkingen. Deze set partiële differentiaalvergelijkingen wordt, in dit werk, op een cartesiaans equidistant rooster gediscretiseerd met behulp van de Finite Volume Method (FVM). Deze vergelijkingen worden vervolgens numeriek opgelost met behulp van de fractional-step method. Het WALE LES (Large Eddy Simulation) model wordt gebruikt als turbulentiemodel. Het LES-model lost wervels numeriek op, op roosternivo,

terwijl de wervels op subroosternivo worden bepaald met behulp van een ruimtelijk filter. Transportvergelijkingen worden gebruikt voor het transport van elke sedimentfractie. Een numeriek schema, dat negatieve waardes van de volumeconcentratie voorkomt, wordt gebruikt voor het advectieve deel van de transportvergelijking. Dit soort schema's worden TVD (Total Variation Diminishing) genoemd. Het bezinken van deeltjes wordt gedaan met behulp van een extra deeltjessnelheid, de zogenaamde driftsnelheid. Deze driftsnelheid hangt af van de deeltjesgrootte en van de volumeconcentratie van de gesupendeerde deeltjes.
Deeltjes in een suspensie, bezinken bij een lagere snelheid, vergeleken met de snelheid van een enkel deeltje in een oneindig domein. Dit effect wordt hindered settling genoemd. Hier wordt de relatie van Richardson en Zaki gebruikt. Deze relatie beschrijft het effect van een lagere bezinksnelheid als functie van de volume concentratie van deeltjes in een suspensie.
Ter validatie van het model zijn, onder andere, experimenten van een open kanaalstroom gebruikt. Snelheids- en concentratieprofielen uit experimenten zijn vergeleken met numerieke resultaten. De overeenstemming tussen de numerieke en experimentele resultaten is bevredigend. Eén experiment vormt hierop echter een uitzondering. Het vermoeden is dat de lengte van het kanaal bij het experiment onvoldoende was voor een stabiele eindtoestand. Dit moet echter verder worden onderzocht, dit bij voorkeur met aanvullende experimenten waarbij kanaallengte voldoende groot is gekozen.
De eigenschappen van een zandwatermengsel veranderen, in geval van een sedimentbed. Dit gebeurt bij een volumeconcentratie vanaf ongeveer 50 procent Er wordt dan gesproken van een dicht granulair medium. Het dynamisch gedrag van deze dichte zandwatermengsels is gemodelleerd als een niet-Newtonse, Bingham-achtige vloeistof. Een Bingham-vloeistof wordt gekenmerkt door een drempelwaarde, de zogenaamde zwichtspanning. Indien de schuifspanning lager is dan de zwichtspanning, dan gedraagt de vloeistof zich als een vaste stof. Als de schuifspanning de zwichtspanning overschrijdt, dan gedraagt het materiaal zich als een vloeistof. De waarde van de zwichtspanning wordt bepaald met behulp van Coulombse wrijving. Deze is afhankelijk van een wrijvingscoefficiënt en een druk.
De wrijvingscoefficiënt is een functie van een dimensieloos getal, wat afhankelijk is van de afschuifsnelheid van het mengsel. De druk bestaat uit twee componenten, het onderwatergewicht en de poriëndruk van het sediment. De poriëndruk hangt af van de deeltjesgrootte, de initiële volumeconcentratie en de afschuifsnelheid van het materiaal. De initiële volumeconcentratie van een

dichte granulaire stroming is belangrijk in het stromingsgedrag. Het hierboven beschreven gedrag is opgenomen in het numerieke model en gevalideerd met experimentele resultaten.
Het is bekend uit de literatuur dat een dicht granulair medium zich op twee manieren kan gedragen. Dit is onderzocht met een experiment, waarbij een ondergedompelde sedimentkolom bezwijkt onder het eigen gewicht. Hierbij is er onderscheid gemaakt, in het experiment, tussen een los-en dicht gepakt sediment. Bij een losse pakking is de bezwijksnelheid en de lengte van het sediment van de sediment groot. Dit in tegenstelling tot de aanvankelijke dichte pakking. Het materiaal stroomt, in dat geval, veel langzamer. De uiteindelijke hellingshoek, bij een initiëel dichte pakking, is steiler ten opzichte van de losse initiële pakking. Bovendien is de lengte van de uiteindelijke afzetting, bij een initiëel dichte pakking, kleiner in vergelijking met de losse initiële pakking.
In dit werk is het numerieke model voor zowel een losse en dichte initiële pakking gevalideerd met de experimenten. De numerieke resultaten komen goed overeen met de experimentele resultaten.

List of Tables

List of Figures

Chapter 1

Introduction

1.1 Background

Hydraulic transport of sediment is an efficient way of transporting large amounts of solids. This method is commonly used in the dredging and the hydraulic mining. Hydraulic mining was originally used in the Roman empire around the year zero Anno Domini in the gold mine of Las Médulas in Spain, see Andreau (1991). A good example of the use of hydraulic transport of sediment in mining is the extraction of oil from tar sands in Canada, CAPP (2018).

Land reclamation projects have been carried out mainly using hydraulic transport of sediment. The construction of the Tweede Maasvlakte, the Hamad International Airport in Doha, Qatar, and the world-famous Palm Islands in Dubai are just a few examples of such projects, see DEME (2014) and VanOord (2001) respectively.

The sand is transported to the reclamation site using a dredging vessel. The sand is loaded and stored in a hopper hydraulically using Trailer Suction Hopper Dredgers (TSHD's) equipped with large dredge pumps. TSHD's are connected to pipelines which deliver the sediment-water mixtures to the land reclamation sites. More information on TSHD's can be found in Bray et al. (1997). The hydraulic transport of sediment comes at a high cost and

Figure 1.1: Vox Maxima, owned by dredging company Van Oord, constructing an island using the method rain-bowing.

Figure 1.2: Dredge pump typical dimensions are 3 $[m]$ and a power of 5 $[MW]$.

maintenance of equipment, such as dredge pumps, pipes, etc. due to abrasive wear. A good understanding of the interaction between water and the suspended solids (natural grains) processes involved is important. Understanding of the fundamental physical processes at hand contributes to optimization of the design of components (e.g. dredge pumps, pipes, valves etc.). Improvements can be made in hopper offloading, energy use, or abrasive wear of components. However, it is impossible to make optimizations and design improvements without a model describing the flow of mixtures. Therefore, this research is the first step in answering these questions.

Figure 1.1 shows the TSHD Vox Maxima, rain-bowing dredged sand to the shore, this method is used to construct an island. The ship was built by Royal IHC for the Dutch dredging company Van Oord. Figure 1.2 shows dredge pumps, the pumps have a dimension of about 3 $[m]$ and a pump power ranging from $3 - 5$ $[MW]$. These pumps are installed on dredging vessels.

Dredging is a broad discipline and in this section, a very short introduction is given. An elaboration of the topics in dredging engineering can be found in Herbich (2000) and an overview of hydraulic transport technology can be found in Van den Berg (2013) or Miedema (2016) for instance.

1.2 Hydraulic sediment transport in dredging

Several pieces of equipment are used to excavate and transporting sediment hydraulically in dredging. A commonly used vessel is highlighted here shortly,

namely the Trailer Suction Hopper Dredger (TSHD). This is done with the emphasis on the processes in which sand water mixtures play an important part. Another important piece of equipment is the Cutter Suction Dredger (CSD). The workings of this vessel and other dredge vessels can be found in Herbich (2000) and will not be covered here.

Trailer Suction Hopper Dredger (TSHD)

A Trailer Suction Hopper Dredger (TSHD) is a vessel which is used for dredging waterways, maintaining and deepening harbors and canals or constructing new land. Other uses of a TSHD is the replacement of sand which is eroded by waves and storms at beaches. A TSHD has a large loading bin, which is called a hopper. Oftentimes, a TSHD is characterized by the volume of the hopper and is a measure of how much sand a vessel can carry. The hopper itself is filled using a large dredge pump. The power of these pumps are typically several megawatts and the typical size is in the range of meters. The TSHD is equipped with one or two suction pipes, which are connected to the pumps.

Hopperloading

When loading the hopper the pipes are lowered to the sea-bed and the sand is sucked up via a drag-head. In most cases, the sand, at the sea-bed, is fluidized using so-called jets, which are mounted in the drag-head. Now the sand/water mixture is transported hydraulically through the suction tube, passing the pump and eventually discharged in the cargo hold, the hopper. In the hopper, a separation process of sediment takes place, caused by gravity. In general, not all the sediment settles in the hopper. Finer fractions of the sediment along with the excess water flow through the overflow. These fine fractions or small particles are eventually spilled in the environment. The most interesting range for the particle diameter, at which the overflow losses are most profound, is approximately between $100 - 300[\mu m]$, see Van Rhee (2002).

Discharging

Discharging the hopper can be done in several ways. The most obvious is discharging the hopper via doors which are installed at the bottom of the vessel. By opening these bottom doors the sand disappears into the surrounding water by the action of gravity. Another way of unloading a hopper is by rain-bowing,

shown in Figure 1.1. Sand in the hopper is fluidized with water using high-pressure pumps and pumped ashore with dredge-pumps. The sand is discharged by using two methods. One method is the so-called rainbow method, where the sand mixture is discharged via a nozzle, mounted at the front of the vessel, into the environment. This method is applied when making land close to the vessel. The other method is to connect the vessel to a pipe and pump the mixture to shore over long distances (typically a couple of kilometers).

From this short description, of the workings of a TSHD, it can be immediately seen that in several processes hydraulic transport of sand is involved. These processes range from erosion and fluidization of sand, hydraulic (turbulent) transport through a pipe, passing of the sand/water mixture through the pump, up until the settling of sand in the hopper. Hydraulic transport of particles is the key part in dredging. Therefore, research in this field is of great importance in order to understand and eventually further improve dredge operations.

1.3 Related work

Hydraulic transport of sediment (sand) in dredging engineering has been subject to research for many decades. Hydraulic pressure loss and the amount of suspended sand in the pipeline is an important factor, for instance in the construction design of a land reclamation project. These factors govern the number of pumps and pipes to be used and the deployment of dredging vessels. All these have cost implications for executing a project. A two-layer model was developed by Matousek (1997) describing a steady and unsteady flow of suspended sand, or slurries. This model was based on the two layer models of Wilson (1976) and Gillies (1993). Moreover, the model of Matousek, based on the work of Gillies and Wilson, was validated with smaller scale laboratory and full scale field tests. This was done with both horizontal and inclined pipes. The experimental results of the concentration profiles and hydraulic pressure losses, see Matousek (2002), are used nowadays as a benchmark for CFD (Computational Fluid Dynamics) codes, Swamy et al. (2015) or Nabil et al. (2014).

A numerical investigation, based on the kinetic theory of granular flows, in combination with a RANS (Reynolds-averaged Navier-Stokes) turbulence model, was conducted by Ekambara et al. (2009). This was done for a pipe flow for mixtures consisting of one particle size. In the study, the commercial CFD

code Ansys CFX was used. In the paper, a wide range of flows was compared with existing experimental data of concentration profiles. The agreement was close between the experimental data and numerical results

The rich mineral deposits at about $1400 - 5000\,[m]$ below the ocean's surface has attracted renewed attention over the past decade, see Scott (2006). A possible solution transporting these deposits from the deep sea is by continuous hydraulic transport using booster stations. Recently, Van Wijk (2016), flow assurance was investigated for such a hydraulic Vertical Transport System (or VTS in short). Especially clogging of such a system poses a big risk in the mining operation. The clogging can be caused by differences in transport velocities of particles fractions. This difference in velocity is due to the difference in sizes and densities of the particles.

The earlier mentioned overflow losses can be up to $30\% - 40\%$ of the total hopper load and strongly depends on the particle size distribution, PSD, see Van Rhee (2001). Different models, see Ooijens (1999) and Vlasblom (1995), were used quantifying the overflow losses, and are based on the model of Camp (1946). However, the details of the velocity field and the sediment distribution in the hopper is not predicted by these models. This has been done by Van Rhee (2002), who developed a validated 2D CFD model using a RANS turbulence model. The settling of a particle decreases when the volume concentration of solids is increased. This is accounted for by using the hindered settling formulation of Richardson and Zaki, see Richardson and Zaki (1954b). The 2D CFD model of Van Rhee (2002) predicts the overflow losses, using multiple fractions sizes, accurately. Moreover, the sediment distribution and the velocity field in the hopper can be examined using the simulation. The spillage of the overflow losses into the environment on a large scale was investigated by De Wit (2014). A 3D CFD model, using a Large Eddy Simulation (LES) turbulence model, was developed investigating the dispersion of overflowed fine sediments from the hopper, in the vicinity, approximately $300\,[m]$, of a TSHD.

For suspensions with a volume concentration higher than of approximately 50% a regime change of the flow takes place. The viscous forces dominate over the inertia forces in the suspension. This is a dense granular flow and the material can be described as a fluid using stress-strain or stress deformation relations, so-called constitutive equations. A constitutive relation describing the flow of dry granular flow was found by Jop et al. (2006). In this model, a so-called friction law was proposed which depends on a friction coefficient, μ_I,

and the particle pressure, P_p.

Experiments were conducted, see Van Rhee and Bezuijen (1998), investigating the physical principles of breaching of compacted sand while fully submerged in water. Experiments showed the importance of negative pore pressures on the stability of the breach. The slope of the breach can be large as a result of the negative pore pressure. Pore volumes of dense sand are increased as a result of shear deformation. This effect is called dilatancy. The negative pore pressures effectively stiffen the sediment, due to an increased effective pressure, and increases the resistance to shear.

The effect of the initial volume concentration on the flow behavior of dense granular flows was investigated by Rondon et al. (2011). Experiments of the collapse of a dam break, on a small scale, were conducted. This was done by using glass beads, $d_p = 225\,[\mu m]$, with a low, 50%, and high, 60%, initial concentration. When the initial volume concentration of the glass beads was low the dam collapsed rapidly $t < 1\,[s]$. At a dense initial concentration the dam took, $t \approx 60\,[s]$ to collapse.

1.4 Research questions and objective

The following questions can be distinguished in this research:

1. When do the assumptions of the drift-flux model break down?

2. How does a dense granular flow behave and what are the governing (physical) parameters?

The objective of this research is to gain insight in the hydrodynamical behavior of sand water mixtures. The volume concentrations of sediment range from 0% to 60%, i.e. from a dilute suspension to a dense granular flow. The model has to be able to handle multiple particle sizes or fractions. The sediment distribution and the resulting velocity field in the domain need to be resolved. Finally, the model has to take into account different (settling) transport velocities of the fractions.

1.5 Approach

The motion of a fluid is described by the Navier-Stokes equations. This set of partial differential equations are based on Newton's second law and the fluid is assumed to be incompressible. This forms a set of pressure linked equations, where the pressure depends on the velocity and vice versa. Using the incompressibility constraint the pressure and velocity field coupled. By describing each phase as a continuum, the liquid and particulate phase, the motion of each phase is solved separately using a momentum balance. This is done with the so-called Euler/Euler approach and is used often for multiphase flows. The motion of each phase is described and solved numerically using a separated momentum balance. The computational costs are limited in the case of two or three phases. This method has been used by Konijn (2016) simulating a multiphase mixture in hopper loading. However, when dealing with multiple phases or particle sizes this method becomes computational prohibitively large. In the hydraulic transport of sediment, in mining or dredging industry, for instance, the transported sediment consists of multiple fractions or phases. The modeling of these multiple phases needs to be incorporated in the model, at an acceptable computational cost.

Another approach is the so-called drift-flux model, which is a simplification of the Euler/Euler model. The momentum balance for each fraction is summed, yielding one momentum equation which describes the motion of the mixture flow. In turn, the bulk, or mixture, flow is described by the Navier-Stokes equations. The motion of each fraction is described with transport equations. The velocity, of the sediment phase, is governed by the bulk flow and a (small) correction velocity. This correction velocity is the so-called drift velocity. It is assumed that the particle reaction time of particles is rapid. Therefore, a relative fine sediment is described with this model. This drift velocity is determined using a closure relation. In this work the relation of Richardson and Zaki is used, see Richardson and Zaki (1954a) and Mirza and Richardson (1979). This relation accounts for the increased drag of a particle due to the presence of other sediment fractions and hence an increased volume concentration of solids.

A Large Eddy Simulation (LES) model is used as a turbulence model. In the LES model, small length scales are ignored and modeled using a low pass filter. This is done using a spatial filter. Here the WALE (Wall-Adapting Local Eddy-viscosity) model of Nicoud and Ducros (1999) is used.

In this work, a dense granular flow model is used in which sand is assumed to behave as a non-Newtonian fluid. The flow becomes dense when the volume concentration of solids is higher than 50%. The constitutive relations, or stress deformation relations, were introduced by Jop et al. (2006) for dry granular flows and has been applied to investigate collapsing columns, see Staron et al. (2011). When sand is submerged pore pressures play an important role in the hydrodynamical behavior of the sand. The pore pressures depend on the particle size, the volume concentration, and the surrounding fluid viscosity. These are calculated using Poisson's equation.

The resulting partial differential equations, for the Navier-Stokes, transport of sediment fractions and the dense granular flows are solved numerically. The equations are discretized using the Finite Volume Method (FVM) on a collocated grid, see Versteeg and Malalasekera (1995), Ferziger and Peric (1999) or Hirsch (1990) for more information. In a collocated grid all the field variables, such as pressures, velocities, densities etc. are located at the center of a grid cell. However, a collocated grid suffers from pressure velocity decoupling. This decoupling is prevented by using the Rhie and Chow interpolation, see Rhie and Chow (1983). The Navier-Stokes, i.e. the mixture momentum equations are solved with the Fractional Step Method, see Chorin (1968). This method is relatively simple to implement and has been applied successfully simulating flows for the gaming and movie industry, see Stam (1999). In this work, an own developed C++ code was used. An own developed code provides a flexible test environment.

1.6 Outline

The outline is as follows, in Chapter 2, a background is given on the involved physics. The chapter constitutes the foundation of the remainder of this work. In Chapter 3 the Navier-Stokes equations, with a variable density, and the LES turbulence model is introduced. Turbulent closures on the passive scalar transport are discussed. Except for a small drift velocity, turbulent modeling of sediment transport is similar to turbulent transport of a passive scalar quantity. In Chapter 4 the drift-flux model is introduced. First the mixture momentum equations are elaborated and subsequently, an analysis is given of the equation of motion of a single particle, settling in a velocity field. Furthermore, the closure relation of Richardson and Zaki is elaborated in this chapter. In Chapter 5 the numerical implementation is discussed. In

this chapter, the discretization of the partial differential equations using the FVM is given. Furthermore, both an explicit and implicit formulation of the fractional step method is elaborated.

In Chapter 6, the complete numerical model is validated with experimental data found in the literature. The LES WALE turbulence model is validated with a flow between two parallel plates and a plain impinging jet. A numerical batch sedimentation case is validated with experiments, see Klerk et al. (1998). Various hindered settling parameters are varied in order to assess the sensitivity on the outcome of the numerical results. Furthermore, in the same chapter, a benchmark study has been carried out concerning the concentration and velocity profiles of an open channel flow. A dense granular flow is validated with experimental data, see Rondon et al. (2011). The role of the initial volume fraction of a granular collapse in a fluid is investigated. Finally, in Chapter 8 the sediment bed velocity is determined numerically and compared with the experimental results of a closed flume experiment.

Chapter 2

Description of granular flows and solid-liquid interaction

A description of the underlying physics is introduced in this chapter. First settling of particles is discussed and is done in Section 2.1. The viscosity of a mixture depends on the number of suspended particles or volume fraction. The mixture viscosity increases as the volume fraction of solids increases. Several models exist for describing the relation between the viscosity and of the volume fraction of solids and is discussed in Section 2.3. Moreover, for highly concentrated suspensions, the material exhibits non-Newtonian behavior and is described using so-called stress strain or constitutive relations. This topic is covered in Section 2.2. The chapter is concluded with remarks.

2.1 Particle settling

The terminal settling velocity of a freely settling single spherical particle, in a quiescent and an infinite domain (see Figure 2.1), is governed by three forces. These are the drag, buoyancy and the gravitational force and are in equilibrium.

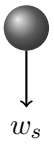

Figure 2.1: Settling of a single particle in an infinite domain and quiescent surrounding fluid, so-called free settling.

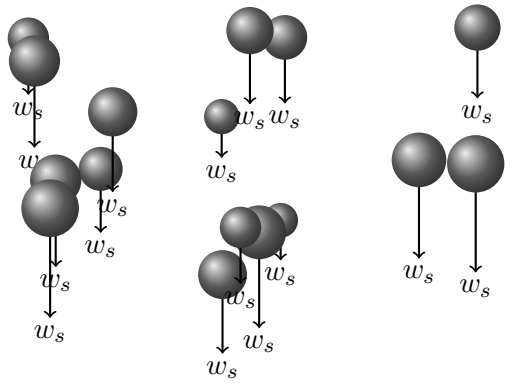

Figure 2.2: Settling of multiple particles, with different sizes, in an infinite domain, so-called hindered settling.

Now the equation of motion of a single particle is:

$$\frac{1}{2}\, C_d A_p \rho_f w_{p\infty}^2 = V_p\, (\rho_p - \rho_f)\, g_z \tag{2.1}$$

where V_p and A_p is the particle volume and the projected area in the velocity direction of the particle respectively. The terminal settling velocity of a particle, in z-direction, is $w_{p\infty}$. The drag coefficient is given by C_d and depends on the particle Reynolds number, $Re_p = \rho_f\, d_p\, w_{p\infty}/\mu_f$. In which ρ_f and μ_f is the density and molecular viscosity of the fluid respectively. Now the terminal settling velocity, Eq. (2.1), is expressed as:

$$w_{p\infty} = \sqrt{\frac{4\, g_z\, d_p\, (\rho_p - \rho_f)/\rho_f}{3\, C_d}} \tag{2.2}$$

In case of a multiple particle system, see Figure 2.2, the settling velocity is reduced with respect to the terminal settling velocity of a single particle. The

reduced settling velocity is caused by interactions with neighboring particles, back flow, inter particle collisions etc. The hindered settling velocity is obtained with an empirical relation:

$$w_s = w_{p\infty} V(\alpha_t) \tag{2.3}$$

where w_s is the hindered settling velocity and $V(\alpha_t)$ is the hindered settling function. This empirical function depends on the total volume concentration of solids, α_t. The settling equation given in form stated in Eq. (2.3) is valid for mono dispersed spherical particles. However, natural sediments consist of particles with multiple particle sizes resulting in different settling velocities.

2.2 Rheology

Sir Isaac Newton stated, at the end of the seventeenth century, that the viscous fluid stresses depend linearly on the deformation rate of the fluid. Fluids with this property are called Newtonian fluids. Examples are water, honey, beer or motor oil.

However, a vast class of fluids shows a non-linear relation between deformation rate and fluid stress. This class of fluids is called non-Newtonian. The discipline which is concerned with the study of non-Newtonian fluids is rheology. This term was introduced by E.C. Bingham studying fluids with non-linear behavior. Examples of non-Newtonian fluids are yogurt, ketchup or paint. These fluids exhibit a reduction of viscosity when the shear rate, i.e. stirring, is increased and are called thixotropic.

Other fluids exhibit the opposite behavior. The stresses in fluids increase when the shear rate increases and are called to be dilatant or shear thickening. An example of such a fluid is a mixture of cornstarch and water, which is applied as a thickening agent in liquid-based foods.

2.2.1 Newtonian fluids

The relation, between stress and deformation rates of a liquid, is described using a constitutive equation. For a Newtonian fluid the relation between stress and deformation rate is proportional to the molecular viscosity, μ:

$$\tau = \mu\dot{\gamma} \tag{2.4}$$

This is the one dimensional case in which $\dot{\gamma} = \partial u/\partial y$ is the shear rate. This relation can be expanded to 3D as follows. First, the deformation tensor is introduced, using the index notation, this tensor reads:

$$\mathbf{S} = S_{ij} = \frac{1}{2}\left(\frac{\partial u_i}{\partial x_j} + \frac{\partial u_j}{\partial x_i}\right) \tag{2.5}$$

in which S_{ij} is the deformation tensor. The stress tensor, T_{ij}, is obtained by multiplying with the viscosity:

$$\mathbf{T} = T_{ij} = 2\mu S_{ij} \tag{2.6}$$

This completes the stress deformation description of a Newtonian fluid. In the next section non-linear constitutive relation are introduced.

2.2.2 Non-Newtonian fluids

Bingham plastic

A Bingham plastic, named after E.C. Bingham, see Bingham (1922), is a fluid which both can behave as a solid or a fluid. The state of the fluid depends on a threshold of the shear stress, τ, the so-called yield stress, τ_0. When the shear stress, τ, is less than the yield stress τ_0, the fluid acts as a solid. The fluid flows when the shear stress exceeds the yield stress. If the yield stress is exceeded, the shear stress is proportional to the amount shear rate, $\dot{\gamma}$. The constitutive relation for a Bingham fluid is expressed as:

$$\tau = \tau_0 + \eta\dot{\gamma} \tag{2.7}$$

where τ is the shear stress and η the plastic viscosity. Figure 2.3 shows the flow behavior of a Bingham fluid. It should be noted that if the yield stress is $\tau_0 = 0$, the Bingham fluid reduces to a Newtonian fluid. Now rewriting Eq. (2.7) as follows:

$$\begin{aligned} \dot{\gamma} &= 0 && \text{if} \quad \tau < \tau_0 \\ \dot{\gamma} &= \frac{\tau - \tau_0}{\eta} && \text{if} \quad \tau \geq \tau_0 \end{aligned} \tag{2.8}$$

The constitutive equation, Eq. (2.8) for a Bingham material is presented here for 1D. Now extending Eq. (2.8) to 3D, see Prager (1989), is done with the

second invariant of the deformation and stress tensor. The second invariant, I_2, of the deformation tensor, S_{ij}, is given by:

$$I_2 = \frac{1}{2} S_{ij} S_{ij} \tag{2.9}$$

and the second invariant, J_2 of the stress tensor, T_{ij}, defined as:

$$J_2 = \frac{1}{2} T_{ij} T_{ij} \tag{2.10}$$

now the constitutive relation for a Bingham material, in 3D, using the definitions, Eq. (2.9), Eq. (2.10) and Eq. (2.5) yields:

$$\begin{aligned} S_{ij} &= 0 && \text{if} \quad \sqrt{J_2} < \tau_0 \\ T_{ij} &= \left(2\eta + \frac{\tau_0}{\sqrt{I_2}}\right) S_{ij} && \text{if} \quad \sqrt{J_2} \geq \tau_0 \end{aligned} \tag{2.11}$$

The constitutive relation given in Eq. (2.11) is discontinuous and cumbersome to implement numerically. In order to overcome this problem the following continuous expression was introduced by Papanastasiou (1987):

$$T_{ij} = \left(2\eta + \frac{\tau_0}{\sqrt{I_2}} \left[1 - e^{-m\sqrt{I_2}}\right]\right) S_{ij} \tag{2.12}$$

where m is the stress growth exponent and controls the amount of plasticity. This equation, Eq. (2.12), mimics the ideal Bingham plastic for $m \geq 100$ and it provides a better approximation to real data for visco-plastic materials for $0 < m < 100$, see Mitsoulis et al. (1993) and Papanastasiou (1987). The extreme case would be $m = 0$, in that case Eq. (2.12) describes the behavior of a Newtonian fluid. The influence of the parameter m on the shear stress as a function of the shear rate is shown in Figure 2.4. Figure 2.5 shows the derivative of Eq. (2.12), which is the regularized viscosity, η for various values of the parameter m. Increasing the value of m yields an increased value for the viscosity. Moreover, the viscosity changes rapidly in a small range of the shear rate for higher values of m. An increased value of the viscosity leads to numerical instabilities, this can be circumvented by using smaller time step sizes. This is addressed in Section 5.1.4.

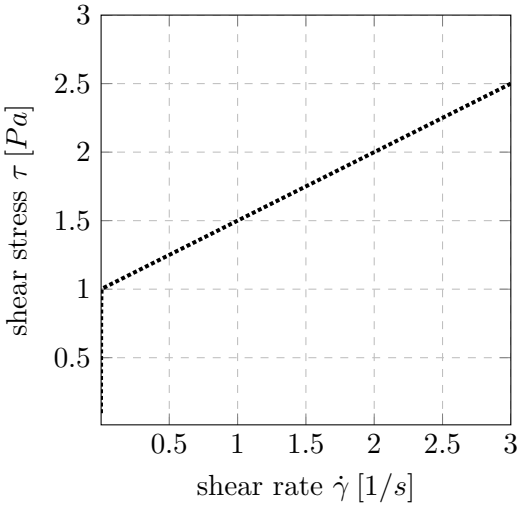

Figure 2.3: Behavior of a Bingham material, the shear stress, τ, is given as a function of the shear rate, $\dot{\gamma}$.

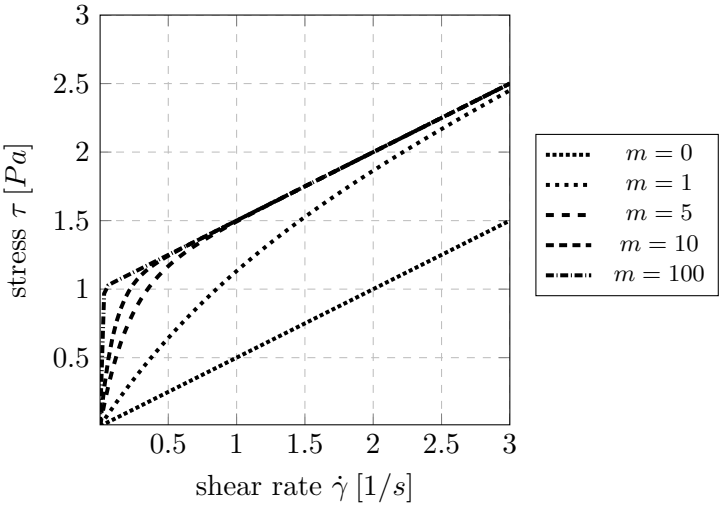

Figure 2.4: Influence of parameter m on the visco-plastic behavior, see Eq. (2.12).

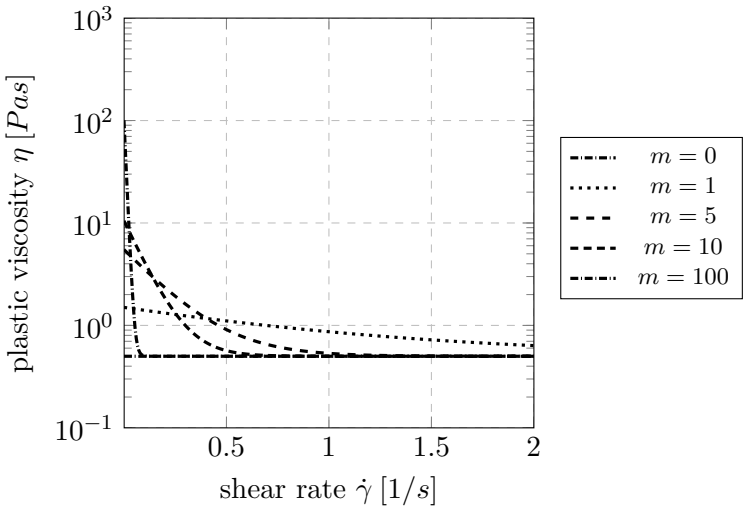

Figure 2.5: Influence of parameter m on the regularized viscosity, η, see Eq. (2.12).

Herschel-Bulkley

Here another constitutive relation is introduced, the so-called Herschel-Bulkley model. This constitutive equation is an extension of the Bingham model and is given by (in 1D):

$$\tau = \tau_0 + K\dot{\gamma}^k \tag{2.13}$$

in which τ_0 is the yield stress, below this value the material behaves as a solid. The parameter K is the so-called consistency index and k is the flow index. This defines the degree of the non-Newtonian behavior of the fluid. These constants are determined empirically. The resistance to shear increases for $k > 1$, called shear thickening, and decreases for $k < 1$, shear thinning. If $k = 0$, Eq. (2.13), reduces to the Bingham constitutive relation, Eq. (2.7). The Herschel-Bulkley constitutive relation has more degrees of freedom, namely the parameters τ_0, K and k, characterizing a non-Newtonian fluid. The derivation of extending the Herschel-Bulkley equation to 3D is analog to the 3D extension of the Bingham model. The 3D Herschel Bulkley model is given as follows, see

Mitsoulis et al. (1993):

$$\begin{aligned} S_{ij} &= 0 && \text{if} \quad \sqrt{J_2} < \tau_0 \\ T_{ij} &= \left(2\eta(\sqrt{I_2})^{k-1} + \frac{\tau_0}{\sqrt{I_2}}\right) S_{ij} && \text{if} \quad \sqrt{J_2} \geq \tau_0 \end{aligned} \tag{2.14}$$

The constitutive relation introduced here, Eq. (2.14), reduces to the Bingham relation, Eq. (2.11), by choosing the empirical parameter $k = 1$. The same regularization holds for the Herschel-Bulkley constitutive relation as for the Bingham model, see Eq. (2.12). Now by rewriting Eq. (2.14) using Eq. (2.12) the following expression is obtained:

$$T_{ij} = \left(2\eta\left(\sqrt{I_2}\right)^{k-1} + \frac{\tau_0}{\sqrt{I_2}}\left[1 - e^{-m\sqrt{I_2}}\right]\right) S_{ij} \tag{2.15}$$

Note here that, Eq. (2.12) is recovered, by substitution of $k = 1$ in Eq. (2.15). Now two important classes of non-Newtonian fluids have been introduced. Other non-Newtonian models can be found in literature, see for instance Akker and Mudde (2014) or Bird et al. (2002), and won't be discussed in this work. The Bingham model introduced here forms the basis of describing the flow behavior of (packed) sand or dense granular flow.

2.3 Mixture viscosity

The viscosity of a mixture or slurry depends on the total volume concentration of solids. Einstein (1906) proposed a relation describing the relative viscosity as a function of the volume concentration of solids:

$$\mu_r = 1 + 2.5\,\alpha_t \tag{2.16}$$

In which $\mu_r = \mu_m/\mu$ with μ_m and μ_r is the mixture and relative mixture viscosity respectively. The Einstein relation Eq. (2.16) only holds for dilute suspensions. An extension of Eq. (2.16) to suspensions, for spherical particles, with higher volume concentrations is introduced by Thomas (1965):

$$\mu_r = 1 + 2.5\,\alpha_t + 10.05\,\alpha_t^2 + A\exp(B\alpha_t) \tag{2.17}$$

Where the factors A and B are found from fitting empirical data $A = 0.00273$ and $B = 16.6$. Eilers (1941) proposed the following relation,

$$\mu_r = \left(1 + \frac{1.25\,\alpha_t}{1 - \alpha_t/\alpha_{tmax}}\right)^2 \tag{2.18}$$

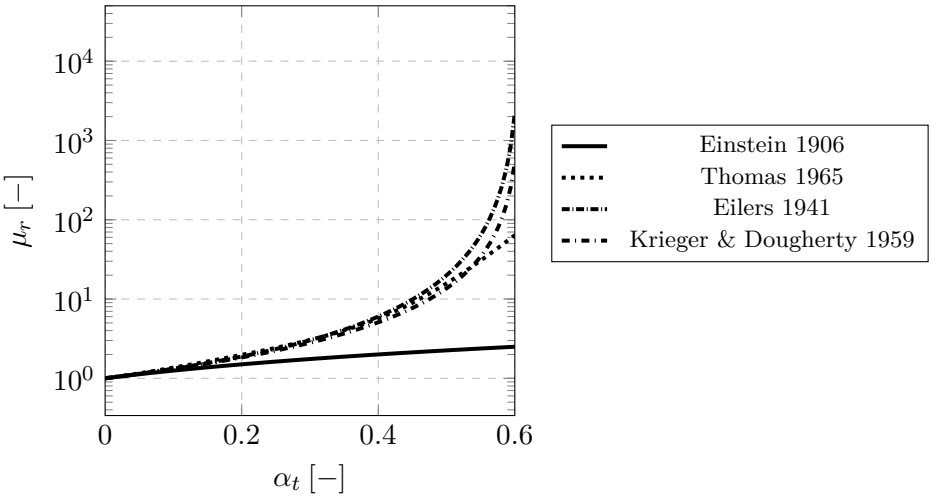

Figure 2.6: Here four relative viscosity are given graphically, Einstein Eq. (2.16), Thomas Eq. (2.17) Eilers, Eq. (2.18), and Krieger Eq. (2.19). The Einstein model is only valid for dilute suspensions. The relative viscosity, μ_r, becomes very high at $\alpha_t \approx \alpha_{tmax}$ for the models of Eilers and Krieger.

From Eq. (2.18) it is readily seen that if the volume concentration, α_t, reaches the maximum volume concentration, α_{tmax}, the relative viscosity μ_r becomes infinite. This implies that at the maximum volume concentration no deformations is possible. Another well known relation was proposed by Krieger and Dougherty (1959),

$$\mu_r = \left(1 - \frac{\alpha_t}{\alpha_{tmax}}\right)^{-2.5\alpha_{tmax}} \tag{2.19}$$

It can be seen from Eq. (2.19) the relative viscosity becomes infinite if the volume concentration of solids for $\alpha_t = \alpha_{tmax}$. Analog to the model of Eilers (1941), Eq. (2.18), the deformations possible at the maximum volume concentration, α_{tmax}. There are numerous other mixture viscosity models derived, see for example Stickel and Powell (2005) or for an overview. Figure Figure 2.6 shows the equations of Einstein, Eq. (2.16), Thomas Eq. (2.17) Eilers, Eq. (2.18), and Krieger Eq. (2.19). In Figure 2.6 it can be seen that all the models coincide for small values of α_t. However for large values of α_t the models diverge. The Einstein model, Eq. (2.16), is only valid for dilute suspensions up to $\alpha_t \approx 0.1$. The other three models Thomas Eq. (2.17), Eq. (2.18) and

Eq. (2.19) are valid for higher volume concentrations of solids. From the models of Krieger and Dougherty (1959) and Eilers (1941) it can be seen that at the maximum volume concentration of solids, α_{tmax}, the relative viscosity becomes very large. In this case, the mixture stops flowing. Note that the relative viscosity, μ_r, only depends on the volume concentration. The influence of the size and/or the density of sediment particles is not present. In the next section, sediment is modeled as fluid with help of a constitutive relation.

2.4 Stratification

Stratification occurs when fluid masses with different densities form layers in vertical direction. The degree of stratification is expressed by the Richardson number which is the ratio between the buoyancy term and the flow shear term:

$$Ri = \frac{-g_z \frac{\partial \rho}{\partial z}}{\rho \left[\left(\frac{\partial u}{\partial z} \right)^2 + \left(\frac{\partial v}{\partial z} \right)^2 \right]} \tag{2.20}$$

where g_z is the gravitational constant (in z-direction), ρ the density and u, v denotes a governing flow speed. In case of a large flow shear, so $Ri \ll 1$, buoyancy is less important. When $Ri \gg 1$ buoyancy term dominates in the flow. The flow does not contain sufficient kinetic energy to homogenize the flow. A transition of the flow takes place at a critical value $Ri_c \approx 1$. The Richardson number is used in a variety of geophysical flows. Examples are atmospheric and oceanic flows. In atmospheric flows, the density difference is caused by variations of temperature, where a lower temperature leads to a heavier layer of air. In oceanic flows, the density difference occurs due to the difference in salinity among layers in the ocean.

When dealing with sediment water mixtures density differences occur due to the spatial varying sediment distribution. In case of a high-density gradient and low shear, i.e. $Ri \gg 1$, the flow is stable and no mixing of the flow occurs, this is when a sediment bed is formed. Increasing the flow speed, i.e. increasing the flow shear, the sediment is picked up from the bed and brought into suspension. The Richardson number is then $Ri \ll 1$. Increasing the shear rate even further eventually leads to a homogeneous sediment distribution in the z-direction of the domain. A more detailed discussion of stratified flows

in combination with sediment can be found in Winterwerp (2001) or Gillies (1993).

2.5 Granular flows

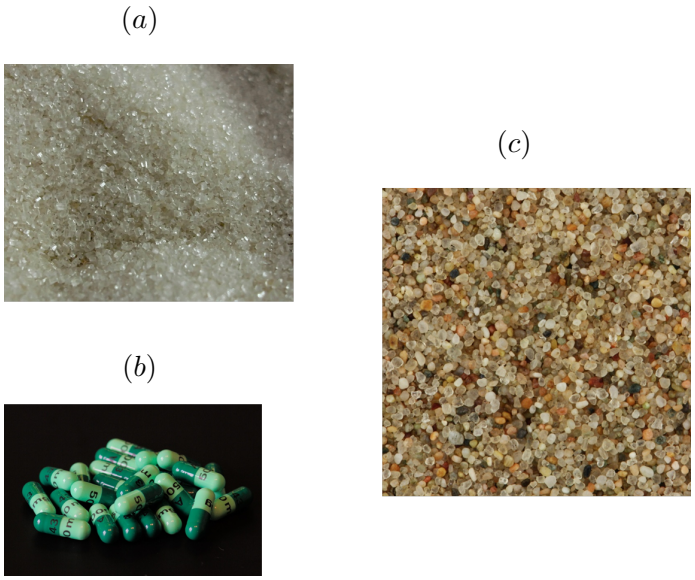

Figure 2.7: Some examples of granular materials, sugar plot a, pills, plot b and sand grains, plot c.

Granular matter is commonly found in natural and industrial settings, examples are sand, gravel, rice, sugar, corn, snow, medicines in the form of pills or plastic granules. Figure 2.7 shows some examples of granular materials. A broad range in dynamical behavior is characteristic of the physics of granular media, see Jaeger et al. (1996). Granular materials can behave macroscopically as both a solid or a liquid. As a solid, sand can be strong enough to support buildings, yet can flow as a liquid seen in hourglasses. Another example of the liquid-like behavior of the granular material is the flow of the material when discharging a hopper. The internal angle of the hopper has a profound effect on the discharge rate, see Albaraki and Antony (2014). Furthermore, granular solids can be transported by a medium, air or water, forming dunes. These can be observed in coastal areas, deserts or riverbeds. On Mars, dune forming has

Figure 2.8: Photograph shows part of the Bagnold Dune Field on Mars. These Dunes are named after Brigadier Ralph Alger Bagnold, (source: NASA, https://photojournal.jpl.nasa.gov/jpeg/PIA20755.jpg).

been observed due to the interaction of sand-grained sized sediment and the Martian atmosphere, see Thomas (1982). Figure 2.8 shows part of the Bagnold Dune Field on Mars. These dunes were named after Brigadier Ralph Alger Bagnold in honor of his pioneering contributions in scientific understanding of granular structures such as dunes and ripples.

Now typical particles sizes of granular media are in the order of magnitude of 100 $[\mu m]$. Therefore, the motion of particles is Brownian and dominated by contact and friction, see Fortrerre and Pouliquen (2009). Even a volume 1 $[cm^3]$ of sugar contains approximately 1×10^6 particles. At todays available computing power it is impossible to calculate all the states governing the motion of the particles. Therefore, a continuum approach is used, describing the averaged quantities of the granular medium.

Bagnold

A continuum description, for characterizing regimes of grain-grain interactions of a granular flow, was introduced by Bagnold, see Bagnold (1954) and Bagnold

(1956). The flow regimes are characterized by the Bagnold number, Ba:

$$Ba = \frac{\rho_p \, d_p^2 \, \sqrt{\lambda}}{\mu} \, \dot{\gamma} \tag{2.21}$$

where ρ_p is the particle density, d_p the particle diameter, $\dot{\gamma}$, the shear rate and μ the molecular or dynamic viscosity of interstitial fluid. The Bagnold number is the ratio of the collision to viscous forces. In Eq. (2.21) is λ the linear concentration and is defined as:

$$\lambda = \left(\left(\frac{\alpha_{tmax}}{\alpha_t} \right)^{0.33} - 1 \right)^{-1} \tag{2.22}$$

where α_t is the solids volume fraction and α_{tmax} the maximum possible volume concentration of solids. Three flows regimes can be distinguished from the Bagnold number, Ba. In flows with $Ba < 40$ the viscous fluid stresses dominate, this is the so-called "macro-viscous" regime. For flows with $Ba > 450$ the grain collision stresses dominate and is known as the "grain-inertia" regime. The transitional regime is valid for values of $40 < Ba < 450$. Another formulation of the Bagnold number, Ba, was introduced by Iverson, see Iverson (1997), Parsons et al. (2001) and Kaitna and Rickenmann (2007), where:

$$\sqrt{\lambda} = \left(\left(\frac{\alpha_{tmax}}{\alpha_t} \right)^{0.33} - 1 \right)^{-1/2} \tag{2.23}$$

was substituted with, $\alpha_t/(1 - \alpha_t)$, changing the values $Ba < 15$ where the viscous fluid stresses dominate and $Ba > 180$, where grain collision stresses dominate. Now the Bagnold number is written as:

$$Ba = \frac{\alpha_t}{\mu(1 - \alpha_t)} \rho_p d_p^2 \dot{\gamma} \tag{2.24}$$

In the viscous regime, Bagnold (1954), a semi empirical relation was introduced, correlating the shear rate and the shear stress:

$$\tau = \mu \, (1 + \lambda) \left(1 + \frac{1}{2} \lambda \right) \dot{\gamma} \tag{2.25}$$

This relation, Eq. (2.25), is similar to the relations found for the relative viscosity models discussed in Section 2.3. Now rewriting Eq. (2.25) as a relative

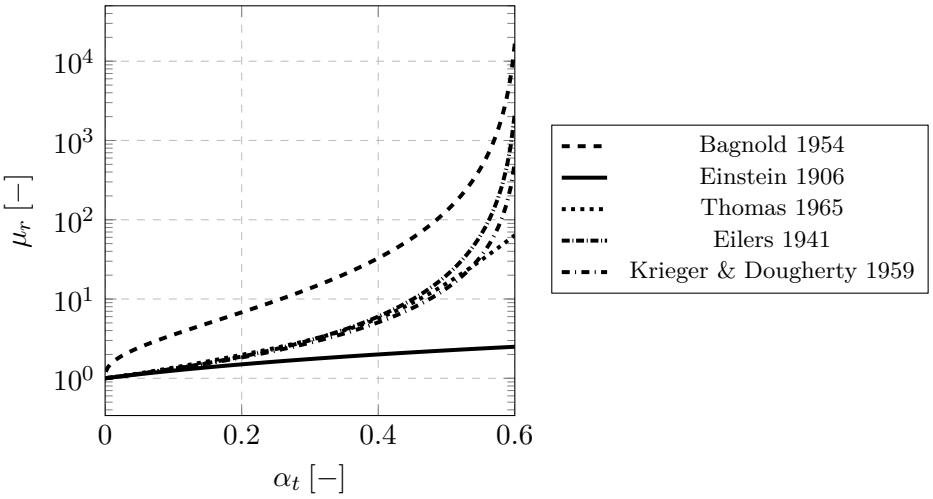

Figure 2.9: Here five relative viscosity models are plotted, Bagnold Eq. (2.26) valid for the viscous regime, Einstein Eq. (2.16), Thomas Eq. (2.17) Eilers, Eq. (2.18), and Krieger Eq. (2.19). The graph is the same as Figure 2.6 extended with the mixture viscosity of Bagnold.

viscosity yields:

$$\mu_r = (1 + \lambda)\left(1 + \frac{1}{2}\lambda\right) \tag{2.26}$$

The relation is valid for the viscous regime and depends only on the volume fraction of solids. In Figure 2.9 the relative viscosity of Bagnold is given, Eq. (2.26), as a function of the volume of solids. This is the same graph as Figure 2.6 extended with the mixture viscosity of Bagnold in the viscous regime. The relative mixture of Bagnold is higher in comparison with other mixture viscosity models shown in Figure 2.9. The overestimation of the relative viscosity can be attributed to secondary flows or eddy viscosity in the suspension experiments done. This is reported in a critical review by Hunt et al. (2002).

Dry granular flows

Examples of dry granular flows are rock avalanches, flows of dry sand (e.g. in case of discharging) or bulk processing of grain. The dense granular material

behaves in these cases as a liquid with peculiar stress-strain properties. The flow of the material is dominated by friction and collisions, see Fortrerre and Pouliquen (2009). Now considering mono-dispersed materials, dense granular flows, i.e. granular flows close to the maximum packing limit, are characterized by a threshold. This threshold is governed by friction and can be described as a yield stress, as done with visco-plastic materials, see Section 2.2. When this threshold is exceeded the granular material starts to flow and behaves similarly to a viscous fluid. By applying a Coulomb friction criterion the yield stress, or the threshold at which the granular material starts to flow, is expressed as:

$$\tau_0 = \mu_s P_p \tag{2.27}$$

in which τ_0 is the yield stress, μ_s a friction factor and P_p the normal stress or particle pressure. The particle pressure consists of the weight of the particles, P_p. The strength of a granular or sand bed increases with an increasing depth of the granular bed, see Lalli and Mascio (1997). This results in a higher yield stress, τ_0. In Eq. (2.27), the static friction factor μ_s, is equal to the angle of repose. The angle of repose is the slope angle at which a loosely poured granular material is stable, i.e. the material does not flow. This is the lower limit of the shear stress. When the yield stress is exceeded the granular material starts to flow in a liquid-like manner. The friction factor μ_s is not constant as the material flows and depends on the shear rate, $\dot{\gamma}$, and the particle pressure, P_p. Now Eq. (2.27) can be reformulated into the following constitutive relation, in $1D$, see Jop et al. (2006):

$$\tau = \mu_I \, P_p \tag{2.28}$$

In which I is the so-called inertia number and is a dimensionless shear rate, see GDR-MiDi (2004):

$$I = \frac{\dot{\gamma} \, d_p}{\sqrt{P_p/\rho_p}} \tag{2.29}$$

in which $\dot{\gamma}$ is the shear rate, d_p the particle diameter and ρ_p is the particle density. The inertia number, I, is the ratio between the inertia, $\dot{\gamma} d_p$ to the confining stress, P_p/ρ_p. The friction coefficient, depending on the dimensionless shear rate coefficient, μ_I, see Eq. (2.28), can be obtained from numerical simulations or indirectly by experiments for flow down inclined planes, Pouliquen (2005):

$$\mu_I = \mu_s + \frac{\mu_2 - \mu_s}{I_0/I + 1} \tag{2.30}$$

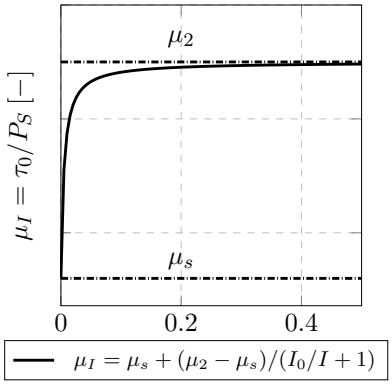

Figure 2.10: Friction coefficient, μ_I, as a function of the inertia number, I.

where I_0 is a constant and is equal to $I_0 = 0.3$. Furthermore, the coefficients μ_s and μ_2 are found to be equal to $\mu_s = \tan 21^o$ and $\mu_2 = \tan 33^o$. The stress strain relation can be generalized in three dimensions, Fortrerre and Pouliquen (2009):

$$T_{ij} = \eta_{eff} S_{ij} \tag{2.31}$$

where η_{eff} is the effective viscosity and is obtained by rewriting Eq. (2.28):

$$\eta_{eff} = \frac{\mu_I \, P_p}{I_2} \tag{2.32}$$

in which I_2 is the second invariant of the deformation tensor. The effective viscosity becomes infinite when $I_2 \to 0$. In this case, a threshold exists, which is given by:

$$\sqrt{J_2} > \mu_s P_p \tag{2.33}$$

This material behavior is the same as the behavior of a Bingham plastic described earlier. However, a Bingham plastic the viscosity only depends on the shear rate. The viscosity of a dry granular material depends both on the shear rate and the particle pressure, P_p.

Immersed granular flows

In the hydraulic transport of (dense) sediment flows the material is immersed in a liquid. The presence of a liquid in changes the motion or the rheology of

the flow. Therefore, another constitutive relation (or the stress deformation relation) of the medium is needed. The constitutive relation depends on the timescales at which particles reach terminal velocity. The time scales at which a single particle travels over one particle diameter, d_p, in a dense granular medium, is of importance, see Cassar et al. (2005) and Fortrerre and Pouliquen (2009). These scales can be compared using the typical time of the deformation is $t_{macro} = 1/\dot{\gamma}$ and the typical time for rearrangement of the of particle t_{micro} With help of these timescales, the dimensionless shear rate can be determined which governs the rheology of the dense immersed granular material.

The work of Courrech du Pont et al. (2003), who analyzed the free fall of a particle under gravity, showed that different regimes, i.e. time and length scales, could be distinguished. The equation of motion of a small particle is as follows:

$$\frac{\pi}{6}\rho_p d_p^3 \frac{du}{dt} = \frac{\pi}{6} d_p^3 (\rho_p - \rho_f) g_z - F_d \tag{2.34}$$

in which F_d is the drag force of a particle. When a particle is submitted to a confining particle pressure, P_p, along the vertical direction of the particle, Cassar et al. (2005), Eq. (2.34) can be rewritten into the following form:

$$\frac{\pi}{6}\rho_p d_p^3 \frac{du}{dt} = \frac{\pi}{4} P_p d_p^2 - F_d \tag{2.35}$$

Note that for a submerged particle, by setting equal the first terms on the LHS of Eq. (2.34), $\frac{\pi}{6} d_p^3 (\rho_p - \rho_f) g_z$, and Eq. (2.35), $\frac{\pi}{4} P_p d_p^2$, the confining pressure, P_p, can be re-casted into the form:

$$P_p = \frac{2}{3}(\rho_p - \rho_f) g_z d_p \tag{2.36}$$

The following definitions are introduced, $m_p = \pi/6 \rho_p d_p^3$, where m_p is the particle mass, and $u = dz/dt$. The equation of motion of a particle, by substitution of these variables in Eq. (2.35), is expressed as, Fortrerre and Pouliquen (2009):

$$m_p \frac{d^2 z}{dt^2} \simeq P_p \, d_p^2 - F_d \tag{2.37}$$

Now three regimes can be distinguished depending on the timescale at which particles move.

- Free fall regime:

  The drag force caused by the surrounding fluid can be neglected. The motion is controlled by the force $P_p\, d_p^2$, which is equal to the acceleration, Eq. (2.37), d^2z/dt^2. The time it takes for a particle to travel one particle diameter is $t = t_{micro}^{fall} \simeq d_p/\sqrt{P_p/\rho_p}$. This is the case for dry granular flows.

- Viscous regime:

  In this regime, the motion of the particle is governed by the viscous drag and the pressure. The particle rapidly reaches the terminal settling velocity. The drag force is of the form $F_d \simeq \eta d_p \frac{d\,z}{dt}$ and gives a viscous micro time scale, $t_{micro}^{visc} \simeq \eta/P_p$.

- Inertial regime:

  In the inertial range the motion of the particle is governed by so-called inertial drag force, given by $F_d \simeq C_d\, d_p^2\, \rho_f (dz/dt)^2$ in which C_d is the drag coefficient. The inertial time scale is similar to $t = t_{micro}^{inert} \simeq d/\sqrt{P_p/(\rho_f\, C_d)}$

From the introduced micro timescales the transition between the different regimes can be estimated. This is done using a Stokes number, St, and a number r. The Stokes number is the ratio of the free fall timescale over the viscous time-scale. The number r is the ratio of the free fall timescale and the inertial time scale:

$$St = \frac{t_{micro}^{fall}}{t_{micro}^{visc}} \simeq \frac{d\sqrt{\rho_p P_p}}{\eta} \tag{2.38}$$

$$r = \frac{t_{micro}^{fall}}{t_{micro}^{inert}} \simeq \frac{\rho_p}{\rho_f C_d} \tag{2.39}$$

With help of the Stokes number, St, and the timescale ratio r an estimation of the governing flow regime can be determined. For dry granular the longest timescale is t_{micro}^{fall}, for this case the following applies $St \gg 1$ and $r \gg 1$. In this case, the effect of the interstitial fluid can be neglected. In the viscous regime the longest timescale is t_{micro}^{visc}, this is the case when $St \ll 1$ and $r \gg St$. When

the longest timescale is t_{micro}^{inert}, the regime is said to be inertial, for this case the following applies, $St \ll r$ and $r \ll 1$. Figure 2.11 shows the three regimes as a relation of the Stokes number and r. For each regime, the dimensionless shear rate is given. By using the friction law and the dimensionless shear rate I, which depends on the regime, the rheology of the granular material is determined. For a granular material, immersed in a liquid, the regime would be the viscous regime:

$$\tau = \mu_{I_v} P_p \tag{2.40}$$

Now according to Fortrerre and Pouliquen (2009) there is no distinct way, test or direct measurement, based on the typical timescales, to determine the three regimes, except for the dry granular case. However, for the viscous number, indirect measurements exist indicating that this number can be applied successfully. These tests concerned an immersed granular flow down an inclined plane and showed that the viscous number, I_v, yields similar results as for the dry case, see Cassar et al. (2005) and Pailha and Pouliquen (2009).

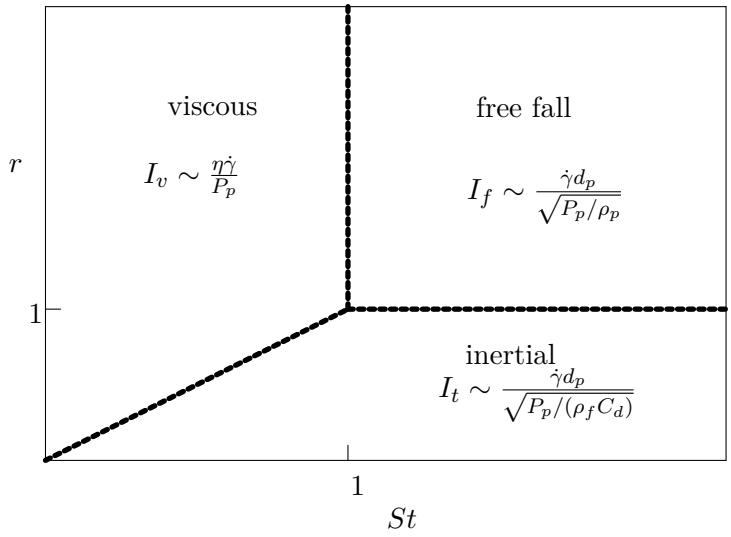

Figure 2.11: Three granular regimes with the dimensionless number shear rate or number. Where I_i, with the subscript $i = v, f, t$ indicates the viscous, free fall and inertial regime respectively.

In granular rheology, the stress deformation relation depends both on the friction coefficient, μ_{I_v} (given here for the viscous regime), and on the particle

or confining pressure P_p. This follows from the dimensionless shear rates given in Figure 2.11. The particle pressure, P_p, consists of several parts. One part is, obviously, the submerged weight of the granular material. Another part is caused by the deformation of the material subjected to shear. This is the case for instance in a granular bed in which a liquid moves above the bed, subjecting the bed to shear and thus deforming the bed. The motion of the particle is caused by the velocity difference between the liquid and the bed, eventually eroding the bed as the particles move into suspension. Another case, in which a granular material is subjected to shear, is the dynamics of submerged avalanches. The granular material can either compact or dilate depending on the initial state of the material. When a material is loosely packed and shear is applied, the interstitial liquid flows out of the granular material liquefying the bed. When a granular material is densely packed and is subjected to shear, the surrounding liquid flows into the material increasing the shear resistance. This is called dilatancy. The flow behavior described, has been observed by Rondon et al. (2011) in small-scale tests and on a larger scale by Iverson (2005) investigating landslides. Both dilatancy and compacting changes the particle pressure P_p, caused by changes in pore pressures. This is initiated by the inflow or outflow of the surrounding liquid, and therefore, changing the flow dynamics. Large-scale tests were performed, see Van Rhee and Bezuijen (1998), investigating the stability of a sandy slope or sand column. In the experimental setup, the eroded sand from the slope was removed hydraulically at the bottom of the slope. The removed sand/water mixture was re-injected at the top the slope. This was done using a pump and pipe system. During the tests pore pressure in sediment was measured. At the sloped interface of sand and water, a pore pressure reduction was observed. This reduction in pore pressure or under pressure results in an increased effective pressure increasing the resistance to shear. This is increased resistance, using the Coulomb friction law results in a higher effective viscosity as can be seen from Eq. (2.32).

Chapter 3

Single-phase turbulent flow with variable density

3.1 Equations of Motion

The equations of motion of a fluid are governed by the Navier-Stokes equations and are the following equations:

$$\frac{\partial \rho \, \mathbf{u}}{\partial t} + \nabla \cdot (\rho \, \mathbf{uu}) = -\nabla p + \nabla \cdot \left(\mu \left(\nabla \mathbf{u} + \nabla \mathbf{u}^T \right) \right) + \rho \, \mathbf{g} \tag{3.1}$$

here $\mathbf{u}$, ρ and μ are the velocity density and molecular viscosity respectively. Finally, the hydrodynamic pressure is given by p. Due to the conservation of mass for an incompressible fluid the following expression is valid:

$$\frac{\partial \rho}{\partial t} + \nabla \cdot (\rho \, \mathbf{u}) = 0 \tag{3.2}$$

Now Eq. (3.1) and Eq. (3.2) describe the hydrodynamic behavior of a fluid. A fluid can be incompressible and still have a non-constant density. Wrongfully a fluid with variable density is attributed to only compressible fluids. Which is in some case not true, see Wesseling (2000). An example of an incompressible fluid with a variable density is a fluid with two densities, such as a salt and freshwater mixture. In such a fluid the density, $\rho \neq constant$. Another example of non-constant density incompressible flow is a sediment-water mixture.

The computational cost of fully solving the Navier-Stokes, this is a so-called Direct Numerical Simulation or DNS, is non-practical for Engineering applications, with the currently available computing power. Therefore, in order to reduce the computational cost, a closure model is employed modeling turbulence. Here an eddy viscosity model is employed, the so-called Large Eddy Simulation, (LES). This is discussed next.

3.1.1 Kolmogorov

In a turbulent flow the energy present, or energy which drives the flow, is eventually dissipated and turned into heat. The kinetic energy, present at the largest scale of motion, transfers to smaller and smaller scales until at the smallest scales this energy is dissipated by viscous forces. This process is called an energy cascade. At the smallest scales the energy is transformed into heat and this is called the Kolmogorov length scale:

$$\eta_l = \left(\nu^3/\epsilon\right)^{1/4} \tag{3.3}$$

in which ϵ is the rate of dissipation of turbulent kinetic energy per unit mass and ν the kinematic viscosity. The Kolmogorov timescale is defined as:

$$\tau_{\eta l} = (\nu/\epsilon)^{1/2} \tag{3.4}$$

and finally the velocity scale is given by:

$$u_{\eta l} = (\nu\epsilon)^{1/4} \tag{3.5}$$

now from these scales there is only one unknown, which is the energy dissipation rate per unit mass, ϵ. The rate can be estimated using the following scaling, Pope (2000):

$$\epsilon \sim \frac{U^3}{L_l} \tag{3.6}$$

where U is the typical velocity of a system and L_l the typical length scale. With help of the definitions given above and the estimation of the dissipation rate ϵ the correlation of the smallest length, velocity and time scales with respect to the largest scales can be determined:

$$\eta_l/L_l \sim Re^{-3/4} \tag{3.7}$$

$$u_{\eta l}/U \sim Re^{-1/4} \tag{3.8}$$

$$\tau_{\eta l}/T \sim Re^{-1/2} \tag{3.9}$$

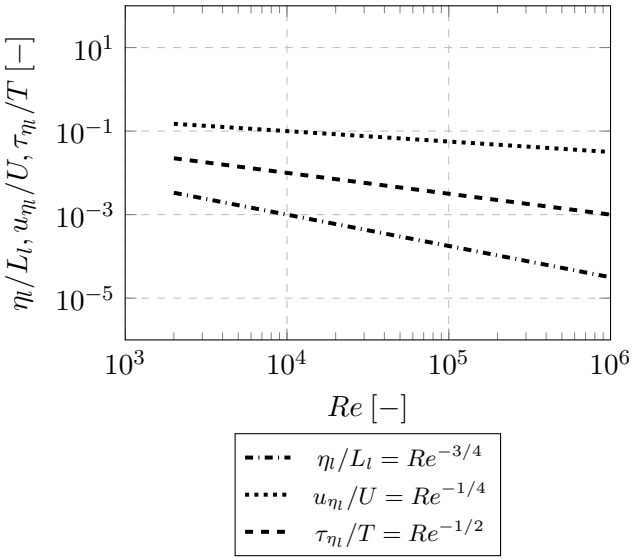

Figure 3.1: Kolmogorov scales as function of Reynolds number, Re.

Figure 3.1 shows length, velocity and timescales as a function of the Reynolds number, with $Re = \rho U_l L/\mu$. Figure 3.1 shows that the smallest eddies occur at a Reynolds number of, for instance, $Re = 1 \times 10^4$. This is approximately 1/1000 of the typical length scale of the flow, L_l.

3.1.2 Computational costs

Starting from the Navier-Stokes equations Eq. (3.1) turbulent flows can be solved numerically without any turbulence modeling. This is done with a Direct Numerical Simulation (DNS) and takes a huge amount of computing power. The number of grid cells for a DNS solution depends on the Reynolds number. The largest length scale L_l, the scale of the largest eddies, relate to the smallest scale η_l, the smallest eddies to the Reynolds number as follows:

$$\frac{L_l}{\eta_l} \sim \left(\frac{\rho\, U\, L_l}{\mu}\right)^{3/4} = Re^{3/4} \tag{3.10}$$

where U is the bulk flow velocity. Now the number of grid cells needed to describe a flow with a Reynolds of 10^5 is proportional to $10^{15/4}$. Turbulent flows are 3 dimensional so the number of grid cells is approximately 10^{10}.

The computational costs are prohibitively large for these kinds of numerical calculations with the presently available computing power. Therefore, another approach is needed and this is elaborated in the following sections.

3.2 Spatial filter properties

Before the Large Eddy Simulation is discussed in more detail, first an introduction about spatial filtering of physical quantities is given in this section. Let ϕ be some physical quantity:

$$\phi = \overline{\phi} + \phi'' \tag{3.11}$$

Here ϕ is the unfiltered or real quantity, $\overline{\phi}$ is low pass spatial filtered quantity, or grid resolved quantity, and ϕ'' is the sub grid quantity. Now introducing a filtering operation in order to obtain the filtered velocity $\overline{\phi}$:

$$\overline{\phi} = \int_{-\infty}^{\infty} G(x-\xi)\phi(\xi)d\xi \tag{3.12}$$

in which G is the so-called filter function. This can be any function with domain $(-\infty, \infty)$ and with the following properties, see Ghosal and Moin (1995):

1. The filter function is symmetric,

$$G(\xi) = G(-\xi) \tag{3.13}$$

2. Constants are conserved,

$$a\int_{-\infty}^{\infty} G(\xi)d\xi = a \tag{3.14}$$

where a is a constant.

3. Sufficiently fast decay $G(\xi) \to 0$ as $|\xi| \to \infty$, so that all moments:

$$\int_{-\infty}^{\infty} G(\xi)\xi^r d\xi$$

$(r \geq 0)$ exist.

4. $G(\xi)$ is localized in $(-\Delta/2, \Delta/2)$, where Δ is a filter width.

Now an example of such a filter function is the Gaussian filter,

$$G(\xi) = \sqrt{\frac{2}{\pi}} \exp(2\xi^2) \tag{3.15}$$

Another example is the box filter:

$$G(\xi) = \begin{cases} \frac{1}{\Delta} & \text{if } |\xi| < \frac{\Delta}{2} \\ 0 & \text{if } |\xi| \geq \frac{\Delta}{2} \end{cases} \tag{3.16}$$

Other filters are also possible, see for instance Sagaut (2001) or Ghosal and Moin (1995). Here some useful properties, regarding derivatives, of this choice of the filter are introduced. The filtered temporal derivative is equal to the temporal derivative of the filtered quantity,

$$\overline{\left(\frac{\partial \phi}{\partial t}\right)} = \frac{\partial \overline{\phi}}{\partial t} \tag{3.17}$$

Furthermore if the filter is spatially homogeneous, i.e. the shape of the filter remains constant as ξ varies, the filtered spatial derivative is equal to the derivative of the spatial filtered quantity,

$$\overline{\frac{\partial \phi}{\partial x}} = \frac{\partial \overline{\phi}}{\partial x} \tag{3.18}$$

A more detailed discussion on filtering can be found in e.g. Deardorff (1970), Ghosal and Moin (1995) or Sagaut (2001).

3.3 Large Eddy Simulation

Turbulence modeling, using the Large Eddy Simulation method (LES) is introduced in this section. Eddies larger than the grid size are simulated as is, eddies smaller than the grid size are resolved using a sub-grid-scale model. The sub-grid-scale model (SGS) uses a turbulent eddy viscosity. In the following two methods are described. The Smagorinsky model, see Smagorinsky (1963), is discussed in section 3.4.1. In section 3.4.2 the sub-grid stress model proposed by Nicoud and Ducros (1999), the WALE (Wall Adopting Local Eddy-viscosity) model, is elaborated. The derivation of the spatial filtered Navier-Stokes equations is discussed first.

3.3.1 Spatial filtered Navier-Stokes

In this section, the derivation is given of the LES equations. The flow has a variable density when transporting sediment using a liquid. In order to simplify the filtered equations a mass-weighted average, or Favre averaging, is applied, see also Eq. (4.6). Any Favre averaged quantity, for instance, the velocity can be decomposed into the following parts:

$$\mathbf{u} = \tilde{\mathbf{u}} + \mathbf{u}'' \tag{3.19}$$

Where $\tilde{\mathbf{u}}$ is the Favre averaged velocity and $\mathbf{u}''$ is the fluctuating velocity part. The Favre averaged velocity is given by:

$$\tilde{\mathbf{u}} = \frac{\overline{\rho \mathbf{u}}}{\overline{\rho}} \tag{3.20}$$

The Favre averaged velocity is multiplied by the instantaneous density, ρ, before filtering, see Bilger (1975). So multiplying Eq. (3.19) by ρ gives:

$$\rho\, \mathbf{u} = \rho \tilde{\mathbf{u}} + \rho \mathbf{u}'' \tag{3.21}$$

and applying a filter to Eq. (3.21):

$$\overline{\rho\, \mathbf{u}} = \overline{\rho \tilde{\mathbf{u}}} + \overline{\rho \mathbf{u}''} \tag{3.22}$$

in which:

$$\overline{\rho \tilde{\mathbf{u}}} = \overline{\rho} \tilde{\mathbf{u}} \tag{3.23}$$

and:

$$\overline{\rho \mathbf{u}''} = 0 \tag{3.24}$$

Now by using Favre averaging, the filtered fluctuating part $\overline{\rho \mathbf{u}''}$, is eliminated. This results in simplified expressions of the continuity and momentum equations. The continuity equation is the following:

$$\frac{\partial \overline{\rho}}{\partial t} + \nabla \cdot (\overline{\rho} \tilde{\mathbf{u}}) = 0 \tag{3.25}$$

Here it is assumed that the filtering commutes with derivative operation, see Eq. (3.18) and Eq. (3.17). Now the Favre averaged momentum equation is

given by:

$$\frac{\partial \overline{\rho}\tilde{\mathbf{u}}}{\partial t} + \nabla \cdot (\overline{\rho}\tilde{\mathbf{u}}\tilde{\mathbf{u}}) = \\ -\nabla \overline{p} + \nabla \cdot \left(\mu \left(\nabla \tilde{\mathbf{u}} + \nabla \tilde{\mathbf{u}}^T\right)\right) - \nabla \cdot \tilde{\mathbf{T}}_{sgs} + \mathbf{s} \tag{3.26}$$

where $\tilde{\mathbf{T}}_{sgs}$ is the following:

$$\tilde{\mathbf{T}}_{sgs} = \overline{\rho}\,(\widetilde{\mathbf{u}\,\mathbf{u}} - \tilde{\mathbf{u}}\,\tilde{\mathbf{u}}) \tag{3.27}$$

in which $\tilde{\mathbf{T}}_{sgs}$ is the sub grid stress tensor and is unclosed and therefor needs to be modeled. This can be done with help of a turbulent eddy viscosity, ν_t, and can be written in the following form,

$$\tilde{\mathbf{T}}_{sgs} \approx 2\,\overline{\rho}\,\nu_t \tilde{S}_{ij} = -\overline{\rho}\,\nu_t \left(\nabla \tilde{\mathbf{u}} + \nabla \tilde{\mathbf{u}}^T\right) \tag{3.28}$$

Now by substituting Eq. (3.28) in Eq. (3.26), the following equation is obtained,

$$\frac{\partial \overline{\rho}\tilde{\mathbf{u}}}{\partial t} + \nabla \cdot (\overline{\rho}\tilde{\mathbf{u}}\tilde{\mathbf{u}}) = \\ -\nabla \overline{p} + \nabla \cdot \left(\mu + \overline{\rho}\nu_t \left(\nabla \tilde{\mathbf{u}} + \nabla \tilde{\mathbf{u}}^T\right)\right) + \mathbf{s} \tag{3.29}$$

Now Eq. (3.29) is the filtered momentum equation. The derivation of a filtered turbulent scalar transport equation is discussed next.

3.3.2 Turbulent scalar transport

The transport of a scalar, an example of a scalar is a sediment fraction, can be described using the transport equation. The transport equation for some generic scalar ϕ is given by, see Chumakov (2005) or Ahmadi and Ma (1990):

$$\frac{\partial \rho\phi}{\partial t} + \nabla \cdot (\rho \mathbf{u}\,\phi) = 0 \tag{3.30}$$

By applying a filter to Eq. (3.30) the following expression is obtained:

$$\frac{\partial \overline{\rho\phi}}{\partial t} + \nabla \cdot (\overline{\rho \mathbf{u}\,\phi}) = 0 \tag{3.31}$$

By Favre averaging, with help of Eq. (3.19)-Eq. (3.24), $\overline{\rho\phi}$ is rearranged as:

$$\overline{\rho\phi} = \overline{\rho}\tilde{\phi} \tag{3.32}$$

and $\overline{\rho \mathbf{u}\, \phi}$ is written as:

$$\overline{\rho \mathbf{u}\, \phi} = \overline{\rho} \widetilde{\phi\, \mathbf{u}} \tag{3.33}$$

with help of Eq. (3.32) and Eq. (3.33), Eq. (3.31) is formulated as:

$$\frac{\partial \overline{\rho} \tilde{\phi}}{\partial t} + \nabla \cdot (\overline{\rho} \widetilde{\phi\, \mathbf{u}}) = 0 \tag{3.34}$$

and rearranging yields the final form:

$$\frac{\partial \overline{\rho} \tilde{\phi}}{\partial t} + \nabla \cdot (\overline{\rho} \tilde{\phi}\, \tilde{\mathbf{u}}) = -\nabla \cdot \tilde{\mathbf{t}}_{sgs} \tag{3.35}$$

Here $\tilde{\mathbf{t}}_{sgs}$ is called the sub grid scale scalar flux and is expressed as:

$$\tilde{\mathbf{t}}_{sgs} = \overline{\rho}(\widetilde{\phi\, \mathbf{u}} - \tilde{\phi}\, \tilde{\mathbf{u}}) \tag{3.36}$$

The sub grid scale scalar flux is unclosed and needs to be modeled. This can be done using the gradient diffusion hypothesis, see Pope (2000), so Eq. (3.36) can be approximated by the following:

$$\tilde{\mathbf{t}}_{sgs} = \overline{\rho}(\widetilde{\phi\, \mathbf{u}} - \tilde{\phi}\, \tilde{\mathbf{u}}) \approx -\overline{\rho}\, \Gamma_t \nabla \tilde{\phi} \tag{3.37}$$

Here Γ_t is the turbulent diffusion coefficient. This coefficient depends on the eddy viscosity and the turbulent Schmidt number, Sc_t:

$$\Gamma_t = \frac{\nu_t}{Sc_t} \tag{3.38}$$

The turbulent Schmidt number is the ratio of momentum diffusivity to mass diffusivity in a turbulent flow:

$$Sc_t = \frac{\nu_t}{\Gamma_t} \tag{3.39}$$

Therefore, if the turbulent Schmidt number is known, the turbulent diffusivity can be estimated. An estimation of the value of the turbulent Schmidt will be given in Section 4.3. Now the complete scalar transport equation is:

$$\frac{\partial \overline{\rho} \tilde{\phi}}{\partial t} + \nabla \cdot (\overline{\rho} \tilde{\phi}\, \tilde{\mathbf{u}}) = \nabla \cdot \left(\overline{\rho}\, \Gamma_t \nabla \tilde{\phi} \right) \tag{3.40}$$

the turbulent eddy viscosity, ν_t, is yet to be determined. This is done with help of sub grid scale models and is elaborated in the next section.

3.4 Turbulence modeling using sub-grid-scale models

In turbulence modeling a closure equation is needed to account for the Reynolds stresses. Boussinesq introduced the turbulent viscosity hypothesis in order to model these Reynolds stresses. In this hypothesis the stresses are modeled using the concept of an eddy viscosity. The eddy viscosity in LES (Large Eddy Simulation) is modeled using a low pass spatial filter. There are many spatial filters which can be used, the most well-known filter is the Smagorinsky model, see Smagorinsky (1963). A complete list can be found in Sagaut (2001) and references therein. The choice of this spatial filter depends on the flow. The mixture flow is described as a continuum in which sharp interfaces can occur. For instance, when a sand bed is formed. The mixture changes then from a liquid to a solid state. A sharp interface is formed above the sand bed and the sand bed acts as a wall boundary. The filter length needs to be adjusted near this interface or walls. An often used solution is to apply a damping function, see Van Driest (1956), near walls or interfaces. However, this damping function is cumbersome to implement in complex geometries and time varying sand bed interfaces. With these requirements there is a need for a model that can automatically adjust the filter length near interfaces or walls. A LES filter is introduced which meets the requirements mentioned above and is discussed in Section 3.4.2.

3.4.1 Smagorinsky

In the Smagorinsky SGS model, proposed by Smagorinsky (1963), the sub grid scale stress tensor, $\tilde{\mathbf{T}}_{sgs}$, is approximated by:

$$\tilde{\mathbf{T}}_{sgs} \approx 2\,\mu_t \tilde{S}_{ij} = \mu_t \left(\nabla \tilde{\mathbf{u}} + \nabla \tilde{\mathbf{u}}^T \right) \tag{3.41}$$

with:

$$\mu_t = -\,\overline{\rho}\,(C_s \Delta)^2 \sqrt{2\,\tilde{S}_{ij}\,\tilde{S}_{ij}} \tag{3.42}$$

and:

$$\tilde{S_{ij}} = \frac{1}{2}\left(\frac{\partial \tilde{u}_i}{\partial x_j} + \frac{\partial \tilde{u}_j}{\partial x_i} \right) \tag{3.43}$$

Here the turbulent eddy viscosity is denoted by μ_t and C_s is the Smagorinsky constant. This constant is $C_s \approx 0.17$, see Pope (2000). The filter width, Δ, given by $\Delta = (\Delta_x\, \Delta_y\, \Delta_z)^{1/3}$ with Δ_x, Δ_y and Δ_z is the grid spacing in x, y and z direction respectively. From Eq. (3.42) and Eq. (3.43) it can be seen that the eddy viscosity model is dissipative. So when shear occurs in the flow, the eddy viscosity, μ_t, increases. This is the case near the walls or boundaries.

Hence special care needs to be taken at the boundaries. A common solution is applying a damping function at the walls reducing the eddy viscosity to zero. This can be done with the van Driest damping function, see Van Driest (1956),

$$\overline{\nu_t} = \kappa\, \overline{\nu}\, y^+ \left(1 - exp(-y^+/A^+)\right)^2 \tag{3.44}$$

in which the so-called von Kármán's constant is $\kappa \approx 0.4$, the variable, A^+, is a constant with a value 19 and y^+ is the dimensionless wall coordinate, defined as $y^+ = y_w u_\tau/\nu$. Here $\overline{\nu}$ is the kinematic viscosity and is formulated as $\overline{\nu} = \mu/\overline{\rho}$. Incorporating this damping function, Eq. (3.44), in complex geometries is cumbersome. Furthermore, the flow is assumed to be turbulent, which is not always the case, or can be determined a priori. In the next section, the WALE model is presented. With this type of SGS model, it is possible to describe flows which overcome the difficulties described above.

3.4.2 WALE LES model

The WALE model, proposed by Nicoud and Ducros (1999), is discussed in this section. The model can handle complex geometries without the need for ad hoc damping functions in the vicinity of the walls. Furthermore, this model is able to describe the transition between laminar and turbulent flow. However, this is restricted to non-complex 3-dimensional flows. Using the Einstein notation the gradient velocity tensor is defined as:

$$g_{ij} = \frac{\partial \tilde{u}_i}{\partial x_j} \tag{3.45}$$

note here the velocity, $\tilde{u}_i$, is Favre filtered. The traceless symmetric part of the square of the velocity gradient tensor is defined as:

$$S^d_{ij} = \frac{1}{2}\left(g^2_{ij} + g^2_{ji}\right) - \frac{1}{3}\,\delta_{ij}\, g^2_{kk} \tag{3.46}$$

here the square of the gradient velocity tensor, g_{ij}^2, is given by $g_{ij}^2 = g_{ik}g_{kj}$. Finally the Kronecker symbol is denoted as δ_{ij}. From Eq. (3.46) it can be readily seen that the trace of the tensor S_{ij}^d is zero. With help of the deviator Eq. (3.46), the eddy viscosity, proposed by Nicoud and Ducros (1999) reads:

$$\mu_t = \overline{\rho}\,(C_w\Delta)^2\,\frac{(S_{ij}^d\;S_{ij}^d)^{3/2}}{(S_{ij}\;S_{ij})^{5/2} + (S_{ij}^d\;S_{ij}^d)^{5/4}} \tag{3.47}$$

in pure shear (so $gij = 0$ except for g_{12}), $S_{ij}^d S_{ij}^d$ in Eq. (3.47) reduces to zero. This is shown next, see Nicoud and Ducros (1999). First the antisymmetric part, Ω_{ij}, of the gradient velocity tensor, g_{ij}, is defined as:

$$\tilde{\Omega}_{ij} = \frac{1}{2}\left(\frac{\partial\tilde{u}_i}{\partial x_j} - \frac{\partial\tilde{u}_j}{\partial x_i}\right) \tag{3.48}$$

Rewriting the tensor, S_{ij}^d, Eq. (3.46), in the form:

$$S_{ij}^d = \tilde{S}_{ik}\tilde{S}kj + \tilde{\Omega}_{ik}\tilde{\Omega}_{kj} - \frac{1}{3}\delta_{ij}\left(\tilde{S}_{mn}\tilde{S}_{nm} - \tilde{\Omega}_{mn}\tilde{\Omega}_{nm}\right) \tag{3.49}$$

By using the Cayley-Hamilton theorem, relation Eq. (3.49) and assuming incompressibility, the following is obtained:

$$S_{ij}^d S_{ij}^d = \frac{1}{6}\left(S^2\;S^2 + \Omega^2\;\Omega^2\right) + \frac{2}{3}S^2\Omega^2 + 2IV_{S\Omega} \tag{3.50}$$

where:

$$S^2 = \tilde{S}_{ij}\tilde{S}_{ij}, \qquad\qquad \Omega^2 = \tilde{\Omega}_{ij}\tilde{\Omega}_{ij} \tag{3.51}$$

and:

$$IV_{S\Omega} = \tilde{S}_{ik}\tilde{S}_{kj} \tag{3.52}$$

From Eq. (3.50) a LES model detects turbulence structures with strain rate rotation strain or both. Now in case of pure shear, i.e. $g_{ij} = 0$, except for g_{12}, so $S^2 = \Omega^2 = 4\tilde{S}_{12}$ and $IV_{S\Omega} = -\frac{1}{2}S^2S^2$ upon substitution in Eq. (3.50), $S_{ij}^d S_{ij}^d$ is zero. Shear zones contribute to a smaller extent to energy dissipation then eddies. Moreover, almost no eddy-viscosity is produced in a wall-bounded laminar flow, for instance, a Poiseuille flow. This leads to a negligible amount

of diffusion in pure shear and the development of unstable waves would be possible. This is an advantage over the Smagorinsky model where the shear is large for wall-bounded flows. In the Smagorinsky model, the eddy viscosity in pure shear i.e. at the walls or at an obstacle in the flow is large. This is caused by the nonvanishing term $\tilde{S}_{ij}\tilde{S}_{ij}$ in contrast with the WALE model wherein pure shear the eddy viscosity reduces to zero.

3.5 Turbulent boundary layer

Fully resolved LES computations are computationally expensive at high Reynolds numbers, see Chapman (1979), Wang and Moin (2002) or Choi and Moin (2012). An estimation can be made of the number of grid cells needed for a wall-resolved LES calculation, i.e. without the use of wall functions. The amount of grid cells for a fully or wall-resolved LES calculation is proportional to $N \sim Re^{9/5}$, Chapman (1979). The number of grid cells for the wall modeled calculation is proportional to $N \sim Re^{2/5}$. Here is $Re = \rho UL/\mu$, L is the length of a flat plate in the streamwise direction. So in order to reduce the computational cost, wall modeling is applied here. For clarity in the rest of this section the notation of a filtering operator, spatial or Favre, ($\bar{\cdot}$, $\tilde{\cdot}$), is dropped.

3.5.1 Log law

Hydraulically smooth walls

The computational cost of fully resolving the velocity near walls in a turbulent flow is high. This cost is reduced using wall modeling and can be done for wall-bounded flows. Using the eddy viscosity concept the wall shear stress is the following:

$$\tau_w = \rho\left(\nu + \nu_t\right)\frac{\partial u}{\partial y} \tag{3.53}$$

Where ν_t is the kinematic eddy viscosity and u the velocity in x-direction at a certain distance from the wall. Another expression for the wall shear stress, introducing a wall shear velocity u_τ:

$$\tau_w = \rho u_\tau^2 \tag{3.54}$$

The kinematic eddy viscosity is approximated using a damping function. Repeating here the van Driest damping function, Van Driest (1956), given

earlier, see Eq. (3.44):

$$\nu_t = \kappa\, \nu\, y^+ \left(1 - exp(-y^+/A^+)\right)^2 \tag{3.55}$$

The variable y_w is some distance from the wall (in numerical calculations this is the first grid point from the wall). The equations Eq. (3.53) and Eq. (3.55) show that the wall shear stress is a function of the distance to the wall, y_w. Near the wall, the wall distance y_w is approximately zero, $y_w \approx 0$. Now by using Eq. (3.55), the eddy viscosity, $\nu_t \ll \nu$, so Eq. (3.53) can be rewritten as:

$$\tau_w = \rho\nu \frac{\partial u}{\partial y} \tag{3.56}$$

by using Eq. (3.54) and integration of Eq. (3.56) over distance y_w yields the following relation:

$$\frac{\nu u}{y_w} = u_\tau \tag{3.57}$$

Finally, by defining the dimensionless wall coordinate $y^+ = y_w u_\tau/\nu$ and the dimensionless velocity $u^+ = u/u_\tau$, Eq. (3.57) becomes:

$$u^+ = y^+ \tag{3.58}$$

Eq. (3.58) is the so-called viscous sublayer and is valid if $y^+ \lessapprox 5$, see White (1999). For an increasing dimensionless coordinate, y^+, the kinematic viscosity is negligible with respect to the turbulent kinematic viscosity, so $\nu_t \gg \nu$. Now Eq. (3.53) is re-casted in the form:

$$\frac{\tau_w}{\rho} = \nu_t \frac{\partial u}{\partial y} = u_\tau^2 \tag{3.59}$$

Using Eq. (3.55) the turbulent kinematic eddy viscosity for large y^+, becomes:

$$\nu_t = \kappa\nu y^+ \tag{3.60}$$

substitution of Eq. (3.60) in Eq. (3.59) yields:

$$\frac{\partial u}{\partial y^+} = \frac{u_\tau}{\kappa y^+} \tag{3.61}$$

and integration over y^+ gives:

$$\int \frac{\partial u}{\partial y^+} dy^+ = \int \frac{u_\tau}{\kappa} \frac{1}{y^+} dy^+ \tag{3.62}$$

and after some elaboration the final form becomes:

$$u^+ = \frac{1}{\kappa} \ln y^+ + C \tag{3.63}$$

In which C is an integration constant and is $C \approx 5$ for hydraulic smooth surfaces. Furthermore, Eq. (3.63) is valid for values of $y^+ \gtrapprox 30$. This is the so-called log law region. In Figure 3.2 the log law region and the viscous sublayer is given graphically. Also, DNS data from Moser et al. (1999) is plotted. If the value of y^+ ranges between 5 and 30, or $5 \lessapprox y^+ \lessapprox 30$, then either Eq. (3.58) or Eq. (3.63) do hold. This region is called the buffer layer. If the dimensionless velocity, u^+, is known the wall shear stress can be determined. However, it is seen from Eq. (3.63) that the value of u^+ occurs at both sides of the equation. Here u^+ is determined using an iterative numerical method.

Hydraulically rough walls

In the previous section, the wall boundaries were given for hydraulically smooth walls. In some cases the wall is not smooth but rough, this is the case for a sediment bed or if sand grains are glued to the walls simulating a rough wall boundary. For a hydraulically rough flow, the following expression is used as a wall function:

$$u^+ = \frac{1}{\kappa} \ln \frac{y_w}{y_0} \tag{3.64}$$

where y_0 is expressed as:

$$y_0 = \frac{k_s}{30} \tag{3.65}$$

where k_s is the roughness height according to Nikuradse (1933). In the next section, the wall shear stress will be extended for 3 dimensional flow problems. This will be done on the basis of Eq. (3.63).

3.5.2 Shear stress

In this section, the wall shear stress is given and is applied to 3 dimensional flow modeling. The determination of the wall shear stress is done for only a hydraulically smooth wall, Eq. (3.63), with $y^+ > 11.68$. The wall shear stress for a hydraulically rough wall can be derived similarly. Rewriting Eq. (3.63) into the form:

$$\frac{u}{u_\tau} = \frac{1}{\kappa} \ln \frac{y_{wall} u_\tau}{\nu} + C \tag{3.66}$$

Repeating the wall shear stress Eq. (3.54):

$$\tau_{wall} = \rho u_\tau^2 \tag{3.67}$$

From Eq. (3.66) the dimensionless velocity u_τ is determined and is done by using an iterative method. The wall shear stress is obtained by substituting the velocity u_τ in Eq. (3.67). The wall shear stress only acts at the boundary layer in the flow direction. In a Cartesian coordinate system the flow direction at a

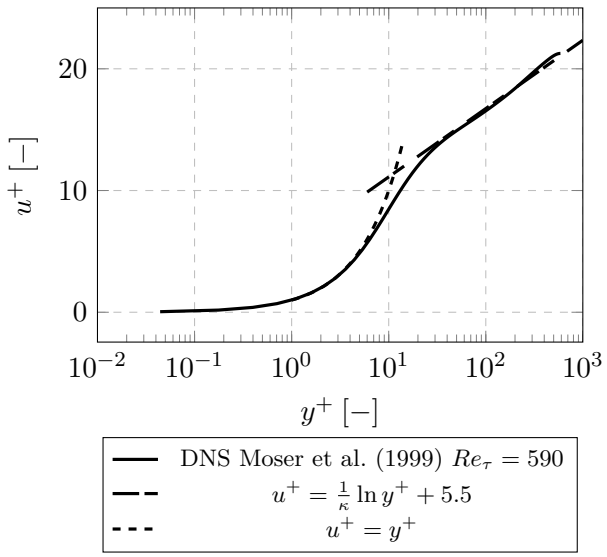

Figure 3.2: Plot of the law of the wall. The continuous line are DNS data taken from Moser et al. (1999), the dashed lines are the the log law, Eq. (3.63), and the viscous sublayer, Eq. (3.63).

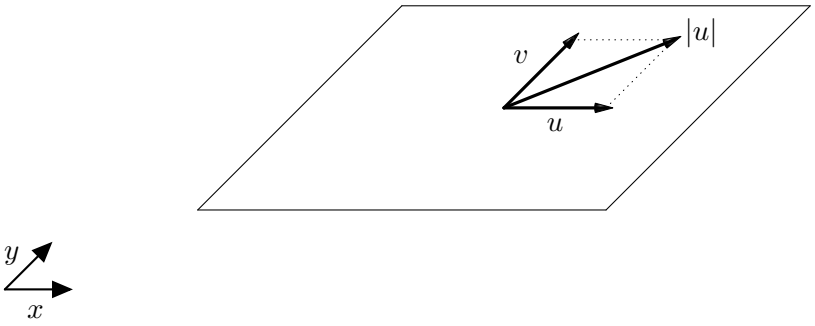

Figure 3.3: Velocity and wall shear stress decomposition in the xy plane, see Eq. (3.69) and Eq. (3.69).

boundary layer is in both stream-wise and span-wise direction, see Figure 3.3. This implies that shear stress needs to be decomposed in the x and y directions, in case of a xy plane. The wall shear stress is obtained using Eq. (3.66) and Eq. (3.67):

$$|u| = \frac{u_\tau}{\kappa} \ln \frac{y_w u_\tau}{\nu} + C \tag{3.68}$$

in which, $|u| = \sqrt{u^2 + v^2}$, is the total velocity at the boundary layer, see Figure 3.3. If $|u|$ is known, u_τ can be determined with help of Eq. (3.68) using an iterative procedure or Eq. (3.57). An example is given for the decomposition of the wall shear stress, τ_w, in the x, y plane, see Figure 3.3, in the x direction:

$$\tau_{xw} = \tau_w \frac{u}{|u|} \tag{3.69}$$

and the wall shear in the y direction is:

$$\tau_{yw} = \tau_w \frac{v}{|u|} \tag{3.70}$$

The derivation of the direction of the wall shear stress in other planes, (e.g. xz, yz etc.) is analog to the one given above. There are other wall models which are commonly used, these are not discussed here but can be found in literature, see for example Werner and Wengle (1993). A more complete overview of wall models is given in Sagaut (2001).

Chapter 4

Drift-flux Modeling

Sediment suspensions consist of a carrier fluid, or liquid phase, and several sediment phases. The sediment phase, in turn, consists of volume fractions with different particle sizes. A sediment suspension can be described as a fluid with multiple phases or volume fractions. Here we use the drift-flux model, in which it is assumed that these sediment fractions can be described as a continuum. That is to say that the mixture is described as if it were one fluid. Several derivations of the drift-flux model can be found in Zuber and Findlay (1965), Ishii (1975), Ishii and Hibiki (2006), Drew (1983), Manninen and Taivassalo (1996), Jakobsen (2014), Hiltunen et al. (2009). An interesting application of the drift-flux model can be found in Van Rhee (2002) modeling sedimentation in hoppers. The derivation is given of the drift-flux model starting with the basic equations.

4.1 Basic equations

4.1.1 Definitions

It is impossible to describe the motion for every sand particle in a flow individually in large domains, i.e. with respect to the particle size. Therefore, a continuum approach is employed here. In order to derive the drift-flux model first, some definitions are introduced. The average amount of volume occupied

by a sediment fraction, α_k, is defined as:

$$\alpha_k = \frac{V_k}{V_0} \tag{4.1}$$

here α_k is the volume averaged quantity of phase k, which is the ratio of the volume occupied by a fraction k, V_k and the total volume V_0. This volume is defined as the sum of the volume occupied by all the fractions, including the fluid phase, $V_0 = \sum_{k=1}^{N} V_k$. The total volume concentration, i.e. all the phases including the liquid phase is by definition:

$$\sum_{k=1}^{N} \alpha_k = 1 \tag{4.2}$$

The volume concentration of solids is defined as:

$$\alpha_t = \sum_{k=2}^{N} \alpha_k \tag{4.3}$$

where $k = 2...N$ are the solid fractions and $k = 1$ denotes the liquid fraction:

$$\alpha_f = \alpha_1 \tag{4.4}$$

The variable α_f is the liquid volume fraction and α_t is the total volume concentration of solids. The mixture density is expressed as:

$$\rho_m = \sum_{k=1}^{N} \rho_k \alpha_k \tag{4.5}$$

where N is total amount of fractions in the mixture and ρ_k the density of each fraction including the liquid fraction. The mixture velocity is obtained by mass weighted averaging, or Favre averaging:

$$\mathbf{u}_m = \frac{1}{\rho_m} \sum_{k=1}^{N} \rho_k \alpha_k \mathbf{u}_k \tag{4.6}$$

in which $\mathbf{u}_k$ is the velocity of phase k. The advantage of using Favre averaging is that it gives a simple form of the continuity equation, Ishii (1975). The mass fraction c_k is given by:

$$c_k = \frac{\rho_k \alpha_k}{\sum_{k=1}^{N} \rho_k \alpha_k} = \frac{\rho_k \alpha_k}{\rho_m} \tag{4.7}$$

The relative velocity is the difference of velocity between the carrier fluid, $\mathbf{u}_f$ and the velocity of the phase k, $\mathbf{u}_k$. This velocity is defined as:

$$\mathbf{u}_{kr} = \mathbf{u}_k - \mathbf{u}_f \tag{4.8}$$

Note here that when $k = 1$, ,which is the liquid phase or fraction f, the relative velocity $\mathbf{u}_{kr} = 0$. The mixture volumetric flux, $\mathbf{j}$, is the summation of the velocities of all the phases including the carrier fluid or continuous phase:

$$\mathbf{j} = \sum_{k=1}^{N} \alpha_k \, \mathbf{u}_k \tag{4.9}$$

The diffusion velocity, $\mathbf{u}_{km}$, is the difference between the particulate phase $\mathbf{u}_k$ and the mixture velocity, $\mathbf{u}_m$, Eq. (4.6):

$$\mathbf{u}_{km} = \mathbf{u}_k - \mathbf{u}_m \tag{4.10}$$

The summation over all fractions of the diffusion velocity, $\mathbf{u}_{km}$ is by definition zero or rewritten in mathematical form,

$$\sum_{k=1}^{N} \alpha_k \rho_k \mathbf{u}_{km} = 0 \tag{4.11}$$

The drift velocity is the difference between the volumetric flux $\mathbf{j}$ and the dispersed phase velocity, $\mathbf{u}_k$:

$$\mathbf{u}_{kj} = \mathbf{u}_k - \mathbf{j} \tag{4.12}$$

In which $\mathbf{u}_{kj}$ is the drift velocity. Now with the definitions given the mixture continuity and the mixture momentum equations can be derived.

4.1.2 Mixture continuity

The mixture continuity is given in the following here. The filtered mixture continuity for one fraction or phase is:

$$\frac{\partial \alpha_k \, \rho_k}{\partial t} + \nabla \cdot \alpha_k \rho_k \mathbf{u}_k = \Lambda_k \tag{4.13}$$

In Eq. (4.13) the source term Λ_k denotes a phase transition. In the case of sediments phase transitions are absent so Λ_k reduces to zero. The phase continuity equation is the following:

$$\frac{\partial \alpha_k \, \rho_k}{\partial t} + \nabla \cdot \alpha_k \rho_k \mathbf{u}_k = 0 \tag{4.14}$$

Now by summing over all the fractions the mixture continuity equation is obtained:

$$\frac{\partial}{\partial t}\sum_{k=1}^{N}\alpha_k\,\rho_k + \nabla\cdot\sum_{k=1}^{N}\alpha_k\rho_k\mathbf{u}_k = 0 \tag{4.15}$$

Substitution of Eq. (4.5) and Eq. (4.6) in Eq. (4.15) gives the mixture continuity equation:

$$\frac{\partial\rho_m}{\partial t} + \nabla\cdot(\rho_m\mathbf{u}_m) = 0 \tag{4.16}$$

4.1.3 Mixture momentum

Assuming that each volume fraction, α_k, can be described using the Navier-Stokes equations, the momentum equation of volume fraction or dispersed phase, α_k, is given by:

$$\begin{aligned}&\frac{\partial\alpha_k\rho_k\mathbf{u}_k}{\partial t} + \nabla\cdot(\alpha_k\rho_k\mathbf{u}_k\mathbf{u}_k) = \\ &-\nabla\alpha_k p_k + \nabla\cdot\left(\alpha_k\mathbf{T}_k + \alpha_k\mathbf{T}_k^t\right) + \alpha_k\rho_k\mathbf{g} + \alpha_k\mathbf{m}_k\end{aligned} \tag{4.17}$$

The tensors $\mathbf{T}_k$ and $\mathbf{T}_k^t$ are respectively the contributions due to viscous and turbulent stresses. The source term $\mathbf{m}_k$ is the interacting force of each volume fraction. The pressure of phase k is given by p_k and finally $\mathbf{g}$ is the gravitational constant vector. The mixture momentum equation is obtained by summing over all the volume fractions of Eq. (4.17):

$$\begin{aligned}&\frac{\partial}{\partial t}\sum_{k=1}^{N}\alpha_k\rho_k\mathbf{u}_k + \nabla\cdot\sum_{k=1}^{N}(\alpha_k\rho_k\mathbf{u}_k\mathbf{u}_k) = \\ &-\nabla\sum_{k=1}^{N}\alpha_k p_k + \nabla\cdot\sum_{k=1}^{N}\left(\alpha_k\mathbf{T}_k + \alpha_k\mathbf{T}_k^t\right) + \\ &\sum_{k=1}^{N}\alpha_k\rho_k\mathbf{g} + \sum_{k=1}^{N}\alpha_k\mathbf{m}_k\end{aligned} \tag{4.18}$$

Using Eq. (4.11) and substituting Eq. (4.5), Eq. (4.6), Eq. (4.10) in Eq. (4.18) the mixture momentum equation is obtained:

$$\frac{\partial \rho_m \mathbf{u}_m}{\partial t} + \nabla \cdot \rho_m \mathbf{u}_m \mathbf{u}_m = \\ -\nabla p_m + \nabla \cdot \left(\mathbf{T}_m + \mathbf{T}_m^t - \sum_{k=1}^{N} \alpha_k \rho_k \mathbf{u}_{km} \mathbf{u}_{km} \right) + \rho_m \mathbf{g} + \mathbf{m}_m \tag{4.19}$$

Now the internal forces, $\mathbf{m}_m$, in the mixture momentum equation cancel out, reducing $\mathbf{m}_m$ to zero.

4.2 Force balance equation

In drift-flux modeling, the difference in velocity between the continuous phase and the particle phases account for the forces acting on a particle, see Manninen and Taivassalo (1996). Therefore, slip velocities between the particulate and the continuous phase are of importance. Repeating Eq. (4.17) the momentum equation of the particulate phase is:

$$\frac{\partial \alpha_k \rho_k \mathbf{u}_k}{\partial t} + \nabla \cdot (\alpha_k \rho_k \mathbf{u}_k \mathbf{u}_k) = \\ -\nabla \alpha_k p_k + \nabla \cdot \left(\alpha_k \mathbf{T}_k + \alpha_k \mathbf{T}_k^t \right) + \alpha_k \rho_k \mathbf{g} + \alpha_k \mathbf{m}_k \tag{4.20}$$

Here $\mathbf{m}_k$ is force per unit volume exerted by the continuous phase on the sediment phase. Examples of these forces are viscous drag forces added, mass forces etc.. In order to determine this force slip velocities between the fluid and a particulate phase needs to be derived. With Eq. (4.17) or Eq. (4.20) the momentum equation of the dispersed phase can be rewritten as follows:

$$\alpha_k \rho_k \frac{\partial \mathbf{u}_k}{\partial t} + \alpha_k \rho_k \mathbf{u}_k \cdot \nabla \mathbf{u}_k = \\ -\nabla \alpha_k p_k + \alpha_k \nabla \cdot \mathbf{S}_k + \alpha_k \rho_k \mathbf{g} + \alpha_k \mathbf{m}_k \tag{4.21}$$

Where $\mathbf{S}_k = \mathbf{T}_k + \mathbf{T}_k^t$ is the summation of the viscous and the turbulent stresses respectively for each fraction k. Summation over all the fractions in Eq. (4.21) yields the following mixture momentum equation:

$$\rho_m \frac{\partial \mathbf{u}_m}{\partial t} + \rho_m \mathbf{u}_m \cdot \nabla \mathbf{u}_m = -\nabla p_m + \nabla \cdot \mathbf{S}_m + \rho_m \mathbf{g} \tag{4.22}$$

With $\mathbf{S}_m = \mathbf{T}_k + \mathbf{T}_k^t - \sum_{k=1}^{N} \alpha_k \rho_k \mathbf{u}_{km} \mathbf{u}_{km}$. Now subtracting Eq. (4.21) from Eq. (4.22) and assuming $p_m = p_k$:

$$\begin{aligned}
&\alpha_k \rho_k \frac{\partial \mathbf{u}_k}{\partial t} - \alpha_k \rho_m \frac{\partial \mathbf{u}_m}{\partial t} + \\
&\alpha_k \rho_k \mathbf{u}_k \cdot \nabla \mathbf{u}_k - \alpha_k \rho_m \mathbf{u}_m \cdot \nabla \mathbf{u}_m = \\
&\alpha_k \left(\nabla \cdot \mathbf{S}_k - \nabla \cdot \mathbf{S}_m \right) + \alpha_k \left(\rho_k - \rho_m \right) \mathbf{g} + \alpha_k \mathbf{m}_k
\end{aligned} \tag{4.23}$$

In order to simplify Eq. (4.23) the following assumption is made, Manninen and Taivassalo (1996):

$$\mathbf{u}_k \cdot \nabla \mathbf{u}_k \approx \mathbf{u}_m \cdot \nabla \mathbf{u}_m \tag{4.24}$$

Using definition Eq. (4.10) and substitution of Eq. (4.24) in Eq. (4.23) yields:

$$\begin{aligned}
&\alpha_k \rho_k \frac{\partial \mathbf{u}_{km}}{\partial t} + \alpha_k \rho_k \frac{\partial \mathbf{u}_m}{\partial t} - \alpha_k \rho_m \frac{\partial \mathbf{u}_m}{\partial t} \\
&\alpha_k \rho_k \mathbf{u}_k \cdot \nabla \mathbf{u}_k - \alpha_k \rho_m \mathbf{u}_m \cdot \nabla \mathbf{u}_m = \\
&\alpha_k \left(\nabla \cdot \mathbf{S}_k - \nabla \cdot \mathbf{S}_m \right) + \alpha_k \left(\rho_k - \rho_m \right) \mathbf{g} + \alpha_k \mathbf{m}_k
\end{aligned} \tag{4.25}$$

Now with small slip velocities, $\mathbf{u}_{km}$, the term $\partial \mathbf{u}_{km}/\partial t$ can be neglected, so $\partial \mathbf{u}_{km}/\partial t \approx 0$. Finally, it is assumed that the diffusive terms are small in comparison with the inertia terms:

$$\nabla \cdot \mathbf{S}_k - \nabla \cdot \mathbf{S}_m \ll \left(\rho_k - \rho_m \right) \frac{\partial \mathbf{u}_m}{\partial t} + \left(\rho_k - \rho_m \right) \mathbf{u}_m \cdot \nabla \mathbf{u}_m \tag{4.26}$$

Hence the diffusive terms are neglected. Finally the expression for $\mathbf{m}_k$ is obtained:

$$\mathbf{m}_k = \left(\rho_k - \rho_m \right) \left(\frac{\partial \mathbf{u}_m}{\partial t} + \mathbf{u}_m \cdot \nabla \mathbf{u}_m - \mathbf{g} \right) \tag{4.27}$$

The particle velocity, $\mathbf{u}_k$, depends on forces, $\mathbf{m}_k$, acting on a single particle and the volume concentration of solids, α_t. Here $\mathbf{m}_k$ is the force per unit volume.

In the next section, an expression for the transport velocity $\mathbf{u}_k$ is given. The phase continuity equation, Eq. (4.14), is used describing the transport of sediment fractions.

4.3 LES spatial filtering

In LES equations a spatial filter is applied solving only large-scale structures of a turbulent flow. This filter is applied to the fraction continuity equation and the mixture momentum equation. Sediment-water suspensions vary in density both in time and space. The derivation of the averaged equations derived here is similar to the derivation introduced in Section 3.3 modeling turbulence in LES.

4.3.1 Continuity

First, the derivation of the spatially filtered mixture continuity is given in the following. The scalar transport equation is given by:

$$\frac{\partial \alpha_k \, \rho_k}{\partial t} + \nabla \cdot \alpha_k \rho_k \mathbf{u}_k = 0 \tag{4.28}$$

now by applying a straight filter, as defined in see Eq. (3.2), the following is obtained:

$$\frac{\partial \overline{\alpha_k \, \rho_k}}{\partial t} + \nabla \cdot \overline{\alpha_k \rho_k \mathbf{u}_k} = 0 \tag{4.29}$$

summing over all the fractions:

$$\frac{\partial}{\partial t} \sum_{k=1}^{N} \overline{\alpha_k \, \rho_k} + \nabla \cdot \sum_{k=1}^{N} \overline{\alpha_k \rho_k \mathbf{u}}_k = 0 \tag{4.30}$$

now the mixture density is given by:

$$\overline{\rho}_m = \sum_{k=1}^{N} \overline{\alpha_k \, \rho_k} \tag{4.31}$$

and the Favre averaged velocity, $\tilde{\mathbf{u}}_m$:

$$\tilde{\mathbf{u}}_m = \frac{1}{\overline{\rho}_m} \sum_{k=1}^{N} \overline{\alpha_k \rho_k \mathbf{u}_k} \tag{4.32}$$

finally the filtered continuity equation is:

$$\frac{\partial \overline{\rho}_m}{\partial t} + \nabla \cdot \overline{\rho}_m \tilde{\mathbf{u}}_m = 0 \tag{4.33}$$

from Eq. (4.33) it can be seen that, using Favre averaging, the mixture continuity is formulated in a simple form.

Phase transport equation

The filtered equation of the transport of sediment fractions is formulated. The derivation is similar to the one given in Section 3.3 for a variable density flow. Again the unfiltered phase continuity is given by:

$$\frac{\partial \alpha_k \, \rho_k}{\partial t} + \nabla \cdot \alpha_k \rho_k \mathbf{u}_k = 0 \tag{4.34}$$

applying a filter to the transport equation:

$$\frac{\partial \overline{\alpha_k \, \rho_k}}{\partial t} + \nabla \cdot \overline{\alpha_k \rho_k \mathbf{u}_k} = 0 \tag{4.35}$$

and Favre averaging the term, $\overline{\alpha_k \, \rho}_k$, yields:

$$\overline{\rho}_k \, \tilde{\alpha}_k = \overline{\alpha_k \, \rho_k} \tag{4.36}$$

and the filtered term, $\overline{\rho_k \alpha_k \mathbf{u}_k}$, is written as:

$$\overline{\rho_k \alpha_k \mathbf{u}_k} = \overline{\rho}_k \widetilde{\alpha_k \mathbf{u}_k} \tag{4.37}$$

Now the sediment scalar transport equation can be written as,

$$\frac{\partial \overline{\rho}_k \, \tilde{\alpha}_k}{\partial t} + \nabla \cdot \overline{\rho}_k \, \tilde{\alpha}_k \tilde{\mathbf{u}}_k = -\nabla \cdot \overline{\rho}_k \left(\widetilde{\alpha_k \mathbf{u}_k} - \tilde{\alpha}_k \tilde{\mathbf{u}}_k \right) \tag{4.38}$$

now the right hand side of Eq. (4.38) needs to be closed. This can be done with the gradient diffusion hypothesis, i.e.:

$$-\nabla \cdot \overline{\rho}_k \left(\widetilde{\alpha_k \mathbf{u}_k} - \tilde{\alpha}_k \tilde{\mathbf{u}}_k \right) \approx \overline{\rho}_k \Gamma_t \nabla \tilde{\alpha}_k \tag{4.39}$$

Here Γ_t is the turbulent diffusion coefficient and is a function of the turbulent eddy viscosity, ν_t, and the turbulent Schmidt number, Sc_t, introduced earlier, Eq. (3.39):

$$\Gamma_t = \frac{\nu_t}{Sc_t} \tag{4.40}$$

Now $\overline{\rho}_k$ is constant this term can be dropped from Eq. (4.38). Hence, the complete turbulent sediment transport equation for phase k becomes:

$$\frac{\partial \tilde{\alpha}_k}{\partial t} + \nabla \cdot \tilde{\alpha}_k \tilde{\mathbf{u}}_k = \nabla \cdot \Gamma_t \nabla \tilde{\alpha}_k \tag{4.41}$$

The gradient diffusion hypothesis, used here, requires a value of the turbulent Schmidt number, Sc_t. Unfortunately no universally accepted value or methodology exists to date to determine the value of this parameter. However, an estimation, based on experimental studies, can be made obtaining a value of this parameter. This is elaborated in the following.

Turbulent Schmidt number, Sc_t

The turbulent Schmidt number, Sc_t, in Eq. (4.40), varies and is a property of the turbulent flow, see Gualtieri et al. (2017). Therefore, no universal value could be determined and the value of Sc_t is often assumed, as a first approximation, to be of the order of unity. Various experimental and numerical studies have been conducted, of transport of suspensions, obtaining a value of the turbulent Schmidt number, Sc_t, see Gualtieri et al. (2017) and references therein for an overview. Here some of the findings following from the paper are summarized in short. A universal value of Sc_t could not be identified for all cases considered (sediment-laden open channel flows). Values of the Schmidt number varied in the range of $0.2 < Sc_t < 2.11$ and was determined using fitting techniques under different flow conditions. Moreover, the Schmidt number varies locally and increases as the level of stratification of the flow increases. However, no trends could be established, about the parameters, controlling this variability.

The following expression was introduced by Van Rijn (1984), relating the diffusion coefficient, Γ_t, see Eq. (4.40), to the eddy viscosity, ν_t, reflecting the inertia of particles:

$$\Gamma_t = \beta\Theta\nu_t = \frac{\nu_t}{Sc_t} \tag{4.42}$$

where the β factor takes into account the difference in velocity fluctuations between the carrier fluid and the sediment particles. According to Van Rijn (1984) some investigators have concluded that β is smaller than 1 because the particles cannot respond fully to the turbulent velocity fluctuations. Others state that centrifugal forces, on the sediment particles, throw the particles on the outside the eddies, increasing the mixing rate, hence $\beta > 1$. The β factor was analyzed by Van Rijn (1984), fitting an experimental dataset of Coleman (1970), and can be expressed as the following relation:

$$\beta = \frac{1}{\Theta Sc_t} = 1 + 2\left(\frac{w_\infty}{u_\tau}\right)^2 \quad \text{for} \quad 0.1 < \frac{w_\infty}{u_\tau} < 1 \tag{4.43}$$

where w_∞ is the terminal settling velocity of a single particle and u_τ the friction velocity.

The factor Θ expresses the damping effect of the sediment particles on the turbulence structure of the fluid. The is due to the presence of solids increasing

the viscosity, as discussed in Section 2.3. It is unclear whether Eq. (4.43) can be applied in general flow conditions moreover, the damping effect is already included by a mixture viscosity function, dependent on the volume of solids. This function is in turn incorporated in the momentum balance of the mixture flow.

In this work, the turbulent Schmidt number has been taken as a constant and set to a value of $Sc_t = 1$. This is in accordance with a value of the Schmidt number used in literature, see Chiodi et al. (2014).

Momentum

The mixture momentum equation is described here briefly. The form of the mixture momentum equations is the same as the one in Section 3.2, Eq. (3.29). The momentum equations are the following,

$$\begin{aligned} &\frac{\partial \overline{\rho}_m \tilde{\mathbf{u}}_m}{\partial t} + \nabla \cdot (\overline{\rho}_m \tilde{\mathbf{u}}_m \tilde{\mathbf{u}}_m) = \\ &- \nabla \overline{p} + \nabla \cdot \left(\mu + \overline{\rho}_m \nu_t \left(\nabla \tilde{\mathbf{u}}_m + \nabla \tilde{\mathbf{u}}_m^T \right) \right) + \mathbf{s} \end{aligned} \tag{4.44}$$

in which the sourceterm, $\mathbf{s}$, is given by,

$$\mathbf{s} = \sum_{k=1}^{N} \alpha_k \rho_k \mathbf{u}_{km} \mathbf{u}_{km} + \overline{\rho}_m \mathbf{g} \tag{4.45}$$

Note here that the velocities, $\mathbf{u}_{km}$ are not averaged. Dealing with a strongly coupled system, it is assumed that the particles instantaneously react to velocity changes, see also Section 4.4.4 for an estimation of the validity of this assumption. This means that there is no turbulent dispersion in the slip velocities. The continuity and momentum balances of both the volume fractions and the mixture have been derived. With help of these balances, the interaction between the particulate phase and continuous phase is treated in the next section.

4.3.2 Slip velocity

The transport of sediment fractions is derived with help of the phase continuity equation, Eq. (4.14), repeating the phase continuity:

$$\frac{\partial \alpha_k \, \rho_k}{\partial t} + \nabla \cdot (\alpha_k \rho_k \mathbf{u}_k) = 0 \tag{4.46}$$

In case of a constant fraction density, ρ_k, Eq. (4.46) can be simplified to:

$$\frac{\partial \alpha_k}{\partial t} + \nabla \cdot (\alpha_k \mathbf{u}_k) = 0 \tag{4.47}$$

In Eq. (4.47) $\mathbf{u}_k$ is the fraction transport velocity. With help of Eq. (4.10) Eq. (4.47) can be rewritten as:

$$\frac{\partial \alpha_k}{\partial t} + \nabla \cdot (\alpha_k \mathbf{u}_m + \alpha_k \mathbf{u}_{km}) = 0 \tag{4.48}$$

In this equation the diffusion velocity, $\mathbf{u}_{km}$, is unknown. Here a derivation is given for the diffusion velocity. Now the velocity $\mathbf{u}_k$ is given by:

$$\mathbf{u}_k = \mathbf{u}_{km} + \mathbf{u}_m = \mathbf{u}_{km} + \sum_{k=1}^{N} c_k \mathbf{u}_k \tag{4.49}$$

using:

$$\mathbf{u}_k = \mathbf{u}_{kr} + \mathbf{u}_f \tag{4.50}$$

and substitution of Eq. (4.50) in Eq. (4.49) yields an expression for $\mathbf{u}_{km}$:

$$\mathbf{u}_{km} = \mathbf{u}_k - \sum_{k=1}^{N} c_k \mathbf{u}_k = \mathbf{u}_{kr} + \mathbf{u}_f - \sum_{k=1}^{N} c_k \mathbf{u}_{kr} - \sum_{k=1}^{N} c_k \mathbf{u}_f \tag{4.51}$$

By definition, $\sum_{k=1}^{N} c_k = 1$, hence the diffusion velocity is the following:

$$\mathbf{u}_{km} = \mathbf{u}_{kr} - \sum_{k=1}^{N} c_k \mathbf{u}_{kr} \tag{4.52}$$

The relative velocity, $\mathbf{u}_{kr}$, with respect to the fluid or continuous phase is determined using a closure relation. This closure relation is a function of the volume concentration of solids, α_t, and the so-called particle Reynolds number, Re_p. This is elaborated in the next section.

4.4 Particle settling

4.4.1 Equation of motion of a single particle

The motion of a single particle is described using the second law of Newton:

$$\mathbf{F} = m_p \, \mathbf{a}_p \tag{4.53}$$

Here $\mathbf{F}$ is the sum of all particle forces acting on a single particle, m_p is the mass of the particle and $\mathbf{a}$ is the particle acceleration.

For a particle in a uniform fluid flow the hydrodynamic forces of Eq. (4.53) are the following, see Prosperetti and Tryggvason (2009):

$$\mathbf{F} = \mathbf{F}_d + \mathbf{F}_b + \mathbf{F}_g + \mathbf{F}_a + \mathbf{F}_h \tag{4.54}$$

In which $\mathbf{F}_d$, $\mathbf{F}_b$, $\mathbf{F}_g$, $\mathbf{F}_a$ and $\mathbf{F}_h$ are the drag, buoyancy, gravitational, added mass and history forces respectively. Now first the particle Reynolds number, Re_p, is introduced:

$$Re_p = \frac{\rho_f |\mathbf{u}_f - \mathbf{v}_p| d_p}{\mu_f} \tag{4.55}$$

Where $\mathbf{v}_p$ is the velocity of the particle, μ_f the viscosity of the fluid and d_p the particle diameter. An equation of motion in a non-uniform flow field for a small rigid particle and low particle Reynolds number $Re_p \ll 1$ is derived by Maxey and Riley (1983). A simplified version of this equation is used here, see Ling et al. (2013):

$$m_p \frac{d\mathbf{v}_p}{dt} = m_p \mathbf{g} + \rho_f V_p \left(\frac{D\mathbf{u}_f}{Dt} - \mathbf{g} \right) + \mathbf{F}_d + \mathbf{F}_a + \mathbf{F}_h \tag{4.56}$$

In Eq. (4.56) m_p and V_p are the particle mass and volume respectively. The gravitational and the buoyancy force are given by:

$$\mathbf{F}_b + \mathbf{F}_g = m_p \mathbf{g} + \rho_f V_p \left(\frac{D\mathbf{u}_f}{Dt} - \mathbf{g} \right) \tag{4.57}$$

The term $D\mathbf{u}_f/Dt$ accounts for the acceleration of the fluid where $D/Dt = \partial/\partial t + \mathbf{u} \cdot \nabla$ is the material derivative. Now for small Re_p, the drag force for the Stokes regime, $\mathbf{F}_d$ in Eq. (4.56), is expressed as:

$$\mathbf{F}_d = 3\pi d_p \mu_f \left(\mathbf{u}_f - \mathbf{v}_p \right) \tag{4.58}$$

The added mass force, $\mathbf{F}_a$, is given by:

$$\mathbf{F}_a = \frac{1}{2} \rho_f V_p \left[\frac{D\mathbf{u}_f}{Dt} - \frac{d\mathbf{v}_p}{dt} \right] \tag{4.59}$$

And the history or Basset force is:

$$\mathbf{F}_h = \frac{3}{2} {d_p}^2 \rho_f \sqrt{\pi \frac{\mu_f}{\rho_f}} \int_0^t \frac{dt'}{(t-t')^{1/2}} \left[\frac{D\mathbf{u}_f}{Dt'} - \frac{d\mathbf{v}_p}{dt'} \right] \tag{4.60}$$

The history or Basset force, Eq. (4.60), and the added mass force, Eq. (4.59) are unsteady terms. The LES turbulence model only resolves the motion of the flow at grid scale, at sub-grid scale turbulence is modeled using a closure relation. When particles are smaller than the sub-grid scale, the history and added mass force can be omitted i.e. the particles follow the motion of the flow at resolved-scale instantly. The unsteady forces must be accounted in closure models, see Ling et al. (2013). This omission of the unsteady terms, Eq. (4.60) and Eq. (4.59) greatly simplifies the particle equation of motion. Now Eq. (4.56) has the following form:

$$m_p \frac{d\mathbf{v}_p}{dt} = m_p \mathbf{g} + \rho_f V_p \left(\frac{D\mathbf{u}_f}{Dt} - \mathbf{g} \right) + \mathbf{F}_d \tag{4.61}$$

The drag force, $\mathbf{F}_d$, given by Eq. (4.58) is only valid for Stokes flow, i.e. for low Re_p. A more general expression for the drag force is given by:

$$\mathbf{F}_d = \frac{1}{2} C_d \rho_f A_p |\mathbf{u}_f - \mathbf{v}_p| \left(\mathbf{u}_f - \mathbf{v}_p \right) \tag{4.62}$$

In which C_d is drag coefficient and A_p is the projected area of a particle in the direction of the flow. The value of the drag coefficient, C_d, depends on the Reynolds particle number, Re_p. The final form of the equation of motion of a single particle in a fluid is obtained by substituting Eq. (4.62) in Eq. (4.61):

$$\begin{aligned} &m_p \frac{d\mathbf{v}_p}{dt} = \\ &m_p \mathbf{g} + \rho_f V_p \left(\frac{D\mathbf{u}_f}{Dt} - \mathbf{g} \right) + \frac{1}{2} C_d \rho_f A_p |\mathbf{u}_f - \mathbf{v}_p| \left(\mathbf{u}_f - \mathbf{v}_p \right) \end{aligned} \tag{4.63}$$

With help of Eq. (4.63) the terminal velocity of a particle can be derived. This velocity depends on the value of the drag coefficient, C_d. In turn, the drag

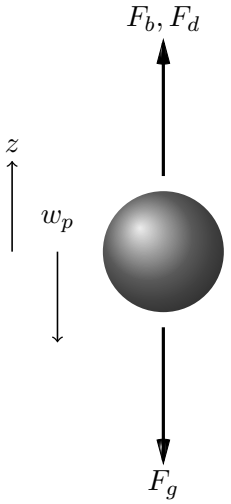

Figure 4.1: Forces acting on a non rotating settling particle in a quiescent fluid. Here F_b, F_d and F_g are the buoyancy, drag and gravitational force respectively. The particle velocity in downward z-direction is denoted as w_p $[m/s]$.

coefficient depends on the Re_p number. In the next section the determination of the value of the drag coefficient, C_d, is elaborated in the next section.

4.4.2 Terminal settling velocity

A single particle with a certain size settling in a quiescent fluid moves at some point in time at a finite rate. This rate is called the terminal settling velocity and is caused by the drag force. The value of the drag coefficient, C_d, is important for determining the terminal settling velocity of a particle. The drag coefficient depends on the particle Reynold number, Re_p, which in turn depends on the particle size. Here the value of the drag coefficient is given and finally, an expression for the terminal settling velocity is determined. Now the equation of motion of a particle in a quiescent fluid is the following:

$$m_p \frac{d\mathbf{v}_p}{dt} = m_p \mathbf{g} - \rho_f V_p \mathbf{g} + \frac{1}{2} C_d \rho_f A_p |\mathbf{u}_f - \mathbf{v}_p| \left(\mathbf{u}_f - \mathbf{v}_p\right) \tag{4.64}$$

This equation, Eq. (4.78), is same as, Eq. (4.63), with the fluid acceleration set to zero, $D\mathbf{u}_f/Dt = 0$, i.e. quiescent surrounding fluid.

4.4.3 Explicit formulation terminal settling velocity

In literature numerous explicit expressions for the calculation of the terminal settling velocity of a particle can be found, see for instance Zanke (1977), Hallemeier (1981), Cheng (1997) or Van Rijn (1989). In this section two explicit terminal settling expressions are introduced namely Ferguson and Church (2004) and Haider and Levenspiel (1989).

Ferguson and Church

Here a simple explicit expression is presented from Ferguson and Church (2004) and describes the terminal settling velocity a large range of particle sizes. This expression is able to determine the terminal settling velocity for particle Reynolds numbers, see Eq. (4.55), ranging from laminar, intermediate to turbulent regimes. Moreover, the explicit formulation is able to describe not only smooth spherical particles but also natural shaped grains.
The particle settling velocity depends on the drag coefficient, C_d. The drag coefficient, in turn, is a function of the particle Reynolds number, Re_p. The particle Reynolds number varies from 1 for small particles to 1×10^5 for large particles. The authors Ferguson and Church (2004) propose an explicit validated equation for the terminal settling velocity of natural shaped grains. In the following, this equation is discussed. For small particle Reynolds numbers, i.e. $Re_p < 1$, the terminal settling velocity is given by:

$$w_{p\infty} = \frac{R\, g_z\, {d_p}^2}{C_1 \nu_f} \tag{4.65}$$

Here $w_{p\infty}$ is the terminal settling velocity in z-direction and $\nu_f = \mu_f/\rho_f$ is the kinematic viscosity and $R = (\rho_p - \rho_f)/\rho_f$. Where ρ_p and ρ_f is the density of the particle and water respectively. In Eq. (4.65) the value of C_1 varies between $18 < C_1 < 24$, depending on the shape of the grain. With Re_p numbers in the range of $10^3 < Re_p < 10^5$ the terminal settling velocity reads:

$$w_{p\infty} = \sqrt{\frac{4\, R\, g_z\, d_p}{3\, C_2}} \tag{4.66}$$

Here C_2 is the drag coefficient, C_d, and has a value of $C_2 \approx 0.4$ for smooth spherical particles. For natural shaped grains the value of C_2 varies between 1

and 1.2. The coefficient C_2 can be rewritten in the following form:

$$C_2 = \frac{4\, g_z\, R\, d_p}{3\, w_{p\infty}^2} \tag{4.67}$$

now from Eq. (4.65) and Eq. (4.66) the low and high Reynolds number cases have been described. However the Reynolds particle number in the intermediate range, $1 < Re_p < 10^3$, is not covered yet. By combining Eq. (4.65) and Eq. (4.66), the authors Ferguson and Church (2004) found an explicit expression which covers the whole range of particle Reynolds number:

$$w_{p\infty} = \frac{R g_z d_p^2}{C_1 \nu_f + (0.75 C_2 R g_z d_p^3)^{1/2}} \tag{4.68}$$

From Eq. (4.68) it can be seen that for large particles, so large Re_p, Eq. (4.68) is approximately the same as Eq. (4.66). For small values of Re_p Eq. (4.68) takes the form of Eq. (4.65), the Stokes flow.

Figure 4.2 shows the settling velocity as a function of the particle diameter d_p. The angularity of the grains can be changed by adjusting the coefficients C_1 and C_2. For natural shaped grains the value of the coefficient C_1 varies between $18 < C_1 < 24$ and the value of C_2 between $1.0 < C_2 < 1.2$. The symbols ($\circ$) in Figure 4.2 are experimental data from Ferguson and Church (2004). In Figure 4.3 the Reynolds particle number is plotted as function of the particle diameter with $C_1 = 18$ and $C_2 = 1$. The dashed line is the calculated Re_p with help of Eq. (4.68) and the dots are the experiments from Ferguson and Church (2004). The Reynolds particle number $Re_p < 1000$ for particles with a diameter smaller than $d_p < 1000\,[\mu m]$. So the Reynolds particle number ranges from the Stokes and the intermediate regime.

Haider and Levenspiel

Another explicit formulation determining the terminal settling velocity of a natural grain particle is introduced. At steady state, or terminal settling velocity in a quiescent fluid, Eq. (4.64) reduces to, see also Figure 4.1:

$$\frac{1}{2}\, C_d A_p \rho_f w_{p\infty} = V_p(\rho_p - \rho_f) g_z \tag{4.69}$$

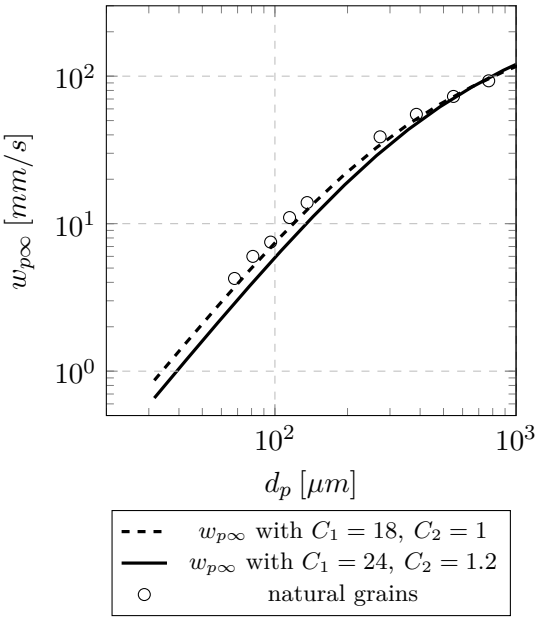

Figure 4.2: Settling velocity as function of the particle diameter. The terminal settling velocity is calculated with Eq. (4.68). Here the coefficients C_1 and C_2 are varied with values of $C_1 = 18$ and $C_2 = 1.0$ $C_1 = 24$ and $C_2 = 1.2$. The ($\circ$) symbols denote natural grains (retrieved digitally from Sylvester (2013) and originally from Ferguson and Church (2004)).

rearringing the terminal settlig velocity, $w_{p\infty}$ is recovered:

$$w_{p\infty} = \sqrt{\frac{4}{3}\,\frac{\rho_p - \rho_f}{\rho_f}\,\frac{d_p}{C_d}\,g_z} \tag{4.70}$$

In most practical sediment flows the particles are non-spherical. In order to model non-spherical particles a particle shape factor is introduced, see Wadell (1932):

$$\varphi = \frac{s}{S} \tag{4.71}$$

where s is the reduced surface area of a sphere with the mean reduced particle diameter, and S the actual surface area of the particle with the mean particle

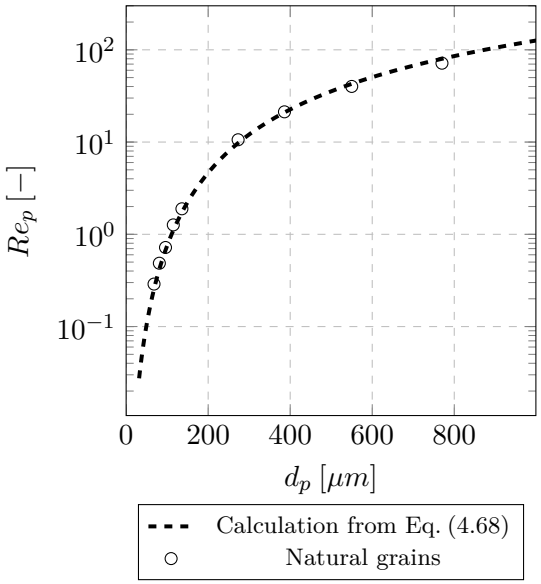

Figure 4.3: Reynolds particle number as function of the particle diameter. The dashed line is the calculated Re_p with help of Eq. (4.68), with $C_1 = 18$ and $C_2 = 1$. The symbols (∘) are the experiments from Ferguson and Church (2004). The data is retrieved digitally from Sylvester (2013). The Re_p ranges from the Stokes regime for $d_p \approx 100\,[\mu m]$ to the intermediate regime, $Re_p \approx 100$ for $d_p \approx 1000\,[\mu m]$.

diameter. Now substituting the shape factor Eq. (4.71) in equation Eq. (4.70) gives:

$$w_{p\infty} = \sqrt{\frac{4}{3}\,\frac{\rho_p - \rho_f}{\rho_f}\,\frac{\varphi d_p}{C_d}\,g_z} \tag{4.72}$$

A commonly used value for the shape factor is $\varphi = 0.7$. The drag coefficient, C_d depends on the Reynolds particle number, Re_p. In order to calculate the terminal velocity, Eq. (4.72), the drag coefficient, C_d, needs to be determined. The following formulation for calculating the value of C_d was introduced by Haider and Levenspiel (1989). This equation is valid for both spherical and

non-spherical particles and is a function of a shape factor φ:

$$C_d = \frac{24}{Re_p}(1 + ARe_p^B) + \frac{C}{\left(1 + \frac{D}{Re_p}\right)} \tag{4.73}$$

The coefficients, A, B, C and D are,

$$A = \exp\left(2.3288 - 6.4581\varphi + 2.4486\varphi^2\right) \tag{4.74a}$$
$$B = 0.0964 + 0.5565\varphi \tag{4.74b}$$
$$C = \exp\left(4.905 - 13.8944\varphi + 18.4222\varphi^2 - 10.2599\varphi^3\right) \tag{4.74c}$$
$$D = \exp\left(1.4681 + 12.2584\varphi - 20.7322\varphi^2 + 15.8855\varphi^3\right) \tag{4.74d}$$

substitution of Eq. (4.74) in Eq. (4.73) yields an expression for the drag coefficient the particle Reynolds number and the shape factor:

$$C_d = \frac{24}{Re_p}\left(1 + \exp\left(2.3288 - 6.4581\varphi + 2.4486\varphi^2\right)\right) Re_p^{(0.0964+0.5565\varphi)} + \frac{Re_p \exp\left(4.905 - 13.8944\varphi + 18.4222\varphi^2 - 10.2599\phi^3\right)}{Re_p + \exp\left(1.4681 + 12.2584\varphi - 20.7322\varphi^2 + 15.8855\varphi^3\right)} \tag{4.75}$$

Figure 4.4 shows the results of different values of the shape factor φ, namely $\varphi = 0.7$, $\varphi = 0.85$ and $\varphi = 1.0$. The shape factor, $\varphi = 1.0$, corresponds to spherical particles. An irregular shaped particle yields larger values of the drag coefficient, C_d, or lower values of the particle shape factor, φ. This results in a lower settling velocity due to the increased drag coefficient and therefore an increased drag force.

In Eq. (4.72) the value of C_d depends on the Reynolds particle number Re_p, which in turn depends on the terminal settling velocity $w_{p\infty}$. In order to obtain the terminal settling velocity with the right value of the drag coefficient, Eq. (4.72), Eq. (4.73) and Eq. (4.75) must be solved iteratively. Figure 4.5 shows the terminal settling velocity as a function of the particle size diameter with 3 different shape factors. From Figure 4.5 it is seen that the influence of the shape of the grain on the the terminal settling velocity is not negligible.

In Table 4.1 an overview is given of the terminal settling velocities determined with the model of Ferguson and Church (2004) and Haider and Levenspiel (1989) for different particle diameters in μm. The terminal settling velocities calculated using Ferguson and Church (2004), Eq. (4.68), are higher than the

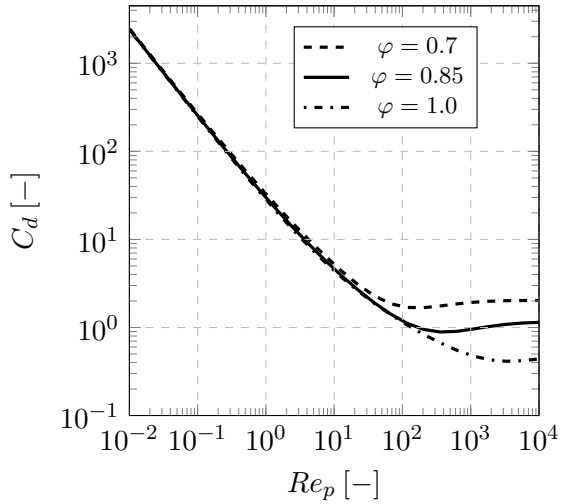

Figure 4.4: Influence of the shape particle shape factor φ on the drag coefficient, C_d. Here the C_d is given as a function of the Reynolds particle number, Re_p.

velocities resulting from Haider and Levenspiel (1989), Eq. (4.72) - Eq. (4.75). The cause of this difference is the use of the shape factor in Eq. (4.72). The shape factor results in an smaller effective volume of the particle. This is equivalent to an effective smaller diameter if a particle. Hence a smaller terminal settling velocity of the particle is the result.

4.4.4 Reaction time particle - Stokes number

The reaction time of a particle is an important property. The response time, or reaction time, can be expressed by a dimensionless number, the Stokes number,

$$St = \frac{\tau_p}{\tau_h} = \frac{\tau_p U}{L} \tag{4.76}$$

In which τ_p is the particle response time, i.e. the time it takes for a particle to adept to the flow field. The variable $\tau_h = L/U$ is the hydrodynamic time scale. Where L is a typical length scale and U is the velocity at the length scale, L. When the Stokes number is small, i.e. $St \ll 1$ the particles follow the flow field instantly. This is the case for small particles. If the Stokes number is large, $St \gg 1$, the particle does not react due to changes in the velocity of the flow field, as is the case for large particles.
Now in previous sections, it was assumed that the particle instantaneous follow velocity changes in the flow. This means that the Stokes number is small,

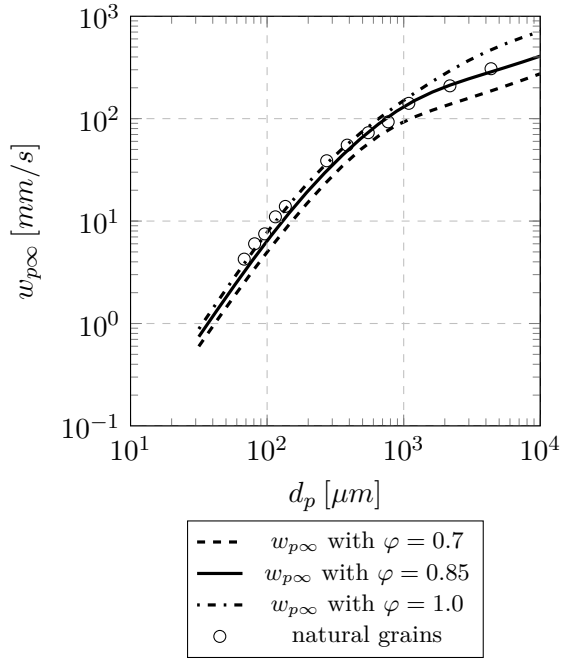

Figure 4.5: Terminal settling velocity, $w_{p\infty}$, for different shape factors, φ, as a function of the particle size diameter, d_p. The dots are natural grains and the data originate from Ferguson and Church (2004).

Table 4.1: Comparison of terminal settling velocities determined explicitly. The terminal settling velocity calculated with Ferguson and Church (2004), with ($C_1 = 18.0\, C_2 = 1.0$, see Eq. (4.68)), corresponds to the settling velocity determined with Haider and Levenspiel (1989) for natural shaped particles ($\varphi = 0.85$, see Eq. (4.75)).

model	Ferguson and Church	Haider and Levenspiel	viscosity
particle size $[\mu m]$	$w_{p\infty}$ $[mm/s]$	$w_{p\infty}$ $[mm/s]$	μ_f [Pas]
70	3.96	3.38	0.001
100	7.54	6.41	0.001
140	13.35	11.32	0.001
200	23.25	19.79	0.001
300	40.35	35.15	0.001
450	63.95	58.58	0.001
800	106.98	107.74	0.001

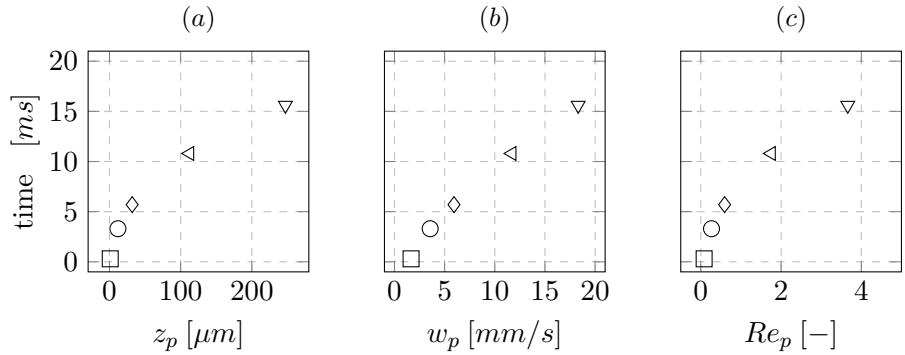

Figure 4.6: Particle reaction time of particles settling under gravity in a quiescent fluid. In plot (a) the time is given as function of the covered distance z_p. In (b) the velocity is presented and in plot (c) the particle Reynolds number, Re_p, is given. The symbols $\square$, $\circ$, $\diamond$, $\triangleleft$, $\triangledown$, correspond with the particle sizes $50, 75, 100, 150, 200$ $[\mu m]$ respectively.

$St \ll 1$, here it is investigated if this assumption is valid. Using the equation of motion of a particle settling under gravity, see Eq. (4.63), the particle response time is obtained. A simple forward Euler numerical integrator is used in order to solve Eq. (4.63). Here the reaction time for 5 particle grain sizes is determined, namely $50, 75, 100, 150, 200$ $[\mu m]$. The drag coefficient, C_d, is obtained with Eq. (4.75). In this calculation a shape factor value of $\varphi = 0.8$ has been choosen. In Figure 4.6 (a), (b) and (c) the particle response time is given as a function of velocity, distance and Reynolds particle number,Re_p, respectively. The symbols $\square$, $\bigcirc$, $\diamond$, $\triangleleft$, $\triangledown$, correspond with the particle sizes $50, 75, 100, 150, 200$ $[\mu m]$ respectively. The calculation is terminated if 99% of the terminal velocity of a particle has been reached. From Eq. (4.6) is can be seen that the particle response time, of a particle settling under gravity, is in the order of magnitude of milliseconds. The covered distance of a particle is close to a particle diameter, Figure 4.6 and the particle Reynolds numbers range from $Re_p \approx 1...4$.

4.4.5 Reaction time particle - velocity fluctuations

In the drift-flux model that the particle size is small, with respect to the domain size, and it is assumed that particles react instantaneously to velocity

fluctuations of the carrier fluid. Here it is assessed at which velocity fluctuations this assumption breaks down. In the previous section, the response time of a settling particle in a quiescent fluid was discussed. However, in a turbulent fluid flow velocity fluctuations exist. The goal is to investigate the influence of the eddy sizes and frequencies, of the carrier fluid, on the particle reaction time. In order to do so only, the drag force is included in the equation of motion of the particle, other forces are omitted. Here a sinusoidally oscillating velocity field is imposed on the equation of motion of the particle. The oscillating velocity field is the simplest case of a turbulent motion of an eddy and can be described by the following expression, given here for 1-direction:

$$u_f(\omega, t) = H_f\, \omega\, \cos(\omega\, t) \tag{4.77}$$

in which $u_f(\omega, t)$ is the flow field, H_f the amplitude and ω the angular frequency. Repeating here the equation of motion of a particle, again in 1 direction, see Eq. (4.78), for a particle settling in a stagnant fluid:

$$m_p \frac{dv_p}{dt} = m_p g - \rho_f V_p g + \frac{1}{2} C_d \rho_f A_p |u_f - v_p| \,(u_f - v_p) \tag{4.78}$$

now by substitution of Eq. (4.77) in Eq. (4.78) and omitting the buoyancy and gravitational force in Eq. (4.78), the following equation is obtained:

$$m_p \frac{dv_p}{dt} = \frac{1}{2} C_d \rho_f A_p |u_f(\omega, t) - v_p| \,(u_f(\omega, t) - v_p) \tag{4.79}$$

in which the fluctuating fluid velocity is equal to $u_f(\omega, t) = H_f\, \omega\, \cos(\omega\, t)$. Using a simple forward Euler integrator Eq. (4.79) is solved numerically. The turbulent fluctuations and the amplitude of the of the fluid flow in Eq. (4.77) are given by the angular frequency ω and the amplitude H_f. Here an estimation is given of the turbulent eddy frequency and the length scales. This is done for a pipe flow with a diameter of D_{pipe}, see Ahmadi (2013). The largest length scale of an eddy in a pipe is of order:

$$L_l = D_{pipe}/2 \tag{4.80}$$

and an eddy frequency of about:

$$f_l = 0.4 \frac{U_0}{D_{pipe}} Re^{-1/8} \tag{4.81}$$

here U_0 is the mean velocity and Re is the Reynolds number. The so-called energy containing eddies have a length scale of:

$$l_e = 0.05\, D_{pipe}\, Re^{-1/8} \tag{4.82}$$

with an eddy frequency of:

$$f_e = 4\frac{U_0}{D_{pipe}} \tag{4.83}$$

The Kolmogorov length scale is given by:

$$l_k = 4\, D_{pipe}\, Re^{-0.78} \tag{4.84}$$

and a frequency of:

$$f_k = 0.06\frac{U_0}{D_{pipe}} Re^{0.56} \tag{4.85}$$

Now finally the size of the dissipative eddies is given by:

$$l_d = 20\, D_{pipe}\, Re^{-0.78} \tag{4.86}$$

and a frequency of:

$$f_d = \frac{1}{3}\, f_k \tag{4.87}$$

In order investigate typical values for the angular frequency ω and the amplitude A_f two pipe diameters are considered here. The outcome for the eddy frequencies and amplitudes are used as input for the sinusoidal fluctuations in Eq. (4.79). The two pipe diameters taken here are $D_{pipe} = 0.05\,[m]$ and $D_{pipe} = 0.8\,[m]$. The flow velocity is $1.5\,[m/s]$ for the small pipe diameter and $4\,[m/s]$ for the large diameter pipe. The eddy size and the corresponding eddy frequencies for $D_{pipe} = 0.05\,[m]$ and $D_{pipe} = 0.8\,[m]$ are given in Table 4.2 and Table 4.3 respectively.

The particle reaction time is investigated for fluctuating flow field. Here 4 particle sizes, $50, 100, 200, 300\,[\mu m]$ are chosen. The density of the particles has a value of $\rho_s = 2650\,[kg/m^3]$, for the fluid a density of $\rho_f = 1000\,[kg/m^3]$ is taken and the molecular viscosity is equal to $\mu_f = 0.001\,[Pas]$. The value of the amplitude, H_f in Eq. (4.77) is set equal to the typical size of an eddy.

Table 4.2: Overview of eddy sizes and corresponding frequencies for a pipe with a diameter of $D_{pipe} = 0.05\,[m]$, a flow velocity of $1.5\,[m/s]$ and a Reynolds number of $Re = 75000$

.

Eddy size	value μm	Eddy frequency	value Hz
l_L	25×10^3	f_L	2.95
l_e	614	f_e	120
l_d	157	f_d	322
l_k	32	f_k	967

Table 4.3: Overview of eddy sizes and corresponding frequencies for a pipe with a diameter of $D_{pipe} = 0.8\,[m]$, a flow velocity of $4.0\,[m/s]$ and a Reynolds number of $Re = 32 \times 10^5$

.

Eddy size	value $[\mu m]$	Eddy frequency	value $[Hz]$
l_L	400×10^3	f_L	0.31
l_e	6150	f_e	20
l_d	134	f_d	440
l_k	27	f_k	1320

The angular frequency, ω, is set equal to the eddy frequency, see Table 4.2 and Table 4.3. In Figure 4.7 (a) and Figure 4.7 (b) the amplitude ratio, H_p/H_f (H_p is the amplitude of the particle), as a function of the frequency is plotted for the given different particle sizes. The data in Figure 4.7 (a) corresponds with the input parameters given in Table 4.2 and Figure 4.7 (b) corresponds with Table 4.3. It can be seen that all particle sizes follow the velocity fluctuations, the amplitude ratio is around 1, up to an eddy frequency of 100 $[Hz]$. In case of higher eddy frequencies the amplitude ratio decays rapidly, especially for the larger particle diameters, $d_p > 100\,[\mu m]$. The eddy frequencies for both the small pipe diameter, $D_{pipe} = 0.05\,[m]$ and the large pipe diameter $D_{pipe} = 0.8\,[m]$ are in the same order of magnitude.

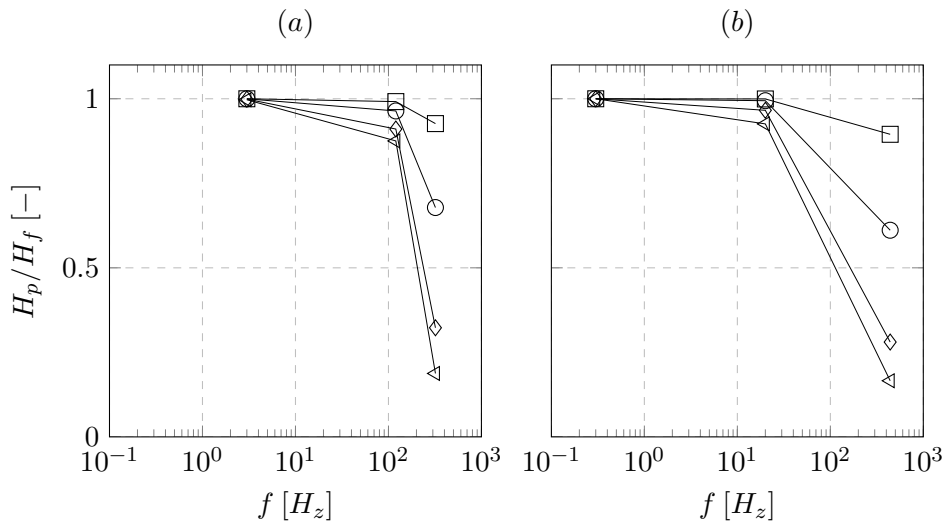

Figure 4.7: Amplitude ratio of a particle as function of the eddy frequency. In (a) and (b) typical values are given for pipe diameter $D_{pipe} = 0.05\,[m]$ and $D_{pipe} = 0.8\,[m]$ respectively. The symbols $\square$, $\circ$, $\diamond$, $\triangleleft$, correspond with the particle sizes $50, 100, 200, 300\,[\mu m]$ respectively.

4.4.6 Remarks particle reaction time

The particle reaction time is instantaneous for larger eddies and frequencies of the carrier fluid. However, when the frequency of the velocity fluctuation is increased and the amplitude of the velocity fluctuation is decreased the particle does not react instantly to the velocity changes.

This is investigated by means of two cases with two different geometries. From these cases the following can be concluded. With a decreasing vortex size the vortex frequency increases, approximately $100\,[Hz]$. In the case of the typical particle size of the order of magnitude of $300[\mu\, m]$, the particle is not able to follow the flow directly. Therefore, the assumption that the particle reaction time is very rapid does not hold. As a consequence the drift-flux model, where it is assumed that the particle reacts instantaneously to velocity fluctuations, breaks down.

It must be remarked that here only the drag force is included in the model. A

more elaborate estimation can be achieved by taking more particle forces into account. Moreover, only a single particle suspended in a fluid is considered. It would be interesting to investigate the effect of the volume concentration on the particle reaction times.

4.4.7 Hindered settling function

Here the settling velocity is discussed for many-particle systems. The terminal settling velocity is smaller than the settling velocity of a single grain. This is caused by an increased mean drag due to interparticle collisions, an increased volume concentration of solids and return flow of the continuous or fluid phase. This is called hindered settling. The forces acting on a particle in a suspension, i.e. many particles, for a steady state are:

$$\mathbf{F}_d + \mathbf{F}_g - \mathbf{F}_b = 0 \tag{4.88}$$

This is the force balance of a single particle at steady state in a quiescent mixture. Due to the increased mixture density the buoyancy force $\mathbf{F}_b$ is higher, so Eq. (4.88) can be written as:

$$\mathbf{F}_d = V_p \, \mathbf{g} \, (\rho_m - \rho_f) \tag{4.89}$$

With ρ_m:

$$\rho_m = \alpha_t \, (\rho_p - \rho_f) + \rho_f \tag{4.90}$$

Now substitution of Eq. (4.90) in Eq. (4.89) and rearranging yields:

$$\mathbf{F}_d = V_p \, \mathbf{g} \, (1 - \alpha_t) \, (\rho_f - \rho_p) \tag{4.91}$$

Note that the RHS of Eq. (4.91) is same as the RHS of Eq. (4.27) with the omission of the terms $\partial \mathbf{u}_m / \partial t + \nabla \cdot (\mathbf{u}_m \mathbf{u}_m)$.

It can be seen from Eq. (4.91) the drag force $\mathbf{F}_d$ is a function of the total volume concentration of solids α_t. From Eq. (4.91) it is seen that the terminal settling velocity of a particle in a suspension can be expressed as the terminal settling velocity of a single particle in a fluid corrected with a function. This function is called the hindered settling function. This was investigated by Richardson

and Zaki (1954b) with help of sedimentation and fluidization experiments. The terminal settling velocity of a particle in a suspension can be expressed as:

$$\mathbf{u}_{p\infty}(\alpha_t) = V_m(\alpha_t)\mathbf{u}_{p\infty} \tag{4.92}$$

where, $V_m(\alpha_t)$, is the hindered settling function, which is a function of the volume concentration, α_t. The hindered settling velocity, $\mathbf{u}_{p\infty}(\alpha_t)$ is relative to the mixture velocity:

$$V_m(\alpha_t) = (1-\alpha_t)^n \tag{4.93}$$

in which n is the so called Richardson and Zaki index. From Eq. (4.93) it follows that the hindered settling function is zero at a volume concentration of $\alpha_t = 1$. This is this is never the case from a practical viewpoint. For granular materials the maximum volume concentration is $\alpha_{tmax} \approx 0.6$. This value is the limit at which the hindered settling function, Eq. (4.93), reduces to zero. Therefore, an adjusted formulation is employed, see Basson et al. (2009), where the hindered settling function, $V_m(\alpha_t)$, is zero when the maximum volume concentration, α_{tmax}, is reached:

$$V_m(\alpha_t) = \begin{cases} (1-\alpha_t)^n & \text{if } \alpha_t < \alpha_{tmax} \\ 0 & \text{if } \alpha_t = \alpha_{tmax}. \end{cases} \tag{4.94}$$

The hindered settling function shown above is not the only one. In literature other formulations of the hindered settling function can be found, see for instance Camenen and van Bang (2011). In these formulations special care has been taken reducing the settling velocity to zero, when the volume concentration approaches the maximum volume concentration. However, in future research, it would be interesting to compare different hindered settling expressions. In this work the settling the expression, Eq. (4.94), has been used.

The Richardson and Zaki index n depends on the Reynolds particle number and is given by the following,

$$n = \begin{cases} 4.65 & \text{if } Re_p < 0.2 \\ 4.35\, Re_p^{-0.03} & \text{if } 0.2 < Re_p < 1 \\ 4.45\, Re_p^{-0.1} & \text{if } 1 < Re_p < 500 \\ 2.39 & \text{if } 500 < Re_p. \end{cases} \tag{4.95}$$

Table 4.4: Coefficients of continuous hindered settling functions.

Model	Rowe (1987)	Garside and Al-Dibouni (1977)	Wallis (1969)
Re_p [−]	$0.2 < Re_p < 1 \times 10^3$	$1 \cdot 10^{-3} < Re_p < 3 \times 10^4$	$0.2 < Re_p < 1 \times 10^3$
α_t [−]	$0.04 < \alpha_t < 0.55$	$0.04 < \alpha_t < 0.55$	$0.04 < \alpha_t < 0.55$
a	4.7	5.1	4.7
b	0.41	0.27	0.71
c	0.175	0.1	0.253
d	0.75	0.9	0.687

Eq. (4.95) can be approximated by the following continuous function, see by Rowe (1987):

$$n = \frac{a + b\, Re_p^d}{1 + c\, Re_p^d} \tag{4.96}$$

This function is more convenient to use numerically. Several values for a, b, c and d are known from literature. Different values for the smoothing function, Eq. (4.96), of the Richardson and Zaki exponent, n, are reported in literature, see Table 4.4. Figure 4.8 shows the hindered settling exponent, n, as a function of the particle Reynolds number, Re_p according to the models given in Table 4.4.

From Eq. (4.95) and Eq. (4.96) it is seen that at low particle Reynolds number, Re_p, the value of a is dominant. So the settling velocity of small particles is dominated by the value of a. The higher a the lower the settling velocity at small Reynolds particle numbers. An the other hand at high particle Reynolds numbers the ratio of the coefficients, b/c, becomes dominant. This ratio controls the settling velocity of large particles.

The hindered settling function, Eq. (4.94), is given relative to the mixture velocity. The hindered settling velocity of the particle relative to fluid is given by, see Mirza and Richardson (1979):

$$V(\alpha_t) = \begin{cases} (1-\alpha_t)^{n-1} & \text{if } \alpha_t < \alpha_{tmax} \\ 0 & \text{if } \alpha_t = \alpha_{tmax}. \end{cases} \tag{4.97}$$

Eq. (4.97) is only valid for a single particle (or fraction) size. For sediments with many particle sizes, each particle species has a different settling velocity. Now Eq. (4.97) is written in the following form, see Mirza and Richardson

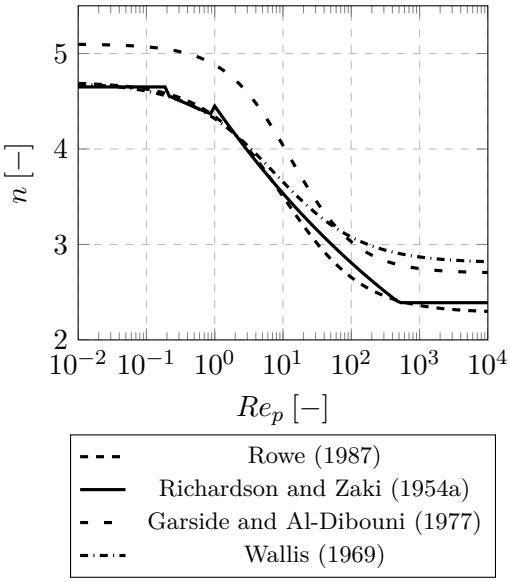

Figure 4.8: Hindered settling exponent, n, as a function of Re_p, several approximations are shown.

(1979):

$$\mathbf{u}_{kr} = \mathbf{u}_{k\infty} V_k(\alpha_t) \tag{4.98}$$

with,

$$V_k(\alpha_t) = \begin{cases} (1-\alpha_t)^{n_k - 1} & \text{if } \alpha_t < \alpha_{tmax} \\ 0 & \text{if } \alpha_t = \alpha_{tmax}. \end{cases} \tag{4.99}$$

Here n_k is the Richardson and Zaki index for each particle species, with the subscript k denoting the particular species. Now the sedimentation velocity is derived for separate particle fractions. With help of Eq. (4.98), Eq. (4.52), Eq. (4.99) and Eq. (4.49) the transport velocity for each fraction can be determined and hereby the closure relation is given.

4.4.8 Settling flux of solids

With the Kynch sedimentation experiment, Kynch (1952), the semi-empirical models describing hindered settling of particles, see Table 4.4, can be quantified.

The influence of these constants on the hindered settling velocity the sediment-flux and maximum solids flux is investigated here. The following semi-empirical models are used for comparison, Rowe (1987), Garside and Al-Dibouni (1977) and Wallis (1969). These models are used for determining the hindered settling, or Richardson and Zaki, index n. Now assuming one fraction of solids, with the same shape and density, the transport of this mono-dispersed mixture is described by:

$$\frac{\partial \alpha_t}{\partial t} + \nabla \cdot (\mathbf{S}_f) = 0 \tag{4.100}$$

In which, α_t, is the volume fraction and S_f is the solid flux of particles through a unit area. The solids flux of particles, $\mathbf{S}_f$ is given by:

$$\mathbf{S}_f = \alpha_t V(\alpha_t) \mathbf{u}_{p\infty} \tag{4.101}$$

where the velocity vector $\mathbf{u}_{p\infty}$ is the terminal settling velocity of a single particle in quiescent fluid and $V(\alpha_t)$ the hindered settling function. Now considering settling in the z-direction, the solids flux of particles, Eq. (4.101) transforms into:

$$S_{fw} = \alpha_t V(\alpha_t) w_{p\infty} \tag{4.102}$$

in which $w_{p\infty}$ is the terminal settling velocity of a particle in the z-direction. The hindered settling function $V(\alpha_t)$ is repeated here, see Eq. (4.94):

$$V(\alpha_s) = (1 - \alpha_t)^n \tag{4.103}$$

substitution of Eq. (4.103) in Eq. (4.102) yields:

$$S_{fw} = \alpha_t \left(1 - \alpha_t\right)^n w_{t\infty} \tag{4.104}$$

By taking the derivative of Eq. (4.104) with respect to α_s and setting this function equal to zero a maximum value can be determined for the solids flux of particles, S_f:

$$\frac{\partial}{\partial \alpha_t} \left(\alpha_t \left(1 - \alpha_t\right)^n w_{p\infty}\right) = 0 \tag{4.105}$$

This maximum value of the volume concentration, α_s, can be expressed as a function of the hindered settling index n, see Camenen and van Bang (2011):

$$\alpha_{tm} = \frac{1}{n+1} \tag{4.106}$$

in which α_{tm} is volume concentration at which the volume flux of solids is maximum. Now the maximum value of the solids flux at a certain volume concentration can be obtained by substitution of Eq. (4.96) in Eq. (4.106). Here Eq. (4.96) is repeated:

$$n = \frac{a + b\, Re_p^d}{1 + c\, Re_p^d} \tag{4.107}$$

Now using Eq. (4.106) the volume concentration at which the solids flux is maximum is expressed as follows:

$$\alpha_{tm} = \frac{1}{n+1} = \frac{1 + c\, Re_p^d}{1 + a + (b + c)\ Re_p^d} \tag{4.108}$$

This equation shows that the maximum of the volume fraction of solids, α_{tm}, is a function of the Reynolds particle number, Re_p and model parameters a, b, c, d. Two particle Reynolds numbers, $Re_p = 0.1$ and $Re_p = 10$, are chosen in order to compare the outcome of different hindered settling models. The settling velocity, as a function of the volume concentration of solids, see Eq. (4.103), is shown in Figure 4.9 (a) and (d) for $Re_p = 0.1$ and $Re_p = 10$ respectively. The volume concentration of solids α_t is shown on the horizontal axis. The settling velocity scaled by the terminal settling velocity is shown on the vertical axis. From these figures, there is no notable difference between the various models. The hindered settling velocity according to Garside slightly deviates with respect to the other models, Rowe and Wallis. This is the case for both the particle Reynolds numbers. The solid flux of particles scaled by the terminal settling velocity is shown in Figure 4.9 (b) and (d) see Eq. (4.104). At $Re_p = 0.1$ the Garside model predicts a lower solids flux, S_{fw}, where the Wallis and Rowe model yields a similar result. However, for higher particle Reynolds numbers the three models give different results. It can be seen that the maximum value of the solids flux increases for $Re_p = 10$. Moreover the volume concentration, α_t, at which this volume concentration occurs also increases. This is shown in Figure 4.9 (c) and (f), where the lines cross the horizontal axis at zero.

Figure 4.10 shows the volume concentration of solids, α_{tm}, at which the maximum solids flux occurs as a function of the particle Reynolds number, according to Eq. (4.108). In the figure the three models are given. The volume concentration increases with increasing Re_p, for all three models and varies between $\alpha_s = 0.16 - 0.17$ at small Re_p and $\alpha_s = 0.25 - 0.26$ for larger, $Re_p = 100$, values.

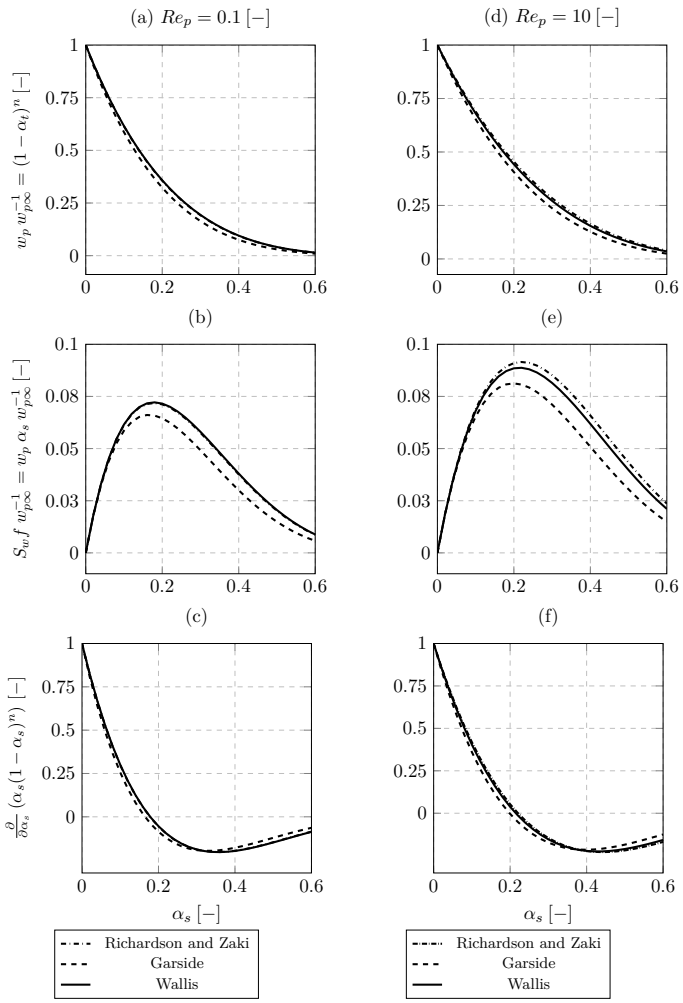

Figure 4.9: Settling curves at different particle Reynolds numbers and determined with different parameters, plot (a) and (d) shows the settling settling velocity, plot (b) and (e) show the settling flux and plot (c) and (f), the derivative of the settling function with respect to the volume concentration α_t.

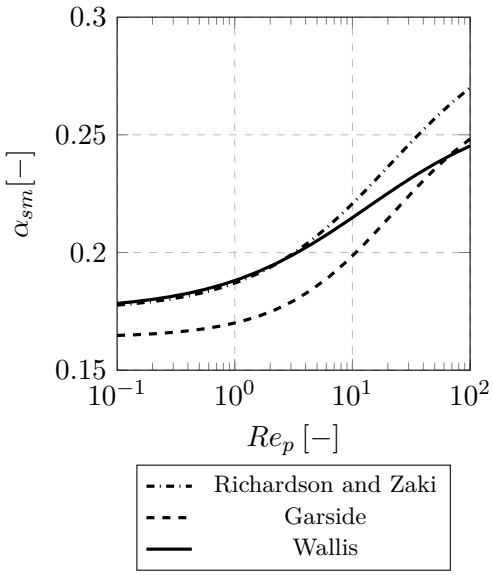

Figure 4.10: Volume concentration of solids at which the solids flux is maximum as a function of particle Reynolds number, Re_p.

Chapter 5

Numerical Implementation

The Navier-Stokes and transport equations are partial differential equations and describe the motion of incompressible fluids. The transport equations describe the motion of sediment. These non-linear, equations are solved numerically on a Cartesian mesh using the Finite Volume Method. Subsequently, the motion of the fluid flow in time is solved with help of the fractional step method of Chorin (1968). This algorithm is elaborated in 5.2. A collocated grid arrangement is used storing the field variables (e.g. velocities, density, viscosity) at the center of a grid cell. This scheme, however, suffers from pressure velocity decoupling. This is prevented by using the interpolation scheme of Rhie and Chow (1983). A sediment bed is formed when a maximum value of the total volume concentration has been reached. A limiter, see Boris and Book (1973), Zalesak (1979) and Kuzmin and Gorb (2012), is used preventing an overshoot of the maximum total volume concentration of solids. The approach is discussed in 5.3.

5.1 Discretization approaches

There are several ways to discretize partial differential equations. The most popular methods are the finite difference method, the finite volume method and the finite element method. These three methods are addressed briefly in the following.

Finite Element Method (FEM)

This method is used in structural analysis, heat transfer, fluid flow and electromagnetic potential for instance. A body (of irregular shape) is subdivided into a system (equivalent) of many smaller bodies, called finite elements. These elements are connected together at (boundary) nodes, interpolating the field quantity over the entire structure in a piecewise manner. This results in a set of simultaneous algebraic equations. Subsequently, this set of equations is assembled into a large set of equations of the following form:

$$\mathbf{Kx} = \mathbf{f} \tag{5.1}$$

where $\mathbf{K}$ is the so-called stiffness matrix, this defines a property of a system, $\mathbf{x}$ the displacement vector and $\mathbf{f}$ the force vector. An important advantage of the FE Method is the ability to handle domains of arbitrary shape. Refinement of the grid is done by subdividing each element. A major drawback of the method is that the resulting matrix ($\mathbf{K}$) of the assembled equations is not well structured making it more difficult to find an efficient solution method, see Ferziger and Peric (1999). Since in this work only non-complex geometries are used, the major advantage of the FEM, namely able to handle domains of arbitrary shape, has no added value. Therefore, this method is not used in this thesis.

Finite Difference Method (FDM)

The oldest method for the numerical solution of partial differential equations is the Finite Difference Method (FDM). This is also the simplest method to use for simple geometries. In general, the solution domain is covered by a Cartesian grid. Subsequently, at each grid point, the differential equation is approximated with difference equations, where the finite differences approximate the derivatives of the (partial) differential equations. Using a structured grid the FD Method is simple and effective. Higher order schemes can be obtained on regular grids. The disadvantage of the FD Method is that the conservation is not enforced without taking special care, see Ferziger and Peric (1999). Since conservation is not a strict requirement solving the pressure Poisson equation, see Eq. (5.54) and Eq. (5.59), the FD Method is used for as a discretization method for this equation.

Finite Volume Method (FVM)

The Finite Volume Method uses the integral form of the conservation equations as the starting point, see Eq. (5.3). The solution domain is then subdivided into a finite number of control volumes (CV's). At the center of the CV, a grid point is located at which the value of the variable is calculated. The rate of change of the calculated variable in the CV is determined by fluxes over the surfaces of the CV. These fluxes at the surfaces are governed by advection and/or diffusion of the partial differential equations. The values at the surfaces of the CV are calculated using interpolation from the nodal values at neighboring CV centers. In this case, an algebraic expression is obtained for each CV, in which neighbor nodal values appear. Using an interpolation method consistently the FV Method is conservative. Moreover, fluxes at boundaries are readily available, providing that the cell face coincides with the domain boundary. The FV Method is simplest to program and understand in comparison with the FDM and FEM. The approximated terms have physical meaning and this is probably why this method is the most popular choice in Computational Fluid Dynamics (CFD). In this work, the FVM is employed as a discretization method of the transport and momentum equations. More details on the finite volume method can be found in Fletcher (1988), Ferziger and Peric (1999), Hirsch (1990), Versteeg and Malalasekera (1995) or Schaefer (2006).

5.1.1 Finite Volume Method-discretization

In this section, the finite volume discretization is given for the transport equation and the Poisson equation. Although the code used in this work is $3D$, the discretization is given in $2D$ in the next sections, clarifying the followed method more easily. First, an example of a transport equation is given, for instance, the conservation of mass.

Transport equation

The transport equation, describing here the conservation of mass in 2 dimensions, is formulated as follows:

$$\frac{\partial \rho}{\partial t} + \nabla \cdot (\rho \mathbf{u}) = 0 \tag{5.2}$$

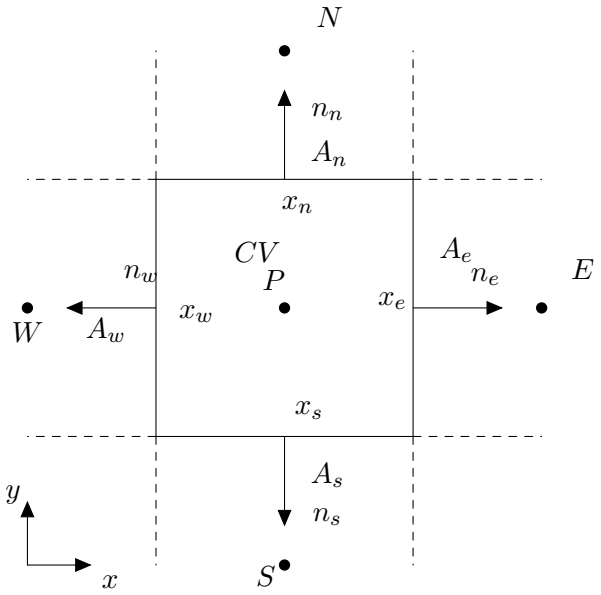

Figure 5.1: Cell Volume and neighboring volumes, with normal vectors, n_i at cell faces, A_i with $i = e, w, n, s$.

rewriting Eq. (5.2) in integral form yields:

$$\int_V \frac{\partial \rho}{\partial t}\, dV + \int_V \nabla \cdot (\rho \mathbf{u})\, dV = 0 \tag{5.3}$$

where V is the volume of the CV. Now applying the divergence, or Gauss's theorem, the following form is obtained:

$$\int_V \frac{\partial \rho}{\partial t}\, dV + \int_A \rho\, \mathbf{u} \cdot \mathbf{n}\, dA = 0 \tag{5.4}$$

in which A is the surface area of the cell or CV. Now by applying the midpoint rule, see Appendix C, to the second term in Eq. (5.4), the following is obtained:

$$\int_A \rho\, \mathbf{u} \cdot \mathbf{n}\, dA \approx \sum_{cell faces} \rho_{cf} \mathbf{u}_{cf} \cdot \mathbf{n}_{cf} A_{cf} \tag{5.5}$$

Here is respectively A_{cf}, $\mathbf{u}_{cf}$, ρ_{cf} and $\mathbf{n}_{cf}$ the cell area, velocity, density and normal vector at the cell faces. Note here that this is an approximation of the

flux rewriting Eq. (5.4) with help of Eq. (5.5) gives the following:

$$\int_V \frac{\partial \rho}{\partial t}\, dV + \sum_{cell faces} \rho_{cf} \mathbf{u}_{cf} \cdot \mathbf{n}_{cf} A_{cf} = 0 \tag{5.6}$$

A two dimensional Cartesian grid is given graphically in Figure 5.2. The compass notation is used. The center, east, west, north and south grid cells are given by the capital letters P, E, W and N, respectively. The interpolated values are given by the lower case letters e, w, n and s. The second term of Eq. (5.6) is discretized by summing the fluxes over the cell faces:

$$\begin{aligned} &\sum_{cell faces} \rho_{cf} \mathbf{u}_{cf} \cdot \mathbf{n}_{cf} A_{cf} = \\ &\rho_e u_e A_e - \rho_w u_w A_w + \rho_n v_n A_n - \rho_s v_s A_s \end{aligned} \tag{5.7}$$

The transient term in Eq. (5.6) is approximated as follows:

$$\int_V \frac{\partial \rho}{\partial t}\, dV = \frac{\rho_P^{n+1} - \rho_P^n}{\Delta t} \Delta V \tag{5.8}$$

Where ρ_P^{n+1} denotes the value of ρ_P^n at position P at time level n. The value of ρ_P^{n+1} is the value of the density at the next time level $n+1$. In the 2 dimensional Cartesian case the cell areas are equal to, see Figure 5.2,

$$\begin{aligned} A_s &= A_n = x_n - x_s = \Delta x \\ A_e &= A_w = y_e - y_w = \Delta y \end{aligned} \tag{5.9}$$

here Δx and Δy are the distances between the cell boundaries in x and y direction respectively. The volume, ΔV, of a grid cell, or CV, is approximated as follows:

$$\Delta V = (x_n - x_s)\,(y_e - y_w) = \Delta x\, \Delta y \tag{5.10}$$

The following should be remarked converting a $3D$ geometry to $2D$. By setting the third dimension, z, to unity, i.e. $\Delta z = 1$, a $3D$ is converted to a $2D$ context. Moreover, there is no exchange of mass or momentum in the z-direction. The volume integral given in Eq. (5.10) the z-direction is omitted in the equation. The volume in $3D$, for instance, reads $\Delta V = \Delta x\, \Delta y\, \Delta z$, by using $\Delta z = 1$ the volume of the CV reduces to, $\Delta V = \Delta x\, \Delta y\, \Delta z (= 1) = \Delta x\, \Delta y$. The same holds

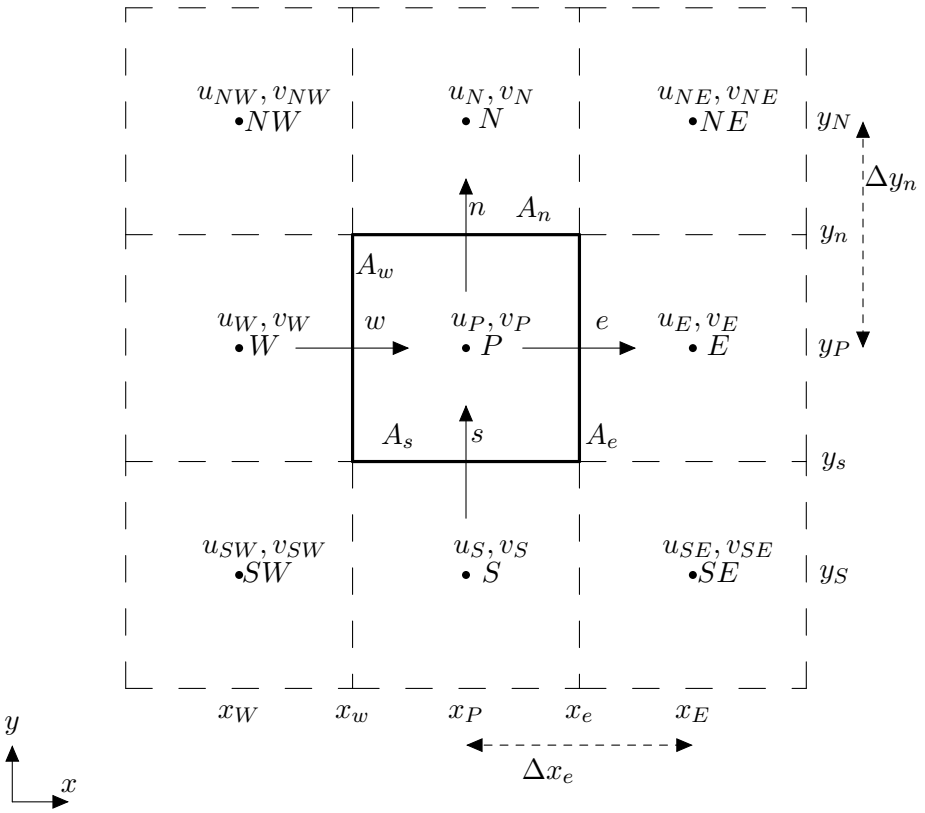

Figure 5.2: Plot of a $2D$ Cartesian grid using the compass notation. The center, east, west, north and south grid cell is given by the capital letters P, E, W and N, respectively. The interpolated values are given by the lower case letters e, w, n and s.

for the cell, CV, areas derived in Eq. (5.9), namely $A_s = \Delta x\, \Delta z = \Delta x\, \Delta z (= 1) = \Delta x$.

From now on, in $2D$, the third dimension is omitted in the derivations and the z-direction is not mentioned explicitly in the text.

Poisson equation

Here the discretization of the diffusive fluxes are derived. This is done on the basis of the Poisson equation. A two dimensional Poisson equation in a Cartesian coordinate system of a quantity, ϕ, is given by:

$$\nabla \cdot (\Gamma \nabla \phi) = f \tag{5.11}$$

in which Γ is the diffusion coefficient and f a source term. Both the source term f and the diffusion coefficient, Γ, are functions of space, viz. $\Gamma = \Gamma(x, y)$ and $f = f(x, y)$. Now rewriting Eq. (5.11) in integral form and applying the divergence theorem, the following equation is obtained:

$$\int_A (\Gamma \nabla \phi) \cdot \mathbf{n} dA = \int_V f dV \tag{5.12}$$

again using the midpoint rule LHS of Eq. (5.12) is approximated as follows:

$$\int_A (\Gamma \nabla \phi) \cdot \mathbf{n} dA \approx \sum_{cell faces} \left(\Gamma_{cf} \nabla \phi_{cf} \right) \cdot \mathbf{n}_{cf} A_{cf} \tag{5.13}$$

for a cartesian coordinate system in a two dimensional case, see Figure 5.2, Eq. (5.13) is discretized as follows:

$$\sum_{cell faces} \left(\Gamma_{cf} \nabla \phi_{cf} \right) \cdot \mathbf{n}_{cf} A_{cf} = \Gamma_e \left(\frac{\partial \phi}{\partial x} \right)_e A_e + \Gamma_w \left(\frac{\partial \phi}{\partial x} \right)_w A_w + \Gamma_n \left(\frac{\partial \phi}{\partial x} \right)_n A_n + \Gamma_s \left(\frac{\partial \phi}{\partial x} \right)_s A_s \tag{5.14}$$

and the source term in Eq. (5.12) is discretized as follows:

$$\int_V f dV \approx f_P \Delta V \tag{5.15}$$

Now here two type of partial differential equations are discretized. The interpolation of the advective and diffusive fluxes over the cell faces will be discussed next.

5.1.2 Discretization advective fluxes

Central Difference Scheme

In order to determine the cell face values interpolation is needed from the known values of the neighboring cells, see Figure 5.2. Now consider a certain

quantity ϕ, this quantity can be anything for instance density, ρ or volume concentration α_t, the cell face value for the east cell face is approximated as follows,

$$\phi_e \approx \lambda_e \phi_E + (1 - \lambda_e)\phi_P \tag{5.16}$$

Where λ_e is the interpolation factor, see Schaefer (2006). The interpolation factor λ_e is both valid for a equidistant and a non-equidistant grid and is defined as,

$$\lambda_e = \frac{x_e - x_P}{x_E - x_P} \tag{5.17}$$

for an equidistant grid, i.e. $x_e - x_P = (x_E - x_P)/2$, Eq. (5.17) reduces to,

$$\lambda_e = \frac{1}{2} \tag{5.18}$$

The interpolation method described in Eq. (5.16) is the so-called arithmetic mean method. Interpolations for other cell faces is analog to the one shown here for the east cell face. The interpolation error of the CDS is second order, see Schaefer (2006). The central difference scheme can give rise to oscillations to the solution of the numerical problem, see Hundsdorfer (2000). Next, another scheme is introduced which does not suffer from these oscillations.

Upwind Difference Scheme

The simplest upwind difference or interpolation scheme the cell face value is approximated using a step function. This function depends on the velocity direction in which the quantity is being transported or advected. The cell-face value is approximated as follows, considering only the east face,

$$\phi_e = \begin{cases} \phi_E, & \text{if } u_e < 0 \\ \phi_P, & \text{if } u_e > 0 \end{cases} \tag{5.19}$$

This scheme is first order accurate and does not suffer from oscillations in the numerical solution. The upwind formulation has been widely used in CFD calculations because of its simplicity. Moreover it can be easily extended in 2 or 3 dimensions. However, besides the aforementioned first order accuracy, the upwind interpolation scheme has a major disadvantage. The scheme suffers from false diffusion and this is especially the case when the flow direction is not aligned with the grid lines, see Versteeg and Malalasekera (1995). In order to prevent this, a higher order interpolation scheme can be deployed such as the QUICK scheme, see Leonard (1979).

Higher order schemes

In simulating sediment transport, it is important to prevent negative values in the solution of sediment concentrations. A negative value of sediment would render a physically impossible outcome. A certain class of interpolation schemes does not suffer from negative values in the outcome of the numerical solution. These schemes are called Total Variational Diminishing schemes (TVD). TVD schemes are monotone and second-order accurate and make use of so-called flux limiters. In this thesis the van Leer flux limiter is used, see Van Leer (1974). More on several other higher order schemes is discussed in Hirsch (1990) or LeVeque (1992).

5.1.3 Discretization diffusive fluxes

The diffusive fluxes are discretized in the following. Here the east cell face flux is considered. The discretization of other cell faces is analog to the one given here:

$$\Gamma_e \left(\frac{\partial \phi}{\partial x}\right)_e \approx \Gamma_e \left(\frac{\phi_E - \phi_P}{\Delta x_e}\right) \tag{5.20}$$

The diffusion coefficient, Γ_e in Eq. (5.20), is determined by linear interpolation. With help of Eq. (5.16), the diffusion coefficient becomes:

$$\Gamma_e \approx \lambda_e \Gamma_E + (1 - \lambda_e)\Gamma_P \tag{5.21}$$

However linear interpolation in some cases does not yield the proper value of the diffusion coefficient. Consider a sharp jump in viscosity over a cell surface, for instance describing a two-fluid system like oil and water. The diffusion over the cell interface is too large if linear interpolation Eq. (5.16) is used. The two fluids, oil and water, will be smeared out over the interface yielding a non-physical solution. In order to prevent this smearing another averaging or interpolation method is introduced here, the so-called harmonic mean method:

$$\Gamma_e \approx \frac{\Gamma_E \Gamma_P}{\lambda_e \Gamma_E + (1 - \lambda_e)\Gamma_P} \tag{5.22}$$

In the case of an equidistant grid, so $\lambda_e = 1/2$, Eq. (5.22), becomes:

$$\Gamma_e \approx \frac{2\Gamma_E \Gamma_P}{\Gamma_E + \Gamma_P} \tag{5.23}$$

From Eq. (5.23) it can be seen that the lowest value of the diffusion coefficient dominates the outcome of the diffusion coefficient at the cell face. More on these and other approximations can be found in e.g. Voller and Swaminathan (1993).

5.1.4 Explicit and implicit methods

First two methods of time level evaluation are introduced. Subsequently, the influence of the time step size on the stability of the numerical solution is discussed. The numerical solution, of time-dependent ordinary and partial differential equations, can be obtained using an explicit or an implicit method. In explicit methods the numerical solution at the new time level, denoted as $n+1$, is obtained by evaluation, explicitly, of the solution at the current time level, n, or:

$$y^{n+1} = y^n + hf(y^n, t^n) \tag{5.24}$$

here y^{n+1} is the approximated numerical solution at the new time level, y^n the solution at the current time level and $hf(y^n, t^n)$ the function evaluated at the current time level.

In the implicit method the numerical solution at the new time level, $n+1$, is obtained by the solution at n and, implicit, evaluation at $n+1$, or:

$$y^{n+1} = y^n + hf(y^{n+1}, t^{n+1}) \tag{5.25}$$

in which $hf(y^{n+1}, t^{n+1})$ is the function evaluated at the new time level. Note that Eq. (5.24) and Eq. (5.25) are examples of the explicit Euler and implicit Euler formulation respectively, see Moin (2010).

For explicit schemes, the stability of a numerical solution is governed by two stability criteria. Both criteria restrict the time step in order to keep the numerical solution stable. It turns out that two dimensionless numbers can be derived from the advection-diffusion equation which governs the maximum allowable time step size. Transport of a scalar is achieved by advection or diffusion or a combination of the two. Both advection and the diffusion determines the maximum time step size. Here a 1 dimensional advection-diffusion equation for a generic scalar, ϕ, is given:

$$\frac{\partial \phi}{\partial t} + \frac{\partial \phi\, u}{\partial x} = \frac{\partial}{\partial x}\left(\Gamma \frac{\partial \phi}{\partial x}\right) \tag{5.26}$$

discretization of Eq. (5.26), with the FVM and using an explicit scheme, yields:

$$\frac{\phi_P^{n+1} - \phi_P^n}{\Delta t}\Delta V + u_e \phi_e^n A_e - u_w \phi_w^n A_w = \\ \Gamma_e \left(\frac{\phi_E^n - \phi_P^n}{\Delta x_e} \right) A_e - \Gamma_w \left(\frac{\phi_P^n - \phi_W^n}{\Delta x_w} \right) A_w \tag{5.27}$$

For an equidistant grid, the distances area and volume are respectively the following $\Delta x_e = \Delta x_w = \Delta x$, $A_e = A_w = \Delta y$ and $\Delta V = \Delta x \Delta y$. Now, setting the velocity to a constant value, so $u_e = u_w = u$. Furthermore, the diffusion coefficient, $\Gamma_{e,w}$, is taken constant, i.e. $\Gamma_e = \Gamma_w = \Gamma$. Here, as an example, the advection term in Eq. (5.27) is approximated using an upwind scheme, see also Eq. (5.19). The following discretized equation can be obtained, assuming $u > 0$:

$$\frac{\phi_P^{n+1} - \phi_P^n}{\Delta t} + \frac{u}{\Delta x}\left(\phi_P^n - \phi_W^n\right) = \frac{\Gamma}{\Delta x^2}\left(\phi_E^n - 2\,\phi_P^n + \phi_W^n\right) \tag{5.28}$$

In order to assess the maximum time step size, two cases are considered. The first case is by setting the diffusion term Γ equal to zero, $\Gamma = 0$. Then the transport of scalar ϕ is governed by advection, assuming $u > 0$:

$$\frac{\phi_P^{n+1} - \phi_P^n}{\Delta t} + \frac{u}{\Delta x}\left(\phi_P^n - \phi_W^n\right) = 0 \tag{5.29}$$

And rewriting Eq. (5.29) yields:

$$\phi_P^{n+1} = \phi_P^n - u\frac{\Delta t}{\Delta x}\left(\phi_P^n - \phi_W^n\right) \tag{5.30}$$

Now from Eq. (5.30) the dimensionless group, $u\Delta t/\Delta x$, can be distinguished and is called the Courant number. This number is the ratio of two velocities, namely the physical velocity u and the so-called grid velocity $\Delta x/\Delta t$. It can be shown that, see Moin (2010), the upwind scheme is stable if the following condition, the CFL (Courant Friedrichs Levy) condition, is met:

$$C_c = \frac{\Delta t}{\Delta x} \leq C_{cmax} \tag{5.31}$$

where C_c is called the Courant number and has a maximum value of C_{cmax}. The value of C_{cmax} depends on the scheme used. The Courant number indicates

that the physical velocity must not exceed the grid velocity for a numerical scheme to remain stable. Here, Eq. (5.31), the upwind scheme is given as an example and for this scheme the value of $C_{cmax} = 1$.

Now transport by diffusion is considered. This is achieved by setting the transport velocity $u = 0$ in Eq. (5.28), leading to the diffusion equation:

$$\frac{\phi_P^{n+1} - \phi_P^n}{\Delta t} = \frac{\Gamma}{\Delta x^2} \left(\phi_E^n - 2\,\phi_P^n + \phi_W^n\right) \tag{5.32}$$

rewriting this equation and denoting $D_c = \Delta t \Gamma / \Delta x^2$, leads to:

$$\begin{aligned} \phi_P^{n+1} &= \phi_P^n + D_c \left(\phi_E^n + \phi_W^n - 2\phi_P^n\right) \\ &= \left(1 - 2D_c\right) \phi_P^n + D_c \phi_E^n + D_c \phi_W^n \end{aligned} \tag{5.33}$$

using the maximum principle property [1], it can be shown that for $1 - 2D_c > 0$ the following is true:

$$\phi_P^{n+1} \leq \left(1 - 2D_c\right) \max \phi_P^n + D_c \max \phi_P^n + D_c \max \phi_P^n \tag{5.34}$$

then:

$$\phi_P^{n+1} \leq \max \left(1 - 2D_c + 2D_c\right) = \max \phi_P^n \tag{5.35}$$

the maximum principle implies the stability of the scheme. Therefore, the stability of the scheme is ensured if the following condition, the viscous CFL condition, is met:

$$D_c = \frac{\Delta t\, \Gamma}{\Delta x^2} \leq \frac{1}{2} \tag{5.36}$$

where D_c is the so called diffusion number. Similarly for a $2D$ case the viscous CFL condition is as follows:

$$D_c = \Gamma \Delta t \left(\frac{1}{\Delta x^2} + \frac{1}{\Delta y^2}\right) \leq \frac{1}{2} \tag{5.37}$$

It is seen from Eq. (5.36) that the time step size is proportional to the grid spacing squared and depends linearly on the diffusion constant Γ. For large

[1] The maximum principle states that a non-constant harmonic function cannot attain a maximum (or minimum) at an interior point of its domain. This result implies that the values of a harmonic function in a bounded domain are bounded by its maximum and minimum values on the boundary, see Hunter (2014) and Evans (1997)

diffusion constants and small grid sizes, the diffusion puts very stringent limitations on the time step size. In order to circumvent a very small time step, an implicit numerical scheme has to be used. This implicit formulation does not suffer from the very strong time step requirement. So if very large diffusion coefficients are to be expected and/or small grid sizes, the diffusion term needs to be treated implicitly in order to reduce computational costs. A fully implicit formulation of the diffusion equation is:

$$\frac{\phi_P^{n+1} - \phi_P^n}{\Delta t} = \frac{\Gamma}{\Delta x^2}\left(\phi_E^{n+1} - 2\,\phi_P^{n+1} + \phi_W^{n+1}\right) \tag{5.38}$$

This leads to a set of equations with N equations with N unknowns, where N is the number of grid cells.

5.2 Numerical solution of the Navier-Stokes equations

5.2.1 Discretization of the Navier-Stokes equations

In this section, the Navier-Stokes equations are discretized. Some basic concepts of discretization techniques have been discussed in previous sections. Here some special aspects in the discretization of the Navier-Stokes equations and the placement of the field variables are discussed. First, the Navier-Stokes equations are repeated, the conservation of momentum is the following,

$$\frac{\partial \rho\,\mathbf{u}}{\partial t} + \nabla\cdot(\rho\,\mathbf{u}\,\mathbf{u}) = -\nabla p + \nabla\cdot\left(\mu\left(\nabla\mathbf{u} + \nabla\mathbf{u}^T\right)\right) + \mathbf{s} \tag{5.39}$$

and the continuity constraint is given by,

$$\frac{\partial \rho}{\partial t} + \nabla\cdot(\rho\,\mathbf{u}) = 0 \tag{5.40}$$

Using the divergence theorem, the advection term of Eq. (5.39) is rewritten as,

$$\nabla\cdot(\rho\,\mathbf{u}\,\mathbf{u}) = \int_A \rho\,\mathbf{u}\,\mathbf{u}\cdot\mathbf{n}dA \tag{5.41}$$

discretization of the advection term with the FVM, given here for 2 dimensions and in the x-direction only, yields,

$$\int_A \rho\, \mathbf{u}\, \mathbf{u} \cdot \mathbf{n} dA \approx$$
$$(\rho\, u\, u)_e A_e - (\rho\, u\, u)_w A_w + (\rho\, u\, v)_n A_n - (\rho\, u\, v)_s A_s \tag{5.42}$$

Now the viscous term, $\nabla \cdot \left(\mu \left(\nabla \mathbf{u} + \nabla \mathbf{u}^T\right)\right)$, from Eq. (5.39), is expanded and discretized. Expanding the viscous term for the u-velocity equation in $2D$ using a Cartesian coordinate system yields:

$$\nabla \cdot \left(\mu \left(\nabla \mathbf{u} + \nabla \mathbf{u}^T\right)\right)_x = \frac{\partial}{\partial x}\left(\mu \frac{\partial u}{\partial x}\right) + \frac{\partial}{\partial y}\left(\mu \frac{\partial u}{\partial y}\right) + s_u \tag{5.43}$$

here the subscript x denotes the expanded viscous term in x direction. In order to make the implementation of the viscous contribution more easily in a numerical code, the viscous term Eq. (5.43) is split into two parts. One part is the first term on the RHS of Eq. (5.43), and the second part is the term s_u, which is:

$$s_u = \frac{\partial}{\partial x}\left(\mu \frac{\partial u}{\partial x}\right) + \frac{\partial}{\partial y}\left(\mu \frac{\partial v}{\partial x}\right)$$

The variable s_u is taken as a source term in the discretized Navier-Stokes equations. This splitting of viscous term Eq. (5.43) into two parts is elaborated in more detail in Appendix D. Using the divergence theorem and Eq. (5.20), Eq. (5.43), is discretized as follows:

$$\begin{aligned}\boldsymbol{D}_x =& \mu_e \left(\frac{u_E - u_P}{\Delta x_e}\right) A_e - \mu_w \left(\frac{u_P - u_W}{\Delta x_w}\right) A_w + \\ & \mu_n \left(\frac{u_N - u_P}{\Delta y_n}\right) A_n - \mu_s \left(\frac{u_P - u_S}{\Delta y_s}\right) A_s\end{aligned} \tag{5.44}$$

where $\boldsymbol{D}_x$ is the discretized viscous term in the x-direction. The discretized source term s_u, using the FVM, becomes:

$$\begin{aligned}s_u \Delta V =& \mu_e \left(\frac{u_E - u_P}{\Delta x_e}\right) A_e - \mu_w \left(\frac{u_P - u_W}{\Delta x_w}\right) A_w + \\ & \mu_n \left(\frac{v_{ne} - v_{nw}}{x_{ne} - x_{nw}}\right) A_n - \mu_s \left(\frac{v_{se} - v_{sw}}{x_{se} - x_{sw}}\right) A_s\end{aligned} \tag{5.45}$$

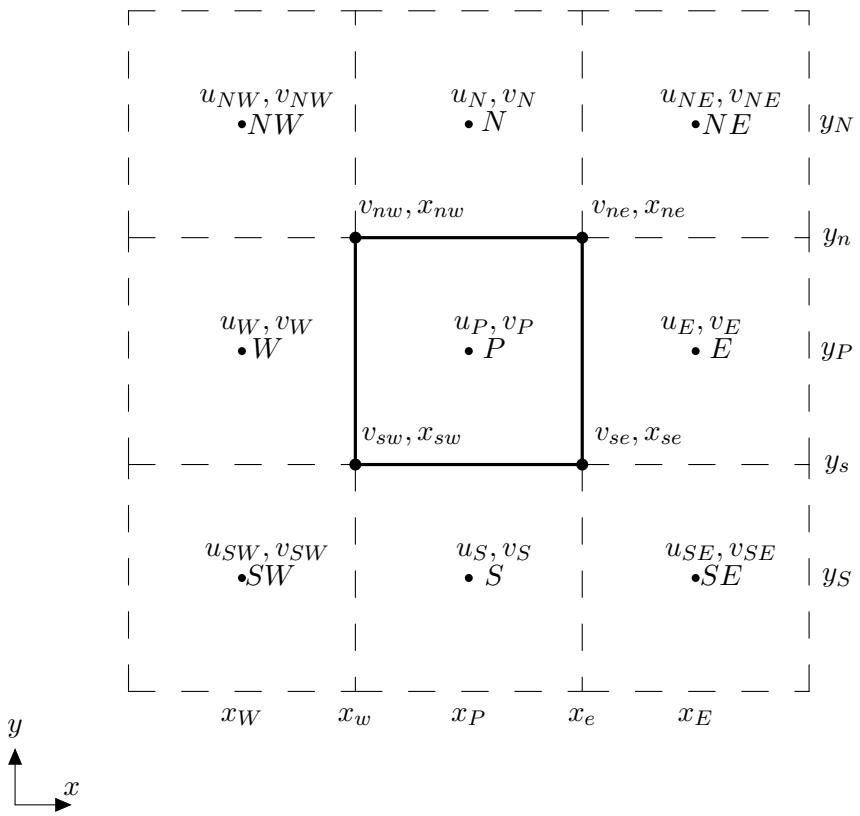

Figure 5.3: Plot of a $2D$ Cartesian grid using the compass notation. The center, east, west, north and south grid cell is given by the capital letters P, E, W and N, respectively. The interpolated values are given by the lower case letters e, w, n and s.

the subscripts ne, nw, se and sw denote the position of the values of the variables the north east, north west, south east and south west corner of a grid cell, see Figure 5.3

More information on discretization methods can be found in e.g. Ferziger and Peric (1999), Versteeg and Malalasekera (1995) or Schaefer (2006). In the next section, the solution of the Navier-Stokes equations is discussed. This is done using a so-called fractional step method.

5.2.2 Fractional step method

Here a method is presented for solving the Navier-Stokes equations in time. This is the so-called fractional step method and was initially introduced by Chorin (1968). This method gained quite a lot of popularity in the gaming or film industry, see Stam (1999). Here a variant is presented of the fractional step method based on the algorithm of Chorin (1968).

Explicit formulation

Incompressible fluid flows are pressure linked equations. The velocity field of the flow depends on the pressure distribution and the pressure distribution depends on the velocity field. In which the velocity field complies with the continuity constraint. Here the fractional step method is layed out. For brevity the following notation is introduced. The viscous term is denoted as, $\boldsymbol{D}(\mathbf{u})$. The advective term is denoted as $\boldsymbol{A}(\mathbf{u})$. The Navier-Stokes equations in semi-discrete form is the following,

$$\frac{(\rho\,\mathbf{u})^{n+1} - (\rho\,\mathbf{u})^{n}}{\Delta t}\Delta V = -\nabla p^{n+1} - \boldsymbol{A}(\mathbf{u}^n) + \boldsymbol{D}(\mathbf{u}^n) + \mathbf{s}^n \tag{5.46}$$

and the continuity is given by:

$$\frac{\partial \rho}{\partial t} + \nabla \cdot (\rho\,\mathbf{u})^{n+1} = 0 \tag{5.47}$$

Now an intermediate velocity $\mathbf{u}^*$ is introduced first and is obtained by splitting the operators and omitting the pressure gradient $-\nabla p^{n+1}$:

$$\frac{(\rho\,\mathbf{u})^{*} - (\rho\,\mathbf{u})^{n}}{\Delta t}\Delta V = -\boldsymbol{A}(\mathbf{u}^n) + \boldsymbol{D}(\mathbf{u}^n) + \mathbf{s}^n \tag{5.48}$$

rearranging Eq. (5.48), the prediction for $\rho\,\mathbf{u}^*$ is obtained:

$$(\rho\,\mathbf{u})^{*} = (\rho\,\mathbf{u})^{n} + \frac{\Delta t}{\Delta V}\left[-\boldsymbol{A}(\mathbf{u}^n) + \boldsymbol{D}(\mathbf{u}^n) + \mathbf{s}^n\right] \tag{5.49}$$

A more accurate prediction of the term $\rho\,\mathbf{u}^*$, with respect to time, can be achieved by averaging the advection term, $\boldsymbol{A}(\mathbf{u})$, in time. This is done by using the Adams-Bashforth scheme. This scheme is explicit and second order accurate in time, Kim and Moin (1985). The advection term is evaluated at two previous time levels and this scheme reads:

$$(\rho\mathbf{u})^{*} = (\rho\mathbf{u})^{n} + \frac{\Delta t}{\Delta V}\left[-\frac{1}{2}\left\{3\boldsymbol{A}(\mathbf{u}^n) - \boldsymbol{A}(\mathbf{u}^{n-1})\right\} + \boldsymbol{D}(\mathbf{u}^n) + \mathbf{s}^n\right] \tag{5.50}$$

where n and $n-1$ denotes the evaluation of the advective and diffusive terms at time level n and time level $n-1$ respectively. The Adams-Bashfort scheme is employed in this thesis.

The continuity constraint, see Eq. (5.47), is used in order to determine the pressure, p. Rearranging Eq. (5.47) and writing this equation in semi discrete form yields:

$$\nabla \cdot (\rho\,\mathbf{u})^{n+1} = -(\rho^n - \rho^{n-1})\frac{\Delta V}{\Delta t} \tag{5.51}$$

subsequently the velocity at the time level $n+1$ is obtained by:

$$(\rho\,\mathbf{u})^{n+1} = (\rho\,\mathbf{u})^* - \Delta t\,\nabla p^{n+1} \tag{5.52}$$

using Eq. (5.51) and Eq. (5.52) gives:

$$\nabla \cdot (\rho\,\mathbf{u})^{n+1} = \nabla \cdot (\rho\,\mathbf{u})^* - \Delta t\,\nabla^2 p^{n+1} = -(\rho^n - \rho^{n-1})\frac{\Delta V}{\Delta t} \tag{5.53}$$

and reordering leads to:

$$\nabla^2 p^{n+1} = \frac{1}{\Delta t}\left(\nabla \cdot (\rho\,\mathbf{u})^* + (\rho^n - \rho^{n-1})\frac{\Delta V}{\Delta t}\right) \tag{5.54}$$

Eq. (5.54) is called the pressure Poisson equation and can be solved using an iterative solver. In this work a multi-grid algorithm is applied, see Section 5.38. Solving this system of equations gives a new pressure p^{n+1}. Applying equation Eq. (5.54) and equation Eq. (5.52) yields the velocity at the new time level $n+1$. Now if the viscous terms are large, the time step requirement becomes very severe, leading to high computational costs. In the next section, an alternative formulation is presented in order to circumvent this time step issue.

Implicit formulation

In the case of large values of the diffusive terms the time step becomes prohibitively small. This leads to high computational costs. In order to circumvent this time step limitation, the diffusive terms are treated implicitly and can be expressed as:

$$\frac{(\rho\,\mathbf{u})^* - (\rho\,\mathbf{u})^n}{\Delta t} = -\frac{1}{2}\left\{3\boldsymbol{A}(\mathbf{u}^n) - \boldsymbol{A}(\mathbf{u}^{n-1})\right\} + \boldsymbol{D}(\mathbf{u}^*) + \mathbf{s}^n \tag{5.55}$$

or rewriting prediction of the velocity, $\mathbf{u}^*$:

$$(\rho\,\mathbf{u})^* - \Delta t \boldsymbol{D}(\mathbf{u}^*) = \rho\,\mathbf{u}^n + \Delta t \left[-\frac{1}{2} \left\{ 3\boldsymbol{A}(\mathbf{u})^n - \boldsymbol{A}(\mathbf{u})^{n-1} \right\} + \mathbf{s}^n \right] \quad (5.56)$$

Again second-order-explicit Adams-Bashforth scheme for the advective terms is used here. Now Eq. (5.56) can be rewritten into a system of equations which is solved with a numerical solver. Here a BiCGstab algorithm is used from the `Eigen`package, see Guennebaud et al. (2010). If the intermediate velocity, $\mathbf{u}^*$, is known, the velocity, $\mathbf{u}$, at time level $n+1$ can be obtained:

$$(\rho\,\mathbf{u})^{n+1} = (\rho\,\mathbf{u})^* - \Delta t \nabla \psi^{n+1} \quad (5.57)$$

It should be noted that a pseudo pressure, ψ, is introduced here. The pseudo pressure is not equal to the actual pressure, p^{n+1}, see Eq. (5.53). This is due to the fact that the velocity $\mathbf{u}^*$, i.e. omitting the pressure gradient ∇p, is solved implicitly and not the actual velocity at the next time level, $\mathbf{u}^{n+1}$.

The pseudo pressure, ψ^{n+1}, is evaluated by taking the divergence of Eq. (5.57):

$$\nabla \cdot (\rho\,\mathbf{u})^{n+1} = \nabla \cdot (\rho\,\mathbf{u})^* - \Delta t \nabla^2 \psi^{n+1} = -(\rho^n - \rho^{n-1}) \frac{\Delta V}{\Delta t} \quad (5.58)$$

and after some rearrangement the following Poisson equation is recovered, Eq. (5.54):

$$\nabla^2 \psi^{n+1} = \frac{1}{\Delta t} \left(\nabla \cdot (\rho\,\mathbf{u})^* + (\rho^n - \rho^{n-1}) \frac{\Delta V}{\Delta t} \right) \quad (5.59)$$

Other splitting strategies of the fractional step method can be found in literature, e.g. Van Kan (1986), Guermond and Salgado (2008), Guermond and Salgado (2009) or Kim and Moin (1985).

Multi-grid method

In order to obtain the solution of the pressure Poisson equation Eq. (5.54) and Eq. (5.59) the Multi-grid method is used in this work. In matrix form the pressure Poisson equation is expressed as:

$$\mathbf{A}\mathbf{x} = \mathbf{b} \quad (5.60)$$

where $\mathbf{A}$ is the system matrix, $\mathbf{b}$ is a vector of known values, i.e. boundary conditions and forces, and $\mathbf{x}$ is the solution vector. It should be noted that the system matrix has only values on a small band around the diagonal. The remaining of the matrix is filled with zeros and this kind of matrices are called sparse. One of the most efficient iterative methods for solving sparse, banded, systems is the Multi-grid method, see Briggs et al. (2000). The multi-grid method solves the system, as can be deduced from the name Multi-grid, using multiple grids. The problem is solved on a coarse grid, using a Jacobi relaxation method, see Press et al. (1992). The problem is cheaper to solve, using the Jacobi method, on coarse grids than on fine grids. Subsequently, the solution of the coarse problem is projected on finer meshes, until the finest mesh. This is repeated several times until convergence is reached. More information about this, vast, topic can be found in for instance Press et al. (1992), Barrett et al. (1994) or Briggs et al. (2000).

5.2.3 Immersed Boundary Method

Modeling fluid-structure interaction poses a number of challenging problems for numerical simulations. This is due to the fact that the structure influences the motion of the fluid and the fluid influences the motion structure. The Immersed Boundary Method (IBM) is a method, modeling fluid-structure interaction, and allows the treatment of moving (complicated) objects in a computational domain. The need for (automatic) grid generation, which is numerically cumbersome in combination with moving bodies, is removed in this method. This is a major advantage. This method is originally developed by Peskin (1972), simulating a beating human heart. An extra body force is added, accounting for the influence of the immersed solid. The predictor step of the fractional step algorithm, see Eq. (5.48), is repeated here:

$$\frac{\rho\mathbf{u}^* - \rho\mathbf{u}^n}{\Delta t} = -\mathbf{A}(\mathbf{u}^n) + \mathbf{D}(\mathbf{u}^*) + \mathbf{s}^n \tag{5.61}$$

where the source term $\mathbf{s}^n$ is split into the following forces:

$$\mathbf{s}^n = \mathbf{f}_{IB}^n + \mathbf{f}_g^n \tag{5.62}$$

in which $\mathbf{f}_g^n$ is the body force due to gravity, assuming gravity acting as the only external body force, and $\mathbf{f}_{IB}^n$ is the immersed force and is yet to be determined. This force is chosen as such that the (imposed) velocity of the immersed solid,

$\mathbf{V}^{n+1}$ is returned:

$$\mathbf{f}_{IB} = \begin{cases} \left(\rho\mathbf{V}^{n+1} - \rho\mathbf{u}^n\right)/\Delta t = & \\ \mathbf{A}(\mathbf{u}^n) - \mathbf{D}(\mathbf{u}^n) - \mathbf{f}_g + \nabla p & \text{if} \quad \text{inside immersed solid} \\ 0 & \text{if} \quad \text{outside immersed solid} \end{cases} \tag{5.63}$$

More on IBM can be found in for instance Peskin (1972), Peskin (2002) or Fadlun et al. (2000). Applications of the IB Method can be found in Goeree et al. (2017), simulating settling particles in a confined space.

5.2.4 Pressure velocity coupling

A collocated grid arrangement leads to pressure velocity decoupling, Ferziger and Peric (1999), which can be prevented by employing the interpolation method of Rhie and Chow (1983). Here the east cell face velocity, with an equidistant grid layout, is taken as an example to clarify the approach. The derivation for other cell face velocities is similar. First velocities are given with corresponding pressure gradients of the grid cell, see Figure 5.4:

$$\rho_P\, u_P = \rho_P\, u_P^* - \Delta t \frac{p_E - p_W}{2\,\Delta x} \tag{5.64}$$

$$\rho_E\, u_E = \rho_E\, u_E^* - \Delta t \frac{p_{EE} - p_P}{2\,\Delta x} \tag{5.65}$$

$$\rho_e\, u_e = \rho_e\, u_e^* - \Delta t \frac{p_E - p_P}{\Delta x} \tag{5.66}$$

and the velocity at the east side is obtained by:

$$\rho_e u_e = \frac{\rho_E\, u_E + \rho_P\, u_P}{2} \tag{5.67}$$

Substitution of the equations Eq. (5.64), Eq. (5.65) and Eq. (5.66) in equation Eq. (5.67) gives:

$$\rho_e\, u_e = \frac{\rho_E\, u_E^* + \rho_P\, u_P^*}{2} + \frac{\Delta t}{4\,\Delta x}\left(p_W - p_E + p_P - p_{EE}\right) \tag{5.68}$$

where:

$$\rho_e\, u_e = \rho_e\, u_e^* - \Delta t \frac{p_E - p_P}{\Delta x} \tag{5.69}$$

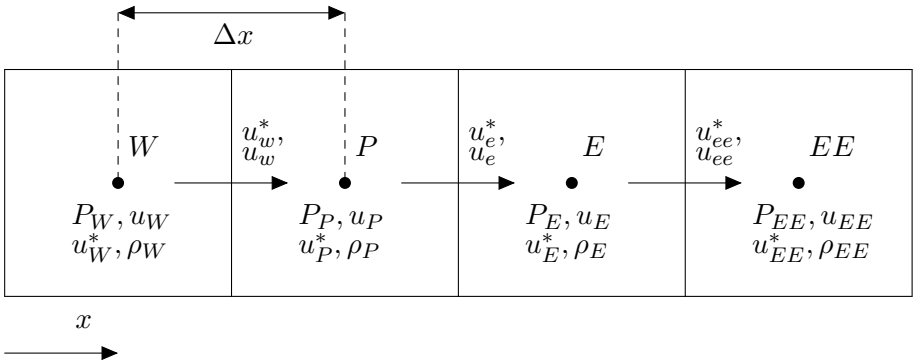

Figure 5.4: Grid with collocated placement of field variables required for the Rhie and Chow interpolation.

substitution of equation Eq. (5.66) in Eq. (5.68) and rearranging gives finally the intermediate east cell face velocity:

$$\rho_e \, u_e^* = \frac{\rho_E \, u_E^* + \rho_P \, u_P^*}{2} + \frac{\Delta t}{4 \, \Delta x} \left(p_W - 3 \, p_P + 3 \, p_E - p_{EE} \right) \tag{5.70}$$

In Eq. (5.70) the pressure is incorporated in the cell face velocity. Note that if the pressure gradient is small the second term, the pressure term, in Eq. (5.70) vanishes. If the pressure gradient is large the second term becomes large. This ensures a coupling between the velocities and pressures.

Similar derivations, preventing pressure velocity decoupling for collocated grids, in combination with the fractional step method can be found in literature, see for instance Armfield and Street (2000) and Armfield et al. (2010).

5.2.5 Boundary conditions - Navier-Stokes

The numerical solution of the Navier-Stokes equations is governed by the boundary conditions. Here the application of wall boundary conditions are treated and the numerical implementation of the boundary conditions is elaborated. Furthermore, periodic boundary conditions are discussed. Here the approach of Ferziger and Peric (1999) is briefly outlined.

No-slip boundary

At the wall a Dirichlet boundary condition is applied, this is also called a no-slip boundary condition. This implies that the velocity of the fluid is equal

to the wall velocity. Now consider the south wall boundary, so $y = 0$, with a wall velocity of $u_{wall} = 0$, see Figure 5.5. From continuity, for an incompressible fluid, it follows that the normal viscous stress is zero at the south wall:

$$\left(\frac{\partial u}{\partial x}\right)_{wall} = 0 \Rightarrow \left(\frac{\partial v}{\partial y}\right)_{wall} = 0 \Rightarrow 2\mu \left(\frac{\partial v}{\partial y}\right)_{wall} = 0 \tag{5.71}$$

Here the subscript *wall* denotes the wall boundary. Now this viscous stress can be expressed as a force as follows:

$$F_s^d = \int_{A_S} 2\mu \left(\frac{\partial v}{\partial y}\right)_{wall} dA_S = 0 \tag{5.72}$$

and can be implemented directly with the FVM. Another, but false, implementation of the normal viscous stress would be to set the velocity $v_S = 0$ at the south boundary. Since the interior point v_P is not zero, a flux over the wall would arise. This is clearly not the case at a wall boundary. A possible numerical implementation of the normal viscous stress is given here. The velocity v_{wall}, or in this case v_s, is zero at the wall boundary, see Figure 5.5. This is achieved by taking the average of the velocities v_S and v_P:

$$v_{wall} = v_s = \frac{1}{2}\left(v_S + v_P\right) = 0 \tag{5.73}$$

the velocity, v_S, can be obtained as follows:

$$v_S = -v_P \tag{5.74}$$

Now the numerical approximation of the shear stress is given. The wall shear stress, expressed as a force, reads:

$$F_s^d = \int_{A_S} \mu \left(\frac{\partial u}{\partial y}\right)_{wall} dA_S \tag{5.75}$$

can be calculated using a one sided approximation:

$$\mu \left(\frac{\partial u}{\partial y}\right)_{wall} \approx \mu_s \frac{u_P - u_s}{\frac{1}{2}(y_P - y_S)} \tag{5.76}$$

where u_s is the wall velocity in x-direction.

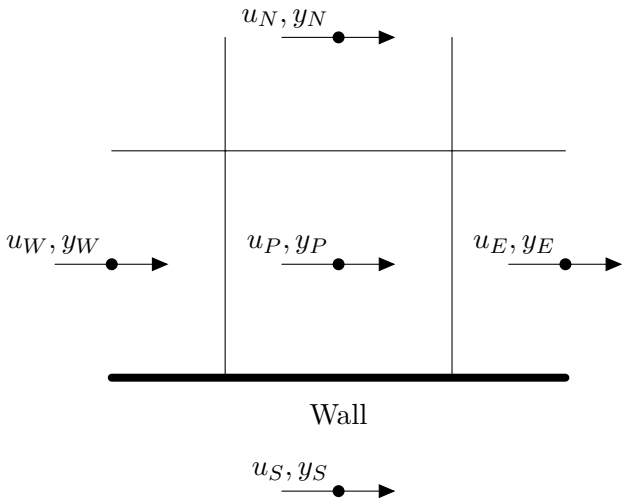

Figure 5.5: Placement of u-velocity at the boundary, see Eq. (5.77).

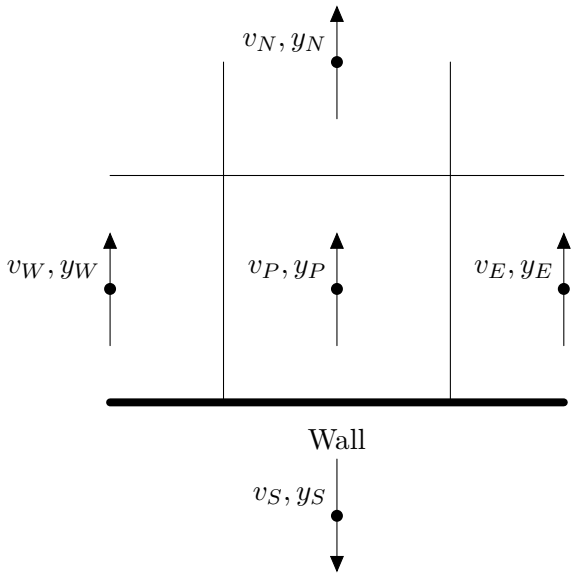

Figure 5.6: Placement of v-velocity at the boundary, see Eq. (5.81).

Free-slip boundary

The free-slip, or symmetry plane boundary, is discussed here, see Figure 5.6. For this type of boundary the shear stress at the wall is zero and the normal

stress is non-zero:

$$\left(\frac{\partial u}{\partial y}\right)_{sym} = 0$$
$$\left(\frac{\partial v}{\partial y}\right)_{sym} \neq 0$$

The diffusive flux of the u-momentum is zero and can be approximated as follows:

$$\left(\frac{\partial u}{\partial y}\right)_{s} \approx \frac{u_P - u_s}{\frac{1}{2}(y_P - y_S)} = 0 \tag{5.77}$$

here u_s is the velocity at the wall. Now for an equidistant grid, the wall velocity is the following:

$$u_{wall} = u_s = \frac{1}{2}(u_P + u_S) \tag{5.78}$$

substitution of Eq. (5.78) in Eq. (5.77) yields:

$$\frac{u_P - u_S}{y_P - y_S} = 0\,; \qquad u_P = u_S \tag{5.79}$$

Now the diffusive flux of the normal stress for the v-momentum is non-zero, expressed as a force:

$$F_s^d = \int_{A_S} 2\mu \left(\frac{\partial v}{\partial y}\right)_{sym} dA_S \tag{5.80}$$

the approximation of the flux, Eq. (5.80) is given as:

$$2\mu \left(\frac{\partial v}{\partial y}\right)_{sym} \approx 2\mu_s \frac{v_P - v_s}{\frac{1}{2}(y_P - y_S)} \tag{5.81}$$

The wall velocity, v_{wall}, at the south boundary is zero:

$$v_{wall} = v_s = \frac{1}{2}(v_P + v_S) = 0\,; \qquad v_P = -v_S \tag{5.82}$$

Boundary $\mathbf{u}^*$ - Fractional Step Method

In the fractional step method the boundary conditions for the estimation of the velocity, $\mathbf{u}^*$, see Eq. (5.46) or Eq. (5.55), are unknown. The intermediate velocity, $\mathbf{u}^*$ is an estimation of the real velocity, $\mathbf{u}$. Since the imposed velocity, $\mathbf{u}$, is known at the boundaries the best estimation for the intermediate velocity the imposed velocity, $\mathbf{u}$. Hence, the intermediate velocity $\mathbf{u}^*$ is set equal to the imposed velocity, $\mathbf{u}$, at the boundaries. Now, this can be restated in a more formal manner. Define a domain Ω where the Navier-Stokes equations need to be solved and $\partial\Omega$ denotes the boundary of the domain,

$$\mathbf{u}^* = \mathbf{u} \qquad \text{on} \quad \partial\Omega \tag{5.83}$$

The boundaries for the intermediate velocity are easy to implement. The boundary conditions of the intermediate velocity, described here is elaborated in Kim and Moin (1985).

The pressure boundary for a collocated arrangement extends to the grid cell face at the wall. The pressure on the cell face at the south boundary can be obtained by using linear interpolation,

$$p_s = \frac{1}{2}\left(p_P + p_S\right) \tag{5.84}$$

The pressure in the south cell p_S is unknown and can be obtained using extrapolation from interior grid points. A simple extrapolation method is as follows,

$$p_S = p_P \tag{5.85}$$

substitution of Eq. (5.85) in Eq. (5.84) yields,

$$p_s = p_S = p_P \tag{5.86}$$

The extrapolation method for the pressure boundary condition given above, Eq. (5.86), is used in this work.

Wall functions

In Section 3.5 turbulent boundary layer and the structure of this layer was introduced. This boundary layer is used in order to reduce computational

cost. A prohibitively large number of grid points would be required in order to resolve all the details in a turbulent boundary layer. The computational cost is reduced by applying so-called wall functions. The numerical implementation of these wall functions is discussed here. Two flow regimes are distinguished, the laminar and turbulent regime. The flow is laminar if $y^+ \leq 11.63$ and is turbulent if $y^+ > 11.63$. The value of y^+ is determined based on the velocity, u_P, at the first grid-cell from the wall.

Laminar

First the laminar case, $y^+ \leq 11.63$, is considered, the wall shear stress is given by, repeating Eq. (5.76) and Eq. (5.75):

$$F_s^d = \int_{A_S} \mu \left(\frac{\partial u}{\partial y} \right)_{wall} dA_S \tag{5.87}$$

with:

$$\mu \left(\frac{\partial u}{\partial y} \right)_{wall} \approx \mu_s \frac{u_P - u_s}{\frac{1}{2}(y_P - y_S)} \tag{5.88}$$

Now, the wall shear stress is given as:

$$\tau_{wall} = \mu_s \frac{u_P - u_s}{\frac{1}{2}(y_P - y_S)} \tag{5.89}$$

where u_s is the wall velocity at the South boundary and $\frac{1}{2}(y_P - y_S)$ the distance from the wall to the first interior grid cell center, P.

Turbulent

When the flow is turbulent i.e. a value of $y^+ > 11.63$, the wall shear stress is expressed as, see also Eq. (3.67),

$$\tau_{wall} = \rho u_\tau^2 \tag{5.90}$$

where u_τ is calculated from, see Eq. (3.63),

$$\frac{|u|}{u_\tau} = \frac{1}{\kappa} \ln \left(\frac{\mu \Delta y}{\rho} u_\tau \right) + C \tag{5.91}$$

the value of u_τ is determined using an iterative method. The wall shear stress can be expressed as a force by integrating over the cell area:

$$F_s^t = \int_A \tau_{wall}\, dA \tag{5.92}$$

this force is decomposed in the directions along the wall plane, see Section 3.5.2 for an example, and put as a source term in the momentum equations.

5.2.6 Boundary conditions - sediment fractions

The motion of sediment fractions is described by the advection-diffusion equation. In case of a wall or a free surface in a computational domain, there is no transport of fractions possible through the boundary. Here Neumann boundary conditions are imposed in order to prevent transport through these surfaces. This can be easily done in the Finite Volume Method by setting the corresponding coefficients, in the discretized set of equations, equal to zero. More on the boundary conditions in combination with the Finite Volume Method can be found in for instance Versteeg and Malalasekera (1995).

5.3 Maximum volume concentration

The distribution of sediment is governed by the velocity field of the mixture and transport equations with a drift-flux. Sediment accumulates at the bottom of a domain forming a sand bed. This occurs at a maximum value of the total volume concentration of solids, $\alpha_t \approx \alpha_{tmax}$, where α_{tmax} is the maximum volume concentration of solids. The maximum value of the volume concentration depends on the particle size distribution and the packing of the sediment. If no special precautions are taken, in limiting this value, an overshoot can occur of this maximum value. In some cases, the maximum value of the volume concentration can be even larger than 1, or, $\alpha_t > 1$. This is clearly a non-physical result and this leads to numerical instabilities. In this section, two methods are given in order to limit the maximum value of the volume concentration. The first method is the penalty method and the second is the use of an overshoot limiter.

5.3.1 Penalty method

The maximum value of the volume concentration in a grid cell is governed by the drift velocity and the mixture velocity of the flow. This means that

the accumulation of sediment can still take place even if the concerning grid cell is at its maximum volume concentration of solids. Or fluxes over the grid cell boundary still exist even if the grid cell has reached its maximum value. The transport of a volume fraction is described using an advection-diffusion equation, repeated here:

$$\frac{\partial \alpha_k}{\partial t} + \nabla \cdot \alpha_k \mathbf{u}_k = \nabla \cdot \Gamma_t \nabla \alpha_k \tag{5.93}$$

The fraction velocity, $\mathbf{u}_k$, is composed by a drift and a mixture velocity:

$$\mathbf{u}_k = \mathbf{u}_{km} + \mathbf{u}_m \tag{5.94}$$

where $\mathbf{u}_m$ is the mixture velocity and $\mathbf{u}_{km}$ is the diffusion velocity. If the maximum value of the volume concentration has been reached, the diffusion velocity, $\mathbf{u}_{km}$ reduces to zero, see also Eq. (4.99). However, the mixture velocity, $\mathbf{u}_m$ is not zero and the accumulation of material in a grid cell can still occur. A possible solution for this is forcing the mixture velocity $\mathbf{u}_m$ to zero if the volume concentration α_t approaches the maximum value α_{tmax}. This is done by adding a penalty term in momentum equations of the mixture. The penalty term is a function of the total volume concentration of solids, α_t and the mixture velocity $\mathbf{u}_m$. The mixture momentum equation with the added penalty term is given by:

$$\begin{aligned} &\frac{\partial \rho_m \mathbf{u}_m}{\partial t} + \nabla \cdot \rho_m \mathbf{u}_m \mathbf{u}_m = \\ &-\nabla p_m + \nabla \cdot (\mathbf{T}_m + \mathbf{T}_m^t - \sum_{k=1}^{N} \alpha_k \rho_k \mathbf{u}_{km} \mathbf{u}_{km}) + \rho_m \mathbf{g} + \mathbf{f}(\alpha_t) \end{aligned} \tag{5.95}$$

now Eq. (5.95) can be expressed in discretized explicit form as follows:

$$\frac{(\rho_m \mathbf{u}_m)_P^{n+1} - (\rho_m \mathbf{u}_m)_P^n}{\Delta t} = -\mathbf{A}(\mathbf{u}_m^n) + \mathbf{D}(\mathbf{u}_m^n) - \nabla (p_m)^n + \mathbf{s}_P^n + \mathbf{f}_P^{n+1}(\alpha_t) \tag{5.96}$$

where the penalty term $\mathbf{f}_P(\alpha_t)$ is imposed at cell center, denoted with subscript P. The term $(\rho_m \mathbf{u}_m)^{n+1})P$ is obtained by rewriting Eq. (5.96):

$$\begin{aligned} &(\rho_m \mathbf{u}_m)_P^{n+1} = (\rho_m \mathbf{u}_m)_P^n + \\ &\Delta t \left[-\mathbf{A}(\mathbf{u}_m^n) + \mathbf{D}(\mathbf{u}_m^n) + \mathbf{s}_P^n - \nabla (p_m)^n + \mathbf{f}_P^{n+1}(\alpha_t) \right] \end{aligned} \tag{5.97}$$

here $\mathbf{f}_P^n(\alpha_t)$ is the penalty term, which is a function of α_t, and can be expressed as:

$$\mathbf{f}_P^{n+1}(\alpha_t) = -\frac{1}{\Delta t}\varepsilon(\alpha_t)\mathbf{u}_m^{n+1} \tag{5.98}$$

In which the function $\varepsilon(\alpha_t)$ has the dimension of $[kg/(m^3\ s)]$. If the maximum volume concentration is reached in grid cell P, the mixture velocity must reduce to zero. This is achieved by increasing the forcing, $\varepsilon(\alpha_t)$ to a very large value, say of the order of magnitude of 10^{10}. In the following a more detailed elaboration is given, now substitution of Eq. (5.98) in Eq. (5.97) yields:

$$\begin{aligned}&(\rho_m\mathbf{u}_m)_P^{n+1} = (\rho_m\mathbf{u}_m)_P^n + \\ &\Delta t\left[-\mathbf{A}(\mathbf{u}_m^n) + \mathbf{D}(\mathbf{u}_m^n) + \mathbf{s}_P^n - \nabla(p_m)^n\right] - \varepsilon(\alpha_t)(\mathbf{u}_m^{n+1})_P\end{aligned} \tag{5.99}$$

by rearrangement of Eq. (5.99) the velocity at time level $n+1$ is found as, so:

$$(\rho_m + \varepsilon\left(\alpha_t\right))(\mathbf{u}_m)^{n+1})_P = (\rho_m\mathbf{u}_m)_P^n + RHS \tag{5.100}$$

with RHS:

$$RHS = \Delta t\left[-\mathbf{A}(\mathbf{u}_m^n) + \mathbf{D}(\mathbf{u}_m^n) + \mathbf{s}_P^n - \nabla(p_m)^n\right] \tag{5.101}$$

and finally the new velocity is obtained:

$$(\rho_m\mathbf{u}_m)_P^{n+1} = \frac{1}{\varepsilon\left(\alpha_t\right)}\left((\rho_m\mathbf{u}_m)_P^n + RHS\right) \tag{5.102}$$

Now it can be seen that when the penalty term $\varepsilon\left(\alpha_t\right)$ is very large, with respect to the terms $(\rho_m\mathbf{u}_m)_P^n + RHS$, the velocity, $\mathbf{u}_m^{n+1}$, reduces to zero:

$$\mathbf{u}_m^{n+1} \approx 0 \tag{5.103}$$

Therefore, the penalty term $\varepsilon\left(\alpha_t\right)$ at maximum value of the solids volume concentration α_{tmax}, needs to be very large. This can be accomplished with a sharply increasing function at maximum volume concentration, α_{tmax}. An example of such a function is of the following form:

$$\varepsilon(\alpha_t) = a_1\left(1 - \frac{\alpha_t}{\alpha_{tmax}}\right)^{-1}\exp\left(\frac{\alpha_t}{\alpha_{tmax}}\right) \tag{5.104}$$

here is a_1 constant and can be tuned so the function behaves accordingly. From Eq. (5.104) it is seen that the value of the penalty is approximately zero if

the volume concentration is smaller than the maximum volume concentration, $\alpha_t < \alpha_{tmax}$. This function increases sharply if the volume concentration $\alpha_t \approx \alpha_{tmax}$. The sediment is effectively "frozen" in a bed as the volume concentration of solids, α_t, approaches the maximum volume concentration, α_{tmax}. The penalty method is employed by Keetels et al. (2007) making solid boundaries using a spectral code. An application creating a sediment bed using the penalty method can be found in Goeree and Rhee (2013). Using this method it is also possible to make solid regions or obstacles in a domain, which is described in more detail in Versteeg and Malalasekera (1995).

5.3.2 Overshoot limiter

The penalty method is simple to implement and a robust method for making solid boundaries or sediment beds. This implies that if the maximum value of solids concentration is reached the mixture velocity reduces to zero, making the sediment, de facto, bed a solid boundary. In some cases, this is not desirable. A sediment bed can still deform at the maximum volume concentration. For instance in the case of a collapsing sediment column or a sliding bed. Another method is introduced here, where the overshoot of the maximum volume concentration is limited. This so-called flux-corrected transport (FCT) algorithm is described by Kuzmin and Gorb (2012). This was done with the Finite Element Method. The method was used in modeling sedimentation of mono-dispersed sediment water mixtures, see Gorb et al. (2013). The FCT limiter is based on the limiter proposed by Boris and Book (1973) and Zalesak (1979). In the original limiter of Zalesak (1979) the upper and lower bound was limited. In the limiter, introduced by Kuzmin and Gorb (2012), the upper bound is limited. This limits the maximum possible value of the volume concentration of solids, α_{tmax}. In this work, the overshoot limiter is used in combination with the Finite Volume Method. Furthermore, the limiter can handle multiple volume fractions or poly-dispersed sediment water mixtures. The overshoot limiter is applied to the transport of a volume fraction. Repeating here the advection-diffusion equation for a volume fraction:

$$\frac{\partial \alpha_k}{\partial t} + \nabla \cdot (\alpha_k \mathbf{u}) = \nabla \cdot \Gamma_t \nabla \alpha_k \tag{5.105}$$

Discretization of Eq. (5.105), in $2D$ on a Cartesian grid, reads:

$$\frac{\alpha_{kP}^{n+1} - \alpha_{kP}^{n}}{\Delta t} \Delta V + F_e^n - F_w^n + F_n^n - F_s^n = 0 \tag{5.106}$$

where F_i for $i = e, w, n, s$ are the fluxes over the east, west, south and north cell-face respectively. Since a TVD scheme is used only overshoots need to be limited. The overshoot is caused by the existence of a drift velocity. A cell can contain the maximum solids concentration and the neighboring cell does not. Therefore, a mass flux can exist over a cell face, causing the maximum value of the volume fraction to overshoot. Here an algorithm is presented which limits the overshoots of the maximum value of the volume concentration, α_t. Here the algorithm described in Kuzmin and Gorb (2012) is summarized in short. A more in-depth discussion can be found in Gorb et al. (2013) and Kuzmin and Gorb (2012). The main idea of this method is to limit the incoming fluxes of concentration, α_t, using a correction factor. This correction factor is determined as such that the volume concentration of solids, α_t, never overshoots the maximum volume concentration α_{tmax}. First the maximum possible incrementation of α_t, per time step, in a CV, with respect to the maximum volume concentration, α_{tmax}, is calculated. Subsequently, the sum of the positive fluxes, of α_t, over the cell faces of the CV is determined. The ratio between the maximum admissible incrementation and the sum of the fluxes is calculated. Finally, the positive fluxes are corrected using this ratio. The algorithm for practical implementation now becomes:

1. Consider a CV at node P, calculate the maximum admissible increment for each time step:

$$Q_P^+ = \frac{(\alpha_{tmax} - \alpha_{tP})}{\Delta t}\Delta V \tag{5.107}$$

   where Q_P^+ is the maximum admissible increment, α_{tP} the volume concentration of solids at CV P and ΔV the volume of the CV.

2. Next calculate the positive incoming flux, P_P^+, over the cell faces:

$$\begin{aligned} P_P^+ = &\max(0, -F_e) + \max(0, F_w) + \\ &\max(0, -F_n) + \max(0, F_s) \end{aligned} \tag{5.108}$$

   where $F_{e,w,n,s}$ is the flux of α_t over the east, west, north and south cell face respectively.

3. Then calculate the correction factor, R_P^+, for each CV's, at cell center P:

$$R_P^+ = \min\left(1, \frac{Q_p^+}{P_P^+}\right) \tag{5.109}$$

4. Finally determine the sign of the unconstrained flux, i.e. without the correction, and calculate the correct cell face flux limiter. The east cell face flux limiter, C_e, becomes:

$$C_e = \begin{cases} R_E^+, & \text{if } F_e \geq 0 \\ R_P^+, & \text{if } F_e < 0 \end{cases} \tag{5.110}$$

where R_E^+ and R_P^+ are the correction factors at the east and center CV respectively. Similarly, the west, north, south, are determined. The west cell face limiter, C_w, is given as:

$$C_w = \begin{cases} R_W^+, & \text{if } F_w \geq 0 \\ R_P^+, & \text{if } F_w < 0 \end{cases} \tag{5.111}$$

north limiter, C_n:

$$C_n = \begin{cases} R_N^+, & \text{if } F_n \geq 0 \\ R_P^+, & \text{if } F_n < 0 \end{cases} \tag{5.112}$$

and south limiter, C_s:

$$C_s = \begin{cases} R_S^+, & \text{if } F_s \geq 0 \\ R_P^+, & \text{if } F_s < 0 \end{cases} \tag{5.113}$$

5. Finally apply the limiters and calculate the new value of the volume concentration for each fraction,

$$\alpha_k^{n+1} = \alpha_k^n - \frac{\Delta t}{\Delta V}\left(C_e F_e^n - C_w F_w^n + C_n F_n^n - C_s F_s^n\right) \tag{5.114}$$

This overshoot limiter only requires a single post processing step and is hence computationally efficient. The functioning of this overshoot limiter will be demonstrated in various benchmark problems described in the upcoming sections.

Chapter 6

Numerical results

In this chapter, every part of the numerical model is validated separately. This is done by using benchmarks known from literature. The benchmarks consist of both experimental and numerical data. The model is tested with increasing level of complexity. The complexity increases from a single phase (turbulent) flow to a particle-laden flow in an open channel. Appendix E, Table E.1 presents a complete overview of the tested models, in this chapter.

First single phase flows, both laminar and turbulent, are compared. Furthermore, a Bingham liquid is validated with an analytical solution. The Bingham model forms the basis of the dense granular flow model described in Chapter 7.

In subsequent sections of this chapter, the model is validated for flows with varying density. A flow with a varying density is not strictly a multiphase flow however, this is an analogy of a multiphase flow. An example of an varying density flow experiment is the lock-exchange experiment. In this experiment, a liquid with two different densities is separated by a lock-gate. When the lock-gate is removed, the liquid starts to flow under the action of gravity, due to the difference in density.

The hindered settling implementation is validated with data from settling experiments, see Klerk et al. (1998). The effect of several methods for determining the Richardson and Zaki index, n, is investigated. Furthermore, explicit methods, for determining the terminal settling velocity of a single particle,

have been varied. This gives an insight of the effect, using these methods on the outcome of the numerical model, when compared to the experimental results.

Finally, the numerical model is validated with open channel flow experiments. In this section all the parts of the numerical model, tested separately in previous sections, (except for the Bingham part), are compared. Both concentration and velocity profiles are validated with experimental data reported in literature.

6.1 Validation of single phase flows

The discretized Navier-Stokes equations and the flow solver, see Eq. (5.46), are validated with benchmarks known from the literature. The data from Ghia et al. (1982), for the lid-driven cavity, are commonly used benchmark validating numerical codes. These data are compared with computational results in Section 6.1.1. Another test case is the flow around a cylinder, simulating a so-called von Karmann vortex street. The frequency of the vortex shedding depends on the Reynolds number and is determined with the dimensionless number called the Strouhal number, S_r. The numerical calculation is validated using this test case, see Section 6.1.2.

Furthermore, a Bingham plug flow benchmark, Poiseuille flow of a Bingham fluid, is performed in Section 6.1.3. Here the influence of the grid resolution and a regularization parameter is assessed on the outcome of the numerical results. Finally, numerical results of the turbulence model are compared with experimental data found in the literature. This has been done for a turbulent flow between parallel plates, Section 6.2 and an impinging jet, of a turbulent slot jet, Section 6.3.

6.1.1 Lid-driven cavity

A classic benchmark in computational fluid dynamics is the lid driven cavity problem. This is a $2D$ numerical viscous flow simulation and consists of a square cavity filled with a fluid. The height and length of the domain is equal to $L = H = 1\,[m]$. At the top of the domain, a lid is placed which drives the flow. The velocity of the lid in x-direction is set to $u = 1\,[m/s]$. The velocity of lid in y-direction is set to $v = 0\,[m/s]$. The velocities in x and y direction, u and v on all other boundaries are equal to $0\,[m/s]$. Furthermore zero gradient pressure boundaries are imposed at all the walls.

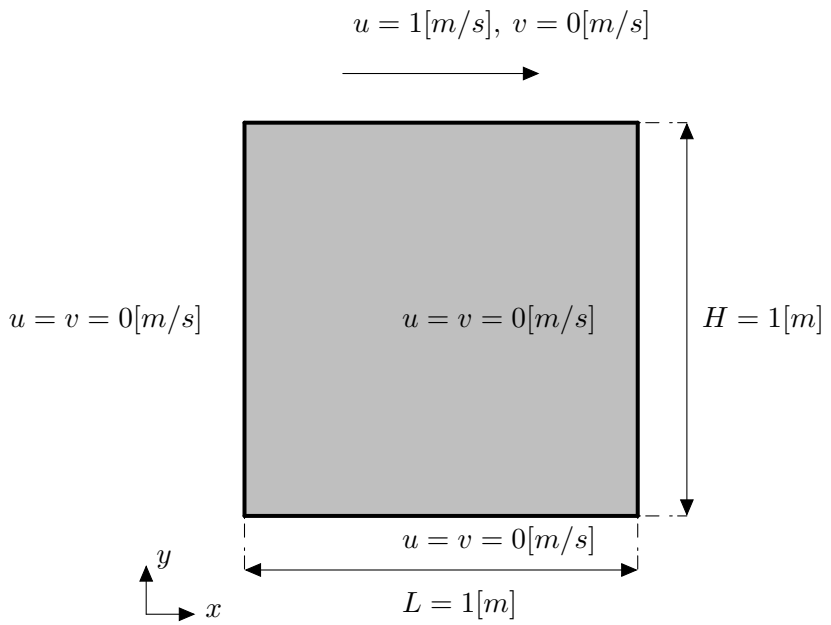

Figure 6.1: Boundary conditions for the lid driven cavity case. The boundary conditions are used for the $Re = 100$, $Re = 400$ and $Re = 1000$ cases. Zero gradient pressure boundaries are imposed over the whole domain.

Three different Reynolds numbers are used viz. $Re = 100, 400, 1000$. The different Reynolds numbers are calculated by varying the viscosity of the fluid, μ, accordingly. An equidistant grid with $n_x \times n_y = 129 \times 129$ subdivisions is used. In Figure 6.2 the results from Ghia et al. (1982) and the present results are compared. The solid lines are the present numerical simulation and the circles are the data from Ghia et al. (1982). The subplots b, e and h of Figure 6.2 show the velocities through the centerline in x-direction, u_c at $Re = 100, 400, 1000$ respectively. Subplots c, f and i of Figure 6.2 show the results over centerline velocity in y-direction, v_c at $Re = 100, 400, 1000$ respectively.

Subplots a, d and g show streamlines at $Re = 100, 400, 1000$ respectively. The center of the rotation moves to the center of the cavity as the Reynolds number is increased. Moreover, the secondary vortices in the lower left and right corners, shown in the streamline plots, increase in size. The present results

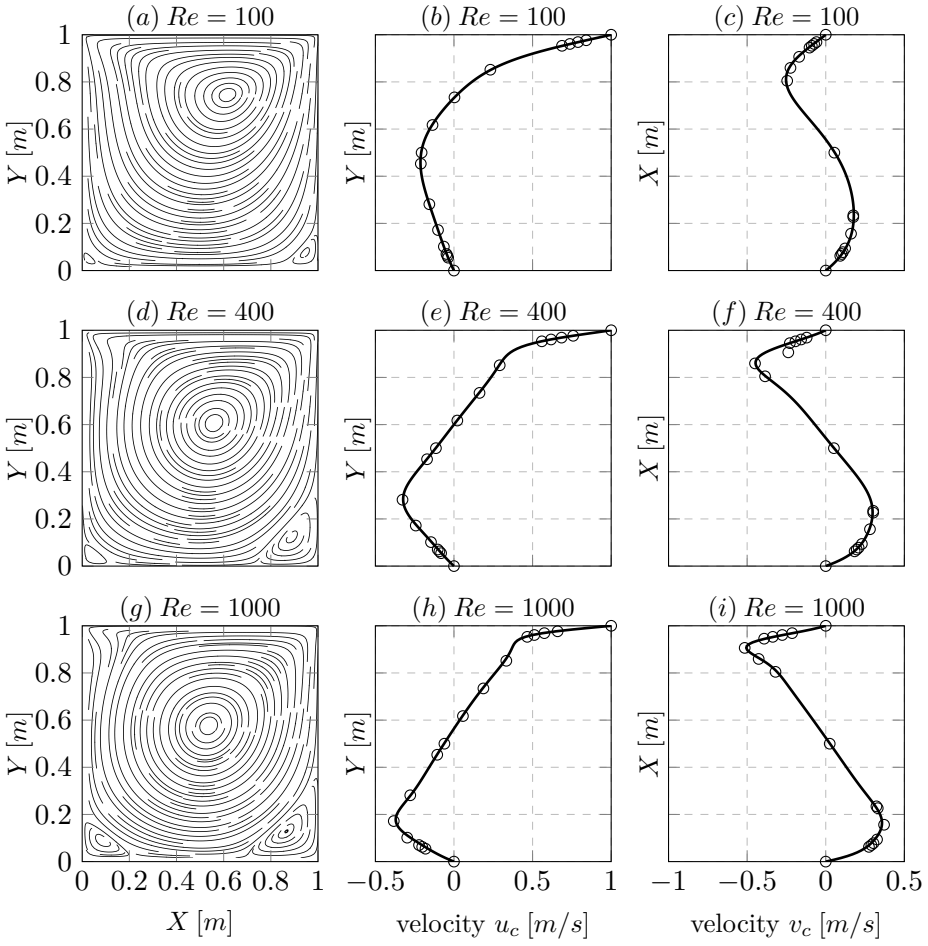

Figure 6.2: Streamline plots, (subplot (a), (d), (g)) and comparison of u-velocity, (subplot (b), (e), (h)), and v-velocity, (subplot (c), (f), (i)) along horizontal lines through geometric center. The symbol $\circ$ represents the results from Ghia et al. (1982) and the solid lines are the present results. Three Reynolds numbers are considered, $Re = 100, 400, 1000$. In subplot $(a), (b), (c)$ results for $Re = 100$ are given, in subplot $(d), (e), (f)$ results for $Re = 400$ are given and in $(g), (h), (i)$ results for $Re = 1000$ are plotted.

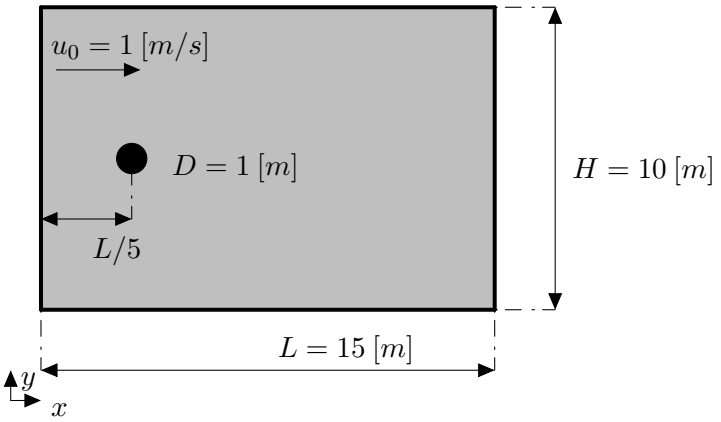

Figure 6.3: Sketch of the geometry of the flow around a cylinder with a Reynolds number of $Re = 150$.

compare well with the data from Ghia et al. (1982) for all three Reynolds numbers.

6.1.2 Flow around a cylinder

The flow around a cylinder is a well known case from both experimental as numerical work. Here laminar flow is investigated. Experimental observations show different flow patterns for this case. The flow pattern depends on the Reynolds number. At a Reynolds number of about $Re \approx 40$ a so-called Strouhal instability occurs. Vortices's appear and are shaken off alternatively away from the cylinder at a constant frequency. The flow is considered $2D$ and a Reynolds number of $Re = 150$ is chosen. The Strouhal number is given by the following expression:

$$S_r = \frac{fD}{u_0} \tag{6.1}$$

where S_r is the Strouhal number, u_0 the upstream fluid velocity, f the vortex shedding frequency and D the diameter of the cylinder. The Strouhal number depends on the Reynolds number and can be calculated directly with the following empirical formulation, see Roshko (1954) or Tritton (1959),

$$S_r = \frac{fD}{u_0} = 0.212 - \frac{4.5}{Re} \tag{6.2}$$

The Strouhal number from Eq. (6.2) is compared with a 2 dimensional numerical calculation. The following boundary conditions are used. The velocity, $u_0 = 1\,[m/s]$, is imposed at the in- and outlet boundary and at the top and bottom free-slip boundaries are used. Neumann boundaries are used for the pressure. The Reynolds number in the computation is $Re = 150$. The contour of the cylinder is made using the Immersed Boundary Method (IBM), see Section 5.2.3. The computational domain has a length $L = 15\,[m]$ and a height $H = 10\,[m]$ and the diameter of the cylinder is $D = H/10\,[m]$ and is placed at $x_0 = L/5\,[m]$ from the inlet at $y_0 = H/2:\ [m]$. The computational domain is subdivided in $n_x \times ny = 129 \times 385$ grid cells. Figure 6.3 shows the imposed boundary conditions.

The Strouhal number resulting from the numerical calculation is $S_r = 0.2$ from the calculation and obtained by Eq. (6.2) is $S_r = 0.182$. The number from the calculation is slightly overestimated. However, the agreement of the Strouhal number, from the calculation, with the experimental determined Strouhal number is satisfactory. Figure 6.4 shows streamline plots at the time instances $t = 39\,[s]$, $t = 43\,[s]$ and $t = 47\,[s]$.

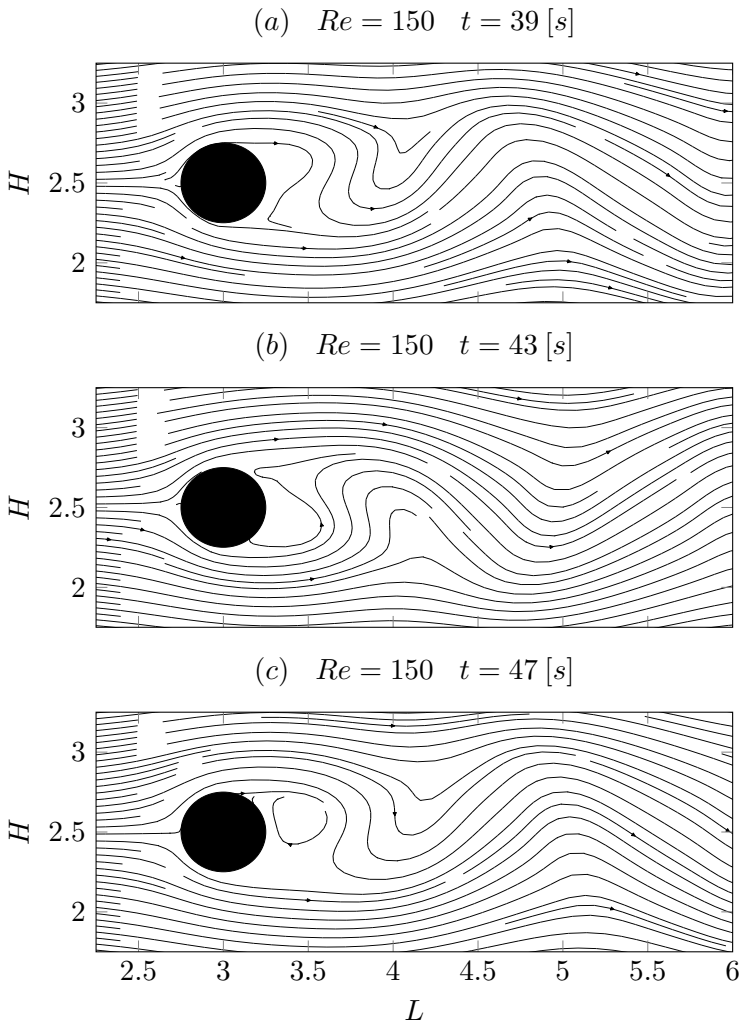

Figure 6.4: Vortex shedding at $Re = 150$. Stream line graphs of the velocity are plotted at time $t = 39\,[s]$, subplot (a), $t = 43\,[s]$, subplot (b) and $t = 47\,[s]$, subplot (c).

6.1.3 Poiseuille flow of a Bingham fluid

The Bingham model is validated with an analytical steady-state solution of the Navier-Stokes equations. This is a Poiseuille, or pressure driven, flow and yields a velocity profile. The analytical solution of the Poiseuille flow for a Bingham fluid depends on the pressure gradient, viscosity, μ, and the height of the domain, H. Introducing the analytical solution for a Bingham material of a pressure driven flow, see Prager (1989):

$$u(y) = \frac{1}{2\mu}\frac{\partial p}{\partial x}\left(y(H-y) - 2\tau_0\left(\frac{\partial p}{\partial x}\right)^{-1} y\right) \tag{6.3}$$

in which H is the height of the domain, $\partial p/\partial x$ the pressure gradient and τ_0 the yield stress. Now Eq. (6.3) is valid for $0 \leq y \leq y_1$, with y_1:

$$y_1 = \frac{H}{2} - \tau_0\left(\frac{\partial p}{\partial x}\right)^{-1} \tag{6.4}$$

from Eq. (6.3) it is seen that the velocity at $y = 0$ is 0, so $u(y = 0) = 0$. At a certain value of y at $y = y_1$, the shear stress drops below the yield stress τ_0. In this case the material acts as a solid and the solid region is characterized by a plug. Now, the velocity of this plug is obtained by substitution of Eq. (6.4) in Eq. (6.3):

$$U = u(y_1) = \frac{1}{2\mu}\frac{\partial p}{\partial x}\, y_1^2 \tag{6.5}$$

the solid region, or plug, extends to $y = H - y_1$ exceeding the yield stress and the material is in a liquid state. The velocity at the boundary $y = H$ is $u(y = H) = 0$. This is a 2D calculation performed on 3 three grid resolutions, $n_x \times n_z = 21 \times 63$, $n_x \times n_z = 33 \times 99$ and $n_x \times n_z = 45 \times 139$. The parameters used in the calculation are presented in Table 6.1 and are carefully chosen. The parameters are chosen as such that the physical phenomena, characteristic for a Bingham liquid, show up nicely. In the presented case both a yielded region and an unyielded region can be distinguished. Moreover these regions are distributed, approximately, equally over the height, H, of the domain. However, the yield stress, τ_0, can be chosen differently. If the yield stress is chosen too high no flow would occur. On the other hand if yield stress is chosen too low, the non-yielded region would not show up. Figure 6.6 (a) shows the numerical and analytical results of a pressure-driven plug flow. Figure 6.6 (b) shows the

difference between the numerical results of various grid resolutions and the analytical solution. It can be seen that the difference between the analytical and numerical solution decreases as the resolution increases. Moreover, the legend of Figure 6.6 (b) shows the L_2 norm. The L_2 norm is defined as, see Roy (2003):

$$L_2 = \left(\frac{1}{N} \sum_{i=1}^{N} (u_{i,ana} - u_{i,num})^2 \right)^{1/2} \tag{6.6}$$

where the velocities $u_{i,ana}$ and $u_{i,num}$ are the analytical solution and numerical velocity profiles respectively. The difference between the analytical and numerical solution, $u_{i,ana} - u_{i,num}$, is summed over the number of points N (with the number of points $N = 21, 33, 45$).

Table 6.1: Parameters of numerical and analytical calculation, see Eq. (6.3)

Parameter	Value	Description	unit
μ	0.1	viscosity	$[Pas]$
$\partial p/\partial x$	-1.0	pressure gradient	$[Pa/m]$
τ_0	0.2	yield stress	$[Pa]$

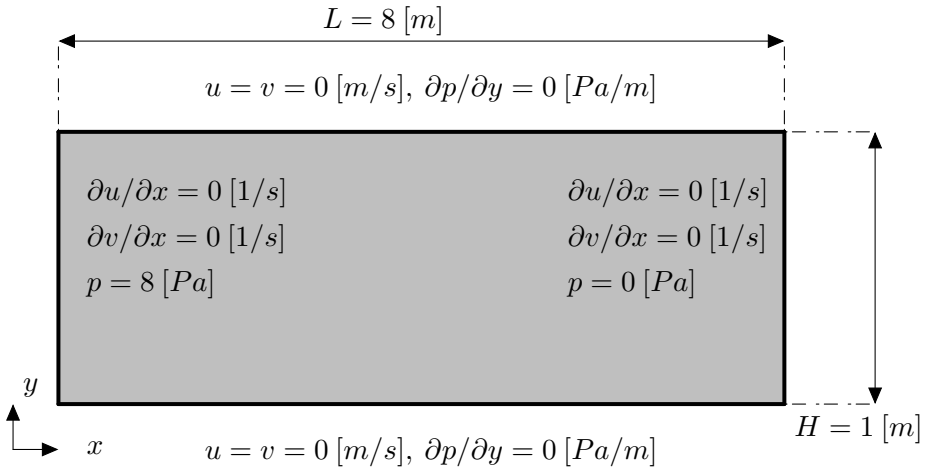

Figure 6.5: Boundary conditions of the $2D$ Poiseuille flow of a Bingham fluid.

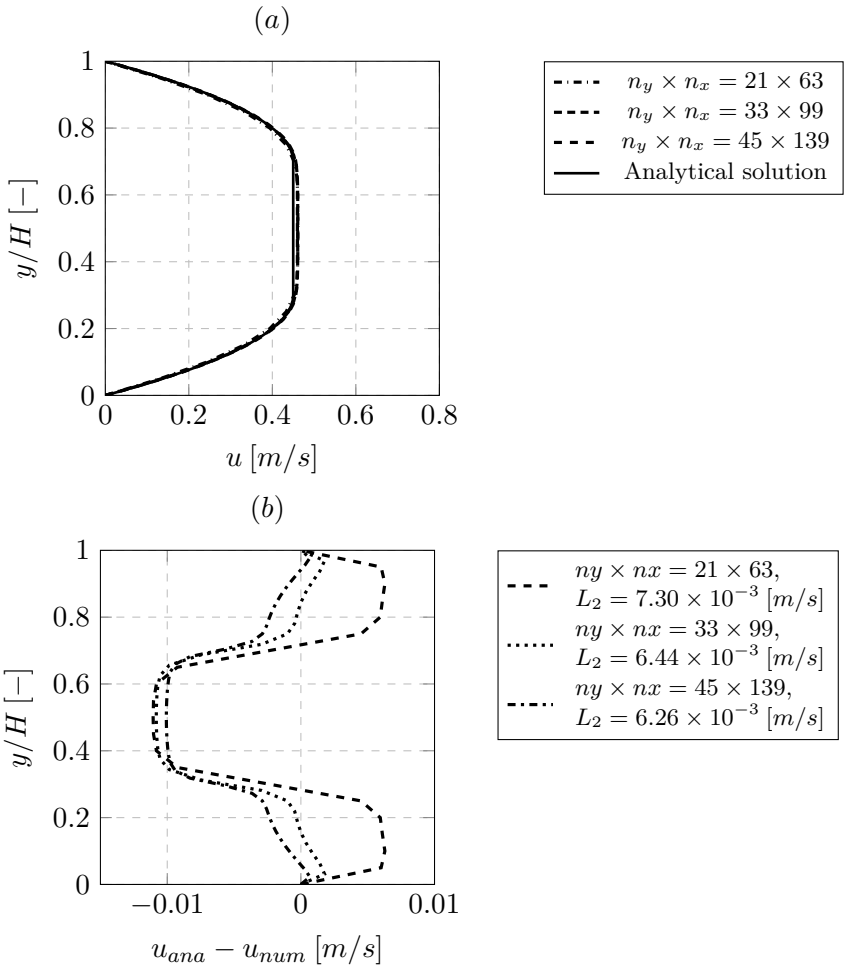

Figure 6.6: Plot (a), shows the numerical and analytical results of a pressure driven plug flow. Here 3 increasing grid resolutions were used, the parameter is $m = 50$. Plot (b) shows the difference between the analytical and numerical solution for the 3 grids. In the legend the L_2 norm is given for each grid resolution.

Figure 6.7 (a) compares the results of a plug flow of a Bingham material between the analytical and the numerical solution. The numerical solution agrees well with the analytical solution for all three of the grid resolutions.

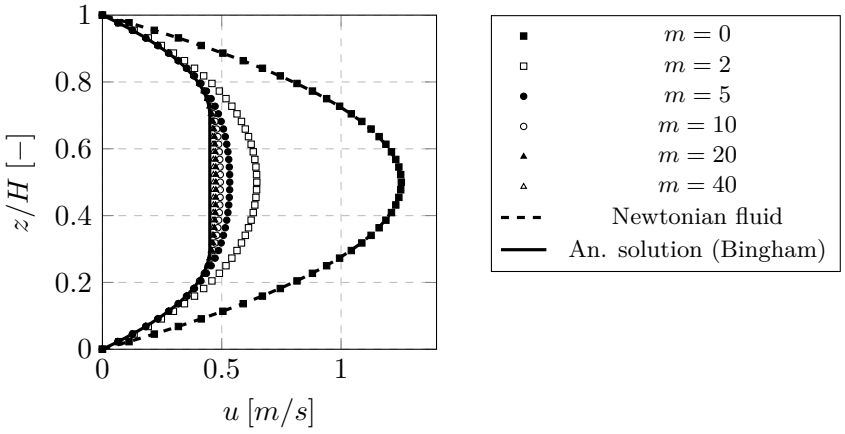

Figure 6.7: Velocity profiles for different values of parameter m. The parameters used in this calculation are tabulated in Table 6.1.

However, the numerical solution is slightly larger than the analytical solution for the three resolutions used here. This difference can be attributed to the influence of the regularization parameter m, which controls the degree of plasticity. In this calculation, a value of $m = 50$ is used. If the parameter $m = 0$, then the flow is perfectly Newtonian. The influence of the parameter m on the fluid behavior is discussed in more detail in Papanastasiou (1987).

6.2 Turbulent Flow Between Parallel Plates

The WALE LES turbulence model is compared with data from a Direct Numerical Simulation (DNS) Moser et al. (1999). This was done for a flow between two parallel plates. Moser et al. (1999) investigated turbulent flows at three different friction Reynolds numbers, namely at $Re_\tau = 180$, $Re_\tau = 360$ and $Re_\tau = 590$. Here the $Re_\tau = 590$ case is used as a benchmark. The friction Reynolds number, $Re_\tau = 590$, corresponds with a Reynolds number of $Re \approx 11000$ Küng (2007). The Re_τ number is defined as follows:

$$Re_\tau = \frac{u_\tau h_c}{\nu} \tag{6.7}$$

in which h_c is the half height of the channel and u_τ is the friction velocity. The kinematic viscosity ν is given by:

$$\nu = \frac{\mu_f}{\rho_f} \tag{6.8}$$

with ρ_f the density of the fluid and μ_f the viscosity of the fluid. The Reynolds number, based on the mean flow at half the height, reads:

$$Re = \frac{U h_c}{\nu} \tag{6.9}$$

where U is the mean flow velocity, which is obtained by volume averaging:

$$U = \frac{1}{V} \int_V u(x, y, z)\, dV \tag{6.10}$$

with V being the volume of the computational domain.

6.2.1 Numerical setup

Figure 6.8 shows the computational geometry and boundary conditions used in the numerical calculation. Here the length, depth and height is chosen respectively, $L = 2\pi h_c$, $D = \pi h_c$ and $H = 2h_c$. The top and bottom walls are located at $z = 2h_c$ and $z = 0$. The center of the flow is at $z = h_c$. The LES calculation was performed with a resolution of $n_x \times n_y \times nz = 99 \times 57 \times 67$ with a time step size of $\Delta t = 5 \times 10^{-5}$ $[s]$. This time step size is sufficiently small in order to conserve the Courant-Friedrichs-Lewy (CFL) condition:

$$C_c = \frac{U \Delta t}{\Delta x} \leq C_{cmax} \tag{6.11}$$

in which $C_{max} = 1$. At the in- and outlet of the domain, periodic boundaries are imposed. Wall functions are used at the top and the bottom walls. This wall function reads:

$$\frac{u}{u_\tau} = 2.5 \ln \frac{z_p\, u_\tau}{\nu} + 5.5 \tag{6.12}$$

where u_τ is the friction velocity and z_p is the distance from the first interior grid point to the wall, at $z = 0$ and $z = H$. Free-slip boundary conditions are imposed at the sidewalls of the domain. In Figure 6.8 a schematic sketch is given of the computational domain. A body force is imposed, by means of a feedback control system, to obtain the required bulk velocity. The feedback control system ensures a constant Reynolds number.

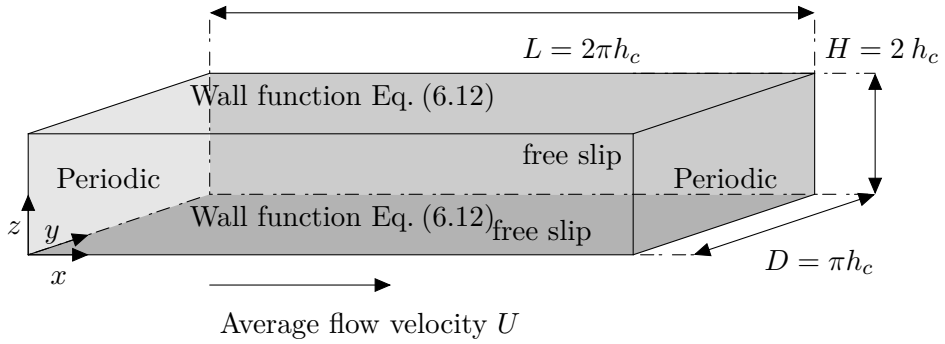

Figure 6.8: Sketch of the computational geometry and the boundary conditions used.

Validation numerical results

The LES model is validated with the DNS calculations using statistical averages calculated from the flow field. The flow is fully developed, or turbulent, within a distance of approximately 40 times the flow height, $2h_c$, or $80h_c$. The time required for a fully turbulent flow is $t = 80h_c/U$. The results of the calculation are validated with the time and spatially averaged velocity in the x-direction, U.

6.2.2 Results

In Figure 6.9 (a), Figure 6.11 (a) and Figure 6.13 (a) the time averaged velocity profiles of the u-velocity are shown for increasing grid resolutions. The velocity profile is plotted for the half height, h_c, of the channel. The computational results of the LES WALE turbulence calculation are represented with the symbol, $(\circ)$, and the continuous line, $(-)$, are the DNS data from Moser et al. (1999). On the horizontal axis the u-velocity is normalized with the horizontal velocity, u_c, at channel center, h_c. On the vertical axis, z, is normalized with the channel height, h_c. For the coarsest calculation the velocity profile is slightly overestimated, see Figure 6.9. However, for higher resolutions the agreement of the velocity profile with the DNS data is increasingly better, see Figure 6.11 (a) and Figure 6.13 (a). The solution of the calculation converges to the solution of the DNS calculation.
In Figure 6.9 (b), Figure 6.11 (b) and Figure 6.13 (b) the dimensionless velocity

u^+ is given as a function of the wall coordinate y^+. The continuous line, $(-)$, represents the DNS data and the results from the LES calculation is given by the symbol $(\circ)$.
The influence of the grid resolution on the unresolved eddies can be seen from the RMS values of the velocity fluctuations. Less eddies are resolved using coarser grids, so the RMS values, i.e. less fluctuations, are lower. The RMS values for u, v and w velocities are plotted in Figure 6.10 $(a), (b), (c)$, Figure 6.12 $(a), (b), (c)$ and Figure 6.14 $(a), (b), (c)$. In these figures, the RMS values, plotted on the vertical axis, are normalized with the friction velocity. The horizontal axis z is normalized with the height at the channel center, h_c. The results from the DNS calculation are plotted with the continuous line $(-)$. The RMS values of the LES calculation are given by the dashed,$(- -)$, line. The agreement of the RMS values of the velocity with the values from the DNS calculation increases with an increasing grid resolution.

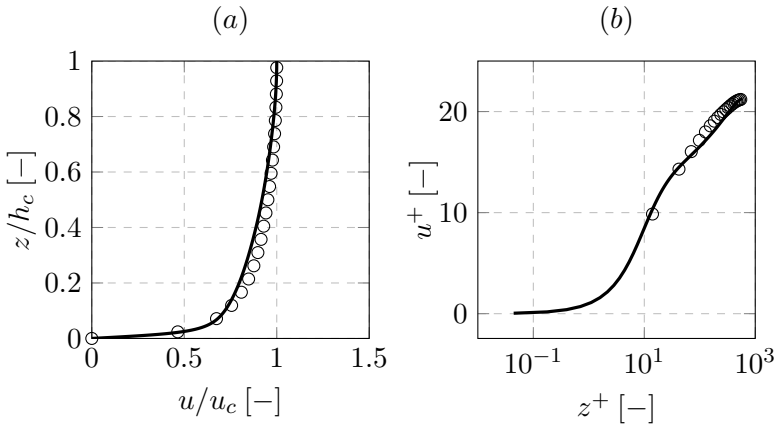

Figure 6.9: Velocity profiles given here with resolution of $n_x \times n_y \times n_z = 67 \times 33 \times 43$. The continous line, (−), are the DNS data from Moser et al. (1999) at $Re_\tau = 590$ and the open dots, (∘), are the results from the LES calculation.

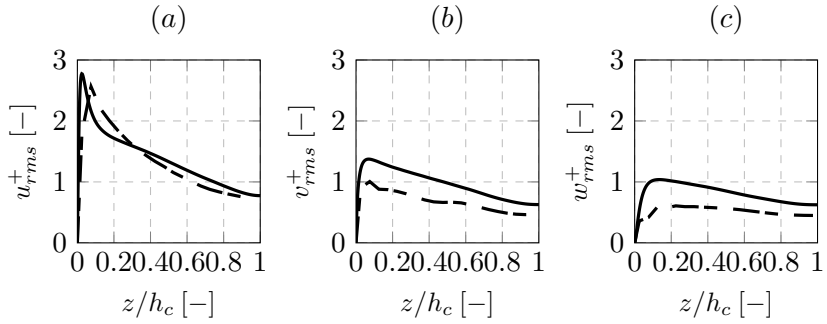

Figure 6.10: Values of RMS for u, v and w velocity with resolution of $n_x \times n_y \times n_z = 67 \times 33 \times 43$. The dashed line, (−−), are the LES results and the continuous line, (−), are the DNS data from Moser et al. (1999) with $Re_\tau = 590$.

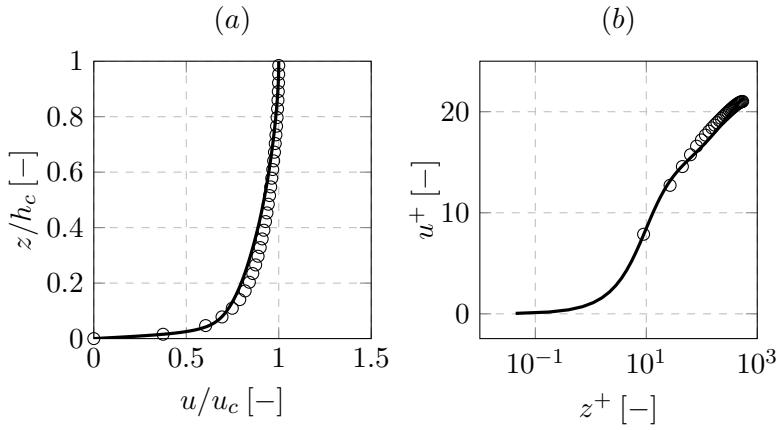

Figure 6.11: Velocity profiles given here with resolution of $n_x \times n_y \times n_z = 99 \times 57 \times 67$. The solid line, $(-)$, are the DNS data from Moser et al. (1999) at $Re_\tau = 590$ and the open dots, $(\circ)$, are the results from the LES calculation.

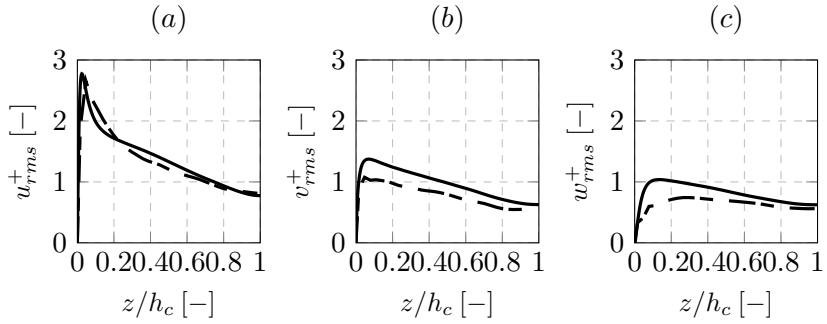

Figure 6.12: Values of RMS for u, v and w velocity with resolution of $n_x \times n_y \times n_z = 99 \times 57 \times 67$. The dashed line, $(--)$, are the LES results and the solid line, $(-)$, are the DNS data from Moser et al. (1999) with $Re_\tau = 590$.

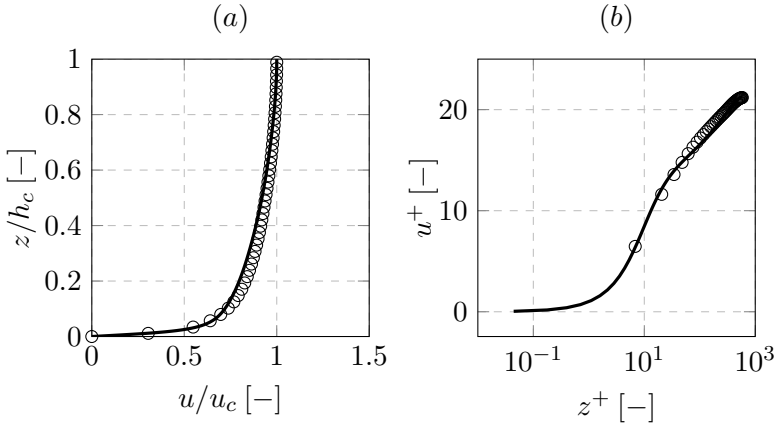

Figure 6.13: Velocity profiles given here with resolution of $n_x \times n_y \times n_z = 129 \times 67 \times 87$. The solid line, $(-)$, are the DNS data from Moser et al. (1999) at $Re_\tau = 590$ and the open dots, $(\circ)$, are the results from the LES calculation.

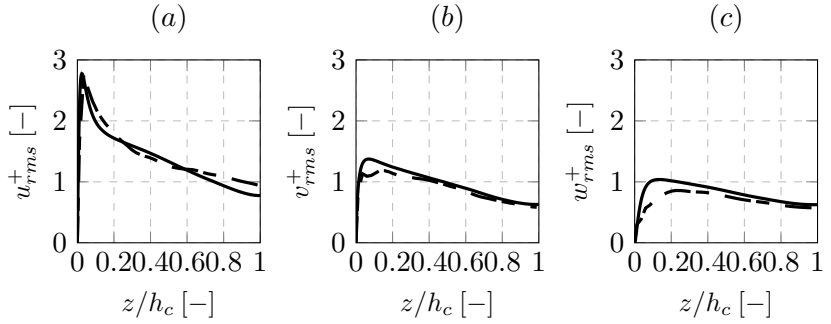

Figure 6.14: Values of RMS for u, v and w velocity with resolution of $n_x \times n_y \times n_z = 129 \times 67 \times 87$. The dashed line, $(--)$, are the LES results and the continuous line, $(-)$, are the DNS data from Moser et al. (1999) with $Re_\tau = 590$.

6.3 Plane impinging slot jet

Here a calculation is described for a plane impinging jet slot. This case is well defined and several experimental tests can be found in literature, see for instance Maurel and Solliec (2001). In this experiment, air has impinged onto a flat plate. The plane jet nozzle could be placed at several standoff distances from the plate. The nozzle width was varied in the experiments.
Several numerical investigations of a turbulent plane impinging jet, using LES turbulence modeling approach, have been performed by Hoffmann and Benocci (1994), Voke and Gao (1995), Cziesla et al. (2001) or Beaubert and Viazzo (2002). In the last paper computational results were actually compared with experimental data. In this section, a plane impinging jet is simulated and the results are compared with experimental data reported by Maurel and Solliec (2001).

6.3.1 Computational setup

Here a calculation is performed of a jet with a Reynolds number with respect to the jet width nozzle, B, of $Re = 13500$. Here the width of the nozzle is fixed to a value of $B = 1$. The rectangular computational domain has a dimension of $H \times L \times D$, see Figure 6.15. The length, L, is $L = 12\,B$ and is approximately of the same size as reported in Cziesla et al. (2001). The width D is set equal to $D = 6\,B$ and the height is fixed to $H = 10\,B$. These dimensions are in accordance with the dimensions in the simulation of Beaubert and Viazzo (2002). The number of subdivisions in the x, y and z-direction is respectively $n_x \times n_y \times n_z = 145 \times 53 \times 83$. The time step size $\Delta t = 0.001\,[s]$ and is sufficiently small to prevent numerical instabilities. Here the explicit solver, discussed in Section 5.2.2, has been used.
At the top and bottom of the domain, wall functions are imposed and at the front and the back of the domain zero Neumann boundaries are imposed for the velocity. At the outflow, the wall velocities in the tangential direction are set to zero. The wall-normal velocity is directed in the outward direction of the wall. Neumann boundaries for the pressure were used at the top, bottom, front and back wall of the domain.

At the top inflow, a constant block velocity, w_0, is imposed, see Figure 6.15, which is in accordance with the imposed velocity used in the calculations of Beaubert and Viazzo (2002). This imposed velocity deviates from the experiments of Maurel and Solliec (2001), where the velocity at the inflow is

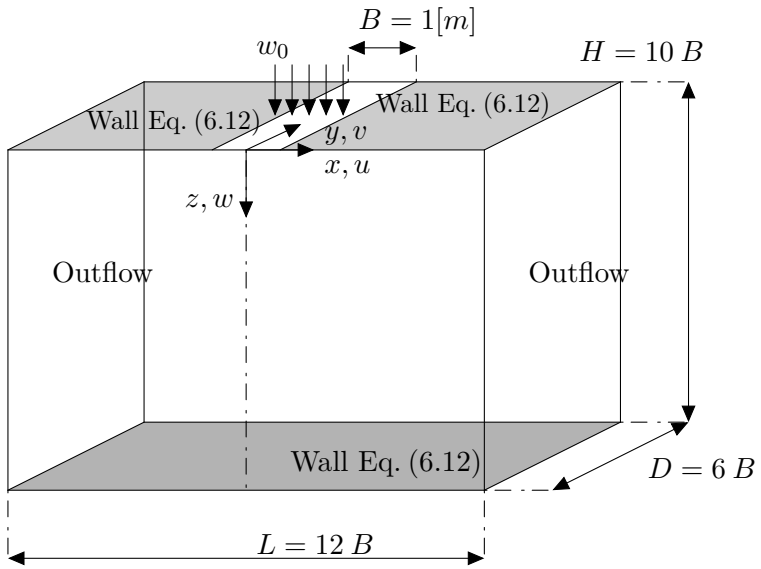

Figure 6.15: Sketch of the numerical domain with initial conditions, boundary conditions and dimensions used in the calculations.

expected to be turbulent. The inflow boundary condition, in the calculations, can be made turbulent, using a separate calculation of a flow in a rectangular duct and periodic boundary conditions. Subsequently, the complete turbulent velocity field is calculated and imposed as an inflow boundary condition. However, doing this complicates the calculation considerably and is, therefore, not performed in this relatively small-scale benchmark problem, shown. The same boundary and initial conditions are used, as described by Beaubert and Viazzo (2002), in their calculations. The numerical calculation of the $Re = 13500$ case is described in more detail, where Beaubert and Viazzo (2002) reported partial results of the $Re = 13500$ case.

In Table 6.2 an overview is given of the parameters used. Note that the fluid viscosity, μ_f, in the calculations, is varied in order to achieve the corresponding Reynolds number, in this case, $Re = 13500$.

Table 6.2: Parameters used, in the numerical calculation for the plane impinging jet.

	No. grid points	Δt	density ρ	viscosity μ_f	Re	w_0
unit	[-]	$[s]$	$[kg/m^3]$	[Pas]	$[-]$	$[m/s]$
	$145 \times 53 \times 83$	0.001	1000	0.0741	13500	1

6.3.2 Computational results

The computational results are discussed in this subsection. The flow quantities from the calculation are averaged in both time and space. The spatial averaging is done in the y-direction for all the grid points. The averaging in time is done for 10.000 steps.

In Figure 6.16 the centerline, z/B, mean vertical velocity, w/w_0, is shown. The vertical flow velocity is maintained at the inflow flow velocity, $w/w_0 = 1$, up to a distance of, $z/B = 4$. This is the so-called potential core. The length of the potential core is predicted well by the numerical model. The zone with a distance of $z/B \approx 4$ up to $z/B \approx 8$ is called the transition zone. The so-called impinging zone the ranges from $z/B \approx 8$ up to $z/B = 10$. In this

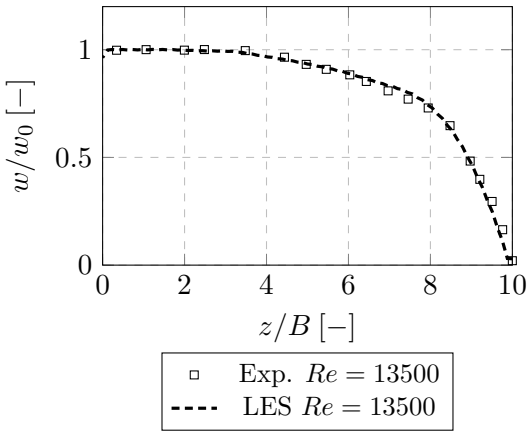

Figure 6.16: Mean vertical velocity along the jet axis, experiment, □ , of Maurel and Solliec (2001)

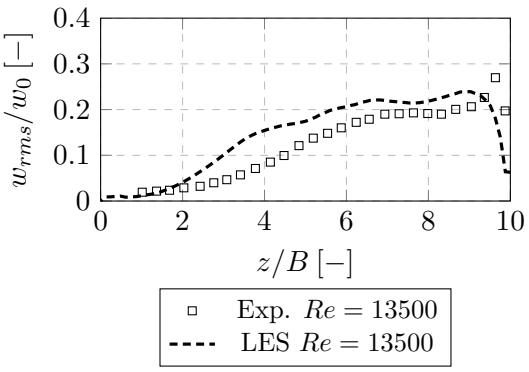

Figure 6.17: Root Mean Square values along jet axis, experiment, □ , of Maurel and Solliec (2001)

zone, the mean velocity along the jet axis goes to zero. The model prediction of the velocity in z-direction at the center line, is good in comparison with the experimental results.

In Figure 6.17 the RMS profiles of the vertical velocity are shown along the jet-axis for both experiments and the results from the LES calculation. At the impinging zone, an increase can be seen in both the experiment and the calculation. The RMS values of the calculation are higher in comparison with the values of the experiments. Except close to the wall at $z/B \approx 10$. Here the RMS values are under-predicted. This is due to the unresolved fluctuations. An improvement can be achieved by increasing the grid resolution. The discrepancy between in RMS values in the potential core and transition zone is probably due to the difference in the shape of the mean inflow velocity profile, see Beaubert and Viazzo (2001).

Figure 6.18 shows the distribution of the normalized axial velocity w/w_c along x/b_w at three heights, namely $z = 6\,B, 5\,B, 4\,B$. Here w_c is the velocity at the jet axis. The variable b_w is the half width of the jet. This is the distance from the jet axis at which the axial velocity is half of the velocity at the jet axis. The axial velocity profile compares quite well with the experimental results obtained by Namer and Ötügen (1988). Figure 6.19 shows the RMS values uw_{rms}/w_0^2 along x/B at $z = 5\,B$. The computational RMS values are in the same order of magnitude in comparison of the experimental results.

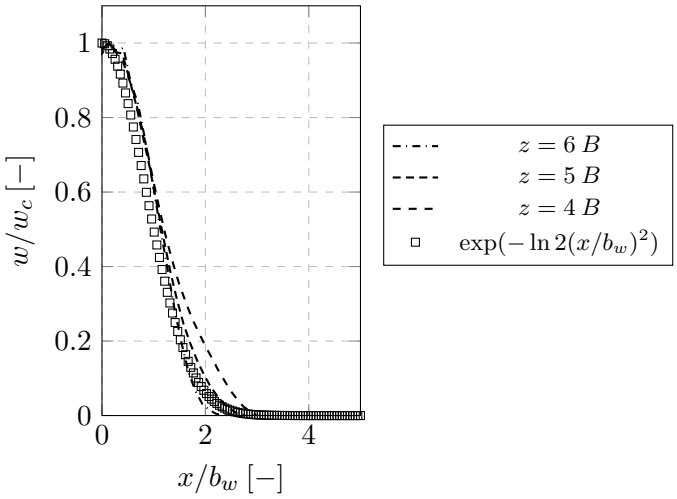

Figure 6.18: Normalized axial velocity distribution plotted at heights $H = 6\,B, 5\,B$ and $H = 4\,B$. The experimental results originate from Namer and Ötügen (1988).

The evolution of the jet in time is given in Figure 6.20 $(a) - (d)$ at time $t = 15, 30, 60$ and $120\,[s]$. At $15\,[s]$ the jet is developing, at $t = 30\,[s]$ the jet impinges onto bottom wall. From $t = 60\,[s]$ up to $t = 120\,[s]$ the jet is fully developed.

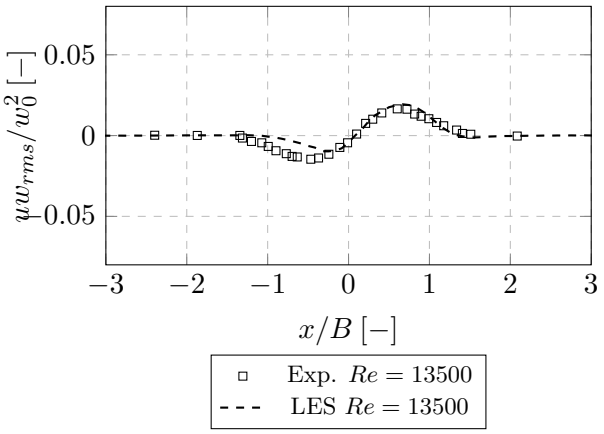

Figure 6.19: RMS values, uw_{rms}/w_0^2, at $H = 5\,B$. The experimental results are taken from Maurel and Solliec (2001).

(a) time $t = 15$ $[s]$

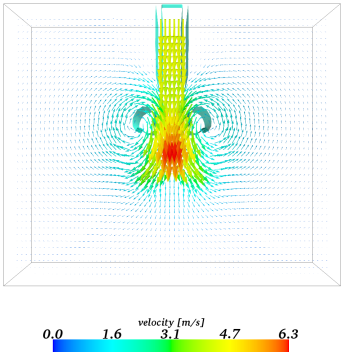

(b) time $t = 30$ $[s]$

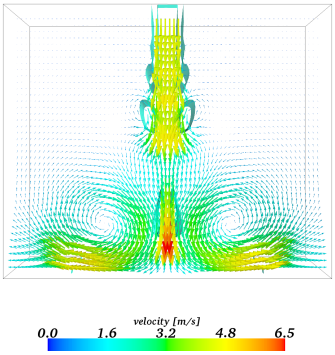

(c) time $t = 60$ $[s]$

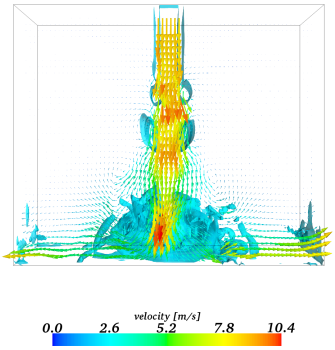

(d) time $t = 120$ $[s]$

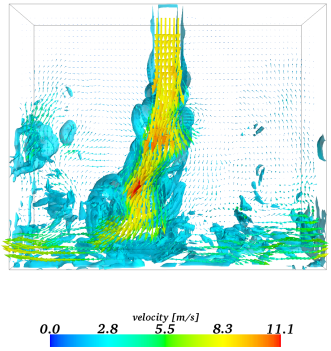

Figure 6.20: Snapshots of the evolution of the jet at various time intervals.

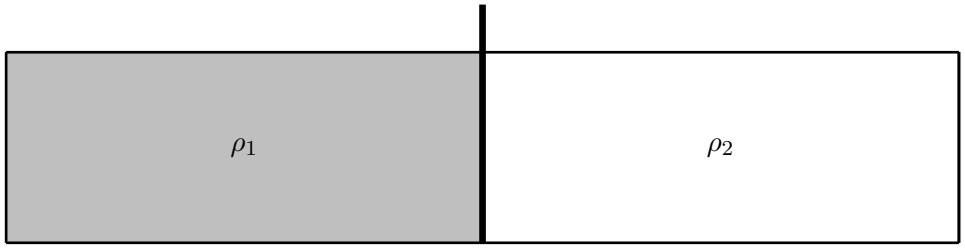

Figure 6.21: Schematic sketch of the setup for the lock-exchange experiment. The variables ρ_1 and ρ_2 denote the density. Here is $\rho_1 > \rho_2$.

6.4 Gravity currents

In a two-density fluid system, fluid starts to flow caused by the density differences and the action of gravity. These fluid flows are called gravity-driven flows, or gravity currents. An example of gravity-driven flow is a system in which salt is dissolved and the existence of a density gradient due to the salinity difference. Another example is the flow of sediment-laden systems. Due to the presence of sediment, a density difference exists causing motion of the fluid. A well-known experiment for investigation of this motion is the lock exchange experiment. In this experiment fluids of different densities are separated by a barrier or lock gate in a tank. At a certain point in time, the lock-gate is removed and the fluid starts to move. In the experiment, two fronts occur, where the front of the lighter fluid is running at the top of the tank in one direction. The front of the denser fluid is running at the bottom of the tank in the opposite direction of the lighter fluid. In this section two numerical calculations are setup and the results are compared with lock-exchange experiments reported by Lowe et al. (2005). Two different density ratios, $\gamma = \rho_2/\rho_1$, are compared with the outcome of the experiments. The density ρ_1 has a larger value than ρ_2, or $\rho_1 > \rho_2$.

In the first experiment the density differences are small, see Lowe et al. (2005) $\gamma = 0.993$, and is called a Boussinesq lock exchange.

In the second experiment a large density ratio is taken, $\gamma = 0.681$, this is the so-called non-Boussinesq lock exchange. In the experiments, for the Boussinesq case, the density is increased with sodium chloride (NaCl).

A large density ratio, for the non-Boussinesq case, is created by adding sodium iodide (NaI). Figure 6.21 shows a schematic 2D representation of the experimental layout. In the experiments from Lowe et al. (2005) the position of both density fronts are tracked in time. The position is given as a function of a dimensionless time t^*. The time t^* is expressed as follows, $t^* = t\sqrt{g(1-\gamma)/H}$, where g is the gravitational constant, t, the time and H the height of the tank.

6.4.1 Initial and boundary conditions

This section describes the numerical setup. Figure 6.22 shows a 2D sketch of the imposed initial and boundary conditions. It must be noted, that the numerical calculation is done in 3D. For the velocities wall boundary conditions, see Eq. (6.12), are imposed at the East, West, South, North and Top, Bottom walls in the computational domain. The wall boundaries are assumed to be hydraulically smooth. A zero gradient boundary condition is imposed for the pressure at the wall boundaries. The length, height and depth of the domain is respectively, $L = 1.83\,m$, $H = 0.2\,m$ and $D = 0.23\,m$ in the x, y and z direction. The number of subdivisions in x, y and z-direction is resp. $n_x = 201$, $n_y = 55$ and $n_z = 55$. The WALE LES turbulence model is used in the calculation. Two density ratios γ are applied, $\gamma = 0.993$ and $\gamma = 0.681$, representing the Boussinesq and the non-Boussinesq case. The time step for both numerical calculations is $\Delta t = 2 \times 10^{-4}\ s$.

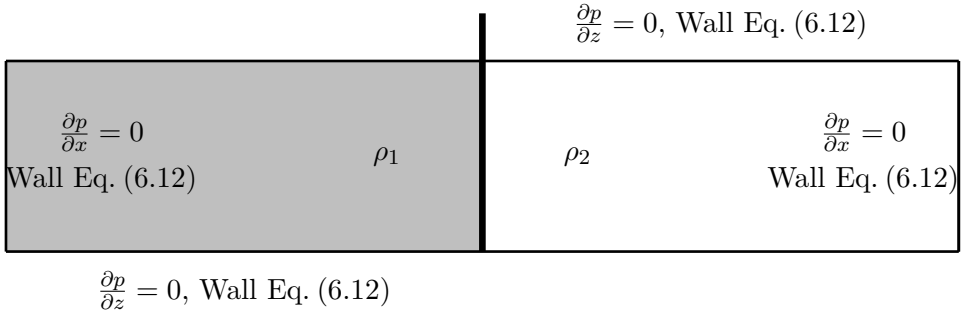

Figure 6.22: Numerical setup, wall boundary conditions for the velocity and zero gradients for the pressure boundaries used. The walls are assumed to be hydraulically smooth. The density ratio is taken $\gamma = 0.993$ for the Boussinesq case and $\gamma = 0.681$ for the non-Boussinesq case.

6.4.2 Results

Boussinesq case

This section discusses the Boussinesq lock exchange. In the experiments, carried out Lowe et al. (2005), the density fronts are tracked in time. Figure 6.23 (a) and (b) show the position, x, normalized with the fluid height, H, or, x/H, of the heavy and light fluid and is plotted with respect to the dimensionless time, t^*. The heavy fluid is the flow along the bottom wall of the tank and the lighter fluid is the front along the top wall of the tank. The filled dots, $(\bullet)$ are the computational results. The fronts, from the computational results, of the light and heavy fluids are tracked with help of the density difference.

The open dots, $(\circ)$, are the results of the experiment. The experimental tracking error of the front position is approximately 0.5 $[cm]$ and the time measuring error is approximately $1/30\,[s]$. An overview is given in Table 6.3 of some of the used parameters and values (Boussinesq case).
The position of the fronts of both the heavy and light fluid from the calculation and the experiment agree well. However, the front speed in the experiment is slightly faster in comparison with the results from the calculation. It can be seen that the front propagation of the light and heavy fluid is the same and that the front speeds are constant. Figure 6.25 shows a plot of the front

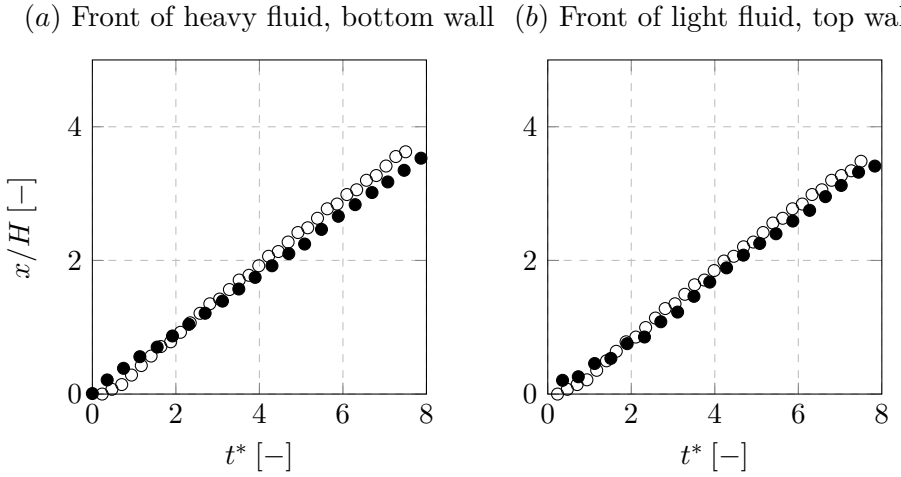

Figure 6.23: Position, x/H, of the density fronts as a function of the dimensionless time $t^* = t\sqrt{g(1-\gamma)/H}$ for the Boussinesq case. The density ratio is $\gamma = 0.993$. The computational results are plotted with the filled dots, (•). The experimental results of Lowe et al. (2005) are represented by (○). In subplot (a) the position of the front of the heavy fluid is given. In subplot (b) the position of the front of the light fluid is given.

position from the calculation, the solid line (−), and the front position of the actual experiment, shown as the background image. In the calculation Kelvin-Helmholtz instabilities occur, see Figure 6.25 (c). However, from the experiment, these instabilities cannot be distinguished visually.

Table 6.3: Experimental parameters and values for both the Boussinesq and non-Boussinesq case, data originate from Lowe et al. (2005). Re number in the last column is based on the maximum front velocity of the density current.

Case	Run	$\gamma = \rho_1/\rho_2$	$\rho_1\ [kg/m^3]$	Re
Boussinesq (NaCl)	A	0.993	1005.1	10800
non-Boussinesq (NaI)	H	0.681	1466.3	95500

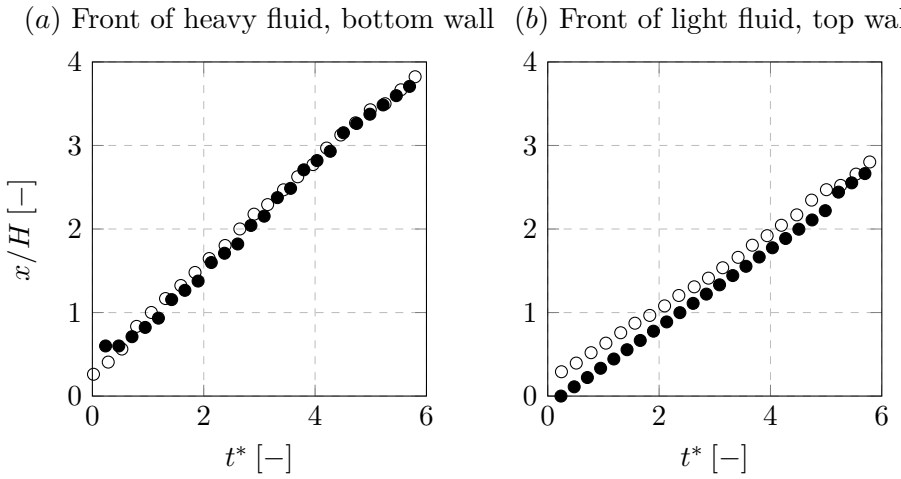

Figure 6.24: Propagation of the front of the heavy fluid, subplot (a), and the light fluid, subplot (b) for the non-Boussinesq case. The experimental results of Lowe et al. (2005) are given with the symbol ($\circ$) and the computational results are given by the filled dots ($\bullet$). A small correction was made for the offset for the front of the heavy fluid, subplot (a).

Non-Boussinesq case

The computational results for the non-Boussinesq case are validated with experimental results. Similar to the Boussinesq case, both the position of the fronts of the light and the heavy front is tracked in time. The heavy fluid flows along the bottom wall of the tank and the light fluid flows along the top wall of the tank. It is reported that the velocity of the flow is constant for both fronts. The front velocity of the heavier fluid is significantly larger than the front of the lighter fluid. The non-dimensional front velocity of the lighter fluid is the same as for the Boussinesq case. The symmetry in front speed between the light and the heavy front is lost.

The gate is removed manually during the experiments and as a result, a small offset occurred in the position in the front of the heavy front. A correction in the offset has been made in the numerical results. This is not serious since only front velocities are used for validation.

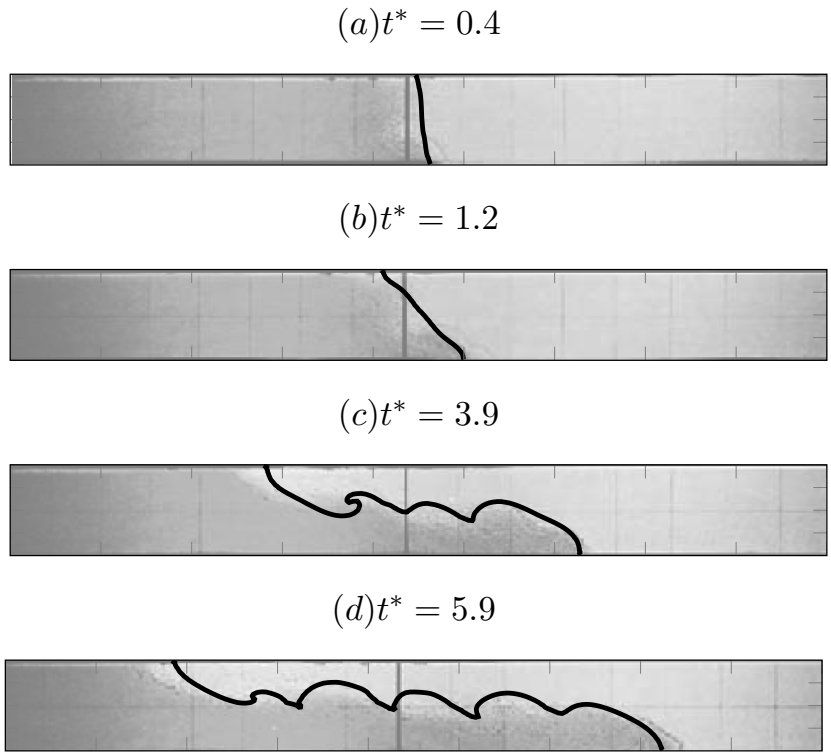

Figure 6.25: Boussinesq lock-exchange, comparison of the results from experiment of Lowe et al. (2005), and the calculation at dimensionless times $t^* = 0.4$, 1.2, 3.9 and 5.9 (subplot $(a), (b), (c)$ and (d) resp.). The continuous line (-) is the computational result and the background picture is the actual experiment. The density ratio is $\gamma = 0.993$.

In Figure 6.24 both the front velocities of the heavy fluid, subplot (a), and the light fluid, subplot (b), are given graphically. In both figures, the open dots, $(\circ)$, are the experimental results and the filled dots, $(\bullet)$, are the computational results. On the horizontal and vertical axis the non-dimensional time $t^* = t\sqrt{g(1-\gamma)/H}$ and the position of the front, x, scaled with the flow height H, or x/H, are given respectively. The front speeds from the calculation and the experiment compare well.
In Figure 6.26 the actual experiment (background image) and the front position,

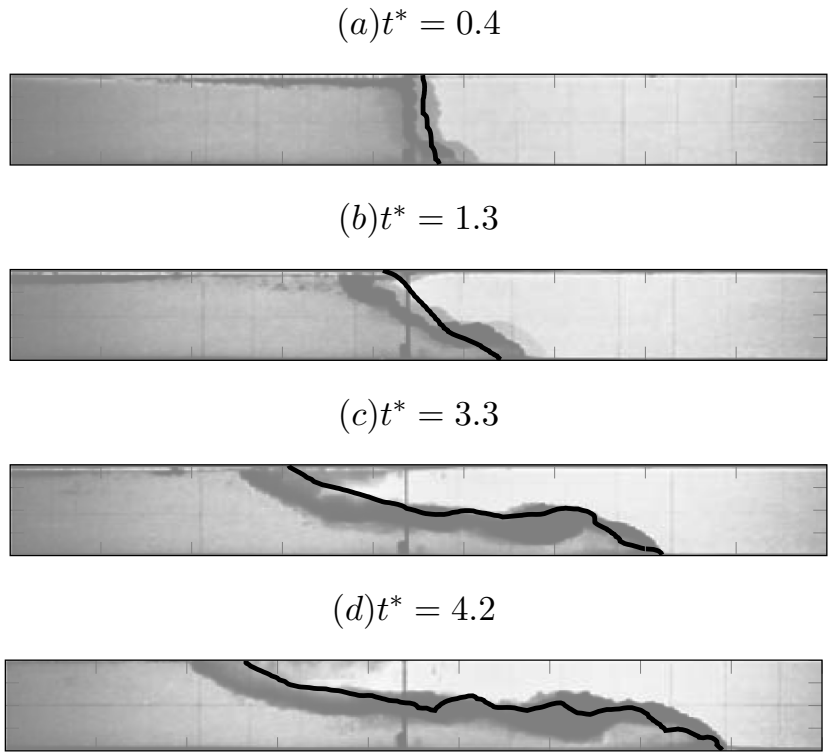

Figure 6.26: Non-Boussinesq lock-exchange, comparison of the results from experiment of Lowe et al. (2005), and the calculation at dimensionless times $t^* = 0.4$, 1.3, 3.3 and 4.2 (subplot $(a), (b), (c)$ and (d) resp.). The continuous line, (-), is the computational result and the background picture is the actual experiment. The density ratio is here $\gamma = 0.681$.

solid line (-) from the calculation are shown. This is done at various time intervals. The calculated front position is captured well with respect to the experiment. From the background image, it can be seen that the front is more diffuse. This is attributed to the existence of turbulence and mixing, see times $t^* > 3.3$ in
Figure 6.26 (c) and (d). Figure 6.27 shows a snapshot of the $3D$ Boussinesq calculation. In the figure, the Kelvin-Helmholtz instabilities can be seen. Figure 6.28 shows a snapshot of the Boussinesq case. Here the Kelvin-Helmholtz

instabilities are less pronounced. Furthermore, more small-scale structures can be distinguished. This is due to the higher Reynolds number with respect to the Boussinesq case, see Table 6.3.

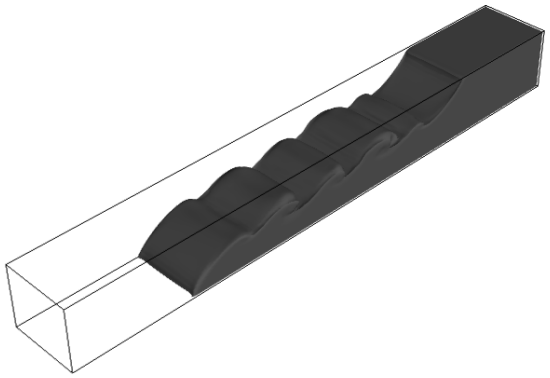

Figure 6.27: A 3D visualization shown of the density current is shown of the Boussinesq case at $t^* = 5.9$.

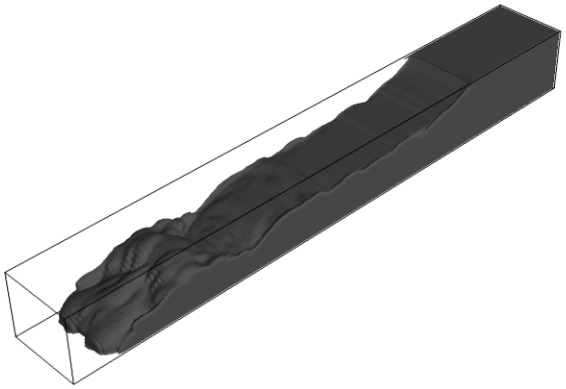

Figure 6.28: A 3D visualization shown of the density current is shown of the non-Boussinesq case at $t^* = 4.2$.

6.5 Sediment settling

The influence of the empirical fits for the parameter n, the hindered settling coefficient, on the particle settling is investigated in this section. Moreover, terminal settling velocities of particles are determined explicitly in 2 different ways. In total three calculations are performed with three different combinations of terminal settling velocities and hindered settling coefficients. With this, the influence of the different approaches on the numerical results is assessed. Furthermore, the numerical results are compared with experimental results, which are clearly defined in batch settling experiments. A description of the settling experiment is given followed by the numerical setup. Finally, the numerical results are compared with the results from experiments of Klerk et al. (1998).

6.5.1 Setup settling experiment

Experiments have been carried out in order to measure volume concentrations at various heights during the settling of sand, see Klerk et al. (1998) and Van Rhee (2011). This has been done using a cylinder or settling column. Over the height of the cylinder 12, two-point conductivity sensors were mounted

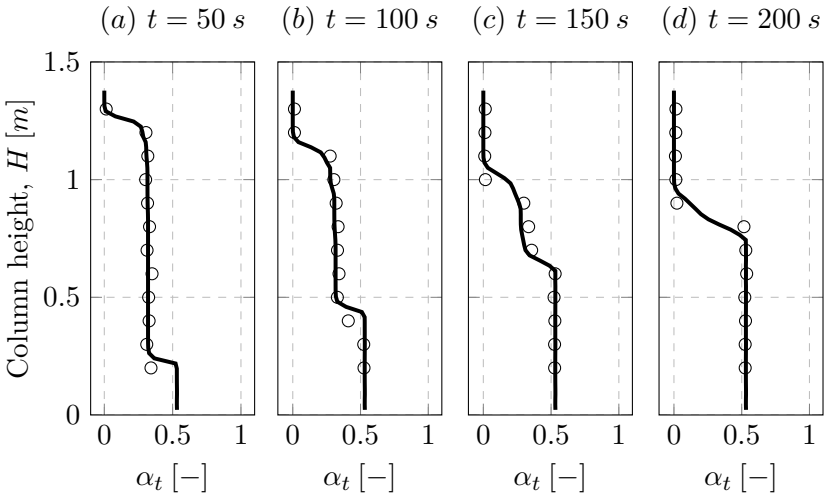

Figure 6.29: Settling of sediment, experiment and calculation at 4 snapshots in time. This is according to Haider and Levenspiel in combination with the Richardson and Zaki indices. The solid line (-) and the symbol (∘) denote the computational and experimental results respectively.

at a distance of approximately 0.2 $[m]$ from each other. The cylinder has a diameter of approximately 0.28 $[m]$ and a height of 1.4 $[m]$. In this cylinder, a rotating frame was mounted. With this frame, it is possible to generate both turbulence and a homogeneous mixture.

Here one settling experiment, see Klerk et al. (1998), is selected and is described briefly in the following. During the experiment, the turbulence in the flow was minimized. The initial volume concentration of the sediment was taken $\alpha_{ti} = 0.32\,[-]$ and the median particle size $d_{50} = 160\,[\mu m]$. Table 6.4 shows the particle size distribution. Note that in the table the particle sizes are scaled with the initial volume concentration, α_{ti}.

6.5.2 Numerical setup

Here three $2D$ numerical calculations with three combinations of settling models are worked out. This is done to investigate the influence of different models on the batch settling of the sediment. The following models are used in the calculation. In the first calculation the terminal settling velocity is determined

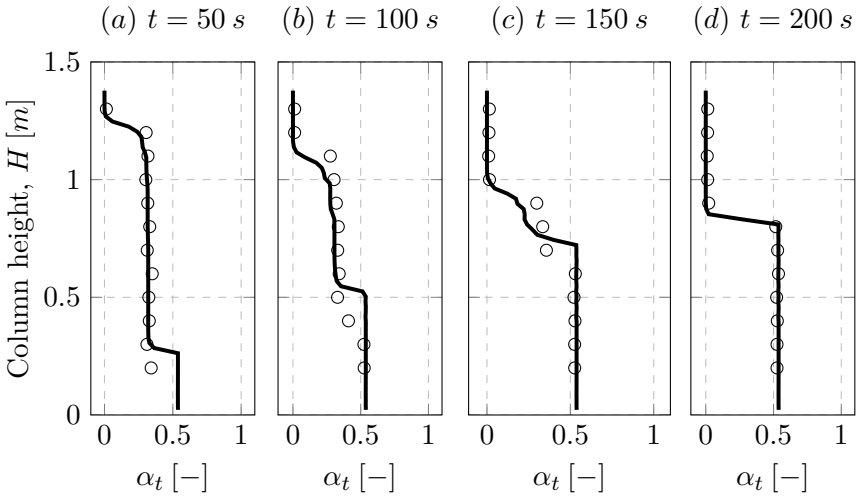

Figure 6.30: Settling of sediment, experiment and calculation at 4 snapshots in time. This is according to Ferguson and Church in combination with the Richardson and Zaki indices. The solid line (-) and the symbol (∘) denote the computational and experimental result respectively.

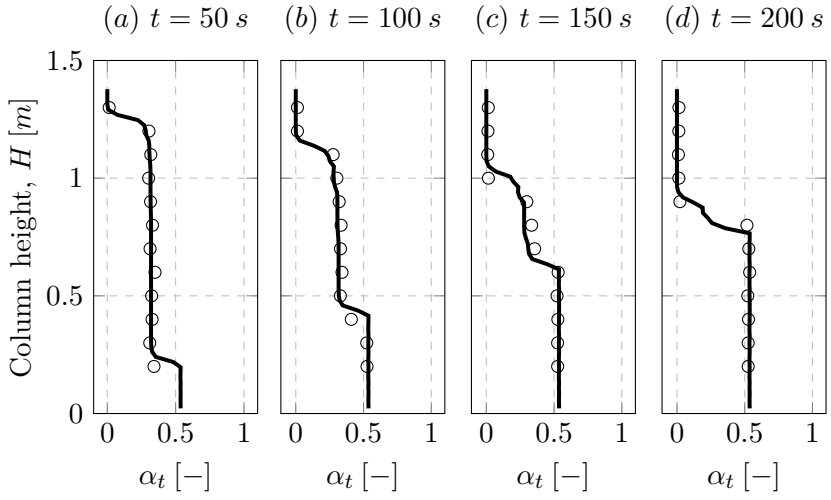

Figure 6.31: Settling of sediment, experiment and calculation at 4 snapshots in time. This is according to Ferguson and Church in combination with the Garside indices. The continuous line (-) and the symbol (∘) denote the computational and experimental results respectively.

Table 6.4: Particle diameters and volume fractions of the sedimentation experiment.

Particle diameter $d_p\,[\mu m]$	Sediment fraction $\alpha_k/\alpha_{ti}\,[-]$
76.5	0.02
98	0.04
115.5	0.15
137.5	0.22
163.5	0.29
194.5	0.2
231	0.06
302.5	0.02

using Haider and Levenspiel (1989), see Section 4.4.3, Eq. (4.72), Eq. (4.73) and Eq. (4.74). The grain shape factor is set to, $\varphi = 0.7$ in Eq. (4.74). The hindered settling function is calculated with the Richardson and Zaki indices, Eq. (4.95). In the subsequent settling test, the terminal settling velocity is determined using the equation of Ferguson and Church (2004), Eq. (4.68), in combination with the Richardson and Zaki indices. The last calculation is done with the terminal settling velocity according to Ferguson and Church, Eq. (4.68), in combination with the Garside and Al-Dibouni (1977) indices. An overview of the Richardson and Zaki and Garside indices can be found in Table 4.4.

The computational domain has a width, D and a height H of , $D = 0.28\,[m]$ and $H = 1.4m$. The number of subdivisions is, $n_x \times n_z = 41 \times 93$, for the width, W, and height, H, respectively. Here the time step is set to $\Delta t = 0.05\,[s]$. The maximum volume concentration of solids is $\alpha_{tmax} = 0.535\,[-]$ and the density of the solids is $\rho_s = 2650\,[kg/m^3]$. The maximum volume concentration is limited by using the FCT algorithm discussed in Section 5.3.2. The results of the batch settling calculation is given in Figure 6.29, Figure 6.30 and Figure 6.31. From Figure 6.29, terminal settling velocity of a particle in combination with the Richardson and Zaki indices, it is seen that the experimental results agree fairly well with the numerical outcome. In Figure 6.30 the settling velocity is determined using the equation of Ferguson and Church (2004), Eq. (4.68), in combination with the indices of Richardson and Zaki for the hindered settling function. The settling velocity from the calculation is higher

with respect to the experiments. Moreover, with the used values, $C_1 = 24$ and $C_2 = 1.2$, the upper limit of the coefficients is chosen in this case. In the third calculation, the terminal settling velocity is determined again using Eq. (4.68) in combination with the indices of Garside for the hindered settling function. The Garside indices yield a lower settling velocity for the smaller fractions in the sediment. The comparison of the experiment and the calculation is plotted in Figure 6.31. The agreement between the experimental and computational results is satisfactory.

The calculated settling velocity of a sediment batch depends on the used model of the terminal settling velocity in combination with the indices for the hindered settling equation. Three combinations have been used in hindered settling indices and the terminal settling velocity. As can be seen from Figure 6.29, the best agreement with this experiment is obtained by using the terminal settling velocity with Eq. (4.72), Eq. (4.73) and Eq. (4.74) given in Section 4.4.3 in combination with the smoothed Richardson and Zaki indices.

The differences in outcome between the different applied parameters in combination with the terminal settling velocities can be explained as follows. The indices of Wallis Garside and Richardson and Zaki are based on a dataset obtained by settling experiments. The fitted parameters are applied on an independent dataset, such as the experiments conducted by Klerk et al. (1998) used here. The properties of the particles, such as the particle size distribution or the angularity of the grain, influencing the terminal settling velocity, are different from the original dataset. Therefore, these results do not quite match. However, the agreement, despite the uncertainties described above, is satisfactory for all three cases discussed here.

6.6 Open-channel flow

6.6.1 Experiments

Parts of this section have been published in Goeree et al. (2016). Typical volume concentrations of sand suspended in water, in hydraulic transport, are in the range of $10 - 40\,\%$. Experimental data of concentration profiles are known from the literature; for instance Gillies (1993) Matousek (1997) or Ekambara et al. (2009) and references therein. These data have been obtained by experiments in pipes.

Several experimental studies of sediment-laden open-channel flows are known from the literature; for instance Einstein and Chien (1955) or Wang and Qian (1989). Open-channel flow experiments were also conducted by Mastbergen and Winterwerp (1987). In their experiments the concentration of sediment varied from $10 - 40\,\%$. The experimental results from Wang and Qian (1989) and Mastbergen and Winterwerp (1987) are used here for comparison with the numerical model. From the experiments of Mastbergen and Winterwerp, runs 51 and 57 is selected. Natural sediment was used during the runs. The tilting flume had a length of $L = 7\,[m]$. The concentration and velocity sensors were mounted at approximately $S_d = 6.5\,[m]$ from the inlet. The median particle diameter, d_{50}, of the sediment, used in the experiment, is approximately $d_{50} = 120\,[\mu m]$. On the bottom of the flume, coarse sand particles were glued with a size of $d_{50} = 500\,[\mu m]$. The side walls were hydraulically smooth. In the runs, SQ1, SQ2, and SQ3, of Wang and Qian (1989) natural sediment was used. The mean particle diameter was $d_{50} = 150\,[\mu m]$. The volume concentrations varied from $0.5 - 2\%$.
The volume concentration of run SF6 in the experiments of Wang and Qian (1989) was approximately $\alpha_t = 0.13\,[-]$, and the median particle diameter d_{50} was $d_{50} = 266\,[\mu m]$. In this test the material had a solids density of $\rho_s = 1052\,[kg/m^3]$. This is slightly higher than the fluid density $\rho_f = 1000\,[kg/m^3]$. The total length of the flume was $L \approx 20\,[m]$ and the concentration and velocity sensors were mounted at a distance of $S_d = 12.3\,[m]$ from the inlet. The bottom and side walls were hydraulically smooth. Table 6.6 shows a complete overview of the relevant experimental parameters. These values are also used in the calculation. Various models can be found in the literature describing the concentration profiles of sediment. A classic model is the concentration profile of Rouse (1937) which is valid for one particle size diameter. More recently Kaushal et al. (2002) developed a model predicting the concentration profile

of a multi-sized particulate slurry flow through a rectangular duct. Here the numerical results of the concentration profile are compared with experimental data from Wang and Qian (1989) (run SQ1, SQ2, SQ3, and SF6) and the Rouse (1937) concentration profile:

$$\frac{\alpha_t}{\alpha_a} = \left(\frac{z_a}{h - z_a} \frac{h - z}{z} \right)^Z \tag{6.13}$$

where the exponent Z is the suspension parameter:

$$Z = \frac{2.5\, w_\infty}{\beta u_\tau} \tag{6.14}$$

The variable α_a is the reference volume concentration near the bottom boundary at level z_a. In table Table 6.5 an overview is given of the reference values used for z_a and c_a.

An expression of the coefficient β is introduced by Van Rijn (1984) based on data found by Coleman (1970) and is the following:

$$\beta = 1 + 2 \left(\frac{w_\infty}{u_\tau} \right)^2 \quad 0.1 < \frac{w_\infty}{u_\tau} < 1 \tag{6.15}$$

6.6.2 Numerical Setup

The result of the numerical calculation is governed by the initial and boundary conditions. Here the numerical model, as described in the previous sections, is applied to simulate the experiments. The computational domain has a length $L = 0.5\,[m]$, the width of the channel is $D = 0.3\,[m]$, and the flow height, h,

Table 6.5: Parameters z_a and α_a for the Rouse profile Eq. (6.13), values taken from Tsai and Tsai (2000)

run	α_a	z_a $(10^{-3}\, m)$
SF6	0.1515	2.2
SQ1	0.0211	2.1
SQ2	0.0625	2.6
SQ3	0.0832	2.6

Table 6.6: Experimental settings of Wang and Qian (1989) (WQ) and Mastbergen and Winterwerp (1987) (MW). Here is α_t volumetric concentration of solids, U mean flow velocity, ρ_s density of solids, d_{50}, particle diameter, w_∞ terminal settling velocity, u_τ the friction velocity, D the flume width, S_d distance from the inlet at which the velocity and concentration sensors were mounted, and h the flow height

	run	α_t (%)	U ($[m/s$)	ρ_s (kg/m^3)	d_{50} (μm)	w_∞ (cm/s)	u_τ (m/s)	D (m)	S_d (m)	h (cm)
	SQ1	0.54	1.90	2640	150	1.890	0.0737	0.30	12.3	8.0
WQ	SQ2	1.77	1.92	2640	150	1.890	0.0741	0.30	12.3	8.0
	SQ3	2.10	1.88	2640	150	1.890	0.0737	0.30	12.3	8.0
	SF6	13.30	1.92	1052	266	0.197	0.0761	0.30	12.3	8.6
	51	20.9	1.39	2650	120	1.21	0.0868	0.30	6.5	10.81
MW	57	10.8	1.53	2650	120	1.21	0.0991	0.30	6.5	9.81

corresponds with the experiments (see Table 6.6). Other parameters such as mean flow velocities, volume concentrations, mean particle sizes, and particle densities in the calculations are used accordingly (see Table 6.6).

6.6.3 Wall Functions and Initial Conditions

In the following, the used wall functions and initial conditions are described for all the numerical calculations. The domain length does not correspond with the actual length of the open channel as used in the experiments. Calculating the actual domain of the experiments is computationally too expensive. Therefore, periodic boundary conditions were imposed at the inlet and outlet of the domain. An advantage of using periodic boundary conditions is that it can be assessed at which simulation time the flow has reached a steady-state. At the bottom B in Figure 6.32 of the domain there is an increased concentration of solids and for the Mastbergen and Winterwerp experiments sediment particles were glued at the bottom wall. The following partial slip condition is imposed (see Paarlberg (2008), Paarlberg et al. (2009)) and references therein:

$$\tau_b = \rho_m \, A_v \, \frac{\partial u}{\partial z} = \rho_m \, S_b \, u_b \tag{6.16}$$

in which τ_b is the bed shear stress, u_b is the velocity near the bottom wall, and S_b is a slip parameter. This parameter controls the resistance at the bed. The no-slip boundary condition is recovered in the case of an infinite slip

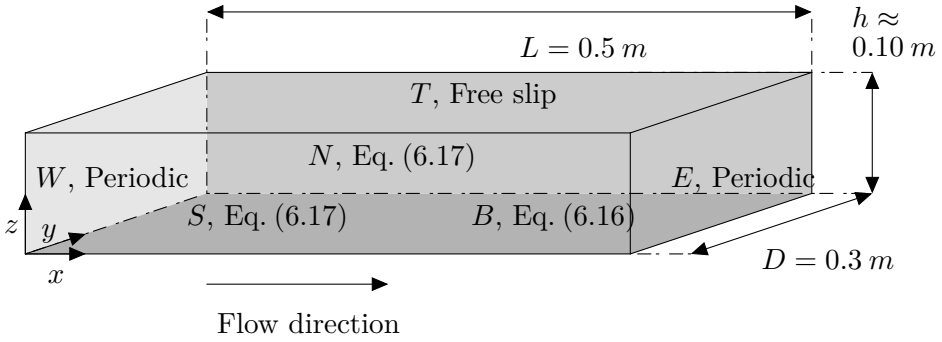

Figure 6.32: Boundary conditions used in the calculation in compass notation. The W and E boundaries are the y, z planes located at $x = 0$ and $x = L$ respectively. The top T and bottom B boundaries are the x, y planes located at $z = h$ and $z = 0$ respectively and the north and south boundaries N and S are the x, z planes at $y = D$ and $y = 0$. At the N and S boundaries, the wall function Eq. (6.17) is used, and at the bottom boundary B, Eq. (6.16) is used as a wall function. A free-slip boundary is imposed at the top T of the domain and periodic boundaries are used at the inlet and outlet, W and E, of the domain.

parameter, $S_b \to \infty$. The eddy viscosity, A_v, is set heuristically to be equal to $A_v = 1 \times 10^{-5}\,[m^2/s]$.
At the north and south boundaries, denoted N and S in Figure 6.32, a law of the wall for hydraulically smooth walls is imposed (see also Eq. (6.12)):

$$\frac{u}{u_\tau} = 2.5\,\ln\frac{y_p\,u_\tau}{\nu} + 5.5 \tag{6.17}$$

where u_τ is the friction velocity and y_p is the distance from the first interior grid point to the wall, at $y = 0$ and $y = D$. The kinematic viscosity is given by $\nu = \mu/\rho$, and μ is the fluid viscosity. At the top boundary T, a free-slip boundary is imposed. In all the numerical calculations the velocity field is initially set equal to zero and the sediment is equally distributed over the flow domain. A driving force is used to maintain a constant average flow velocity. In all the calculations the number of subdivisions of the domain is $n_x \times n_y \times nz = 97 \times 55 \times 55$ and the time step size is $\Delta t = 5 \times 10^{-4}\,[s]$. Here the time step size is sufficiently small for the Courant number, see Eq. (6.11),

Table 6.7: Median particle sizes, d_{50}, and volume fractions, α_k, used in the simulation of Mastbergen and Winterwerp (1987) (MW).

run 51	d_{50} $[\mu m]$	α_k $[-]$
	90	0.02
	120	0.16
	220	0.02
57	90	0.01
	120	0.08
	220	0.01

Table 6.8: Comparison of solution for the velocity $u\,[m/s]$ and concentration $\alpha_t\,[-]$ at height $z/h = 0.33\,[-]$ at various grid resolutions. This is run 57 of Mastbergen and Winterwerp (1987). The inter-grid difference does not exceed 2 % for both the velocity and volume concentration of solids

grid level	$n_x \times n_y \times n_z$ $[-]$	z/h $[m/s]$	$u(z/h)$ $[-]$	$\alpha_t(z/h)$ $[-]$	ε_u [%] $[-]$	ε_{α_t} [%]
1	$63 \times 33 \times 33$	0.33	1.5419	0.1054	–	–
2	$75 \times 43 \times 43$	0.33	1.5528	0.1037	0.70	1.63
3	$97 \times 55 \times 55$	0.33	1.5568	0.1039	0.26	0.16

to be less than 1, i.e. $C_c \leq 1$.
A mono-sized particle distribution is used in the simulation of the Wang and Qian (1989) experiments. In the simulation a median particle diameter, d_{50}, is chosen equal to the diameter given in Table 6.6 for runs SQ1, SQ2, SQ3, and SF6.
The experiments conducted by Mastbergen and Winterwerp (1987) are simulated using a polydisperse mixture. The particle size distribution from the experiments is linearized and represented with three different fractions. The three particle sizes are $90\,[\mu m]$, $120\,[\mu m]$, and $220\,[\mu m]$. In Table 6.7 the particle sizes and the corresponding volume concentrations used in the simulations of runs 51 and 57 are given.

6.6.4 Results and Discussion

The numerical solutions of the velocity and concentration profiles must be grid-independent. Therefore, a grid dependency test was carried out using run 57 of Mastbergen and Winterwerp (1987). The inter-grid difference should not exceed 2 %. Here 3 numerical simulations were conducted at 3 different grid resolutions. The coarsest grid had a resolution of $n_x \times n_y \times n_z = 63 \times 33 \times 33$, and is denoted in Table 6.8 as grid level 1. The intermediate grid has a resolution of $n_x \times n_y \times n_z = 75 \times 43 \times 43$, grid level 2; and for the fine grid a resolution $n_x \times n_y \times n_z = 97 \times 55 \times 55$ was employed, grid level 3.
The numerical solutions for both the velocity and concentration profiles at height $z/h = 0.33$ were compared at successively finer grid resolutions. The inter-grid difference between grid levels 1 and 2 is $\varepsilon_u = 0.70\,\%$ and $\varepsilon_{\alpha_t} = 1.63\,\%$. Here ε_u and ε_{α_t} are the relative inter-grid difference of the velocity and concentration respectively. The inter-grid difference between grid levels 2 and 3 is $\varepsilon_u = 0.26\,\%$ and $\varepsilon_{\alpha_t} = 0.16\,\%$ This is within the limit of 2%. From this it is concluded that the numerical solutions, for both the velocity and concentration profiles, are grid independent. The results from the calculation and the outcome of the experiments of Wang and Qian (1989) are shown in Figure 6.33, Figure 6.34, Figure 6.35, and Figure 6.36. In these figures the calculated concentration profile, $(-)$, the Rouse profile $(--)$, Eq. (6.13), and experimental results, $(\circ)$, are given in subplot (a) and the velocity profile, calculated $(-)$, and experiments $(\circ)$ are given in subplot (b). The velocity and concentration profiles are averaged at half the domain length, $x = L/2$ in the y, z plane. The total simulation time is set to 20 $[s]$ and the averaging starts at $t = 10$ $[s]$, at which time the flow is fully developed. The averaging stops at $t = 20$ $[s]$. The time difference over which it is averaged equals 10 $[s]$. Now an equivalent flume length is calculated:

$$Le = Ut \tag{6.18}$$

where U is the mean flow velocity and L_e is the equivalent flume length. The flow velocity U in the tests from Wang and Qian (1989) and Mastbergen and Winterwerp (1987) (see Table 6.6) varies between $U \approx 1.4$ $[m/s]$ and $U \approx 2$ $[m/s]$. From this, and Eq. (6.18), the equivalent flume length, L_e, with an averaging time period of 10 $[s]$, is roughly 14 $[m] < L_e < 20$ $[m]$. The averaging time has been done for all the numerical calculations performed in this section. The used averaging time and equivalent flume length are sufficient to obtain converged statistics of the velocity and concentration profiles. The

agreement of the velocity profiles between calculations and experiments of Wang and Qian (1989) is close, see Figure 6.33 b, Figure 6.34 b, Figure 6.35 b and Figure 6.36 b. The velocity profile from the calculation is somewhat higher in lower regions, $0 < z/h < 0.5$ in tests SQ1, SQ2, and SQ3. The concentration profiles, both the Rouse profile and the experiments, are predicted well for both lower and relatively high concentrations. This is shown in Figure 6.33 a and Figure 6.36 a. For tests SQ2 and SQ3, Figure 6.34 a and Figure 6.35 a, the predicted concentration profile agrees less closely with the measured profile. The numerical results for velocity and concentration profiles of high concentrations of natural grains with multiple fractions are compared with the experiments conducted by Mastbergen and Winterwerp (1987) in runs 51 and 57. The agreement of the velocity profile with volume concentration $\alpha_t \approx 10\%$ and $\alpha_t \approx 20\,\%$, Figure 6.37b and Figure 6.38 b is less favorable. The velocity profile from the calculations is steeper than the actual measurements. The difference in results between the experiments and calculation of the concentration profile, run 57 (Figure 6.37 a), can be clearly seen. Here the concentration profile is steeper compared to the experiments. The concentration profile of run 51 (see Figure 6.37 b) agrees closely with the experiments. From the above mentioned results it is concluded that for high concentrations ($10\,\% < \alpha_t < 20\,\%$) (see run 51 and run SF6), the concentration profile is well predicted. This is also the case for low concentrations, $\alpha_t < 1\,\%$ (see run SQ1). However, for low to intermediate concentrations, $2\,\% < \alpha_t < 10\,\%$, the concentration profile is too steep compared to results of the experiments. The velocity profiles are predicted accurately for runs SQ1, SQ2, SQ3, and SF6. For runs 51 and 57, some differences are observed between the calculated and measured profiles. In the experiment the flume length was relatively short $L \approx 7\,[m]$. From the calculations, it was observed that at this equivalent flume length, i.e. $L_e = U\,t$ (where U is the mean flow velocity, L_e the equivalent flume length, and t the simulation time), the flow was still developing. This was also observed by Einstein and Chien (1955). They recommended using a flume length of more than $L = 100\,h$, with h being the flow height.

In Figure 6.39 snapshots at time $t = 0, 2, 5, 9\,[s]$ are shown. At $t = 0\,[s]$, the initial condition, the concentration is evenly distributed over the whole domain. At $t = 2\,[s]$, as the flow develops, the sediment tends to settle to the bottom of the domain. At a later point in time, $t = 5\,[s]$ the flow becomes more turbulent and more sediment is being picked up. Finally at $t = 9\,[s]$ the flow is fully turbulent and the sediment distribution reaches its final state.

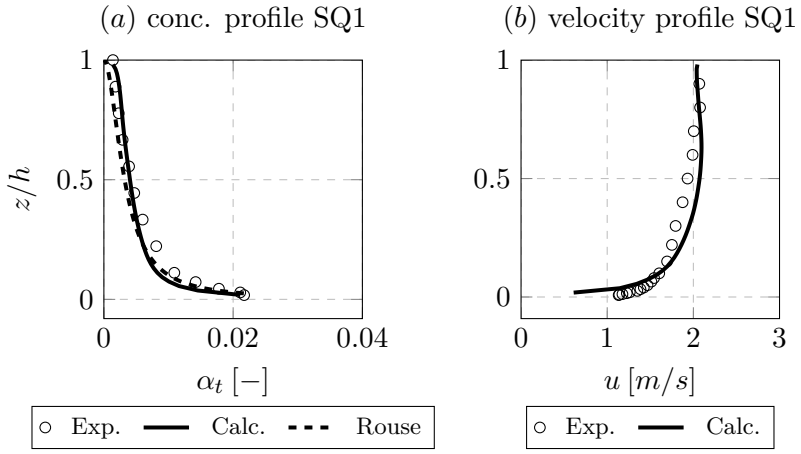

Figure 6.33: Time-averaged concentration (a) and velocity profiles (b) of run SQ1 for a mono-sized mixture.

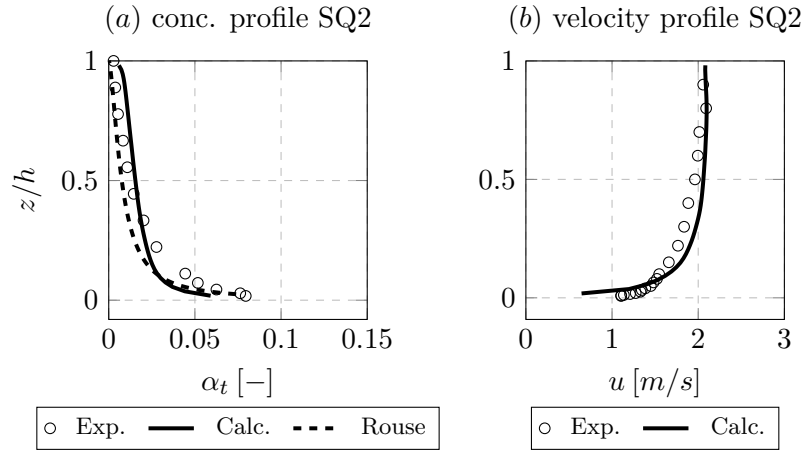

Figure 6.34: Time-averaged concentration (a) and velocity profiles (b) of run SQ2 for a mono-sized mixture.

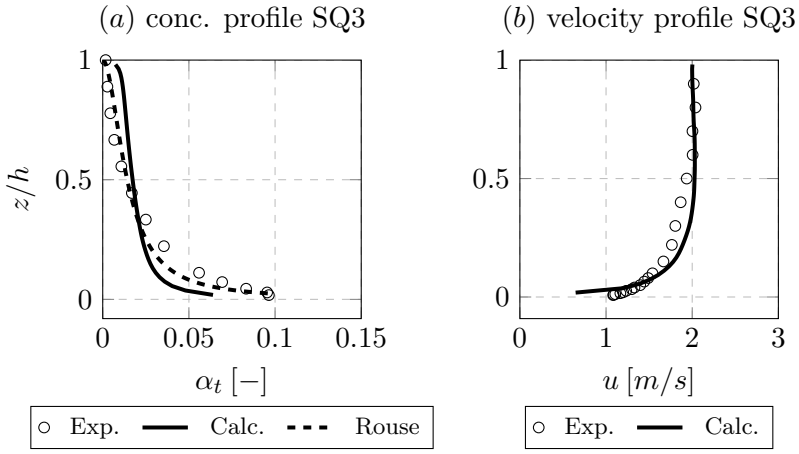

Figure 6.35: Concentration (a) and velocity profiles (b) of run SQ3 for a mono-sized mixture.

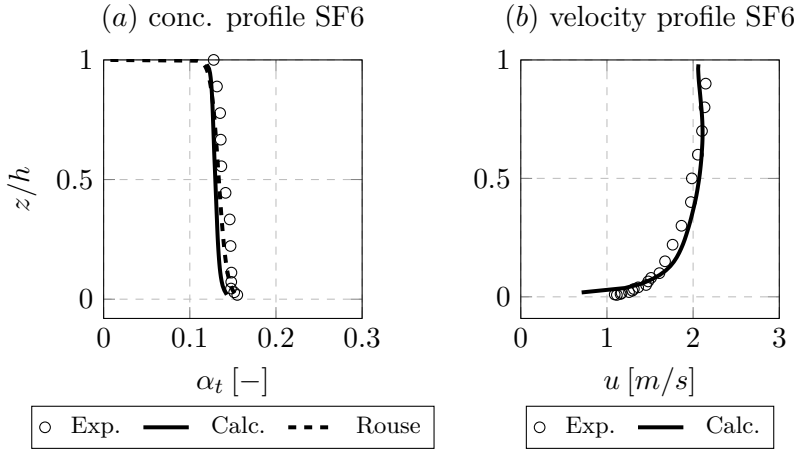

Figure 6.36: Concentration (a) and velocity profiles (b) of run SF6 for a mono-sized mixture.

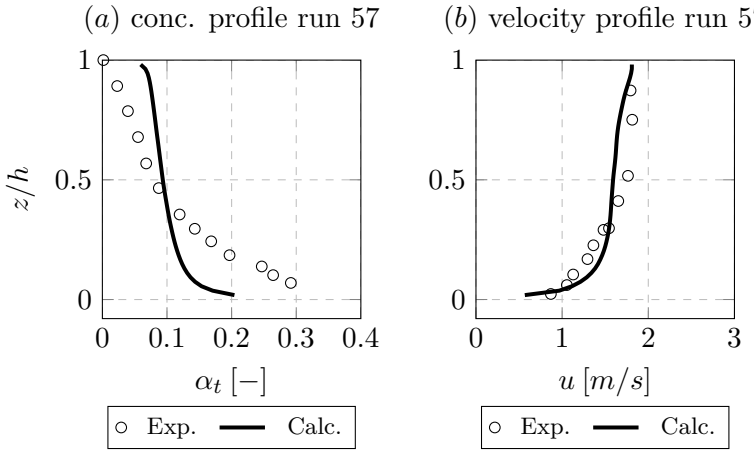

Figure 6.37: Concentration (a) and velocity profiles (b) of run 57. This is done for a multiple sized mixture.

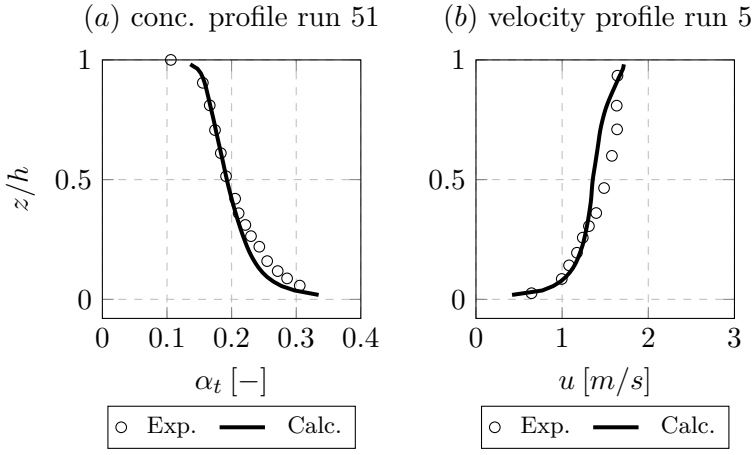

Figure 6.38: Concentration (a) and velocity profiles (b) of run 51. This is done for a multiple sized mixture.

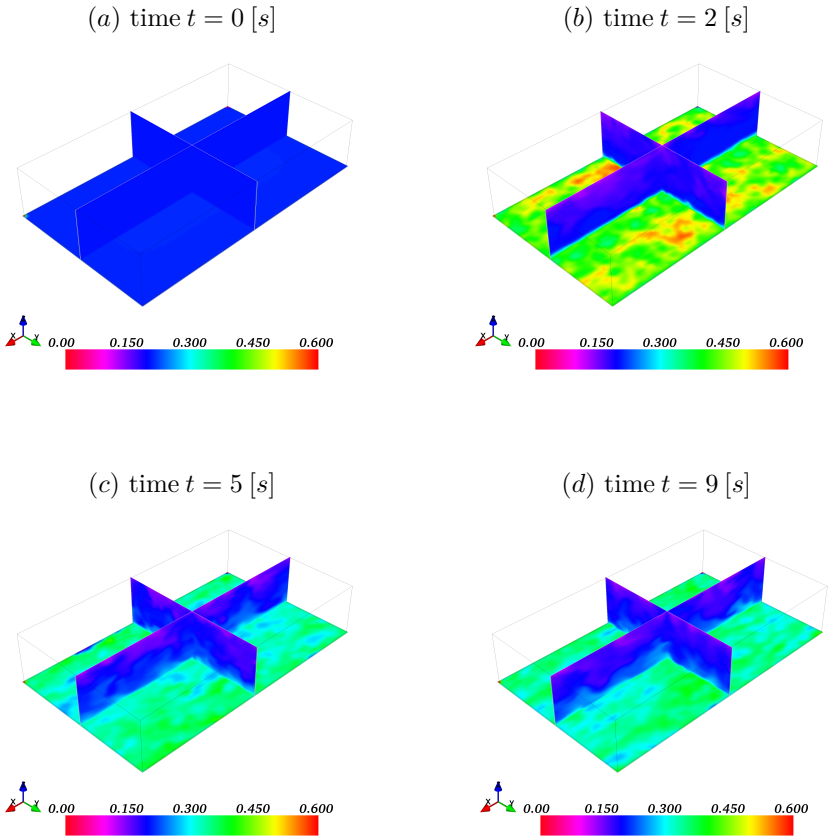

Figure 6.39: The concentration distribution at $t = 0, 2, 5, 9$ [s] this is the calculated run 51 of Mastbergen and Winterwerp (1987). Two cross-sections are given, one in the x, z plane and one in the y, z plane. A cross-section at the bottom is also shown. The flow direction in the figures is from right to left, the x-direction.

Chapter 7

Dense Granular Flow

A sediment mixture changes from a liquid to a solid state if the maximum value of the volume of solids is reached, α_{tmax}. An approach has been discussed earlier solidifying sediment bed at the maximum volume concentration, α_{tmax}, see Section 5.3.1. However, this method does not describe the complex physics at hand of the dynamics of the sediment bed.

When dealing with (dry) grains a difficulty is, that this material can behave as a solid (for instance a pile of sand), a liquid, in an hourglass for instance or even as a gas (when strongly agitated), see Jop et al. (2006) and references therein. Constitutive relations have been proposed in soils mechanics, in case of grains behaving as a solid, or slow plastic flows. When strongly agitated, constitutive relations are used based on the kinetic theory for collisional rapid flows, see Kumaran (2015). However, when dense granular material flows as a liquid, a constitutive equation is not readily available and needs further investigation. The dense granular flows considered here are not collisional dominated.

Especially, in submerged dense granular flows, the dynamical behavior strongly depends on the initial volume concentration and the mean particle size of the granular material, see Rondon et al. (2011) and Van Rhee and Bezuijen (1992). Dense (submerged) granular flows are characterized by a yield criterion (a threshold of the shear stress below which flow does not occur) and a shear

rate dependent friction, which governs the flow behavior. Because of these properties, granular flows share strong similarities with classic non-Newtonian fluids, such as a Bingham, or Herschel-Bulkley fluids, see Section 2.2.

In the following, a (3D) constitutive relation for submerged dense granular flows is presented. The influence of the particle size and the initial volume is incorporated in the model. The numerical model, in which the initial volume is varied, is compared with experimental results from Rondon et al. (2011). The agreement between the experimental and numerical results is good.

7.1 Effective stress

From classical soil mechanics it is known that granular soil is kept rigid by the effective stress and a friction factor. The effective stress is the average stress which is exerted on the granular skeleton and is defined as follows:

$$\sigma'_v = \sigma_v - u_w \tag{7.1}$$

where σ'_v is the effective stress, σ_v is the vertical stress and u_w the pore water pressure. Typically the vertical stress, σ_v, is given by the total weight of the (dry) soil, $\sigma_v = \rho_s g H_s$, where H_s is the height of sediment bed and ρ_s the density of the soil. The pore water pressure, $u_w = \rho_w g H_w$, where H_w is the height of the water level and ρ_w the water density. Now, from the definitions given above the effective stress is given as:

$$\sigma'_v = \rho_s g H_s - \rho_w g H_w \tag{7.2}$$

let $H_w = H_s = H$ and rearranging yields the following:

$$\sigma'_v = (\rho_s - \rho_w)\ g\ H \tag{7.3}$$

now the effective stress corresponds with the submerged weight of the granular material. The pore water pressure, u_w in Eq. (7.1), can be positive or negative. When u_w is negative the effective stress, σ'_v, increases in turn hardening the soil skeleton. When the pore water pressure is positive the effective stress decreases. In the extreme case, the effective stress can become zero or negative liquefying the soil. In the next sections, the effective stress is used in combination with a friction coefficient. The objective is to describe the dynamic soil behavior as a

non-Newtonian liquid. From now on the effective stress is redefined as follows:

$$P_s = \sigma'_v \tag{7.4}$$

and the pore water pressure:

$$P_e = -u_w \tag{7.5}$$

7.2 Constitutive relations

From soil mechanics it is know that soil fails if a certain stress value, or yield stress, is exceeded, see Verruijt (1993) or Andreotti et al. (2013). This failure mechanism can be described by means of a yield stress, using a Coulomb friction law. This friction law, see Eq. (2.27), was introduced in Section 2.5 and is repeated here:

$$\tau_0 = \mu_s \, P_s \tag{7.6}$$

In which τ_0 is the shear stress at which the granular soil fails, μ_s the friction coefficient and P_s the (effective) soil stress. First, a sediment model is discussed based on a Bingham type relation. Subsequently, a more general model, based on granular rheology, is introduced.

7.2.1 Yield stress and relative viscosity

Yield stress

The yield stress depends on the volume concentration, α_t and soil properties such as internal friction angle. When the effective stress is caused by gravity the yield stress, see Eq. (7.6), of soil or sediment, can be described with the following expression, see Lalli et al. (2006):

$$\tau_0 = f(\alpha_t) \, (\rho_k - \rho_f) \, g_z \tan\delta \int_{z_1}^{z_2} \alpha_t \, dz \tag{7.7}$$

Here z_2 is an arbitrary height at which the sediment volume concentration is zero or $\alpha_t = 0$ and δ is the internal friction angle. In Eq. (7.7) the soil pressure, P_s, and soil friction coefficient, μ_s, can be distinguished. The soil pressure, P_s,

consists of the weight of the sediment bed, which is expressed here as P_w. The soil stress, which is equal to the weight of the soil, $P_s = P_w$, reads:

$$P_s = P_w = (\rho_k - \rho_f)\, g_z \int_{z_1}^{z_2} \alpha_t \, dz \tag{7.8}$$

and the friction coefficient, μ_s, reads:

$$\mu_s = f(\alpha_t) \tan \delta \tag{7.9}$$

The function $f(\alpha_t)$ varies between 0 and 1, or $0 < f(\alpha_t) < 1$ and Lalli et al. (2005) proposed the following expression for $f(\alpha_t)$:

$$f(\alpha_t) = \frac{\alpha_t - \alpha_{tm}}{\alpha_{tmax} - \alpha_{tm}} \quad \text{for } \alpha_t \geq \alpha_{tm} \tag{7.10}$$

here α_{tm} is a volume concentration at which there is inter particle friction between the grains. At this volume concentration viscoelastic behavior of the mixture appears. For spherical particles this value is $\alpha_{tm} \approx 0.5$, see Lalli et al. (2005). Other expressions of the function $f(\alpha_t)$, proposed by Lalli and Mascio (1997) and Lalli et al. (2006), are discussed here briefly:

$$f(\alpha_t) = \left(\frac{\alpha_t}{\alpha_{tm}} \right)^a \tag{7.11}$$

Parameter a must be calibrated when visco-plastic behavior is significant. Another expression for $f(\alpha_t)$ is as follows:

$$f(\alpha_t) = \frac{1}{2} \left(1 + \tanh(K\, (\alpha_t - \alpha_{tm})/\alpha_{tmax})\right) \tag{7.12}$$

Where K is a constant related to the mesh size smoothing the transition between Newtonian and non-Newtonian behavior of the mixture flow. The constant K can be defined as $K = kL/\Delta x$, (here L is a length scale and k a constant and Δx the mesh spacing in one direction). Figure 7.1 shows the above mentioned formulations, Eq. (7.10), Eq. (7.11) and Eq. (7.12), $f(\alpha_t)$ as function of α_t.

Relative viscosity

Now a complete model for the mixture viscosity and the sediment bed can be obtained. The relative mixture viscosity, μ_r, is given, see Lalli et al. (2005),

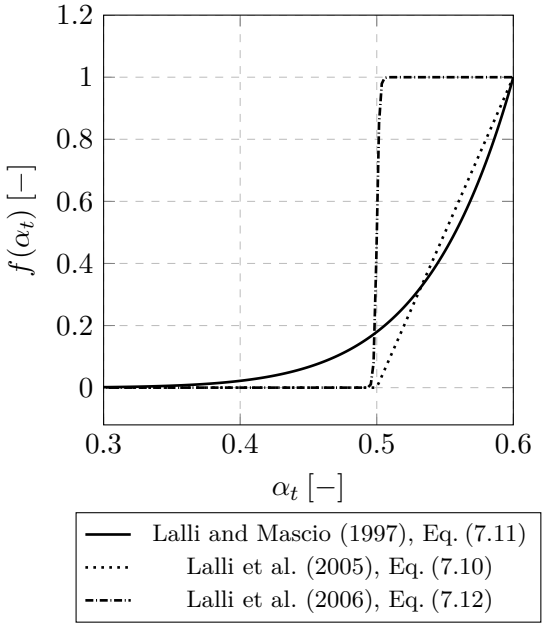

Figure 7.1: The function $f(\alpha_t)$ shown in one figure.

by the model of Eilers (1941), Eq. (2.18). The mixture viscosity is valid if the volume concentration of solids is $\alpha_t < \alpha_{tm}$. If the volume concentration is larger than α_{tm}, $\alpha_t > \alpha_{tm}$, the mixture exhibits visco-plastic behavior, which is expressed as:

$$\mu_r(\alpha_t) = \begin{cases} \left(1 + \frac{0.5\mu_{itr}\,\alpha_t}{1-\alpha_t/\alpha_{tmax}}\right)^2 & \text{if } \alpha_t < \alpha_{tm} \\ \left(1 + \frac{0.5\mu_{itr}\,\alpha_{tm}}{1-\alpha_{tm}/\alpha_{tmax}}\right)^2 + & \\ \frac{1}{2}\frac{\tau_0}{\mu_f}(\sqrt{I_2}+\varepsilon)^{-1/2} & \text{if } \alpha_{tm} \le \alpha_t < \alpha_{tmax}. \end{cases} \tag{7.13}$$

in which I_2 is the second invariant of the deformation tensor, S_{ij}, see Appendix B, and ε a small parameter avoiding singularities in the solution. The intrinsic viscosity μ_{itr} has the value of 3. A continuous flow model is given describing both the influence of the volume concentration of solids and the forming of a sand bed. With this model it is possible to describe transport of sediment. In the following another sediment model is given.

7.3 Granular rheology

In the following, another continuous model is introduced describing a dense granular suspension. This is done first in $1D$ and subsequently generalized to $3D$. First, the Coulomb friction law Eq. (7.6) is repeated here:

$$\tau_0 = \mu_s \, P_s \tag{7.14}$$

The yield stress τ_0 depends on two variables viz. a friction coefficient, μ_s and a pressure contribution P_s. First the friction coefficient is discussed, rewriting Eq. (7.14), see GDR-MiDi (2004) or Pouliquen (2005),

$$\tau_0 = \mu_I \, P_s \tag{7.15}$$

Where the friction coefficient, μ_I, is a function of the dimensionless number I:

$$\mu_I = \mu_{s0} + \frac{(\mu_2 - \mu_{s0})}{I_0/I + 1} \tag{7.16}$$

Here μ_2 and I_0 are constants and experimentally determined. For dry granular media the dimensionless number I, Jop et al. (2006), reads:

$$I = I_t = \frac{\dot{\gamma} d_p}{\sqrt{P_s/\rho_p}} \tag{7.17}$$

Where I_t is called the inertial number, $\dot{\gamma} = \partial u/\partial y$ is the shear rate and ρ_p the density of a particle. The inertial number I_t can be interpreted as the ratio between the rapid time of rearrangement, $t_{micro} = {}^{d_p}/\sqrt{P_s/\rho_p}$ to the macro time $t_{macro} = {}^{1}/\dot{\gamma}$, see da Cruz et al. (2005). For suspensions, Cassar et al. (2005), the dimensionless number, I, can be reformulated as:

$$I = I_v = \frac{\dot{\gamma}\mu_f}{(1-\alpha_t)P_s} \tag{7.18}$$

In which I_v is called the viscous number. By rewriting Eq. (7.16) for granular suspensions the following equation is obtained:

$$\mu_{I_v} = \mu_{s0} + \frac{(\mu_2 - \mu_{s0})}{I_0/I_v + 1} \tag{7.19}$$

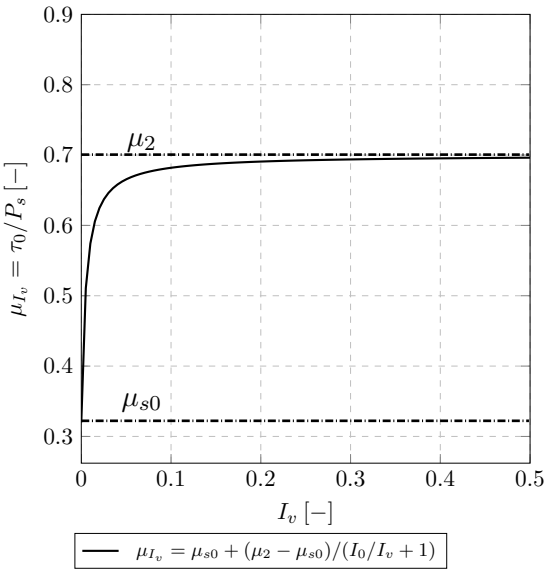

Figure 7.2: Plot of friction coefficient, μ_{I_v}, as a function of I_v Eq. (7.19), with $I_0 = 0.005$, $\mu_{s0} = 0.32$ and $\mu_2 = 0.7$, see Boyer et al. (2011).

Substitution of Eq. (7.19) in Eq. (7.15) gives an expression for the yield stress:

$$\tau_0 = \left[\mu_{s0} + \frac{(\mu_2 - \mu_{s0})}{I_0/I_v + 1}\right] P_s \tag{7.20}$$

In Eq. (7.19) it can be seen that the friction coefficient μ_{I_v} reduces to μ_{s0} if I_v approaches to zero. For larger values of I_v the μ_{I_v} approaches μ_2. The friction coefficient function, μ_{I_v}, is plotted in Figure 7.2. Here the values are $I_0 = 0.005$, $\mu_{s0} = 0.32$ and $\mu_2 = 0.7$, see Boyer et al. (2011). These values are valid for suspensions and determined experimentally.

A generalization of the model in 3D is made next. It is assumed that a dense granular suspension can be considered as an incompressible fluid. Therefore, small volume changes in the dense regime are neglected. The deformation tensor is given by:

$$\mathbf{S} = S_{ij} = \frac{1}{2}\left(\frac{\partial u_i}{\partial x_j} + \frac{\partial u_j}{\partial x_i}\right) \tag{7.21}$$

and the stress tensor T_{ij} in the a dense granular regime, see Eq. (2.6), reads:

$$\mathbf{T} = T_{ij} = 2\,\mu_{I_v} S_{ij} \tag{7.22}$$

with μ_{I_v} is the granular viscosity. This is a function of the deformation tensor. Now introducing the second invariant of the deformation tensor, $\sqrt{I_2} = \sqrt{(\frac{1}{2}\,S_{ij}S_{ij})}$, the one dimensional viscous number I_v, Eq. (7.19) can be rewritten as the following equation:

$$I_v = \frac{\sqrt{I_2}\,\mu_f}{P_s} \tag{7.23}$$

Now a complete 3D model is obtained:

$$\tau_0 = \left[\mu_{s0} + \frac{(\mu_2 - \mu_{s0})}{I_0/I_v + 1}\right]\, P_s \tag{7.24}$$

Where I_v is equal to Eq. (7.23). From Eq. (7.24) it can be seen that the yield stress, τ_0, depends on both the friction coefficient μ_{I_v} and the pressure, P_s, which is exerted on the sediment bed. This is discussed in the next section.

7.4 Pore pressure

The soil pressure consists of several contributions. The most obvious contribution of the soil-pressure, P_s, is the weight of soil. In the case of suspensions, this is the submerged weight. Other contributions are the pressure due to the rearrangements of particles in the suspensions due to shear, Boyer et al. (2011), or the pressure contribution due to dilatancy. Dilatancy causes pore pressures. This can be seen as a body force acting on the sand bed. Here the various pressure contributions to the soil pressure are discussed. So the total soil pressure is the sum of these pressure contributions:

$$P_s = P_w + P_e \tag{7.25}$$

Where P_w and P_e are the pressure due the weight of the sediment bed and pore pressure respectively. The soil-pressure is caused by rearrangements of particles subjected to shear in steady state. Where the contribution of the pore pressure, P_e, is positive when the sediment bed densely packed. The influence of the initial volume concentration, on the motion of a dense granular flow, is described in a nice setup experiment by Boyer et al. (2011). In the following sections the separate pressure contributions, P_e and P_w, are elaborated in more detail.

7.4.1 Pore pressure and initial concentration

The pressure exerted on the granular skeleton depends on the initial volume concentration and the particle size of the sediment, see e.g. Rondon et al. (2011), Van Rhee and Bezuijen (1998), Iverson (2005), Iverson (2013), Pailha and Pouliquen (2009) or Savage et al. (2014). Experiments done by Rondon et al. (2011) showed that the influence of the initial volume concentration of sediment is substantial on the hydrodynamical behavior and the pore pressure of the sediment. A dam break experiment was conducted with two initial volume concentrations, a loose packing and a dense packing. For the loose case, deposits were found to be long and thin. Also, the velocity of the flow was fast. For the dense packing, the dynamics of the dam break were slow. The runout length of the deposits was twice as short in comparison with the loose packing. In the experiments, pore pressure measurements were done. For the loose case excess (positive) pore pressure was found. In the dense packing negative pore pressures were observed. Negative pore pressures, for high initial volume concentrations or dense packing, were also reported in the experiments conducted by Van Rhee and Bezuijen (1998). These experiments showed that the pore pressures play an important role in the dynamics of packed sediment. Using the friction law, Eq. (7.6), the yield stress is obviously higher for a sediment bed with a higher volume concentration. Negative pore pressures give rise to a higher yield stress. This implies a relation between the volume concentration and the pore pressure. Here a model is presented describing a relation between the change in volume concentration, the shear and the pore pressure of a dense granular suspension. Subsequently, the pore pressure is used to calculate the pressure exerted on the granular skeleton increasing the yield stress. This is done using Darcy's law:

$$\mathbf{q} = (1 - \alpha_t)\,(\mathbf{u}_s - \mathbf{u}_f) = -\frac{k_c}{\mu_f}\nabla P_e \tag{7.26}$$

In which $\mathbf{u}_s$ the velocity of the solid grains in a dense granular suspension and $\mathbf{q}$ is the so called specific discharge. The intrinsic permeability is given by k_c. Now in a dense granular suspension the drift velocities are very small. So the mass weighted mixture velocity is approximately equal to the volume weighted velocity, or mixture volumetric flux:

$$\mathbf{u}_m = \sum_{k=1}^{N} \alpha_k\, \mathbf{u}_k \approx \frac{1}{\rho_m} \sum_{k=1}^{N} \rho_k \alpha_k \mathbf{u}_k \tag{7.27}$$

by taken the divergence of $\mathbf{q}$ Eq. (7.26) can be rewritten in the following form:

$$\nabla \cdot \mathbf{q} = -\nabla \cdot \left(\frac{k_c}{\mu_f} \nabla P_e \right) \tag{7.28}$$

From continuity, in the case of a fully submerged suspension, the sum of the divergence of the grain velocity, $\nabla \cdot \mathbf{u}_s$, and the divergence of the specific discharge $\nabla \cdot \mathbf{q}$, is equal to zero, so:

$$\nabla \cdot \mathbf{u}_s + \nabla \cdot \mathbf{q} = 0 \tag{7.29}$$

now substitution of Eq. (7.29) in Eq. (7.28) yields:

$$\nabla \cdot \mathbf{u}_s = -\nabla \cdot \mathbf{q} = \nabla \cdot \left(\frac{k_c}{\mu_f} \nabla P_e \right) \tag{7.30}$$

Now the rate of change of volume concentration can be related to the change of excess pore pressure. In turn, the rate of change of the volume concentration is related to the divergence of the velocity of the soil fraction, see Roux and Radjai (1999) and Iverson (2013). This is expressed as follows:

$$\nabla \cdot \mathbf{u}_s = -\frac{1}{\alpha_t} \frac{D\alpha_t}{Dt} = \sqrt{I_2} \tan \psi \tag{7.31}$$

In which ψ is the dilatancy angle and $\sqrt{I_2}$ is the second invariant of the deformation tensor, introduced earlier. The theory Eq. (7.31) is valid for low level confinement stress and rigid particles, see Pailha and Pouliquen (2009). Furthermore Roux and Radjai (1999) proposed the following linearization of the term $\tan \psi$:

$$\tan \psi = K_3(\alpha_t - \alpha_{teq}) \tag{7.32}$$

In Eq. (7.32) K_3 is a positive constant of order 1, Iverson (2013) and Pailha and Pouliquen (2009). In Eq. (7.32) the equilibrium volume concentration given by α_{teq}.

Now from Eq. (7.26) the permeability of the sediment, k_c, is yet to be determined. The permeability depends on the volume fraction of solids and the size of the particles. This will be discussed in section 7.4.2.

7.4.2 Permeability

The permeability, k_c, of the sediment determines the rate at which the continuous or fluid phase, α_f, flows through a sediment bed. Repeating Darcy's law Eq. (7.26):

$$\mathbf{q} = (1 - \alpha_t)(\mathbf{u}_s - \mathbf{u}_f) = -\frac{k_c}{\mu_f}\nabla P_e \tag{7.33}$$

From this equation it can be seen that the specific discharge, $\mathbf{q}$, with constant pore pressure difference, ∇P_e, is proportional with the intrinsic permeability, k_c. The specific discharge is inversely proportional to the fluid viscosity, μ_f. The hydraulic conductivity depends on volume concentration of solids and the particle size of the sediment. Using the Kozeny-Carman equation, Kozeny (1927) and Carman (1956), the intrinsic permeability k_c can be obtained:

$$k_c = \frac{d_{50}^2}{180}\frac{(1 - \alpha_t)^3}{\alpha_t^2} \tag{7.34}$$

It can be seen from this equation that the permeability depends on a typical value of the particle size diameter d_{50} and the volume concentration of solids. If the particle diameter becomes smaller the sediment permeability decreases. The permeability of a sediment is governed by smaller particle sizes. In Eq. (7.34) the d_{50} is taken as a particle size. The particle size d_{50} increases if there is a fraction present in the sediment with a large particle size. However, the permeability is governed by the fraction with the smaller particle sizes. Therefore, another way to characterize the intrinsic permeability is to use an equation which takes into account this fraction. An expression which does so is introduced by Den Adel (1987), and reads:

$$k_c = \frac{d_{15}^2}{160}\frac{(1 - \alpha_t)^3}{\alpha_t^2} \tag{7.35}$$

In Eq. (7.35) the permeability is a function of the particle diameter d_{15}. In this way the influence of the fraction with the smaller particle sizes is incorporated in the permeability, k_c.

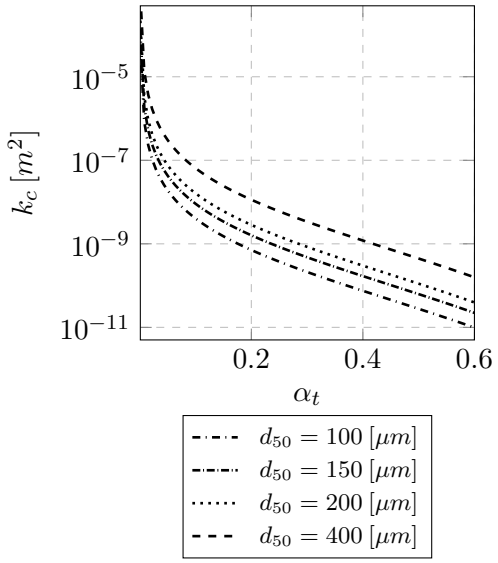

Figure 7.3: Cozeny-Karman equation, intrinsic permeability, $k_c\,[m^2]$, as a function of the mean particle diameter, $d_{50}\,[\mu m]$ and volume concentration of solids, $\alpha_t\,[-]$.

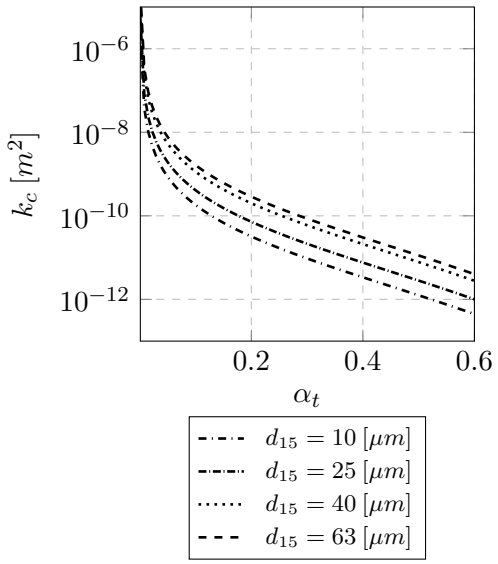

Figure 7.4: Den Adel equation, intrinsic permeability, $k_c\,[m^2]$, as a function of particle diameter, $d_{15}\,[\mu m]$ and volume concentration, $\alpha_t\,[-]$.

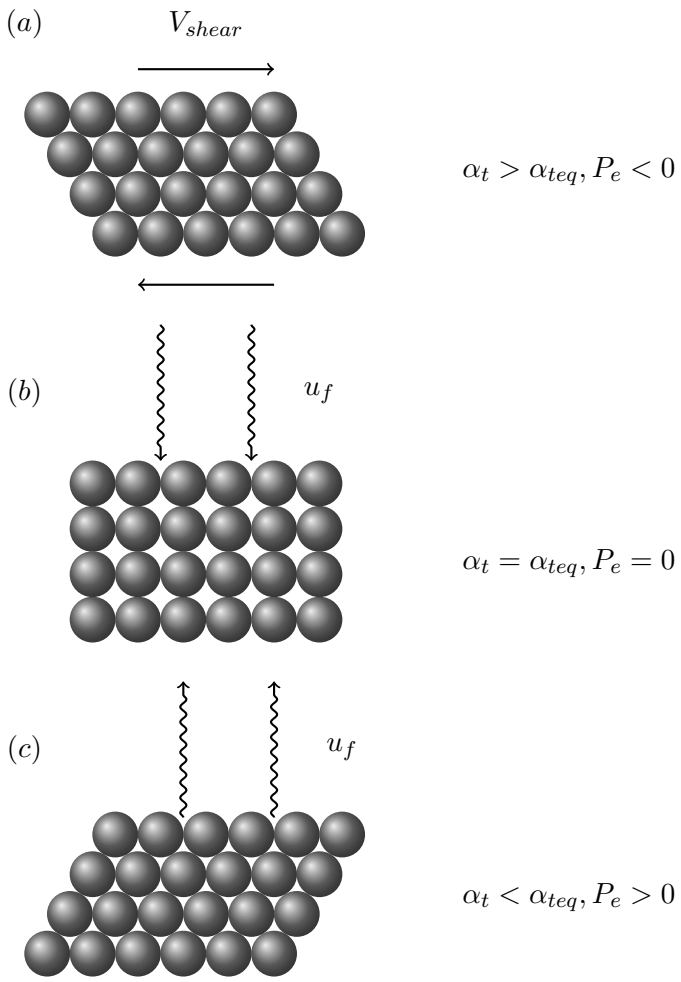

Figure 7.5: Schematic graphic of the evolution of pore pressures, in (a) the sediment is at a compacted state, so $\alpha_t > \alpha_{teq}$. When subjected to shear, V_{shear}, the volume concentration decreases, causing an underpressure in the sediment bed. This yields a stiffening of the granular material. In (b) fluid flows into the bed until $\alpha_t = \alpha_{teq}$ and the pore pressure is $P_e = 0$. If shear is still applied further, see (c), the volume concentration increases again causing interstitial fluid to flow out of the sediment bed. In this case the pore pressure is $P_e > 0$. This leads to a loosening of the material.

7.5 Gravitational collapse of rectangular granular piles

Here a two-dimensional collapse of granular material submerged in a liquid is elaborated. This problem is similar to the classic dam break problem in hydrodynamics.

The packing or the initial volume concentration plays an important role in the dynamics of the flow. These two regimes give different flow dynamics. For the loose case, the flow develops rapid in time and yields a thin and long sediment deposit.

In case of a dense initial volume concentration the flow develops much slower in time. Furthermore, the run-out length of the sediment deposit is smaller compared to the loose initial packing. The difference in flow behavior is explained by the role of the pore pressure. If a loosely packed sediment bed is deformed, the interstitial liquid will flow out of the sediment bed. This causes a positive pore pressure, effectively decreasing the strength of the sediment bed. In this case, the sediment bed behaves more liquid like. If the sediment is densely packed, under shear, fluid will flow towards the packed bed, causing a negative pore pressure, increasing the strength of the sediment. The material behaves now more like a creeping flow. The effect of initial volume concentration was described by Rondon et al. (2011). Here two cases, an initially loose and dense packing or volume concentration of solids, are simulated and compared with experimental results from Rondon et al. (2011). A similar case has been reported by Savage et al. (2014).

The experimental setup is described in Section 7.5.1. Subsequently the setup of the numerical experiment is given in Section 7.5.2. The computational results for the loose an dense initial packing are validated with experimental results in Section 7.5.3 and Section 7.5.3. Finally some remarks are given in Section 7.6.

7.5.1 Description of the experiment

The setup of the experiments conducted by Rondon et al. (2011) is described here. The experiments were done using a perspex tank with a length, $L = 70cm$ a height $H = 15\ [cm]$ and a depth $D = 15\ [cm]$, see Figure 7.8. The tank was filled with a liquid and a layer of particles was glued at the bottom surface. A lock is placed in the tank separating the granular material from

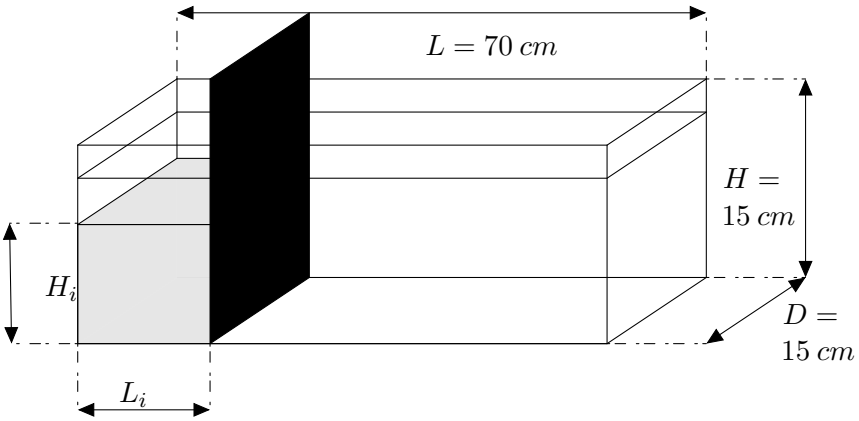

Figure 7.6: Rectangular collapse of granular material (glass beads) with initial dense volume concentration.

the surrounding clear fluid. The lock is mounted in slots and can be removed rapidly causing a dam-break. The lock can be placed at three initial positions, namely, $L_i = 2, 4, 6\ [cm]$.
The clear fluid is a mixture of Ucon oil (75H90000 from Dow) and water. The Ucon oil is soluble in water. In the experiment, two compositions of water and oil were used. One oil-water mixture had a viscosity of $\mu_f = 0.012\ [Pas]$ and the other had a viscosity of $\mu_f = 0.023\ [Pas]$. Glass beads, with a mean particle diameter of $d_p = 225\ [\mu m]$ and a density of $\rho_s = 2500\ [kg/m^3]$, were used as granular material.

An estimation of the volume fraction is obtained by determining the height of the column, H_i. The glass beads are sedimented until the volume fraction reaches its loose sediment packing, approximately $\alpha_t \approx 0.55$. Introduction of vibrations to the tank increases the packing of the glass beads. The dense packing can be estimated by measuring the height after compaction. This can be calculated by the following, $\alpha_{ti} = \alpha_t \frac{H_s}{H_i}$, where H_s is the height of the sediment bed after compaction. Here the experimental results of Rondon et al. (2011) are compared with numerical results, this is a dam break case with a dense initial packing and a loose initial packing. In Table 7.1 and Table 7.2 an overview is given of the relevant parameters, both experimental and computational. In the next section, the numerical setup is discussed.

7.5.2 Numerical setup

Here two cases are validated with the experimental results from Rondon et al. (2011). First, the numerical setup is elaborated. Here a two-dimensional numerical calculation is carried out. This is done for both a dense and a loose initial packing. The flow behavior differs for the loose packing in comparison with the dense initial packing. As granular material slips over a solid wall, the so-called Navier slip condition is applied as a boundary condition, see Artoni et al. (2009) and Savage et al. (2014). This wall boundary is expressed as,

$$\Delta u = u - u_{wall} = \beta \frac{\partial u}{\partial n} \tag{7.36}$$

where u_{wall} is the wall velocity and is taken zero here, u is the velocity of the material parallel to the wall, and n is perpendicular wall coordinate. Here a parameter, β, is introduced, this is is the so-called slip length. The value of this parameter varies between $8 - 10$ particle diameters. However, the value of β is set equal to 4 particle diameters, see Savage et al. (2014).

The interface of the packed bed and the mixture rarely aligns with the grid cell face. The sediment bed interface crosses the grid cell. The sediment fractions are determined using a volume-averaged approach. This implies that if the average of the volume fraction is lower than a maximum sediment packing the material behaves like a fluid. This causes the volume cell to flow more which one would expect. The interface of the mixture and the packed bed lies in the fluid cell itself. So one part of the volume cell is a packed bed and the other part of the volume cell is a mixture. So the fluid at the cell interface is more resilient to deformation as one would expect solely based on the volume averaged sediment present in the cell. In order to mimic the effect of an interface crossing a cell, the granular yield stress, τ_0, is averaged with help of a weighting parameter,

$$\tau_{0P} = \theta \tau_{0P} + \frac{(1-\theta)}{6} \sum_{nb} \tau_{0nb} \tag{7.37}$$

in which θ is a weighting parameter, τ_{0P} is the yield stress at cell center and the variable nb denotes the neighboring cells i.e. $nb = E, W, N, S, T, B$. The weighting parameter is chosen here to be $\theta = 0.8$ and is somewhat arbitrary. However if the weighting factor is, for instance, set to zero, the neighboring cells of the sediment interface are to stiff, causing the flow to stagnate.

Here the results of a 2D calculation are presented. The length and height of the computational domain is $L \times H = 35\,[cm] \times 7\,[cm]$. The number of subdivisions in x and z direction is $n_x = 129$, $n_z = 63$. In the next section, numerical results are presented of both a case of loose initial volume concentration and a dense initial volume concentration.

7.5.3 Numerical results

Loose packing

The numerical results for a loosely packed sediment is validated with experiments done by Rondon et al. (2011). The sediment interface at several time intervals is compared with the experimental results. The experimental results originate from Fig. 2*b* in the paper of Rondon et al. (2011). The position of the bed interface from the experiment is selected at three points in time, namely, $t_0 = 0.66\,[s]$, $t_1 = 1.32\,[s]$ and $t_3 = 1.98\,[s]$. The position of the sediment bed interface is compared with the calculated position of the sediment bed. The interface between the liquid and water in the calculation is taken here at a density of $1650\,[kg/m^3]$. The physical parameters used in the calculation are given in Table 7.1. The initial loose packed granular pile collapses in approximately $2\,[s]$. The material is loosely packed, this means that in case of deformation the interstitial liquid is squeezed out of the material yielding positive pore pressures. This results in a low yield stress, τ_0, causing the granular bed to fail. The material flows like a liquid. The result from the calculation and the experiment at time $t_0 = 0.66\,[s]$, $t_1 = 1.32\,[s]$ and $t_3 = 1.98\,[s]$ are shown in Figure 7.7. The continuous line (-) and the circles ($\circ$) are the results from the calculation and the experiments respectively. From Figure 7.7 (a), (b) and (c) it is seen that the model is able to predict the runout length of the deposits. Also the final calculated angle of repose, Figure 7.7 (c), compares well with the experiments. However, the calculated bed height is lower than the measured bed height, see Figure 7.7 (a) and (b). This is caused by the outflowing liquid being squeezed out of the granular bed dragging granular material with it.

Dense packing

The densely packed bed flows much slower with respect to the loosely packed bed. After removal of the lock the granular pile collapses slowly. Typical collapse times are in the order of magnitude of $20, 30\,[s]$, see the experimental results of Rondon et al. (2011). Here the role of the pore pressure is dominant.

Table 7.1: Parameters used in the simulation for loose granular collapse. The initial length and height, L_i and H_i, are 6 $[cm]$ and 4.8 $[cm]$ respectively.

Property	symbol	value	unit
Density fluid phase	ρ_f	1000	$[kg/m^3]$
Density solids	ρ_s	2500	$[kg/m^3]$
Initial vol.concentration solids	α_{ti}	0.55	$[-]$
Max. vol.concentration solids	α_{tmax}	0.62	$[-]$
Equilibrium vol. concentration	α_{teq}	0.56	$[-]$
Viscosity fluid phase	μ_f	0.012	$[Pas]$
Angle of internal friction	δ	25	$[^\circ]$
Particle diameter(glass bead)	d_p	225	$[\mu m]$
Slip length	β	4	$[-]$

The continuous phase (liquid) is drawn into the densely packed bed, yielding a negative pore pressure effectively increasing the strength of the granular material. The dynamics of the collapse of an initial dense packed sediment is reported by Rondon et al. (2011) and Savage et al. (2014) and described in the following. After removing the gate the column does not collapse at once. At the upper corner, the erosion takes places. This yields a rounded corner at the top, a steep sediment profile and some deposits at the bottom, see Figure 7.8 (a) $(\circ)$. The computational results are given with the continuous line (-). After some time the granular material fails and a triangularly shaped lump of material flows from the pile. This gives rise to a more gentle slope. This process occurs at several time intervals until the slope is gentle and stable. From the calculations, the phenomenon described above is not observed. The erosion of the pile is a continuous process without the sediment pile failing or avalanching. Also, the erosion rate of the sediment is larger. This leads to gentler slopes, see Figure 7.8 (b). In order to predict this failing or avalanching of lumps of material, the model can be extended with a soil fail criterion. However, the granular model is able to predict the final slope of the packed sediment correctly, see Figure 7.8 (c). Moreover, the timescale of granular flow is predicted correctly with respect to with the experiments conducted by Rondon et al. (2011). As mentioned earlier the role of negative pore pressures in the sediment bed is dominant. The negative pore pressures are shown as contour plots in Figure 7.9 $(a), (b)$ and (c). The continuous lines, $(-)$, or contours, are the negative pore pressures and the dashed line (- -) is the

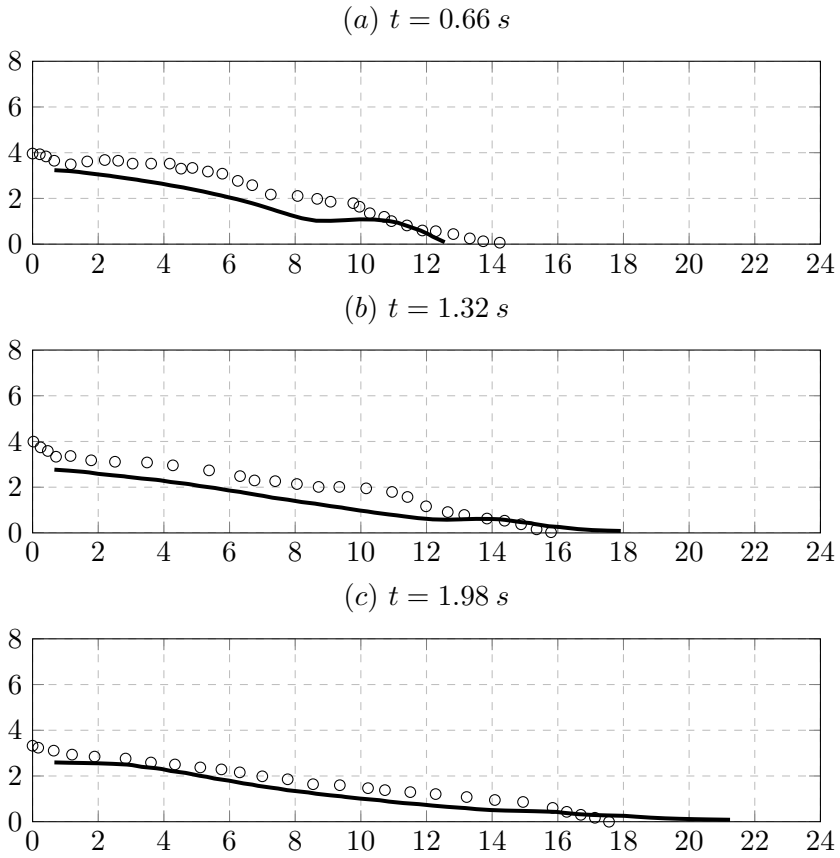

Figure 7.7: Rectangular granular collapse with initial loose volume concentration. Here the bed is presented at various time intervals, the continuous line (-) denotes the computational results where the dots (o) respresent the experimental results.

sediment-water interface. Here the calculated pore pressures are in the order of magnitude of $P_e \approx 100\,[Pa]$. The pore pressure is present in the case of shear, Figure 7.9 (a) and (b), and decreases gradually to zero when the slope reaches its final state, Figure 7.9 (c).

Table 7.2: Parameters used in the simulation for dense granular collapse. The initial length and height, L_i and H_i, are 6 $[cm]$ and 4.2 $[cm]$ respectively.

Property	symbol	value	unit
Density fluid phase	ρ_f	1000	$[kg/m^3]$
Density solids	ρ_s	2500	$[kg/m^3]$
Initial vol. concentration solids	α_{ti}	0.6	$[-]$
Max. vol. concentration solids	α_{tmax}	0.62	$[-]$
Equilibrium vol. concentration	α_{teq}	0.56	$[-]$
Viscosity fluid phase	μ_f	0.012	$[Pas]$
Angle of internal friction	δ	25	$[^\circ]$
Particle diameter	d_p	225	$[\mu m]$
Slip length	β	4	$[-]$

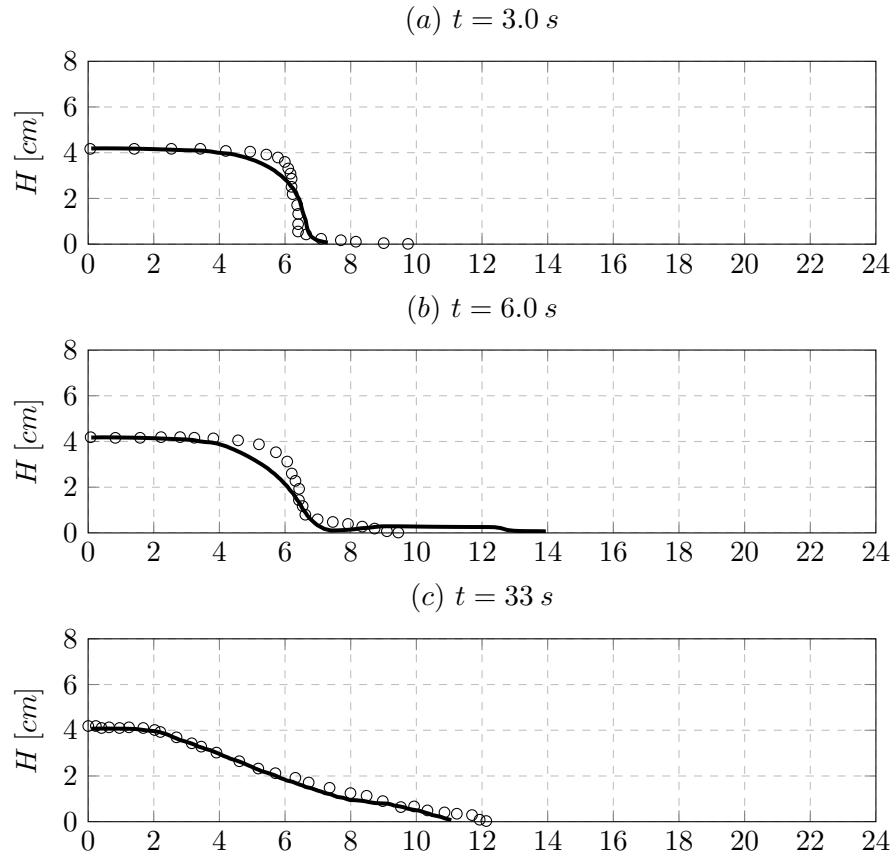

Figure 7.8: Rectangular granular collapse with initial dense volume concentration.Here the bed is presented at various time intervals, the continuous line (-) denotes the computational results where the dots (o) respresent the experimental results.

7.6 Summary and remarks

A model has been introduced here in which the hydrodynamical behavior of dense submerged sediment bed is described. This is done using a Coulomb friction law. This friction law depends both on the exerted pressure on the granular skeleton and a friction coefficient. The friction coefficient depends

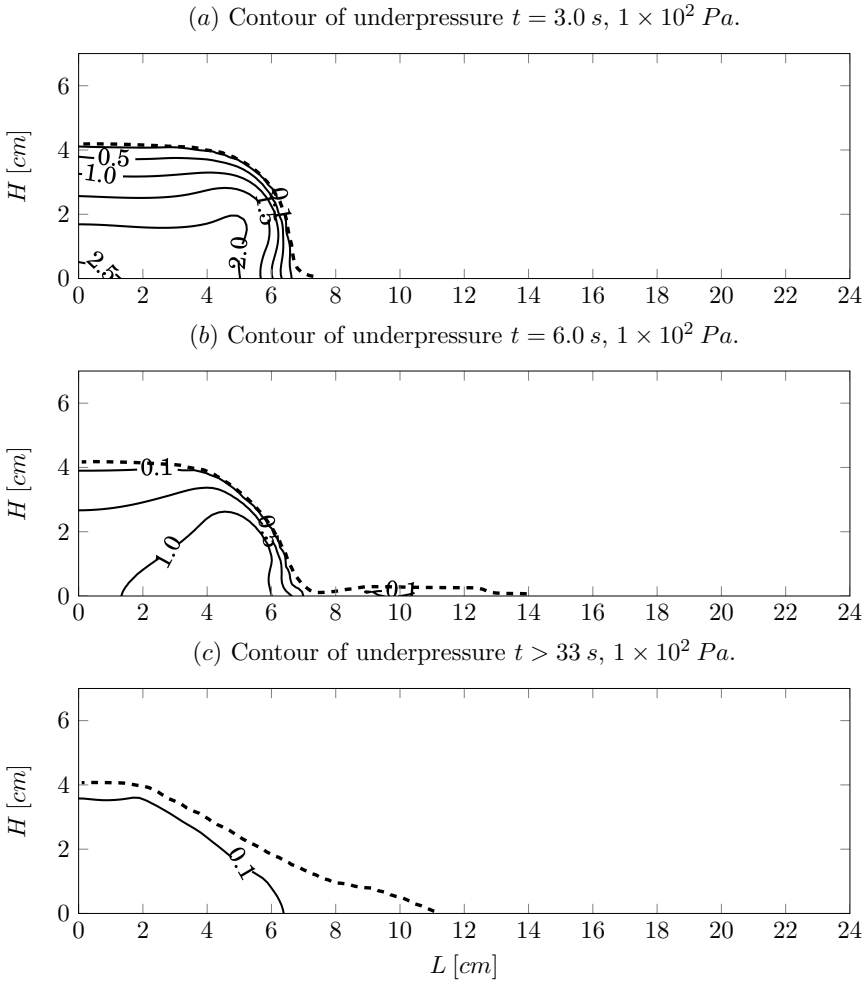

Figure 7.9: Rectangular granular collapse pore pressure distribution.

on the shear rate of the flow and the exerted pressure depends on the in- or outflow of interstitial water of the granular bed. Here the initial volume concentration plays a crucial role. When the initial volume concentration is below a certain equilibrium volume concentration, pore water flows into the sediment bed increasing the pore pressure. This causes the sediment bed to flow slowly. When the initial volume concentration is above the certain

equilibrium concentration, pore water flows out of the sediment bed. This decreases the pore pressure and causes the sediment bed to flow rapidly.

Here the model has been tested for both the dense and loose initial volume concentration. This is done with experiments by Rondon et al. (2011) of a granular collapse of a column. The model predicts the runout length of the sediment and the time at which the sediment bed flows well for both the dense and loose case.

However, the failure mechanism for the dense case is not captured entirely by the model. From the experiments, triangularly shaped lumps avalanching down the slope could be observed. This failure mechanism is not captured by the model. Therefore, it is recommended that more research is needed into this failure mechanism.

Moreover, Rondon et al. (2011) performed pore pressure measurements. This was done at only one location at the bottom wall of the experimental tank. An interesting measurement would be to assess the entire pressure distribution along the sediment region. Especially the pressure at the sediment-water interface gives more information on the water flowing into, in case of a dense initial packing, the sediment bed. Furthermore, measuring the influence of the avalanching triangularly shaped lumps on the pore pressure should give more insight into the failure mechanism at hand.

Chapter 8

Closed flume sedimentation tests

Sedimentation tests, see Van Rhee (2002), are used validating the sediment, or sand bed, velocity. The position of the sand bed is measured in time, using conductivity probes, mounted at several vertical positions. This yields the sand bed velocity, as a derived quantity of the vertical position of the sand bed with respect to time. The objective of these calculations is to see if this (complete) model is able to predict, at least qualitatively, the sand bed velocity.

The model setup and implementation in this chapter is using the complete model as presented throughout the thesis. The components of the model, with references to the relevant equations and sections, are tabulated in Appendix E Table E.2.

First, the experimental setup is discussed. Subsequently, the numerical setup is introduced, including the used parameters. Finally, the experimental results are compared with the numerical results.

8.1 Sedimentation experiments

8.1.1 Experimental setup

Experiments were conducted in order to determine the sedimentation rate of suspended solids. The sedimentation rate governs the velocity at which height, or the position, of the sediment-water interface changes in time. The sedimentation rate can be expressed as follows, see Van Rhee (2002):

$$\frac{dh}{dt} = \frac{E - S}{(\alpha_{tmax} - c_b)\,\rho_s} \tag{8.1}$$

where dh/dt is the rate of change of the sediment-water interface in time, the pickup rate and the settling flux is given by E and S respectively. The solids concentration of the sediment bed is α_{tmax} and c_b the near bed concentration. It can be readily seen if $S > E$ the height of the sediment bed increases in time. The height of the sediment bed decreases in time when $S < E$, in this case, net erosion takes place. Both S and E depend on mixture velocities above the sediment bed.

In order to determine the sedimentation rate at certain mixture velocities, a closed flume loop experiment was set up at the Dredging Technology Research Laboratory of the TU Delft. Figure 8.1 (a) shows a sketch of the experimental setup. The flow velocity in the measurement section could be controlled using a butterfly valve. This valve was mounted in the pipe of the measurement section. By opening and closing this valve the flow velocity was increased or decreased respectively. The opening or closing of the valve was done in a relatively short amount of time. At the start of the experiment, the flow velocity in the system was chosen as such that the sediment was in suspension. Furthermore, the volume concentration of suspended solids was varied at each experiment. The change of the height of the bed in time was measured using 56 conductivity probes, shown in Figure 8.1 (b). These probes were calibrated using a radioactive density sensor. The position of this sensor could be adjusted vertically.

The (bulk) mixture velocity was measured using an alto-flux velocity sensor. Moreover, the (local) velocity and velocity fluctuations, inside the flume measurement section, were measured using an EMS (Electro Magnetic Sensor). This concludes the setup of the experimental setup. A more elaborate discussion of these experiments can be found in Van Rhee (2002).

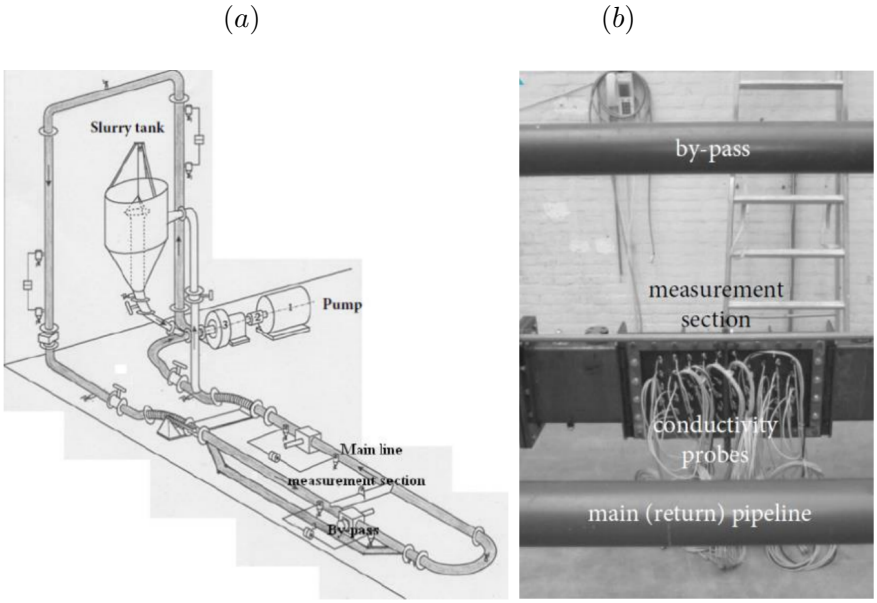

Figure 8.1: Overview flow loop shown in plot (a) and close up of the measurement section, plot (b). Figures reproduced by permission of C. van Rhee and F. Bisschop.

8.1.2 Particle size distribution

In the experiments four different particle sizes were used, with a mean particle size of $d_{50} = 125$, 150, 185 and 270 $[\mu m]$. Here the particle sizes with a $d_{50} = 125$ $[\mu m]$ and $d_{50} = 185$ $[\mu m]$ are used as input for the validation of the numerical experiments and 7 fractions, for both mean particle sizes, are taken as input for the numerical calculations. The particle size distributions are shown in Figure 8.2.

8.1.3 Execution of experiments

At the beginning of the experiment, the flow velocity was set to a high enough value keeping the sediment suspended. Subsequently, the flow velocity was decreased to a desired value. This was achieved by closing the butterfly valve in the measurement section. The suspended solids started to settle forming a bed. The velocity of the sedimentation was measured using conductivity

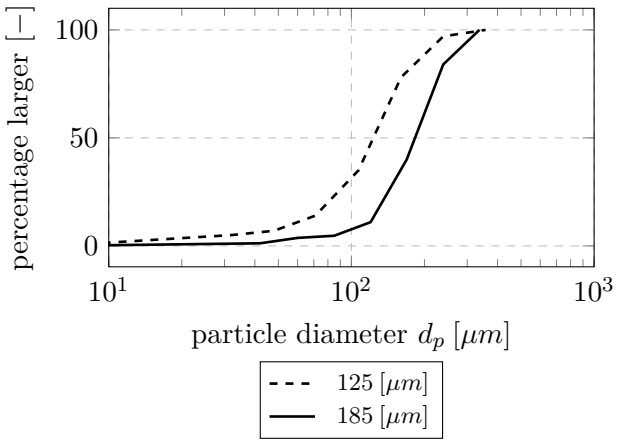

Figure 8.2: Particle size distribution of sand used during tests. These are used as input for the numerical calculations.

probes. These were placed at several vertical positions in the measurement section. During sedimentation, a sudden jump of the volume concentration was registered, typically from $\alpha_t = 0.25\,[-]$ to $\alpha_t = 0.5\,[-]$, marking the passing of the sand water interface. Since the vertical position of each probe is known, the sedimentation velocity can be derived by taking the time difference of each concentration jump of the probe and the subsequent distances between the probes. Multiple experiments have been conducted with several different settings. Here a subset of 4 experiments has been chosen as a validation of the numerical model. This will be discussed in the next section.

8.2 Numerical calculation closed flume tests

8.2.1 Geometry

The layout of the measurement section of the closed flume experiments is as follows. The dimension of the measurement section used in the closed flume experiments was rectangular. The internal dimension was $D \times H = 0.088 \times 0.288\,[m^2]$, were D and H is the width and the height of the domain. The total length of the rectangular domain was $L_{total} = 7\,[m]$ and at both ends connected with diffusers. The diffusers were connected in turn connected to the pipe circuit.

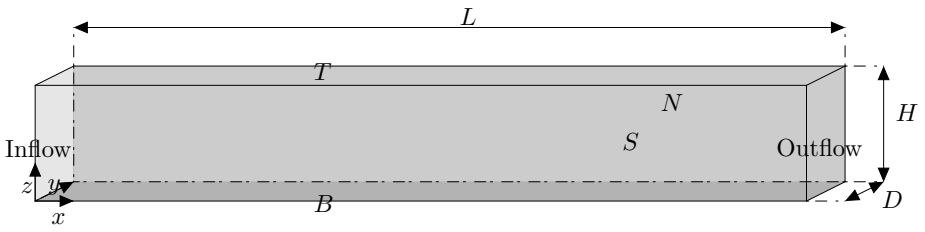

Figure 8.3: Sketch of the computational domain.

At the center of the measurement section, a steel section was mounted with a length of $L = 1.5\,[m]$. In in the middle of this section, a transparent Lexan window was fitted, in which the density probes were installed.

In order to compare the experimental results with the numerical results, the computational domain was set up as follows. A rectangular domain was chosen with a $L \times D \times H = 2 \times 0.09 \times 0.29\,[m^3]$, which slightly deviates from the experimental dimensions. The influence on the numerical results of this deviation is assumed to be small. Furthermore, the domain is assumed to be sufficiently large to exclude transient effects originating from the imposed boundary conditions. The computational domain is subdivided in $n_x \times n_y \times n_z = 183 \times 33 \times 53$ and the time step size is $\Delta t = 1 \times 10^{-4}\,[s]$. A sketch of the computational domain is shown in Figure 8.3.

8.2.2 Initial and boundary conditions

Here the complete implemented model is chosen for validation. The implicit fractional step method, see Section 5.2.2 is used. The advective terms in the discretized Navier-Stokes equations are interpolated with the Quick scheme. The sediment bed is modeled as introduced in Section 7.4. At the wall boundaries, except inflow and outflow boundaries, wall functions are imposed for the velocity, see Eq. (6.17). These walls are denoted, see Figure 8.3, as T, B, N and S, which are the Top, Bottom, North and South wall boundary respectively. At the walls, Neumann boundaries are used for the pressure. Furthermore, it should be noted that in these calculations a grid convergence check was omitted.

At the inflow boundary the velocity is taken constant in the x-direction. Furthermore, the sediment is uniformly distributed over the inflow area, $D \times H$.

Table 8.1: Numerical parameters used in the calculation.

run	Resolution $n_x \times n_y \times n_z$	Length $L\,[m]$	Height $H\,[m]$	Depth $D\,[m]$	Time step $\Delta t\,[s]$	Start vel. $V_b\,[m/s]$	End vel. $V_e\,[m/s]$
1	$183 \times 33 \times 53$	2	0.29	0.09	1×10^{-4}	2.7	0.5
2	$183 \times 33 \times 53$	2	0.29	0.09	1×10^{-4}	2.7	1.3
3	$183 \times 33 \times 53$	2	0.29	0.09	1×10^{-4}	2.4	0.4
4	$183 \times 33 \times 53$	2	0.29	0.09	1×10^{-4}	2.4	1.3

The inflow velocities varies in time and are tabulated in Table 8.1. Where V_b and V_e denote the start and end velocity respectively. For run 1, for instance, the start velocity was set to $V_b = 2.7\,[m/s]$ and is high enough to keep the sediment in suspension. The initial velocity, V_b, is kept constant for $t \approx 3\,[s]$ and reduced in approximately $3\,[s]$ to the end velocity $V_e = 0.4[m/s]$. This time corresponds with the time it took to close the butterfly valve in the actual experiment. As soon as the flow velocity starts to decrease the bed velocity is measured, the lower flow velocity causes the sand to form a sediment bed.

In the experiments, the bed velocity was determined as follows. The time difference, Δt, was measured in which the bed height covered a distance of $d \approx 1[cm]$, at half the length of the domain. By dividing, d, with the amount of time for the sand bed to cover this distance, the bed velocity, dh/dt, is determined.

In the numerical calculations the velocity of the sediment bed is measured half way the length of the domain, at position $x = L/2$, see Figure 8.3. By measuring the amount of time in which the bed height increases over a distance $d \approx 1\,[cm]$, the bed velocity can be determined.

8.3 Comparison experimental and numerical results

The numerical model used is validated with four experiments. The sand bed velocity, dh/dt see Eq. (8.1), is estimated from numerical results. A sharp jump in density is observed during the simulations. The vertical position of the sharp density jump is tracked at two time intervals. By taking the difference in vertical position and dividing by the time interval, the sand bed velocity is obtained. The total simulation time is set to $t_s = 25\,[s]$. Unfortunately, some simulations suffered from numerical instabilities. Therefore, in some cases,

Table 8.2: Physical parameters used in calculation run 1 & 2, see Table 8.1.

Property	symbol	value	unit
Density fluid phase	ρ_f	1000	$[kg/m^3]$
Density solids	ρ_p	2650	$[kg/m^3]$
Initial vol. conc. solids	α_t	0.33	$[-]$
Equilibrium vol. conc. solids	α_{teq}	0.5	$[-]$
Max. vol. conc. solids	α_{tmax}	0.53	$[-]$
Viscosity fluid phase	μ_f	0.001	$[Pas]$
Angle of internal friction	δ	25	$[^o]$
Particle diameter (d_{50})	d_p	125	$[\mu m]$
K_3 Eq. (7.32)	K_3	4	$[-]$

Table 8.3: Physical parameters used in calculation run 3 & 4, see Table 8.1.

Property	symbol	value	unit
Density fluid phase	ρ_f	1000	$[kg/m^3]$
Density solids	ρ_p	2650	$[kg/m^3]$
Initial vol. conc. solids	α_t	0.25	$[-]$
Equilibrium vol. conc. solids	α_{teq}	0.5	$[-]$
Max. vol. conc. solids	α_{tmax}	0.53	$[-]$
Viscosity fluid phase	μ_f	0.001	$[Pas]$
Angle of internal friction	δ	25	$[^o]$
Particle diameter (d_{50})	d_p	185	$[\mu m]$
K_3 Eq. (7.32)	K_3	4	$[-]$

the simulation time was shorter, $t_s \approx 18\,[s]$. However, this is sufficient for determining the bed velocity.

The same procedure for the flow velocity has been followed as done during the closed flume experiments determining the sand bed velocity. First, the start velocity, V_b, is set to the desired flow velocity. After approximately $3\,[s]$, the flow velocity decreases, mimicking the closing the valve. The bed height, at t_1 the first time level, is determined as soon as a bed is formed in the lowest grid cell, at a density of $\rho_m \approx 1850\,[kg/m^3]$. The bed height at t_2 is determined if a distance of $d \approx 1\,[cm]$ is covered. In the runs with a high end-velocity, run 2 and run 4, this was not possible. The sand bed is eroded too rapidly. A possible cause is the relatively short flume length, in comparison with the closed flume

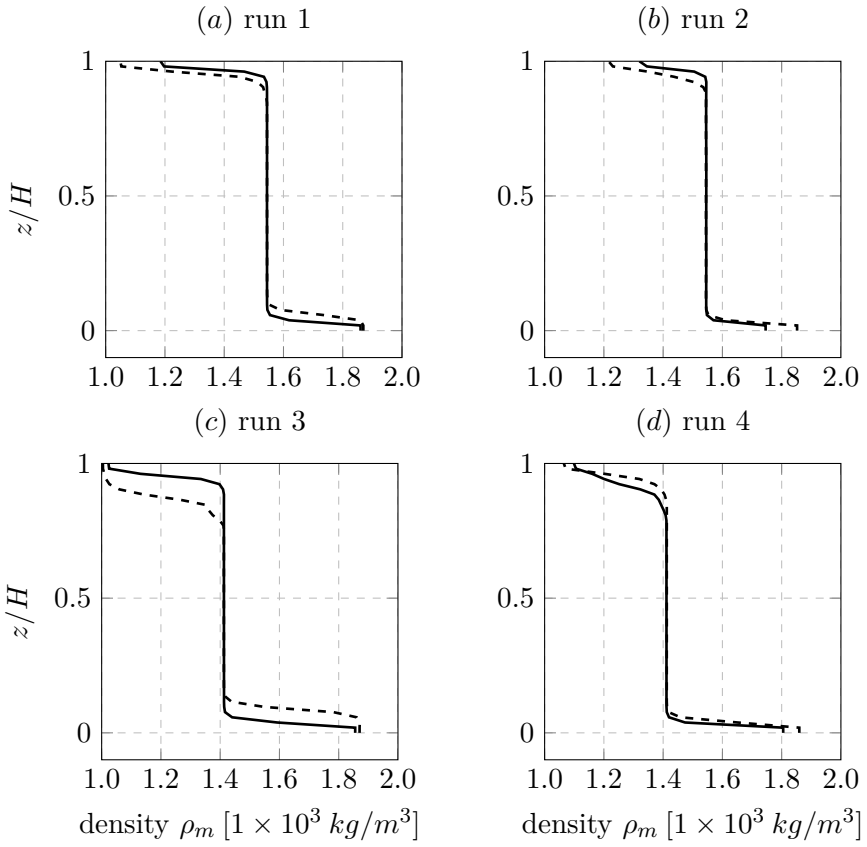

Figure 8.4: Density profiles of the closed flumes at two consecutive time intervals. The continuous line is the density profile at $t = t_1$ and the dashed line at $t = t_2$. Using these profiles the sand bed velocity is estimated.

experiments, used in the calculations. Furthermore, in the numerical model, no erosion model is used. The influence, of the short flume length and an erosion model on the bed velocity, needs to be investigated in additional research. In run 2 and 4 the second time level was set equal to the time when the end flow velocity was reached. Subsequently the difference in bed height, between t_1 and t_2, was determined. The sand bed velocity is obtained by dividing difference of the bed height by the time difference, $\Delta t = t_2 - t_1$. Figure 8.4 $(a) - (d)$ show the density profiles at t_1 (continuous line) and t_2 (dashed line) for run $1 - 4$. From this figure a sharp density jump can be observed demarcating

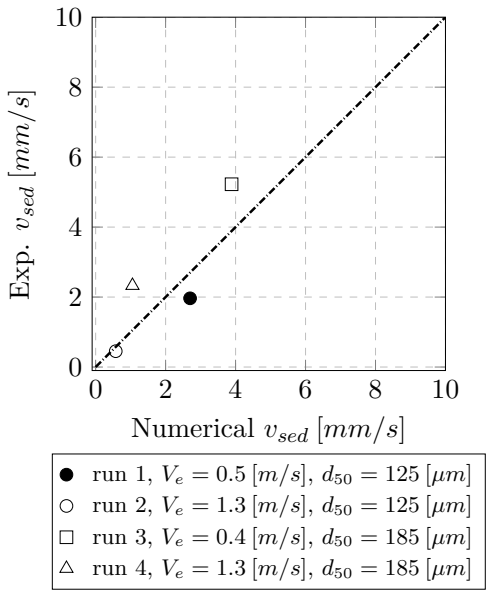

Figure 8.5: Comparison between the experimentally measured sediment bed velocity and the calculated sediment bed velocity.

the sand water interface, or the bed height. The difference in bed heights between the time levels, t_1 and t_2, is less distinct of the calculations with a high end flow velocity, run 2 and run 4. This is to be expected as the end velocity of run 2 and run 4, with a mean particle size of $d_{50} = 125\,[\mu m]$ and $d_{50} = 185\,[\mu m]$ respectively, is $V_e = 1.3\,[m/s]$. When the end velocity is higher the sand bed velocity is lower. The bed height difference is more distinct when the end flow velocity is small, this can be seen from the plots of run 1 and 3. Here the end velocity for run 1 and run 3 is $V_e = 0.5\,[m/s]$ and $V_e = 0.4\,[m/s]$ respectively. The mean particle size for run 1 and run 3 is $d_{50} = 125\,[\mu m]$ and $d_{50} = 185\,[\mu m]$ respectively. In both cases the sand bed velocity is higher due to the lower end velocities.

The calculations with the resulting sand bed velocity are compared with actual experiments. Figure 8.5 shows the results of the experimentally measured (vertical axis) and calculated sand bed velocity (horizontal axis). The markers denote the results of the 4 calculations in comparison with the experimental results. The dashed line in the figure is a line under 45^o. The markers would

collapse on this line if the calculated results exactly correspond with the experimental results. The calculated results are in the same order of magnitude although some differences can be observed between the numerical and experimental results. Nevertheless, the numerical model performs satisfactory, at least qualitatively, in predicting the sediment bed velocity.

8.3.1 Concluding remarks

In this chapter, sand bed velocity has been calculated and compared with experiments. In total 4 calculations have been carried out, in which the start and end-velocity, the particle size and the volume concentration have been varied. It turns out, from the experiments, that bed velocity is low when the end velocity is (relatively) high. Moreover, in case of a large mean particle size, 185 $[\mu m]$, the sand bed velocity is higher in comparison with the smaller particle size 125 $[\mu m]$. During the experiments, the sand bed velocity has been measured over a height difference of 1 $[cm]$. Unfortunately, this distance could not be covered for some numerical calculations. In these cases, the bed velocity was determined over a smaller difference of the sand bed height.

The calculated results are in the same order of magnitude as the experimental results. Moreover, the model is able to predict, at least qualitatively, a high sand bed velocity in case of large mean particle sizes and low end-velocities. Furthermore, the model predicts a low sand bed velocity in case of small mean particle size and a high end-velocity.

Calculations have been performed with the numerical model as is. This has been done without an explicitly modeling the (complex) interactions at the sediment-fluid interface. A possible modeling approach is to adjust the transport equations, of the sediment fractions, near the bed. This is done as such that the pickup flux of the particles corresponds to the experimentally determined pickup flux.

Chapter 9

Conclusions and Recommendations

9.1 Introduction

In this thesis, the hydrodynamical behavior of sand water mixtures was studied and a numerical model was made (the drift-flux model). The volume concentration of solids range from $\alpha_t = 0...0.6\,[-]$, i.e from a very dilute suspension to a dense granular flow. In the next sections, the main conclusions and recommendations are given.

9.2 Suspended particle transport

9.2.1 Drift-flux model

It is assumed, in the drift-flux model that particle sizes are small and that the particle reacts instantaneous, i.e. the particle reaction time is small compared to changes in time of the fluid velocity.

An equation of motion of the particle (using only the drag force), in combination with a fluctuating surrounding fluid, has been used in order to check the validity of this assumption. For larger time and length scales (with respect to the particle size), the particle reacts instantly to velocity fluctuations.

When the frequency of the fluctuation is increased and the amplitude of the velocity fluctuation is decreased. Typically with a decreasing vortex size the vortex frequency increases, approximately $100[Hz]$. For instance with the particle size of the order of magnitude of $d_p \approx 300\ [\mu m]$, the particle is not able to follow the flow directly. When these conditions are met, the drift-flux model breaks down.

9.2.2 Batch sedimentation

The sensitivity of three empirical models, for the Richardson and Zaki index n has been investigated by using a settling column test. This has been done in combination with different empirical models calculating the terminal settling velocity. The results from the calculation have been compared with experimental results. A difference in settling rate between the empirical models could be observed. This is not surprising when dealing with natural sediments.

9.2.3 Open channel flow experiments

Various open channel flow experiments were chosen in which the velocity the (mean) particle size, the particle density and the volume concentration were varied. Velocity and the concentration profiles experiments were compared with the computational results. The agreement of the results was favorable except for one experimental dataset. In these experiments, the flume length was relatively short, in comparison with other experimental setups. It is suspected that, with this short length, the flow was still developing.

9.3 Granular flows

The hydrodynamical behavior of dense granular flows has been modeled. The physical parameters governing the flow of the dense granular bed are the initial volume concentration, the shear rate, the particle diameter. These parameters influence the pore pressures, affecting the dynamics of the dense granular flow.

The model is validated with small-scale experiments concerning a granular collapse of glass beads. The motion of the granular collapse of a column is strongly governed by the initial volume concentration of the granular body. Two different behaviors can be distinguished corresponding to the dense and loose regime.

In the dense case, the column collapses slowly, caused by the water being sucked into the sediment stabilizing the column. This inflow of water increases effectively the pore pressure, in turn increasing the yield stress. The opposite happens in the loose case where the pore water flows out of the sediment column decreasing the yield stress. In this case, the sediment column flows rapidly. The model predicts the aforementioned behavior well for both the loose and dense case. The run-out length and the shape after collapse correspond with the experimental results. It is shown that the pore pressure is an important parameter and needs to be taken into account describing dense granular flows.

9.4 Numerical modeling

9.4.1 Flux Corrected Transport

As sediment settles, sediment accumulates at the bottom of the (computational) domain. The maximum volume concentration at which this occurs is limited to a maximum concentration of $\alpha_t = 0.6\,[-]$. In the model, special precautions need to be taken for limiting the amount of volume concentration of solids to this maximum allowable value. Therefore, a Flux-Corrected Transport limiter has been implemented. This limiter is computationally efficient (using only one time step), and is capable of handling multiple particle sizes.

9.4.2 Implementation boundary conditions

The imposed boundary conditions govern the outcome of the computational results. Special care had to be taken, at the boundaries, for the sediment-laden open channel flows. In these cases, a partial slip velocity was imposed at the boundary (bottom wall) of the channel. Where a constant was chosen heuristically matching the experimental velocity profile in the horizontal direction. This method is robust to use and yields satisfying results. The same approach, i.e. using a partial slip velocity boundary, was used for the dense granular flow tests. The slip length used was chosen equivalent to the values known from the literature. The use of such boundary conditions works well in the model from a numerical point of view. However, fitting is required yielding numerical results which correspond with the experimental results.

9.5 Recommendations

The following recommendations are done regarding the suspended particle transport, mixture flows, sediment bed modeling, and the use of boundary conditions and finally erosion modeling.

9.5.1 Mixture flows

The drift-flux model has been proven to be a good method describing sand/water mixtures, including multiple particle sizes. In this work only the effect of the drag force has been investigated in combination with a fluctuating surrounding fluid. However, when dealing with mixtures, the volume concentration of solids is increased. Therefore, it is recommended to assess the effect of volume concentration on the particle reaction time.

9.5.2 Dense granular flows

In dense granular flows, the pore pressure plays an important role in the motion of the sediment bed. A granular collapse of a sediment column has been used as a benchmark. It is recommended to investigate the pore pressure distribution, using an array of pressure sensors, of a collapsing column. These should be done for both the loose and dense initial volume concentration. These pressures provide data which are used for further calibration of the model.

9.5.3 Boundary conditions

Partial slip velocities were used as a boundary condition at the bottom wall for both the open channel flow tests, and the granular collapse cases (dense and loose). It is recommended, for the open channel flow tests, to investigate the interaction between the wall and the particles and inter-particle interaction near the bottom wall boundary. These interactions (near the boundary) are difficult to determine experimentally. Therefore, a DNS calculation, including particles, is a possible solution for providing the required results. With help of these results relevant spatially averaged quantities which can be incorporated in a non-DNS numerical model.

9.5.4 Erosion modeling

In this work an erosion model, at the sand bed water interface, was not taken into account. However, an important part of hydraulic sediment handling is erosion. Examples, where erosion of sediment plays a major role in dredging, is the use of jets at the drag head or erosion of sand during hopper filling. An extension of the model is, to take into account the erosion of sediment. A possible modeling approach is to adjust the transport equations, for the motion of the sediment fractions, near the bed. This is done in such a way that pickup of particles mimics the movement of this particle near the sediment bed.

Bibliography

Ahmadi, G. (2013). Me637 particle transport, deposition and removal on-line curriculum. http://www.clarkson.edu/projects/crcd/me637/downloads/T1_TURBULENCE.pdf.

Ahmadi, G. and Ma, D. (1990). A thermodynamical formulation for dispersed multiphase turbulent flows—1: Basic theory. *International Journal of Multiphase Flow*, 16(2):323 – 340.

Akker, H. v. d. and Mudde, R. F. (2014). *Transport Phenomena: The Art of Balancing*. Delft Academic Press/VSSD.

Albaraki, S. and Antony, S. J. (2014). How does internal angle of hoppers affect granular flow? experimental studies using digital particle image velocimetry. *Powder Technology*, 268:253 – 260.

Almering, J. (1996). *Analyse*. Delft Academic Press, 6th edition.

Andreau, J. (1991). Claude domergue, les mines de la péninsule ibérique dans l'antiquité romaine. *Annales*, 46(5):1117–1119.

Andreotti, B., Forterre, Y., and Pouliquen, O. (2013). *Granular Media*. Cambridge University Press.

Armfield, S. and Street, R. (2000). Fractional step methods for the navier-stokes equations on non-staggered grids. *ANZIAM J.*, page C134–C156.

Armfield, S., Williamson, N., Kirkpatrick, M. P., and Street, R. (2010). A divergence free fractional-step method for the navier–stokes equations on non-staggered grids. *ANZIAM J.*, pages C654–C667.

Artoni, R., Santomaso, A., and Canu, P. (2009). Effective boundary conditions for dense granular flows. *Phys. Rev. E*, 79:031304.

Bagnold, R. (1954). Experiments on the gravity free dispersion of large solid spheres in a newtonian fluid under shear. *Proceedings of the Royal Society Series A*, 225:40–63.

Bagnold, R. A. (1956). The flow of cohesionless grains in fluids. *Philosophical Transactions A*, 249(964):235–297.

Barrett, R., Berry, M., Chan, T. F., Demmel, J., Donato, J., Dongarra, J., Eijkhout, V., Pozo, R., Romine, C., and der Vorst, H. V. (1994). *Templates for the Solution of Linear Systems: Building Blocks for Iterative Methods, 2nd Edition*. SIAM, Philadelphia, PA.

Basson, D. K., Berres, S., and Buerger, R. (2009). On models of polydisperse sedimentation with particle-size-specific hindered-settling factors. *Applied Mathematical Modelling*, 33(4):1815 – 1835.

Beaubert, F. and Viazzo, S. (2001). Large eddy simulations of plane turbulent impinging jets. In *14th Australian Fluid Mechanics Conference*, pages 425–428, Adelaide University, Adelaide, Australia.

Beaubert, F. and Viazzo, S. (2002). Large eddy simulation of a plane impinging jet. *Comptes Rendus Mécanique*, 330(12):803 – 810.

Bilger, R. W. (1975). A note on favre averaging in variable density flows. *Combustion Science and Technology*, 11(5-6):215–217.

Bingham, E. (1922). *Fluidity And Plasticity*. Mcgraw-Hill Book Company,Inc.

Bird, R., Stewart, W., and N., L. E. (2002). *Transport Phenomena*. John Wiley, second edition.

Boris, J. and Book, D. (1973). Flux-corrected transport I: SHASTA, a fluid transport that works. *Journal of Computational Physics*, 11:38–69.

Botella, O. and Peyret, R. (1998). Benchmark spectral results on the lid-driven cavity flow. *Computers & Fluids*, 27(4):421–433.

Boyer, F., Guazzelli, E., and Pouliquen, O. (2011). Unifying suspension and granular rheology. *Physical Review Letters*, 107:188301.

Bray, R., A.D., B., and Land, J. (1997). *Dredging: A Handbook for Engineers*. Arnold.

Briggs, W. L., Van Emden, H., and McCormick, S. F. (2000). *A Multigrid Tutorial*. Society for Industrial and Applied Mathematics, Philadelphia, PA, USA, second edition.

Camenen, B. and van Bang, D. P. (2011). Modelling the settling of suspended sediments for concentrations close to the gelling concentration. *Continental Shelf Research*, 31(10, Supplement):S106 – S116. Proceedings of the 9th International Conference on Nearshore and Estuarine Cohesive Sediment Transport Processes.

Camp, T. (1946). Sedimentation and the design of settling tanks. *Trans. ASCE*, 111(2285):895 – 936.

CAPP (2018). What are the oil sands? https://www.canadasoilsands.ca/en/what-are-the-oil-sands.

Carman, P. . (1956). *Flow of Gases through Porous Media*. Acad. Press, New York.

Cassar, C., Nicolas, M., and Pouliquen, O. (2005). Submarine granular flows down inclined planes. *Physics of Fluids*, 17(10):103301.

Chapman, D. R. (1979). Computational aerodynamics development and outlook. *AIAA Journal*, 17:1293–1313.

Chapra, S. and Canale, R. (2010). *Numerical Methods for Engineers*. Mc Graw-Hill, 6th edition.

Cheng, N.-S. (1997). Simplified settling velocity formula for sediment particle. *Journal of Hydraulic Engineering*, 123:149–152.

Chiodi, F., Claudin, P., and Andreotti, B. (2014). A two-phase flow model of sediment transport: transition from bedload to suspended load. *Journal of Fluid Mechanics*.

Choi, H. and Moin, P. (2012). Grid-point requirements for large eddy simulation: Chapman's estimates revisited. *Physics of Fluids*, 24.

Chorin, A. J. (1968). Numerical solution of the navier-stokes equations. *Mathematics of Computation*, 22(104):pp. 745–762.

Chumakov, S. (2005). *Subgrid Models for Large-Eddy Simulation: Scalar Flux, Scalar Dissipation and Energy Dissipation*. PhD thesis, University of Wisconsin-Madison.

Coleman, N. L. (1970). Flume studies of the sediment transfer coefficient. *Water Resources Research*, 6(3):801–809.

Courrech du Pont, S., Gondret, P., Perrin, B., and Rabaud, M. (2003). Granular avalanches in fluids. *Physical Review Letters*, 90(4).

Cziesla, T., Biswas, G., Chattopadhyay, H., and Mitra, N. (2001). Large-eddy simulation of flow and heat transfer in an impinging slot jet. *International Journal of Heat and Fluid Flow*, 22(5):500 – 508.

da Cruz, F., Emam, S., Prochnow, M., Roux, J.-N., and Chevoir, F. m. c. (2005). Rheophysics of dense granular materials: Discrete simulation of plane shear flows. *Physical Review E*, 72:021309.

De Wit, L. (2014). *3D CFD modeling of overflow dredging plumes*. PhD thesis, Delft University of Technlogy.

Deardorff, J. (1970). A numerical study of three-dimensional turbulent channel flow at large reynolds numbers. *Journal of Fluid Mechanics*, 41:453–480.

DEME (2014). Opening of new airport in doha is a calling card for deme. https://www.deme-group.com/news/opening-new-airport-doha-calling-card-deme.

Den Adel, H. (1987). Heranalyse doorlatendheidmetingen door middel van de Forchheimer relatie. Technical Report CO-272550/56, GeoDelft.

Drew, D. A. (1983). Mathematical modeling of two-phase flow. *Annual Review of Fluid Mechanics*, 15(1):261–291.

Eilers, H. (1941). Die viskosit at von emulsionen hochviskoser stoffe als funktion der konzentration. *Kolloid-Zeitschrift*, 97(3):313–321.

Einstein, A. (1906). Eine neue bestimmung der moleküldimensionen. *Annalen der Physik*, 19:289–306.

Einstein, H. A. and Chien, N. (1955). Effects of heavy sediment concentration near the bed on velocity and sediment distribution. Technical report, Univ. of California, Institute of Engineering Research and US Army Corps of Engineers.

Ekambara, K., Sanders, R. S., Nandakumar, K., and Masliyah, J. H. (2009). Hydrodynamic simulation of horizontal slurry pipeline flow using ansys-cfx. *Industrial & Engineering Chemistry Research*, 48(17):8159–8171.

Evans, L. (1997). *Partial Differential Equations*. American Mathematical Society.

Fadlun, E., Verzicco, R., Orlandi, P., and Mohd-Yusof, J. (2000). Combined immersed boundary finite difference methods for three dimensional complex flow simulations. *Journal of Computational Physics*, 161:35–60.

Ferguson, R. and Church, M. (2004). A simple universal equation for grain settling velocity. *Journal of Sedimentary Research*, 74(6):933–937.

Ferziger, J. H. and Peric, M. (1999). *Computational Methods for Fluid Dynamics*. Springer, New York, 2nd edition.

Fletcher, C. (1988). *Computational Techniques for Fluid Dynamics 1*. Springer-Verlag.

Fortrerre, Y. and Pouliquen, O. (2009). Granular flows. In *Séminaire Poincaré XIII*, pages 69–100, 5, rue Enrico Fermi 13453 Marseille Cedex 13, France. CNRS-Université de Provence.

Garside, J. and Al-Dibouni, M. (1977). Velocity-voidage relationships for fluidization and sedimentation in solid-liquid systems. *2nd Industrial & Engineering Chemistry Process Design and Development*, 16.

GDR-MiDi (2004). On dense granular flows. *European Physical Journal E*, 14(4):341–365.

Ghia, U., Ghia, K. N., and Shin, C. T. (1982). High-Re solutions for incompressible flow using the navier-stokes equations and a multigrid method. *Journal of Computational Physics*, 48:387–411.

Ghosal, S. and Moin, P. (1995). The basic equations for the large eddy simulation of turbulent flows in complex geometry. *Journal of Computational Physics*, 118(1):24 – 37.

Gillies, R. G. (1993). *Pipeline flow of coarse particle slurries*. PhD thesis, The University of Saskatchewan.

Goeree, J., Keetels, G., and Rhee, C. (2017). Particle settling using the immersed boundary method. In *Proceedings of the 18th International Conference Transport and Sedimentation of Solid Particles*.

Goeree, J. and Rhee, C. v. (2013). Numerical simulation of hydrodynamical behaviour of sand water mixtures. In *Proceedings of the 20th World Dredging Conference (WODCON XX)*.

Goeree, J. C., Keetels, G., Munts, E., Bugdayci, H., and Rhee van, C. (2016). Concentration and velocity profiles of sediment-water mixtures using the drift flux model. *The Canadian Journal of Chemical Engineering*, 94(6):1048–1058.

Gorb, Y., Mierka, O., Rivkind, L., and Kuzmin, D. (2013). Finite element simulation of three–dimensional particulate flows using mixture models. Technical report, Fakultät für Mathematik, TU Dortmund. Ergebnisberichte des Instituts für Angewandte Mathematik, Nummer 484.

Gualtieri, C., Angeloudis, A., Bombardelli, F., Jha, S., and Stoesser, T. (2017). On the values for the turbulent schmidt number in environmental flows. *Fluids*, 2(2).

Guennebaud, G., Jacob, B., et al. (2010). Eigen v3. http://eigen.tuxfamily.org.

Guermond, J.-L. and Salgado, A. (2008). A fractional step method based on a pressure poisson equation for incompressible flows with variable density. *Comptes Rendus Mathematique*, 346(15-16):913 – 918.

Guermond, J.-L. and Salgado, A. (2009). A splitting method for incompressible flows with variable density based on a pressure poisson equation. *Journal of Computational Physics*, 228(8):2834 – 2846.

Haider, A. and Levenspiel, O. (1989). Drag coefficient and terminal velocity of spherical and nonspherical particles. *Powder Technology*, 58(1):63–70.

Hallemeier, R. J. (1981). Terminal settling velocity of commonly occurring sand grains. *Sedimentology*, 28:859–865.

Herbich, J. B. (2000). *Handbook of dredging engineering*. McGraw-Hill„ New York.

Hiltunen, K., Jasberg, A., Kallio, S., Karema, H., Kataja, M., Koponen, A., Manninen, M., and Taivassalo, V. (2009). Multiphase flow dynamics: Theory and numerics. Technical report, VTT.

Hirsch, C. (1990). *Numerical Computation of Internal and External Flows*, volume 1. John Wiley and Sons, Chichester, England.

Hoffmann, G. and Benocci, C. (1994). Numerical simulation of spatially-developing planar jets. In *74th Fluid Dynamics Symposium on Application of Direct and Large Eddy Simulation of Transition and Turbulence*, pages 1–6.

Hundsdorfer, W. (2000). Numerical solution of advection-diffusion-reaction equations. Technical report, CWI Thomas Stieltjes Institute.

Hunt, M. L., Zenit, R., Campbell, C. S., and Brennen, C. E. (2002). Revisiting the 1954 suspension experiments of R. A. Bagnold. *Journal of Fluid Mechanics*, 452:1 – 24.

Hunter, J. (2014). Notes on partial differential equations. https://www.math.ucdavis.edu/~hunter/pdes/pde_notes.pdf.

Ishii, M. (1975). *Thermo-fluid Dynamics Theory of Two-phase Flow*. Eyrolles.

Ishii, M. and Hibiki, T. (2006). *Thermo-fluid dynamics of two-phase flow*. Birkhäuser.

Iverson, R. M. (1997). The physics of debris flows. *Reviews of Geophysics*, 35:245–296.

Iverson, R. M. (2005). Regulation of landslide motion by dilatancy and pore pressure feedback. *Journal of Geophysical Research*, 110, F02015.

Iverson, R. M. (2013). *Handbook of Environmental Fluid Dynamics*. CRC Press / Taylor & Francis.

Jaeger, H. M., Nagel, S. R., and Behringer, R. P. (1996). Granular solids, liquids, and gases. *Reviews of Modern Physics*, 68(4):1259–1273.

Jakobsen, H. (2014). *Chemical Reactor Modeling: Multiphase Reactive Flows*. Springer International Publishing, 2 edition.

Jop, P., Forterre, Y., and Pouliquen, O. (2006). A constitutive law for dense granular flows. *Nature*, 441:727–730.

Kaitna, R. and Rickenmann, D. (2007). Flow of different material mixtures in a rotating drum. In P., C. and C., C., editors, *Debris Flow Hazards Mitigation: Mechanics, Prediction, and Assessment. Proceedings of the 4th International DFHM Conference Chengdu, China*.

Kaushal, D., Seshadri, V., and Singh, S. (2002). Prediction of concentration and particle size distribution in the flow of multi-sized particulate slurry through rectangular duct. *Applied Mathematical Modelling*, 26(10):941 – 952.

Keetels, G., Clercx, H., and van Heijst, G. (2007). Fourier spectral solver for the incompressible navier-stokes equations with volume-penalization. In Shi, Y., van Albada, G., Dongarra, J., and Sloot, P., editors, *Computational Science – ICCS 2007*, volume 4487 of *Lecture Notes in Computer Science*, pages 898–905. Springer Berlin Heidelberg.

Kim, J. and Moin, P. (1985). Application of a fractional-step method to incompressible navier-stokes equations. *Journal of Computational Physics*, 59(2):308–323.

Klerk, A. d., Meulepas, J., Van Rhee, C., and Kranenburg, C. (1998). Bezinken van zand in hopperzuigers, invloed van turbulentie en korrelverdeling. Technical report, Delft University of Technology.

Konijn, B. (2016). *Numerical simulation methods for dense-phase dredging flows*. PhD thesis, University of Twente.

Kozeny, J. (1927). Über kapillare Leitung des Wassers im Boden. *Akademie der Wissenschaften in Wien*, 136:271–306.

Krieger, I. M. and Dougherty, T. J. (1959). A mechanism for non-Newtonian flow in suspensions of rigid spheres. *Transactions of the Society of Rheology*, 3:137–152.

Kumaran, V. (2015). Kinetic theory for sheared granular flows. *Comptes Rendus Physique*, 16(1):51 – 61. Granular physics / Physique des milieux granulaires.

Küng, M. (2007). *Large Eddy Simulation of Turbulent Channel and Jet Flows using the Approximate Deconvolution Model*. PhD thesis, ETH.

Kuzmin, D. and Gorb, Y. (2012). A flux-corrected transport algorithm for handling the close-packing limit in dense suspensions. *Journal of Computational and Applied Mathematics*, 236(18):4944 – 4951. FEMTEC 2011: 3rd International Conference on Computational Methods in Engineering and Science, May 9-13, 2011.

Kynch, G. J. (1952). A theory of sedimentation. *Transactions of the Faraday Society*, 48:166–176.

Lalli, F., Esposito, P. G., Piscopia, R., and Verzicco, R. (2005). Fluid particle flow simulation by averaged continuous model. *Computers & Fluids*, 34(9):1040 – 1061.

Lalli, F., Esposito, P. G., and Verzicco, R. (2006). A constitutive equation for fluid-particle flow simulation. *International Society of Offshore and Polar Engineers*, 16:18–24.

Lalli, F. and Mascio, A. D. (1997). A numerical model for fluid-particle flows. *International Journal of Offshore and Polar Engineering*, 7.

Leonard, B. (1979). A stable and accurate convective modelling procedure based on quadratic upstream interpolation. *Computer Methods in Applied Mechanics and Engineering*, 19:59–98.

LeVeque, R. J. (1992). *Numerical Methods for Conservation Laws*. Lectures in mathematics ETH Zürich. Birkhäuser Basel, 2nd edition.

Ling, Y., Parmar, M., and Balachandar, S. (2013). A scaling analysis of added-mass and history forces and their coupling in dispersed multiphase flows. *International Journal of Multiphase Flow*, 57:102 – 114.

Lowe, R. J., Rottman, J. B. K. W., and Linden, P. F. (2005). The non-boussinesq lock-exchange problem. part 1. theory and experiments. *Journal of Fluid Mechanics*, 537:101.

Manninen, M. and Taivassalo, V. (1996). On the mixture model for multiphase flow. Technical report, VTT Energy.

Mastbergen, D. and Winterwerp, J. (1987). Het gedrag van zand-watermengselstromingen boven water; experimentele vervolgstudie. z46-2, WL|Delft Hydraulics.

Matousek, V. (1997). *Flow Mechanism of Sand-Water Mixtures in Pipelines*. PhD thesis, Delft University of Technology.

Matousek, V. (2002). Pressure drops and flow patterns in sand-mixture pipes. *Experimental Thermal and Fluid Science*, 26(6–7):693 – 702.

Maurel, S. and Solliec, C. (2001). A turbulent plane jet impinging nearby and far from a flat plate. *Experiments in Fluids*, 31(6):687–696.

Maxey, M. R. and Riley, J. J. (1983). Equation of motion for a small rigid sphere in a nonuniform flow. *Physics of Fluids (1958-1988)*, 26(4):883–889.

Miedema, S. (2016). *Slurry Transport*. Delft University of Technology, 1st edition.

Mirza, S. and Richardson, J. F. (1979). Sedimentation of suspensions of particles of two or more sizes. *Chemical Engineering Science*, 34:447–454.

Mitsoulis, E., Abdali, S. S., and Markatos, N. C. (1993). Flow simulation of herschel-bulkley fluids through extrusion dies. *The Canadian Journal of Chemical Engineering*, 71(1):147–160.

Moin, P. (2010). *Fundamentals of Engineering Numerical Analysis*. Cambridge University Press, 2nd edition.

Moser, R. D., J., K., and Mansour, N. N. (1999). Direct numerical simulation of turbulent channel flow up to $Re_\tau = 590$. *Physics of Fluids*, 11(4):943–945.

Nabil, T., El-Sawaf, I., and El-Nahhas, K. (2014). Sand-water slurry flow modeling in a horizontal pipeline by computational fluid dynamics technique. *International Water Technology Journal*.

Namer, I. and Ötügen, M. (1988). Velocity measurements in a plane turbulent air jet at moderate reynolds numbers. *Experiments in Fluids*, 6(6):387–399.

Nicoud, F. and Ducros, F. (1999). Subgrid-scale stress modelling based on the square of the velocity gradient tensor. *Flow, Turbulence and Combustion*, 62:183–200.

Nikuradse, J. (1933). Stromungsgesetz in rauhren Rohren. *vDI Forshungsheft*, 361. in English, in Technical Memorandum 1292, National Advisory Committee for Aeronautics (1950).

Ooijens, S. (1999). Adding dynamics to the camp model for the calculation of overflow losses. *Terra et Aqua*, pages 12–21.

Paarlberg, A. J. (2008). *Modelling dune evolution and dynamic roughness in rivers*. PhD thesis, Universiteit Twente.

Paarlberg, A. J., Dohmen-Janssen, C. M., Hulscher, S. J. M. H., and Termes, P. (2009). Modeling river dune evolution using a parametparameter of flow separation. *Journal of Geophysical Research*, 114.

Pailha, M. and Pouliquen, O. (2009). A two-phase flow description of the initiation of underwater granular avalanches. *Journal of Fluid Mechanics*, 633:115–135.

Papanastasiou, T. C. (1987). Flows of materials with yield. *Journal of Rheology*, 31.

Parsons, J. D., Whipple, K., and Simoni, A. (2001). Experimental study of the grain-flow, fluid-mud transition in debris flows. *The Journal of Geology*, 109:427–447.

Peskin, C. (1972). Flow patterns around heart valves: A numerical method. *Journal of Computational Physics*, 10(2):252 – 271.

Peskin, C. S. (2002). The immersed boundary method. *Acta Numerica*, 11:479–517.

Pope, D. (2000). *Turbulent Flows*. Cambridge University Press, Cambridge.

Pouliquen, O., editor (2005). *How do grains flow: towards a simple rheology for dense granular flows*.

Prager, W. (1989). *Introduction to Mechanics of Continua*. Dover, Mineola, New York, first edition.

Press, W. H., Teukolsky, S. A., Vetterling, W. T., and Flannery, B. P. (1992). *Numerical Recipes*. Cambridge University Press, Cambridge.

Prosperetti, A. and Tryggvason, G. (2009). *Averaged equations for multiphase flow*, chapter 8, pages 256–262. Cambridge University Press.

Rhie, C. M. and Chow, W. L. (1983). Numerical study of the turbulent flow past an airfoil with trailing edge separation. *Aiaa Journal*, 21:1525–1532.

Richardson, J. and Zaki, W. (1954a). Sedimentation and fluidization: I. *Transactions of the Institutetution of Chemical Engineers*, 32(35).

Richardson, J. and Zaki, W. (1954b). The sedimentation of a suspension of uniform spheres under conditions of viscous flow. *Chemical Engineering Science*, 3:65–73.

Rondon, L., Pouliquen, O., and Aussillous, P. (2011). Granular collapse in a fluid: Role of the initial volume fraction. *Physics of Fluids (1994-present)*, 23(7):–.

Roshko, A. (1954). On the development of turbulent wakes from vortex streets. Report 1191, California Institute of Technology.

Rouse, H. (1937). Modern conceptions of the mechanics of fluid turbulence. *Transactions of the American Society of Civil Engineers*, pages 463–543.

Roux, S. and Radjai, F. (1999). Texture-dependent rigid-plastic behaviour. In Herrmann, H., Hovi, J., and Luding, S., editors, *Physics of Dry Granular Media*, pages 229–235, Dordrecht. Kluwer Acad. Pub.

Rowe, P. (1987). A convenient empirical equation for estimation of the richardson and zaki exponent. *Chemical Engineering Science*, 42:2795–2796.

Roy, C. (2003). Grid convergence error analysis for mixed-order numerical schemes. *AIAA Journal*, 41(4):595–604.

Sagaut, P. (2001). *Large eddy simulation for Incompressible flows*. Springer, Berlin.

Savage, S., Babaei, M., and Dabros, T. (2014). Modeling gravitational collapse of rectangular granular piles in air and water. *Mechanics Research Communications*, 56(0):1 – 10.

Schaefer, M. (2006). *Computational Engineering*. Springer.

Scott, S. (2006). Treasure on the ocean floor. *The Economist*, (8506).

Smagorinsky, J. (1963). General circulation experiments with the primitive equations i. the basic experiment. *Monthly Weather Rev.*, 91(3):99–164.

Stam, J. (1999). Stable fluids. In *SIGGRAPH '99: Proceedings of the 26th annual conference on Computer graphics and interactive techniques*, pages 121–128, New York, NY, USA. ACM Press/Addison-Wesley Publishing Co.

Staron, L., Lagrée, P.-Y., and Popinet, S. (2011). The granular column collapse as a continuum: validity of a navier-stokes model with a mu(i)-rheology. *Journal of Fluid Mechanics*.

Stickel, J. and Powell, R. (2005). Fluid mechanics and rheology of dense suspensions. *Annual Review of Fluid Mechanics*, 37:129–149.

Swamy, M., Gonzalez Diez, N., and Twerda, A. (2015). Numerical modelling of the slurry flow in pipelines and prediction of flow regimes. *Computational Methods in Multiphase Flow VIII*, 89:311–322.

Sylvester, Z. (2013). Exploring grain settling with python. http://hinderedsettling.com/.

Thomas, D. (1965). Transport characteristics of suspension: Viii. a note on the viscosity of newtonian suspensions of uniform spherical particles. *Journal of Colloid Science*, 20(3):267 – 277.

Thomas, G. B. and Finney, R. L. (1996). *Calculus*. Addison Wesley, 9th edition.

Thomas, P. (1982). Present wind activity on mars: Relation to large latitudinally zoned sediment deposits. *Journal of Geophysical Research: Solid Earth*, 87(B12):9999–10008.

Tritton, D. J. (1959). Experiments on the flow past a circular cylinder at low reynolds numbers. *Journal of Fluid Mechanics*, 6:547–567.

Tsai, C. and Tsai, C. T. (2000). Velocity and concentration distributions of sediment-laden open channel flow1. *JAWRA Journal of the American Water Resources Association*, 36(5):1075–1086.

Van den Berg, C. (2013). *HC Merwede Handbook for Centrifugal Pumps and Slurry Transportation*. Royal IHC.

Van Driest, E. (1956). On turbulent flow near a wall. *Journal of Aeronautical Sciences*, 23(11):1007–1011.

Van Kan, J. (1986). A second-order accurate pressure correction scheme for viscous incompressible flow. *SIAM Journal on Scientific and Statistical Computing*, 7(3):870–891.

Van Kan, J. and Segal, A. (1993). *Numerieke methoden voor partiële differentiaalvergelijkingen*. DUM.

Van Leer, B. (1974). Towards the ultimate conservative difference scheme ii. monotonicity and conservation combined in a second order scheme. *Journal of Computational Physics*, 14(4).

Van Rhee, C. (2001). Modelling the sedimentation process in a trailing suction hopper dredge. In *4th Int. Conference on Multiphase Flows*, New Orleans, USA.

Van Rhee, C. (2002). *On the sedimentation process in a trailing suction hopper dredger*. PhD thesis, Delft University of Technology.

Van Rhee, C. (2011). One dimensional sedimentation of multi-sized particles. In *15th Transport and Sedimentation Conference*, pages 157 – 168, Wroclaw, Poland.

Van Rhee, C. and Bezuijen, A. (1992). Influence of seepage on the stability of a sandy slope. *Journal of Geotechnical Engineering*, 118(8):1236 – 1240.

Van Rhee, C. and Bezuijen, A. (1998). The breaching of sand investigated in large-scale model tests. In *Proc. Int. Coastal Eng. Conf.*, volume 3, pages 2509–2519.

Van Rijn, L. (1984). Sediment transport, part ii: Suspended load transport. *Journal of Hydraulic Engineering*, 110(11):1613–1641.

Van Rijn, L. (1989). Handbook: sediment transport by currents and waves. Technical report, Delft Hydraulics, Delft, The Netherlands.

Van Wijk, J. (2016). *Vertical Hydraulic Transport*. PhD thesis, Delft University of Technology.

VanOord (2001). The transformation of Dubai. https://www.vanoord.com/activities/dubai.

Verruijt, A. (1993). *Grondmechanica*. DUM.

Versteeg, H. K. and Malalasekera, W. (1995). *An Introduction to Computational Fluid Dynamics, The finite Volume Method*. Prentice Hall, London.

Vlasblom, W.and Miedema, S. (1995). A theory for determining sedimentation and overflow losses in hoppers. In *Proc. WODCON IV, Amsterdam*.

Voke, P. and Gao, S. (1995). Large-eddy simulations of plane impinging jets. *International Journal of Methods in Engineering*.

Voller, V. R. and Swaminathan, C. R. (1993). Treatment of discontinuous thermal conductivity in control-volume solutions of phase-change problems. *Numerical Heat Transfer, Part B: Fundamentals*, 24(2):161–180.

Wadell, H. (1932). Volume, shape, and roundness of rock particles. *The Journal of Geology*, 40(5):pp. 443–451.

Wallis, G. (1969). *One dimensional two-phase flow*. Mc Graw-Hill.

Wang, M. and Moin, P. (2002). Dynamic wall modeling for large-eddy simulation of complex turbulent flows. *Physics of Fluids*, 14:2043–2052.

Wang, X. and Qian, N. (1989). Turbulence characteristics of sediment-laden flow. *Journal of Hydraulic Engineering*, 115(6):781–800.

Werner, H. and Wengle, H. (1993). Large eddy simulation of turbulent flow around a cube in a plane channel. In Durst, F., Friedrich, R., Launder, B., Schumann, U., and Whitelaw, J., editors, *Selected Papers From the 8th Symp. on Turb. Shear Flows*, pages 155–168, New York. Springer.

Wesseling, P. (2000). *Principles of Computational Fluid Dynamics*. Springer-Verlag New York, Inc., Secaucus, NJ, USA.

White, F. M. (1999). *Fluid Mechanics*. WCB McGraw-Hill, fourth edition.

Wilson, K. (1976). Unified physically based analysis of slurry pipeline flow. In *Proceedings Hydrotransport 4*, pages 1–16. BHRA, Cranfield UK.

Winterwerp, J. (2001). Stratification effects by cohesive and noncohesive sediment. *Journal of Geophysical Research*.

Zalesak, S. (1979). Fully multidimensional flux corrected transport algorithms for fluids. *Journal of Computational Physics*, 31:335–362.

Zanke, U. (1977). Berechnung der sinkgeschwindigkeiten von sedimenten. *Mitt. Des Franzius-Instituts fur Wasserbau*, Heft 46:243.

Zuber, N. and Findlay, J. A. (1965). Average volumetric concentration in two-phase flow systems. *Journal of Heat Transfer*, 87(4):453–468.

List of Symbols

Greek symbols

δ	angle of internal friction	–
$\dot{\gamma}$	shear rate	s^{-1}
η	granular viscosity Pas	
Γ	diffusion coefficient	$m^2 s^{-1}$
γ	density ratio	–
λ_l	interpolation factor at cell face l	–
μ_i	intrinsic viscosity	–
μ_m	mixture viscosity	$kgm^{-1}s^{-1}$
μ_r	relative mixture viscosity	–
μ_s	Soil friction coefficient	–
ψ	dilatancy angle	–
ψ	pseudo pressure	$kgm^{-1}s^{-2}$
σ_v	vertical stress	$kgm^{-1}s^{-2}$
σ'_v	effective stress	$kgm^{-1}s^{-2}$

τ_0	Yield stress	$kgm^{-1}s^{-2}$
τ_b	bed shear stress	$kgm^{-1}s^{-2}$
u_w	pore water pressure	$kgm^{-1}s^{-2}$
α_k	volume phase k	–
α_f	liquid volume fraction	–
α_{tmax}	Maximum volume concentration of solids	–
Δ	filter width	m
Δ_x	grid spacing in x-direction	m
Δ_y	grid spacing in y-direction	m
Δ_z	grid spacing in z-direction	m
ϵ	energy dissipation rate per unit mass	$m^2\ s^{-3}$
η_l	length scale of smallest eddies	m
κ	von Kármán constant	–
μ	molecular viscosity	$m^{-1}\ s^{-1}$
ν_t	turbulent eddy viscosity	$m^2\ s^{-1}$
ω	Angular frequency	$rad\ s^{-1}$
φ	particle shape factor	–
ρ	fluid density	$kg\ m^{-3}$
ρ_k	fraction density	$kg\ m^{-3}$
ρ_m	mixture density	$kg\ m^{-3}$
σ_t	Schmidt-Prandtl number	–
α_t	solids volume fraction	–
τ_g	particle response time	s

τ_h	hydrodynamic time scale	s
Ω_{ij}	antisymmetric part of gradient velocity tensor	s^{-1}

Roman symbols

$\mathbf{q}$	specific discharge	ms^{-1}
$\mathbf{u}_s$	solid grain velocity in dense granular suspensions	ms^{-1}
A_v	eddy viscosity for partial slip condition	m^2s^{-1}
A_{cf}	cell face area of a grid cell	m^2
B	Width of the jet nozzle	m
b_w	Half width of the jet	m
C_s	Smagorinsky constant	m
cf	subscript cell face	$-$
D	domain width	m
D	Domain width	m
f	vortex shedding frequency	s^{-1}
H	domain height	m
H	Domain height	m
h_c	domain half height	m
I_2	second invariant of the deformation tensor	$m^2\ s^{-2}$
I_t	inertial number	$-$
I_v	viscous number	$-$
K_3	constant	$-$
k_c	intrinsic permeability	m^2
L	domain length	m

L	Domain length	m
P_s	Soil stress	$kgm^{-1}s^{-2}$
p_k	pressure of phase k	$kg\,m^{-1}\,s^{-2}$
Q_P^+	maximum admissible increment	m^3s^{-1}
R_P^+	correction factor	$-$
S_b	slip parameter	ms^{-1}
S_r	Strouhal number	$-$
S_{ij}	deformation tensor index notation	s^{-1}
t^*	dimensionless timescale	$-$
T_{ij}	stress tensor index notation	$kgm^{-1}s^{-2}$
$u^{'}$	velocity fluctuation in x-direction	ms^{-1}
u_0	fluid velocity upstream	ms^{-1}
u_τ	friction velocity	ms^{-1}
$v^{'}$	velocity fluctuation in y-direction	ms^{-1}
$w^{'}$	velocity fluctuation in z-direction	ms^{-1}
w_c	Velocity in z-direction at jet axis	ms^{-1}
$\mathbf{S}$	deformation tensor	s^{-1}
$\mathbf{T}$	stress tensor	$kgm^{-1}s^{-2}$
A_p	projected area of particle	m^2
C_w	constant WALE LES turbulence model	m
C_d	drag coefficient	$-$
c_k	mass fraction	$-$
D	pipe diameter	m

d_p	particle diameter	m
H_f	amplitude oscillating flow field	m
k_s	roughness height according to Nikuradse	m
L_l	length scale of largest eddies	m
m_p	particle mass	kg
m_p	particle mass	kg
N	total amount of fractions	$-$
n_k	Richardson and Zaki index for fraction k	$-$
n	Richardson and Zaki index	$-$
p	hydrodynamic pressure	$kg\,m^{-1}s^{-2}$
s	reduced surface area of a sphere	m^2
S	actual surface area of a sphere	m^2
St	Stokes number	$-$
U	bulk flow velocity	$m\,s^{-1}$
u^+	dimensionless velocity	$-$
u_τ	wall shear velocity	$m\,s^{-1}$
V_p	particle volume	kg
$w_{p\infty}$	terminal settling velocity of a particle in z-direction	$m\,s^{-1}$
y^+	wall coordinate	$-$
g_{ij}	gradient velocity tensor	s^{-1}
S^d_{ij}	deviatoric deformation tensor	s^{-1}
S_{ij}	deformation tensor	s^{-1}
$\mathbf{T}_{sgs}$	Sub grid-scale stress tensor	$kg\,m^{-1}s^{-2}$

$\mathbf{T}_k$	viscous stress tensor of phase k	$kg\,m^{-2}\,s^{-2}$
$\mathbf{T}_k^t$	turbulent stress tensor of phase k	$kg\,m^{-2}\,s^{-2}$
$\mathbf{a}_p$	particle acceleration	$m\,s^{-2}$
$\mathbf{F}$	sum of forces acting on a particle	$kg\,m\,s^{-2}$
$\mathbf{F}_b$	buoyancy force	$kg\,m\,s^{-2}$
$\mathbf{F}_d$	drag force	$kg\,m\,s^{-2}$
$\mathbf{F}_g$	gravitational force	$kg\,m\,s^{-2}$
$\mathbf{F}_h$	history force	$kg\,m\,s^{-2}$
$\mathbf{g}$	gravitational constant	$m\,s^{-2}$
$\mathbf{j}$	mixture volumetric flux vector	$m\,s^{-1}$
$\mathbf{m}_k$	particle interaction force of phase k per unit volume	$kgs^{-2}m^{-2}$
$\mathbf{s}$	body force	$kg\,m^{-2}\,s^{-2}$
$\mathbf{t}_{sgs}$	sub grid scale flux	$kg\,m^{-2}\,s^{-1}$
$\mathbf{u}$	velocity	$m\,s^{-1}$
$\mathbf{u}_f$	continuous phase velocity	$m\,s^{-1}$
$\mathbf{u}_k$	velocity of phase k	$m\,s^{-1}$
$\mathbf{u}_{k\infty}$	terminal settling velocity vector of fraction k	$m\,s^{-1}$
$\mathbf{u}_{kj}$	drift velocity vector	$m\,s^{-1}$
$\mathbf{u}_{km}$	diffusion velocity vector	$m\,s^{-1}$
$\mathbf{u}_{kr}$	relative phase velocity with respect to continuous phase	$m\,s^{-1}$
$\mathbf{v}_p$	particle velocity	$m\,s^{-1}$

Super Scripts

n	current time step	–

$n+1$	new time step	–
$n-1$	previous time step	–

Abbreviations

2D Two Dimensional.

3D Three Dimensional.

DNS Direct Numerical Simulation.

LES Large Eddy Simulation.

WALE Wall-adapting local eddy-viscosity.

Appendix A

AppendixA

A.1 Grid convergence study

To study the grid convergence the lid-driven cavity is taken as a benchmark problem. Here a Reynolds number of $Re = 100$ has been chosen. The explicit fractional step method is used for solving the incompressible Navier-Stokes equations. Here the advective terms are updated using the Adams-Bashfort method. An accurate solution, using a spectral method, of this problem is presented by Botella and Peyret (1998) for the case of $Re = 100$. The dependence of the numerical solution on the grid resolution is evaluated using successively refined grids. The spatial convergence rate can be estimated using the following formula, see Schaefer (2006) for instance,

$$p \approx \log\left(\frac{f_2 - f_1}{f_3 - f_2}\right)/\log r \tag{A.1}$$

where p is the grid convergence rate, r is the factor at which the grid is refined and $f_{1,2,3}$ is the solution on successively refined grids. In which f_1 is the solution on the coarsest grid and f_3 is the solution on the finest grid. Here 4 schemes are used for the discretization of the advection terms. These schemes are the following, CDS, Upwind, Quick scheme and a TVD scheme. The grid convergence rate p is calculated for these 4 schemes. The grid refinement factor r is set to a value of $r = 1.5$. The minimum value of the u-velocity

Table A.1: Parameters used in the Lid Driven Cavity case at $Re = 100$.

Reference	Disc. method adv.	Grid	$u_{max}\,[m/s]$
present	CDS	145×145	0.213384
present	CDS	97×97	0.212606
present	CDS	65×65	0.210894
present	Upwind	145×145	0.207264
present	Upwind	97×97	0.203899
present	Upwind	65×65	0.199048
present	Quick	145×145	0.213470
present	Quick	97×97	0.212788
present	Quick	65×65	0.211297
present	TVD (van Leer)	145×145	0.213541
present	TVD (van Leer)	97×97	0.212926
present	TVD (van Leer)	65×65	0.211572
Botella and Peyret (1998)	Spectral	$N = 96$	0.2140424
Botella and Peyret (1998)	Spectral	$N = 64$	0.2140424
Botella and Peyret (1998)	Spectral	$N = 48$	0.2140424
Ghia et al. (1982)	Upwind	129×129	0.21090

at center line, u_{min}, is choosen as the solution at which the convergence rate is determined, i.e. $f_{1,2,3}$. Three grid resolutions are used. The coarsest, intermediate and finest grid has a number of subdivisions of $n_x \times n_y = 65 \times 65$, $n_x \times n_y = 97 \times 97$ and $n_x \times n_y = 145 \times 145$ respectively. The time step, Δt is taken here 0.0005 $[s]$ for all the grid resolution and is sufficiently small to have no influence on the outcome of the calculation. In table Table A.1 the maximum value of the u-velocity is given. The convergence rate p is estimated by substituting the maximum value of the u-velocity, of the successively refined grids, in Eq. (A.1). The convergence rate, p, is given is in Table A.2. It is seen from this table that the convergence rate, $p \approx 2$, for CDS, Quick and TVD schemes. For the Upwind case the convergence rate p is $p \approx 1$. Note that the rate of convergence of the Quick scheme is $p = 3$, here it is $p \approx 2$. The difference can be explained by the discretization of the diffusive terms. The diffusive terms are second-order accurate in space.

Table A.2: Convergence rate p, see Eq. (A.1)

Method	convergence rate p
CDS	1.9465
Upwind	0.9023
Quick	1.9279
TVD (van Leer)	1.9422

Appendix B

Tensors are commonly applied in various disciplines of physics, such as the fluid dynamics, mechanics of materials or electricity. Tensors describe a physical phenomenon of a material and the relation between this phenomenon and a material property. In this appendix, some properties of tensors are discussed. The subjects elaborated in this appendix, are discussed in more detail in Prager (1989).

B.1 Tensors and invariants

First, a tensor is introduced, here the symmetric (3×3) stress tensor is taken for now. The symmetrical stress tensor, T_{ij}, is given as:

$$\mathbf{T} = T_{ij} = \begin{bmatrix} T_{11} & T_{12} & T_{13} \\ T_{21} & T_{22} & T_{23} \\ T_{31} & T_{32} & T_{33} \end{bmatrix} \tag{B.1}$$

The elements of this tensor are shown in Figure B.1 on an infinitesimal volume. An important property of tensors are the so-called invariants. Invariants of tensors are scalars and constant in any reference frame. First three invariants

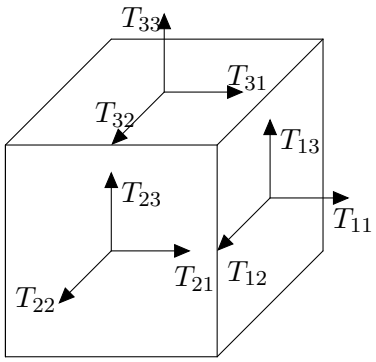

Figure B.1: Stresses on an infinitesimal volume.

are introduced:

$$\begin{aligned}
\bar{J}_1 &= tr(\mathbf{T}) = T_{ii} \\
\bar{J}_2 &= tr(\mathbf{T}^2) = T_{ij}T_{ji} \\
\bar{J}_3 &= tr(\mathbf{T}^3) = T_{ij}T_{jl}T_{li}
\end{aligned} \tag{B.2}$$

where $\bar{J}_i$ for $i = 1, 2, 3$ are the first, second and third invariant of a tensor, in this case the symmetric stress tensor. Using these invariants the basic invariants can be composed, namely:

$$\begin{aligned}
J_1 &= \bar{J}_1 = tr(\mathbf{T}) \\
J_2 &= \frac{1}{2}\left(\bar{J}_2 - \bar{J}_1^2\right) = \frac{1}{2}\left(\mathrm{tr}(\mathbf{T}^2) - (\mathrm{tr}\mathbf{T})^2\right) \\
J_3 &= \frac{1}{6}\left(\bar{J}_1^3 - 3\bar{J}_1\bar{J}_2 + 2\bar{J}_3\right) = \\
&\frac{1}{6}\left((\mathrm{tr}\mathbf{T})^3 - 3\mathrm{tr}(\mathbf{T}^2)(\mathrm{tr}\mathbf{T}) + 2\mathrm{tr}(\mathbf{T}^3)\right) = \det\mathbf{T}
\end{aligned} \tag{B.3}$$

when the trace of a tensor is zero, or $\mathrm{tr}\mathbf{T} = 0$, the tensor is said to be deviatoric. In this case the three invariants, given Eq. (B.3), reduce to:

$$\begin{aligned}
J_1 &= 0 \\
J_2 &= \frac{1}{2}\bar{J}_2 = \frac{1}{2}\mathrm{tr}(\mathbf{T}^2) \\
J_3 &= \frac{1}{3}\bar{J}_3 = \frac{1}{3}\mathrm{tr}(\mathbf{T}^3)
\end{aligned} \tag{B.4}$$

B.2 Deformation tensor

Here the deformation deformation tensor is elaborated. As will be shown in the next paragraph, the second invariant of the deformation tensor is an important variable modeling turbulence and non-Newtonian flow. The deformation or strain rate tensor is, in a 3D Cartesian coordinate system, the following:

$$\mathbf{S} = S_{ij} = \begin{bmatrix} \frac{\partial u}{\partial x} & \frac{1}{2}\left(\frac{\partial u}{\partial y} + \frac{\partial v}{\partial x}\right) & \frac{1}{2}\left(\frac{\partial u}{\partial z} + \frac{\partial w}{\partial x}\right) \\ \frac{1}{2}\left(\frac{\partial v}{\partial x} + \frac{\partial u}{\partial y}\right) & \frac{\partial v}{\partial y} & \frac{1}{2}\left(\frac{\partial v}{\partial z} + \frac{\partial w}{\partial y}\right) \\ \frac{1}{2}\left(\frac{\partial w}{\partial x} + \frac{\partial u}{\partial z}\right) & \frac{1}{2}\left(\frac{\partial w}{\partial y} + \frac{\partial v}{\partial z}\right) & \frac{\partial w}{\partial z} \end{bmatrix} \tag{B.5}$$

the deformation tensor is traceless for an incompressible fluid, the second invariant of the deformation becomes, see Eq. (B.4):

$$I_2 = \frac{1}{2} SijSji = \frac{1}{2}\mathrm{tr}(\mathbf{S}^2) \tag{B.6}$$

for a symmetrical tensor, which is the case in Eq. (B.5), the second invariant is also given as:

$$I_2 = \frac{1}{2} SijSij = \frac{1}{2}\mathrm{tr}(\mathbf{S}^2) \tag{B.7}$$

Now expanding the second invariant, in a 3D Cartesian coordinate system, yields:

$$\begin{aligned} I_2 = & \frac{1}{2}\left\{ \frac{\partial u}{\partial x}^2 + \frac{\partial v}{\partial y}^2 + \frac{\partial w}{\partial z}^2 + \right. \\ & \left. \frac{1}{2}(\frac{\partial u}{\partial y} + \frac{\partial v}{\partial x})^2 + \frac{1}{2}(\frac{\partial u}{\partial z} + \frac{\partial w}{\partial x})^2 + \frac{1}{2}(\frac{\partial v}{\partial z} + \frac{\partial w}{\partial y})^2 \right\} \end{aligned} \tag{B.8}$$

B.3 Cayley–Hamilton theorem

The Cayley-Hamilton theorem states that every square matrix $\mathbf{A}$ satisfies its own characteristic equation. Here the theorem is discussed using the tensor $\mathbf{T}$, see Eq. (B.1). Now the characteristic equation of tensor $\mathbf{T}$ can be found as follows:

$$p(\lambda) = \det\left[\mathbf{T} - \lambda\mathbf{I}\right] \tag{B.9}$$

in which $\mathbf{I}$ is the unity matrix. By expanding the determinant Eq. (B.9) the characteristic equation is obtained:

$$\lambda^3 - J_1\lambda^2 - J_2\lambda - J_3 = 0 \tag{B.10}$$

again here J_1, J_2 and J_3 are the first second and third invariant respectively defined earlier. The characteristic equation, Eq. (B.10), is used to define the following equation:

$$p(\mathbf{X}) = \mathbf{X}^3 - J_1\mathbf{X}^2 - J_2\mathbf{X} - J_3\mathbf{I} = 0 \tag{B.11}$$

substitution of $\mathbf{X} = \mathbf{T}$ in the equation given above, yields:

$$p(\mathbf{T}) = \mathbf{T}^3 - J_1\mathbf{T}^2 - J_2\mathbf{T} - J_3\mathbf{I} = 0 \tag{B.12}$$

by rewriting the equation it can be seen that $\mathbf{T}^3$ is a linear combination of the tensors $\mathbf{T}^2$, $\mathbf{T}$ and the unity matrix $\mathbf{I}$, or:

$$\mathbf{T}^3 = J_1\mathbf{T}^2 + J_2\mathbf{T} + J_3\mathbf{I} \tag{B.13}$$

B.4 Visco-plastic material

A yield criterion describes a three-dimensional stress state. This is a mathematical relation between stress components. In order for the material to yield this relation must satisfy a certain condition. This can condition is formulated as follows:

$$f = J_2 - \tau_0^2 = 0 \tag{B.14}$$

in which the yield function f depends on the second invariant of the stress tensor, J_2, and the yield stress, τ_0. This is the *von Mises* yield criterion. Now the yield function, Eq. (B.14), is reformulated into the following form:

$$F = 1 - \frac{\tau_0}{\sqrt{J_2}} \tag{B.15}$$

and introducing the constitutive relation of a visco-plastic material, a Bingham material:

$$2\eta S_{ij} = \begin{cases} 0 & \text{for} \quad F < 0 \\ F\,T_{ij} & \text{for} \quad F \geq 0 \end{cases} \tag{B.16}$$

from the second part of Eq. (B.16), $2\eta S_{ij} = F\,T_{ij}$, it can be seen that the deformation tensor, S_{ij}, depends on the stress tensor, T_{ij}. This needs to be rearranged in order to make the stress tensor dependent on the deformation. This is done by multiplying each side with itself:

$$4\eta^2 S_{ij} S_{ij} = F^2 T_{ij} T_{ij} \tag{B.17}$$

note here, that the de deformation and the stress tensor is symmetrical, so $T_{ij} = T_{ji}$ and $S_{ij} = S_{ji}$. Therefore, using the invariants defined in Eq. (B.4) and the yield function Eq. (B.15), Eq. (B.17) can be rewritten as follows:

$$4\eta^2 I_2 = F^2 J_2 = \left(\sqrt{J_2} - \tau_0\right)^2 \tag{B.18}$$

where I_2 is the second invariant of the deformation tensor, S_{ij}. It follows from Eq. (B.15) and Eq. (B.18) that:

$$F = \frac{\sqrt{J_2} - \tau_0}{\sqrt{J_2}} = \frac{2\eta\sqrt{I_2}}{\tau_0 + 2\sqrt{I_2}} \tag{B.19}$$

by substituting Eq. (B.19) in the second equation of Eq. (B.16), $2\eta S_{ij} = F\,T_{ij}$, the following equation is obtained:

$$2\eta S_{ij} = \frac{2\eta\sqrt{I_2}}{\tau_0 + 2\sqrt{I_2}} T_{ij} \tag{B.20}$$

and after rearranging Eq. (B.20) yields the expression of the stress tensor as a function of the deformation tensor:

$$T_{ij} = \left(2\eta + \frac{\tau_0}{\sqrt{I_2}}\right) S_{ij} \tag{B.21}$$

Appendix C

The surface integrals over the cell-faces of a CV is approximated with an integration method. The midpoint rule is addressed in this appendix. Although other integration methods exist, the midpoint rule is used in this work, due to its simplicity and ease of implementation, see Schaefer (2006) and Van Kan and Segal (1993). Examples of other integration methods are the trapezoid and the Simpson rule. More details on the midpoint, trapezoid and the Simpson rule can be found in Thomas and Finney (1996), Almering (1996) or Chapra and Canale (2010) for instance.

C.1 Midpoint rule

An integral of a function can be approximated by dividing an interval, $[a, b]$ of a function into, n, (equivalent) sections. Subsequently the function is evaluated at the midpoint of each section. By multiplying the evaluated function value with the section width, the area at each section is determined. Summation of these areas yields the integral if the function. Here the integral of the function is thought of as an area problem using known shapes. The shape is in this case a rectangle. Now consider the following integral of a function $f(x)$, with interval $[a, b]$:

$$\int_a^b f(x)dx \tag{C.1}$$

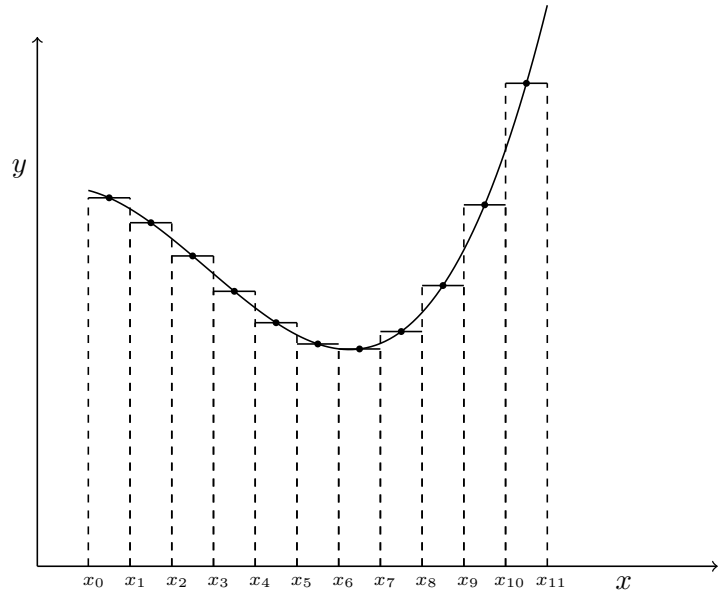

Figure C.1: Estimation of the integral of function $f(x)$ with the midpoint rule. Here the function is subdivided into $n = 11$ sections.

the interval $[a, b]$ is divided into n equal sections with width Δx:

$$\Delta x = \frac{b-a}{n} \tag{C.2}$$

where $a = x_0$ and $b = x_n$, as shown in Figure C.1 as an example for $n = 11$. The midpoint at i-th section between interval $[x_i, x_{i+1}]$ is given by:

$$x_i^* = \frac{x_{i+1} - x_i}{2} \tag{C.3}$$

where x_i^* is the midpoint. The approximation of the integral can be found using the midpoints with the following:

$$\int_a^b f(x)dx \approx \Delta x \sum_{i=0}^{n} f(x_i^*) = \frac{b-a}{n}(f_1 + f_2 + ... + f_n) \tag{C.4}$$

where f_i is defined as, $f_i = f(x_i^*)$.

Appendix D

The source term, which originates from the viscous terms, see Section 5.2.1, is treated in this appendix in more detail. First, the Navier-Stoke equations are expanded on a Cartesian coordinate system. Subsequently, the viscous terms are split into 2 terms. One of which is treated as a source term.

D.1 Viscous source term Navier-Stokes

Now, the Navier-Stokes equations are given in the following form:

$$\frac{\partial \rho\,\mathbf{u}}{\partial t} + \nabla \cdot (\rho\,\mathbf{uu}) = -\nabla p + \nabla \cdot \left(\mu \left(\nabla \mathbf{u} + \nabla \mathbf{u}^T\right)\right) + (\rho_s - \rho_w)\,\mathbf{g} \quad \text{(D.1)}$$

expansion of these equations in $2D$, using a Cartesian coordinate system, yields:

$$\frac{\partial \rho u}{\partial t} + \frac{\partial}{\partial x}(\rho u u) + \frac{\partial}{\partial y}(\rho v u) = \quad \text{(D.2)}$$
$$-\frac{\partial p}{\partial x} + 2\frac{\partial}{\partial x}\left(\mu \frac{\partial u}{\partial x}\right) + \frac{\partial}{\partial y}\left(\mu\left(\frac{\partial u}{\partial y} + \frac{\partial v}{\partial x}\right)\right) + (\rho_s - \rho_w)\,g_x$$
$$\frac{\partial \rho v}{\partial t} + \frac{\partial}{\partial y}(\rho v v) + \frac{\partial}{\partial x}(\rho v u) = \quad \text{(D.3)}$$
$$-\frac{\partial p}{\partial y} + \frac{\partial}{\partial x}\left(\mu\left(\frac{\partial v}{\partial x} + \frac{\partial u}{\partial y}\right)\right) + 2\frac{\partial}{\partial y}\left(\mu \frac{\partial v}{\partial y}\right) + (\rho_s - \rho_w)\,g_y$$

now the source term is obtained by splitting the viscous terms. For example, consider the two-dimensional u-velocity, in Eq. (D.3):

$$2\frac{\partial}{\partial x}\left(\mu\frac{\partial u}{\partial x}\right)+\frac{\partial}{\partial y}\left(\mu\left(\frac{\partial u}{\partial y}+\frac{\partial v}{\partial x}\right)\right)= \frac{\partial}{\partial x}\left(\mu\frac{\partial u}{\partial x}\right)+\frac{\partial}{\partial y}\left(\mu\frac{\partial u}{\partial y}\right)+s_u \tag{D.4}$$

where the source term, s_u, is the following:

$$s_u=\frac{\partial}{\partial x}\left(\mu\frac{\partial u}{\partial x}\right)+\frac{\partial}{\partial y}\left(\mu\frac{\partial v}{\partial x}\right) \tag{D.5}$$

the splitting of the viscous term for the v-velocity is similar.

Appendix E

This appendix gives an overview of the employed models throughout this thesis in the concerning chapters. The tables, Table E.1 and Table E.2, show the chapter and or section with references to the corresponding models and equations.

E.1 Model Overview

Table E.1: Overview of used models in the thesis.

Section	Case	Description
Section 6.1.1	Lid-driven cavity	Fractional-step method Explicit, Section 5.2.2
Section 6.1.2	Flow around a cylinder	Fractional-step method Explicit, Section 5.2.2
Section 6.1.3	Poiseuille flow of a Bingham fluid	Bingham model Eq. (2.12), Section 2.2.2 Fractional-step method Implicit, Section 5.2.2
Section 6.2	Turbulent flow between parallel plates	Fractional-step method Explicit, Section 5.2.2 WALE LES, Section 3.4.2
Section 6.3	Plane impinging slot jet	Fractional-step method Explicit, Section 5.2.2 WALE LES, Section 3.4.2
Section 6.4	Gravity currents	Fractional-step method Explicit, Section 5.2.2 WALE LES, Section 3.4.2 Variable density Transport Eqs., Section 5.1.1
Section 6.5	Sediment settling	Fraction transport Eq. (4.46) Hindered settling (poly-disperse), Eq. (4.99)
Section 6.6	Open-channel flow	Fractional-step method Explicit, Section 5.2.2 Fraction transport, Eq. (4.46) Hindered settling (poly-disperse), Eq. (4.99)

Table E.2: Overview of used models in the thesis (cont.).

Section	Case	Description
Section 7.5	Grav. collapse of rect. granular piles	Fractional-step metod Implicit, Section 5.2.2 Granular rheology, Section 7.3 Pore pressure, Section 7.4 Variable density Transport Eqs., Section 5.1.1 Hindered settling (mono-disperse), Eq. (4.99)
Section 8.2	Numerical calculation closed flume tests	Fractional-step method Implicit, Section 5.2.2 Granular rheology, Section 7.3 Pore pressure, Section 7.4 WALE LES, Section 3.4.2 Variable density Transport Eqs., Section 5.1.1 Hindered settling (poly-disperse), Eq. (4.99)

List of Publications

Journal Publications

J.C. Goeree, G.H. Keetels, E.A. Munts, H.H. Bugdayci, C. van Rhee *Concentration and velocity profiles of sediment-water mixtures using the drift-flux model*, The Canadian Journal of Chemical Engineering, 2016, 94, 1048-1058

Conferences

J.C. Goeree, G.H. Keetels, C. van Rhee, *Continuous flow modeling of soil and sand water mixtures*, CEDA Dredging Days 2015, Rotterdam, The Netherlands, 2015

J.C. Goeree, G.H. Keetels., C. van Rhee, E.A. Munts, H. H. Bugdayci, *Density and velocity profiles of non-dilute poly-disperse sediment water mixtures using the drift-flux model*, Hydrotransport 19 BHR Group, Denver CO, USA, 2014

J.C. Goeree, C. van Rhee, *Numerical simulation of hydrodynamical behavior of sand-water mixtures*, Proceedings of the 20th World Dredging Conference, WODCON XX, Brussels, Belgium, 2013

J.C. Goeree, C. van Rhee, H.H. Bugdayci, *Numerical sediment simulation using a continuous flow model*, 16th International Conference on Multiphase Production Technology, BHR Group, Cannes, France, 2013

J.C. Goeree, *Numerical simulation of sedimentation using the mixture model*, CEDA Dredging Days 2011, Rotterdam, The Netherlands, 2011

Curriculum Vitæ

Johannes Cornelis Goeree

30-12-1972	Born in Geldrop, The Netherlands.

Education

1985–1992	Secondary School Gymnasium Beekvliet, Sint-Michielsgestel
1992–2001	Mechanical Engineering Delft University of Technology
2010–2018	PhD, Offshore and Dredging Engineering Delft University of Technology

Thesis:	Drift-flux modeling of hyper-concentrated solid-liquid flows in dredging applications
Promotor:	Prof. dr. ir. C. van Rhee
Co-promotor:	Dr. ir. G.H. Keetels

Work Experience

2001–2006	Research Engineer, Koninklijke Boskalis Westminster
2006–2008	Research Engineer, Royal IHC
2008–2010	Senior Research Engineer, Royal IHC
2015–2018	Researcher (Blue-Mining), Delft University of Technology
2015–2018	Specialist, Royal IHC

Awards

2001	KNVTS Maritime Students Award
2001	VBKO Waterbouwprijs

Acknowledgements/Dankwoord

Alleerst wil ik mijn promotor Cees van Rhee bedanken. In 2009 benaderde hij mij met de vraag of promoveren niet iets is voor mij. Na een korte bedenktijd, heb ik deze kans gepakt, (wetende dat als ik het niet zou doen er mijn hele leven spijt van zou hebben). Tijdens mijn promotie heb ik genoten van alle discussies tijdens de koffie pauzes. Hierbij werden onder andere de leuke kampeerplekken in Frankrijk uitgewisseld. De samenwerking met Cees heb ik als bijzonder prettig ervaren en kijk met veel plezier terug op de periode tijdens mijn promotie.

Veel dank gaat uit naar mijn co-promotor Geert Keetels. Veel heb ik gehad aan de discussies over numerieke schemas. De uitleg over weerfenomenen en de vertaling hiervan naar het hydraulisch transport van zandwater mengsels vind ik zeer inspirerend.

Ik ben Royal IHC zeer dankbaar dat ik de kans heb gekregen om te promoveren. Vooral Henk van Muijen en Robert van de Ketterij ben ik zeer erkentelijk. Toen ik destijds aan Henk van Muijen vroeg of promoveren iets voor me was, zei hij dat dit een uitstekend idee was. Robert, bedankt voor alle steun van de afgelopen tijd, waarin de tijden niet altijd even makkelijk zijn geweest. Ook wil ik Edwin Munts bedanken die me waardevolle tips heeft gegeven over multigrids algoritmes en advectie schemas. Tevens heeft hij me altijd scherp gehouden met kritische vragen tijdens de voortgangsbijeenkomsten.

Verder wil ik Hassan Bugdayci bedanken voor het opzetten en begeleiden van dit project binnen IHC. Ik zag altijd uit naar onze twee wekelijkse voortgangs-discussies, waarin naast inhoudelijke, ook wereldse zaken werden besproken. Met name de reis naar een conferentie in Cannes staat me bij. Tijdens deze reis zijn we erachter gekomen dat een Fiat Punto een topsnelheid heeft van 190 km/u.

Mijn speciale dank gaat uit naar Jort van Wijk. Ik vond het prettig om de mooie verhalen aan te horen over de experimenten die werden uitgevoerd tijdens je promotie. Op conferenties heb ik genoten van je mooie voordrachten en de vele positieve reacties vanuit het publiek. Verder stel ik de huidige samenwerking bijzonder op prijs.

Leon Seijbel wil ik bedanken voor de steun en de aanmoedigingen tijdens de laatste loodjes van de promotie. Ik heb hier veel aan gehad in de laatste fase

van dit project.

In de laatste periode van de promotie vond ik het erg prettig om samen te werken met Tom Wambeke. Met name de lofzangen over de programmeertaal Python kon ik erg waarderen.

Tijdens mijn promotie heb ik verschillende studenten mogen begeleiden. Eén ervan is Rudy Helmons. Deze is later collega op de TU Delft en kamergenoot geworden. De vele gesprekken over de dagelijkse gang van zaken hebben me geholpen om anders tegen bepaalde zaken aan te kijken. Verder hoop ik onze samenwerking nog voort te zetten de komende tijd via de TU Delft.

Mijn kamergenoten Arno Nobel en Ralph van Rijswick wil ik bedanken. Ralph bedankt voor je goede vragen waardoor ik een beter begrip heb gekregen van de materie. Arno ik vond de samenwerking prettig, waarin ik de laatste fase heb mogen meemaken van je promotie. Hierdoor wist ik wat me nog te wachten stond. Ook wil ik Lynyrd de Wit en Rik Bisschop bedanken, aan wie in het begin van mijn promotie veel heb gehad, dankzij alle inhoudelijke discussies. Tevens de discussies over de vele sportevementen, zoals het WK voetbal en de tour de France, hebben bijgedragen aan het werkplezier.

Ik wil de mede promovendi, Dave, Bas, Xiuhan, Frans, Thijs, Eshard, bedanken voor de leuke tijd die ik heb gehad. Verder wil ik Ed Stok en Freek Brakel voor de hulp bij het opzetten van laboratorium experimenten. Ook wil ik Arno Talmon, Sape Miedema en Henk de Koning Gans bedanken. Ik heb veel van hen geleerd, met name om de huidige gang van zaken in de vakgroep in historisch perspectief te plaatsen.

Verder wil ik mijn fietsmaten Dirk Eekma, Koen Sueters, Marleen Platvoet, Peter Sueters en Martijn Lunter bedanken voor de afleiding die jullie me gaven tijdens het fietsen. Ik heb veel plezier beleefd (en nog steeds) aan de zondagse ritjes Schoonhoven, de tochten door het heuvelland van Zuid-Limburg en de helse beklimmingen in de Italiaanse Alpen.

Ook wil ik mijn ouders bedanken. Ze hebben altijd een luisterend oor en staan voor me klaar. Zonder hun steun was ik niet geworden wie ik nu ben. Verder wil ik mijn (schoon)familie bedanken voor de steun die ze hebben gegeven tijdens deze promotie. De verjaardagen, de kerstvieringen en familieuitjes gaven altijd iets om naar uit te zien en vormden een welkome afleiding.

Zoals altijd worden de belangrijkste personen in je leven in de laatste paragraaf

genoemd. Ik wil Joanne bedanken voor alle onvoorwaardelijke steun, zonder jou was dit project nooit mogelijk geweest. De ruimte, die je me hebt gegeven, en de opofferingen die je hebt moeten doen, geven aan hoeveel je van iemand houdt. Ik hoop nog lang te kunnen genieten van jouw aanwezigheid in mijn leven. Onze kinderen Floortje en Nina wil ik bedanken. Ik heb echt genoten van, onder andere, de vele uren die we hebben doorgebracht tijdens weekeinden op zolder. Hierbij was ik aan het werk en jullie waren, heel lief, allerhande knutselprojecten aan het uitvoeren. Deze creativiteit bewonder ik zeer en ik heb hier hele leuke herinneringen aan.